Multimodal assessment of coma and development of fMRI-based methods to study consciousness in the rat

Dissertation

zur Erlangung des Grades eines
Doktors der Naturwissenschaften

der Mathematisch-Naturwissenschaftlichen Fakultät
und
der Medizinischen Fakultät
der Eberhard-Karls-Universität Tübingen

vorgelegt
von

Patricia Pais Roldán
aus Madrid, Spanien

August - 2019

Tag der mündlichen Prüfung: 05/08/2019

Dekan der Math.-Nat. Fakultät: Prof. Dr. W. Rosenstiel
Dekan der Medizinischen Fakultät: Prof. Dr. I. B. Autenrieth

1. Berichterstatter: Dr. Xin Yu

2. Berichterstatter: Prof. Dr. Cornelius Schwarz

Prüfungskommission: Dr. Xin Yu

                              Prof. Dr. Cornelius Schwarz

                              Prof. Dr. Klaus Scheffler

                              Prof. Dr. Jan Born

Erklärung / Declaration:

Ich erkläre, dass ich die zur Promotion eingereichte Arbeit mit dem Titel: **"Multimodal assessment of coma and development of fMRI-based methods to study consciousness in the rat"** selbständig verfasst, nur die angegebenen Quellen und Hilfsmittel benutzt und wörtlich oder inhaltlich übernommene Stellen als solche gekennzeichnet habe. Ich versichere an Eides statt, dass diese Angaben wahr sind und dass ich nichts verschwiegen habe. Mir ist bekannt, dass die falsche Abgabe einer Versicherung an Eides statt mit Freiheitsstrafe bis zu drei Jahren oder mit Geldstrafe bestraft wird.

I hereby declare that I have produced the work entitled **"Multimodal assessment of coma and development of fMRI-based methods to study consciousness in the rat"***, submitted for the award of a doctorate, on my own (without external help), have used only the sources and aids indicated and have marked passages included from other works, whether verbatim or in content, as such. I swear upon oath that these statements are true and that I have not concealed anything. I am aware that making a false declaration under oath is punishable by a term of imprisonment of up to three years or by a fine.*

Tübingen, den ....
                      Datum / Date   Unterschrift /Signature

Contents

ABBREVIATIONS

B_0	static magnetic field
B_1	radiofrequency field
BOLD	blood oxygen level dependent
Ca	calcium
ChR_2	channel rhodopsin
CT	computerized tomography
DMN	default mode network
DOC	disorder(s) of consciousness
EEG	electroencephalography
γ	gyromagnetic ratio
GABA	gamma-aminobutyric acid
GCaMP	green fluorescent protein(GFP)-Calmodulin fusion protein
H^+	water proton
LC	locus coeruleus
LDT	laterodorsal tegmental nucleus
LFP	local field potential
LH	lateral hypothalamus,
M_0	longitudinal magnetization
M_{xy}	transversal magnetization
NMDA	N-methyl-d-aspartate
PAG	periaqueductal gray matter
PB	parabrachial nucleus
PET	positron emission tomography
PPT	pedunculopontine tegmental nucleus
R	raphe
REM	rapid eye movement
RF	radiofrequency
Ret.F	reticular formation
rs-fMRI	resting-state functional magnetic resonance imaging
RSN	resting state network
T	Tesla
T_1	longitudinal relaxation constant
T_2	transverse relaxation constant
T_2^*	effective T2 or T2-star
VLPO	ventrolateral preoptic nucleus of the hypothalamus
VTA	ventral tegmental area
ω_L	Larmor frequency

ABSTRACT

Despite the continuous research on human coma, some critical questions remain unanswered. For instance, why does the brain become unconscious? what is the reason why some patients awake from a coma while others remain in a persistent unresponsive syndrome? how does the brain recover from this radical unconscious state? The limitations inherent to human research (*e.g.* multiple etiologies, unfeasible timing, etc) harden identification of the key elements underlying the pathophysiology of coma and its recovery. The first goal of this PhD thesis is to provide a new platform whereby studying coma in a systematic and reliable manner is possible. We produced a model of brainstem coma in rats by causing brainstem ischemia. Once the procedure was established, I assessed the acute restoration of brain function using whole brain functional Magnetic Resonance Imaging during rest (rs-fMRI). Multi-modal analysis converged into the identification of a network composed of basal forebrain, basal ganglia and thalamus that seemed to participate in the reactivation of the cerebral cortex during early neurological recovery after coma. Methodologically, imaging the non-paralyzed rodent (*e.g.* non-anesthetized comatose animals) presents the challenge of identifying and eliminating potential motion artifacts derived from spontaneous breathing. To clarify this issue, in a parallel line of study, I imaged the brain of non-paralyzed anesthetized animals under different ventilatory rates and MRI repetition times. Spectral analysis of the acquired signals revealed a pronounced interference of the respiration on the fMRI data, which can be predicted and controlled, to an extent, by choosing appropriate ventilatory settings and sampling rates. Another important limitation of studying coma through fMRI in small animals is the fact that no behavioral assessment can take place inside the MRI scanner. To overcome this constraint, I established a multimodal fMRI platform that includes pupillometry to allow tracking arousal fluctuations in parallel to the MRI scanning. Besides setting up the platform for future animal fMRI studies assessing consciousness, this work identified a series of regions which oscillatory function co-vary with pupil dilations, which may constitute the first pupil-driven arousal network identified in rats and provides a way of tracking pupil-governed brain state changes from the fMRI data. Last, in view of a potential work merging fMRI with stimulation of deep brain structures like the hypothalamus, which appeared overshadowed in the rat coma study, I contributed to implementing an MRI-compatible robotic arm to precisely position optical fibers (for stimulation or recording) into the rat brain. This tool has proven to increase the successful rate and reliability of deep brain targeting in fMRI studies.

This thesis aims at providing a better understanding of the loss and recovery of consciousness by working with the rat as an animal model and fMRI as the main imaging modality. In addition, it attempts to resolve some of the challenges that emerge while performing brain imaging in small animals and presents novel platforms for the investigation of neural mechanisms related to arousal.

PART I. INTRODUCTION TO THE RESEARCH TOPIC

1. CONSCIOUSNESS AND THE UNCONSCIOUS BRAIN

We understand, to an extent, how brain cells work, how they can communicate with each other and how certain groups of neurons are responsible for the transmission of specific signals, but, how do we become aware of those signals? In other words, how are we conscious? What makes the brain of a comatose patient different from that of a person who is just sleeping? While the differences between sleep and wakefulness are beginning to be understood, other unconscious states that emerge upon brain injuries remain largely unknown.

Every day, hundreds of patients enter a coma or other disorders of consciousness (DOC) for a broad diversity of reasons. The rate of chronic patients which brain has "switched off" has especially increased in the last 60 years upon introduction of the artificial ventilation into the clinical practice, which has made it possible for patients to survive live-threatening injuries. However, despite the large number of patients who live unconscious, the key biological mechanisms that fail in these patients remain to be better characterized. To date, there is no standard treatment for coma (although a few individual cases have shown signs of improvement after particular treatments [1-3]); instead, most patients receive symptomatic therapy only, which contributes to stabilize the physiological parameters but does not lead to higher neuropsychological states.

This thesis is intended to facilitate animal research in the field of consciousness, which ultimately should translate into finding potential treatments for DOC patients.

1.1. A short comment about the conceptualization of consciousness

The concept of consciousness has been a topic of interest since the oldest civilizations [4]. In the 2nd century, Galen conducted an experiment on a pig that consisted on the resection of the laryngeal nerves (branch of the cranial nerve X) and produced loss of vocalization [5], which probably constituted the first proof in favor of the brain as the organ that controls the actions of the body [5-7]. In the 17th and 18th centuries, the first psychological definition of Consciousness (*Bewusstsein* in German, *conscientia* in Latin) was provided by Descartes [8], and the term was included in Chamber´s Cyclopedia [9]. Consciousness was presented as either "the reflex act by which a man knows his thoughts to be his own thoughts", "the direct act of thinking or simple sensation", or "the power of self-motion or of beginning of motion by the will" [10, 11]. A series of works have reviewed the multiple discussions concerning the term *consciousness* over the years [10, 12-14]. In the 21th century, consciousness is scientifically described as the state of awareness of one self and of the environment [15-17].

### 1.2. The requirements of consciousness and the unconscious states

In order for a living being to be considered as conscious, it needs to be aroused (awake) and it needs to show signs of internal and external awareness. The most severe disorder of consciousness is *coma* (or brain death, if non-reversible states are considered). A person in coma does not have sleep-wake cycles,

is not aware of him/herself or of the environment and cannot be awaken. Usually, brainstem reflexes are absent during coma, and vital functions, like respiration, may be insufficient, making artificial ventilatory support necessary. In contrast to coma, a sleeping person, although not aware of the surroundings, is self-sufficient and can be awaken with supra-threshold stimulation. **Section 1.4** will briefly discuss how sleep, a natural and necessary state of unconsciousness, differs from pathological coma.

1.3. Disorders of consciousness in the brain-injured patient

Consciousness is not an "all or nothing" condition, an example of it being the different states through which a comatose patient may transit until full recovery (see **Figure 1**). When the brainstem is able of supporting vital functions (*e.g.* respiration, thermoregulation) and exhibiting a certain level of arousal, perceived mainly as eye opening and closing, patients are described as in a *vegetative state*, also called *unresponsive wakefulness state* and previously wrongly referred as *apallic syndrome* ("without cortex"). Many of these patients can evolve to a *minimally conscious state "–"*, with sleep wake cycles and voluntary behaviors like visual tracking or localization of pain or emotions, but low level response to command, and to a *minimally conscious state "+"*, with responses to verbal command. Some of these patients can evolve to a near-normal behavior after transiting through a state of awareness with signs of confusion.
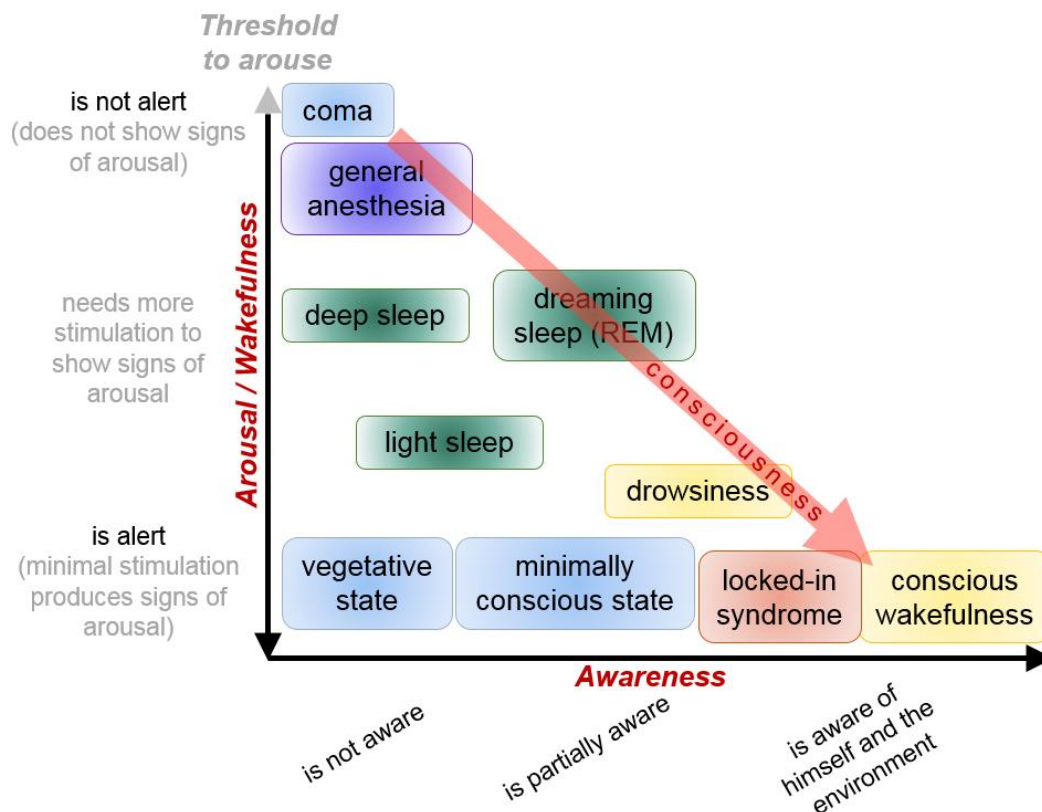
Figure 1. States of consciousness organized by their level of arousal and awareness. *Typical states encountered after brain injuries are shown in blue-shadowed boxes, sleep states are in green, and awake states are in yellow.*

9

Human coma scales have been designed that quantify the behavioral responses of these patients and provide a neuropsychological diagnosis (*section 3* introduces some methodologies used to track the level of consciousness). The differentiation between states of impaired consciousness and the *locked-in syndrome*, characterized by a full awareness that is antagonized by motor unresponsiveness, is one of the most critical steps in the diagnostic process and it largely relies on neuroimaging techniques able of detecting brain activity independently on the behavioral responses displayed by patients (*e.g.* fMRI or EEG-based brain-computer interfaces) [18-21].

1.4. Coma vs. anesthesia vs. sleep. More than one unconscious brain

While the behaviors of a comatose patient, a healthy sleeping subject and a person under anesthesia can seem very similar, the nature of these states is entirely different: sleep is a regulated physiological condition that returns spontaneously to the awake state or is easily resumed with supra-threshold stimulation [22, 23]; anesthesia causes a reversible and dose dependent unresponsive unconscious state [24]; coma is a pathological condition where there is a slow uncertain recovery [25]. In contrast to the presumably different source of unconsciousness, the recovery from anesthesia shows a strong parallelism with that observed from coma patients, although the first one happens at a much faster speed. In both cases, recovery of vital functions takes place first, with later regaining of brainstem reflexes and of voluntary movements and, eventually, evidence of awareness.

The apparent similarity between coma and general anesthesia explains the large number of studies that use general anesthesia in healthy volunteers to investigate potential routes of recovery of consciousness. Nevertheless, neither the mechanisms of coma pathogenesis or recovery, nor the ones underlying anesthesia-induced loss and recovery of consciousness have been completely elucidated. Although there are reports pointing to specific subcortical structures that may mediate the generalized anesthetic effects [26, 27], the multiple sites of action of general anesthetics harden identification of their precise mechanisms of action in the brain. Anesthetics usually bind to inhibitory neurotransmitter receptors (*e.g.* $GABA_A$ agonists) or block excitatory neurotransmitter receptors (*e.g.* NMDA receptor antagonists). $GABA_A$ from interneurons can trigger inhibition of a large population of cortical pyramidal neurons, leading to unconsciousness, but it can also affect nuclei in the ventral medulla or pons, causing cardio-respiratory depression, as well as the ponto-medullary-spinal cord pathways, inhibiting the control of anti-gravitational muscles and causing hypotonia. In contrast to the hypotonia caused by general anesthetics, comatose patients or subjects in slow wave sleep may preserve muscle tone [24], further indicating a different nature of the unconscious state in natural vs. anesthesia-driven unconscious conditions.

Recordings of cortical activity offer a direct measure of brain function. While several well-studied electrophysiological stages are observed from scalp EEG during sleep that reflect the cyclic sleep depth, coma EEG varies largely across subjects and is rather monotonous, although it may resemble particular electrophysiological features of sleep, like slow waves [24, 28, 29]. Certain types of cortical (in)activity are

compatible with both coma and general anesthesia, but not with sleep, like burst-suppression patterns or isoelectricity. The electrophysiological differences between sleep, general anesthesia and coma further emphasize the uniqueness of each one of these unresponsive states, which translates into the need of specific experimental designs to completely understand any one of the three unconscious conditions. Hence, although anesthesia-related studies may shed light into the potential mechanisms of loss and recovery of consciousness, a platform where the natural comatose state can be recreated and reproduced is needed to identify targets that may help awaken patients from their pathological coma. **Table 1** summarizes the main differences between the three unconscious conditions.

Table 1. Comparison between the three main unconscious states: sleep, anesthesia and coma.

UNCONSCIOUS STATE	SLEEP	ANESTHESIA	PATHOLOGICAL COMA
Reversibility	Reversible naturally (spontaneously) or with stimulation.	Reversible, dose dependent.	Variable. If reversed, at a longer time scale.
Main centers involved	- Brainstem - Hypothalamus - Basal forebrain	Diversified and drug-dependent. Mostly: - Brainstem - Cortex - Thalamus	Unclarified and etiology-dependent. Probably: - Brainstem - Cortex - Thalamus
Trigger	Circadian rhythms or homeostatic sleep drivers that switch between the mode governed by wake-promoting (monoaminergic cells from Ret.F, orexinergic LH, cholinergic PPT/LDT) and sleep promoting (GABAergic VLPO) centers.	Drug-dependent. Mainly: GABA$_A$ rec. agonists, NMDA rec. antagonists, K+ channel activators.	The primary cause is variable (traumatic / non traumatic brain injuries). The exact mechanism that causes coma is unknown.
Typical underlying cortical activity	NREM (I→IV): towards waves of low frequency and big amplitude. Particular hallmarks in some stages (*e.g.* spindles or K-complexes). REM: high frequency and small amplitude waves (accompanied by rapid eye movement).	Low frequency - high amplitude waves (chosen for surgery), burst suppression or isoelectricity (chosen for brain protection).	Variable. Commonly, slow wave rhythms or burst suppression patterns (but see reference [29]).

Abbreviations: LH: lateral hypothalamus, LDT: laterodorsal tegmental nucleus, NREM: non-REM, Ret.F: reticular formation, PPT: pedunculopontine tegmental nucleus, REM: rapid eye movement (dreaming sleep), VLPO: ventrolateral preoptic nucleus of the hypothalamus.

2. THE CHALLENGE OF INVESTIGATING COMA FROM HUMAN PATIENTS

Despite the potential similarity between the behaviors displayed by different comatose patients, the leading cause of coma usually differs from one subject to another, which makes the study of pathological (un)consciousness complex and of unattainable generalization. Coma can be caused by a traumatic or a non-traumatic brain injury, with the last one including strokes, anoxic injuries (*e.g.* respiratory failure, cardiac arrest), or brain damage produced by poisoning or metabolic causes (*e.g.* hypoglycemia, hypothermia) [25, 30]. Brainstem strokes cause a direct damage to the reticular activating system, anoxic injuries cause a generalized brain damage, and traumatic accidents are associated to a breakdown in the pathways connecting the brainstem arousal systems with diencephalic structures such as the thalamus and the basal forebrain [31, 32]. As the kind of brain insult varies among comatose patients, a single cause is unlikely to mediate the process of becoming unconscious. However, it is possible that a single circuit is ultimately responsible for the maintenance of consciousness and that different parts of it are selectively affected in each comatose scenario. The dissection of such circuit, by confirming either recovery or loss of consciousness upon its natural or deliberate activation or inhibition, respectively, is a critical task that should be fulfilled to help guide consciousness-promoting therapies.

Human reports provide true but subject- and injury-specific insights into the potential targets of consciousness. In contrast, animal studies using coma models could provide reliable targets for coma treatment, from highly homogeneous samples, of potential translation to the human. Current approaches to investigate the correlates of consciousness in animals are mostly based on anesthesia [33-35], although purposeful lesion of specific nuclei [36] and activation or inhibition of others [27, 37-40] has also been performed that has provided a good understanding of the brain structures that are involved in the transition between wakefulness and unconsciousness [41]. Models to mimic coma after cardiac arrest or percussion models to reproduce traumatic coma have also been reported [42-46], which constitute a good platform to investigate the biological mechanisms behind those coma types. However, it is known that the brain damage after cardiac arrest or traumatic brain injury implies diffuse injuries, swelling or multi-focal lesions involving axonal shearing, which hardens the investigation of the primary players mediating unconsciousness [47-49]. In this PhD work, a coma model was created in rats by disrupting the vasculature that irrigates the main arousal centers in the brainstem (***attached manuscript 1***). The chosen strategy involves injection of the vasoconstrictor endothelin-1 into the pontine parenchyma (basilar artery territory) and is intended to directly interfere with the brainstem function to disrupt arousal, and hence consciousness. The procedure can be used to induce brainstem coma in rats and track the neural dynamics during the immediate aftermath of coma (1 to 6 hours after the comatose insult), which is currently not possible in human coma research.

3.   RESEARCH APPROACHES TO STUDY CONSCIOUSNESS

To have a complete understanding of a particular subject's coma, three main parameters must be taken into account: behavioral performance, anatomical integrity and brain function (*Table 2*). Behavioral tests constitute an efficient tool to provide diagnosis of the neuropsychological state. Following the behavioral assessment, patients undergo a structural scan to investigate the potential injuries that have led to the comatose state. A brain functional assessment (*e.g.* with EEG) can be performed after stabilization to make a prognosis. More detailed functional imaging (*e.g.* fMRI) is usually carried out at later times and mostly with a research purpose.

Table 2. Main methodologies to study consciousness.

Measure	**Behavior**	**Brain lesions**	**Brain function**
Possible tests (for humans, humans or rodents, or rodents)	**"Glasgow Coma Scale"** **"Full Outcome of UnResponsiveness"** **"Coma Scale Revised"** **"Rat Coma Scale"** **Pupillometry**	CT MRI	rs-fMRI PET EEG **LFP / Ca imaging**
Usefulness of the measure	Rate the level of consciousness	Identify the potential cause of unconsciousness	Corroborate the level of consciousness / make prognosis / do research (find the biological signature of unconsciousness)

In the following, a short introduction about the methodologies used in the evaluation of the unconscious patient is provided.

3.1. Measuring behavior

Human **coma scales** have been developed to quantify the neurological function based on the behavioral performance. Among the main measures examined in these scales are: eye opening, eye tracking, verbal response, motor response, auditory function, communication capabilities, brainstem reflexes and respiration (the main features of the three most common human coma scales can be compared on **Table 3**). In some cases, a particular score threshold is provided on the scale that categorizes the neurological state (*e.g.* a score below 8 in the Glasgow Coma Scale denotes coma –maximum is 15-). Occasionally, electromyography is incorporated into a test to reliably detect muscle contractions that may indicate motor response in patients with reduced mobility [50]. Similarly, EEG could be used to facilitate the detection of responses to auditory stimulation [51]. It is worth noting that, while a positive response to command usually

indicates the presence of consciousness, failure to detect evoked signals does not imply unconsciousness, as it is possible that specific pathways that are needed to process the order are selectively impaired.

Animal neurological scales have been designed to track impaired behaviors mostly after stroke (which usually results in motor deficits) but also after other brain injuries possibly resulting in coma [43, 52, 53]. Nevertheless, no standard measure has been previously presented as a rat coma scale. In the ***attached manuscript 1***, we present the development of a rat coma scale and comment on the challenges that emerge when designing a tool for neurological assessment of coma in rats.

Pupil changes in response to light are evaluated as part of the brainstem reflexes tested in some coma scales. Dilations are controlled by noradrenergic fibers of the sympathetic system that contract the pupil dilator muscle, while constrictions depend on acetylcholinergic fibers of the parasympathetic system that act on the iris sphincter muscle. The pupillary reflex measures the integrity of the circuitry involved in pupil constriction upon light stimulation (cranial nerves II and III, and the pretectal and Edinger-Westphal nuclei of the midbrain) and it is thus a good indicator of brainstem damage.

Eye tracking software can be additionally implemented to assess the degree of interaction of the patient with the environment [54]. Besides the pupil response to light and the movement of the eyes, the spontaneous fluctuations of the pupil size in the absence of stimulation can be used to assess consciousness in human subjects. Passive dilations of the pupil have been demonstrated to reflect arousal, attention and cognitive or emotional processing in humans and non-human animals [55-57]. Thus, the establishment of **pupillometry** can provide a direct measure of arousal in individuals with otherwise low communication capabilities.

When combined with other methodologies like fMRI, pupillometry can help identifying brain networks involved in arousal. Although several research centers have established this multimodal approach in humans and identified specific networks in the brain that presumably reflect the level of pupil-based arousal, translational studies using fMRI to study consciousness in rodents have not yet investigated the relationship between the brain networks and the passive dilations of the pupil, mainly due to the challenging environment of small animal MRI (*e.g.* small bore size and high magnetic fields). The merging of brain function and its behavioral output is a critical step to understand conscious processing, and a platform allowing to study both simultaneously in animals would amplify our knowledge on this matter, as invasive manipulations of the brain could be easily incorporated to dissect the neural correlates of consciousness. In one of the works carried out during this PhD, a platform was established that combined fMRI with concurrent pupillometry and calcium imaging in rats (***attached manuscript 2***). This approach allowed us to analyze the neural dynamics of the whole brain in parallel to the spontaneous fluctuations of the pupil size in anesthetized animals. Results from this multimodal study suggest the existence of pupil-governed oscillatory states that correlate with an fMRI pattern involving most cortical areas, thalamus, superior colliculus and the noradrenergic group A5 of the brainstem.

Table 3. Comparison of the three main human coma scales: the Glasgow Coma Scale [58], the Coma Scale Revised [59] and the Full Outcome of Unresponsiveness [60].

	Glasgow Coma Scale		Coma Scale Revised		Full Outcome of UnResponsiveness
RESPIRATION				4	Not intubated, regular breathing
				3	Not intubated, Cheyne-Stokes
				2	Not intubated, irreg. breathing
				1	Breathes above ventilator rate
				0	Breathes with ventilator / apnea
BRAINSTEM REFLEXES				4	Pupil + corneal
				3	One pupil wide and fixed
				2	Pupil or corneal
				1	No pupil or corneal, only cough
				0	No pupil, corneal or cough
EYE RESPONSE / AROUSAL	4	Spontaneous eye open.	3	Attention	4	Eye open.+ track / blink to command
	3	Eye open. to speech	2	Eye open. without stim.	3	Eye open. but no track
	2	Eye open. to pain	1	Eye open. with stim.	2	Eye open. to loud voice
	1	Eyes closed	0	Eyes closed	1	Eye open. to pain
					0	Eyes closed
MOTOR RESPONSE	6	Obeys command	6	Functional object use	4	Obeys hand position
	5	Pain localization	5	Automatic motor response	3	Pain localization
	4	Normal flexion withdrawal	4	Object manipulation	2	Normal flexion withdrawal
	3	Abnormal flexion to pain	3	Pain localization	1	Abnormal extension to pain
	2	Abnormal extension to pain	2	Normal flexion withdrawal	0	No response/myoclonus
	1	No response	1	Abnormal posturing		
			0	No response / flaccid		
VERBAL RESPONSE / COMMUNICATION	5	Oriented	3	Intelligible verbalization		
	4	Confused	2	Vocalization / oral movement		
	3	Inappropriate words	1	Oral reflexive movement		
	2	Incomprehensible sounds	0	None		
	1	No response	2	Functional: accurate		
			1	Non-functional: intentional		
			0	None		
AUDITORY FUNCTION			4	Consistent mov. to command		
			3	Reproducible mov. to command		
			2	Sound localization		
			1	Auditory startle		
			0	None		

VISUAL FUNCTION	**5**	Object recognition
	4	Object localization (reaching)
	3	Visual pursuit
	2	Fixation
	1	Visual startle
	0	None

Score range: **3 - 15**	Score range: **0 - 23**	Score range: **0 - 16**

3.2. Detecting abnormalities in brain structures

In order to better understand the brain damage behind the unconscious state, anatomical images of the brain are needed. A **computed tomography (CT)** scan is the primary imaging modality performed upon admission of the patient into a hospital to distinguish between traumatic and non-traumatic causes of coma [61]. CT produces cross-sectional X-ray images of the brain which can be reconstructed into a 3D volume, where tissues are differentiated based on their density (*i.e.* on their ability to "stop" the X-rays). Additionally, contrast agents may be administered to provide better contrast of soft tissues and detect hemorrhage [62]. The main advantage of CT is that it is inexpensive and relatively fast, although it has the disadvantage of exposing the body to ionizing radiation.

In contrast to the X-ray based CT, **MRI** is a complex technique that uses a combination of high static magnetic field (B_0) and radio frequency (RF) pulses (B_1 field) to generate images with a highly diversified variety of contrasts. All works presented in this thesis use MRI as the main imaging methodology.

The most common MRI sequences are based on the detection of the hydrogen proton (H^+) throughout the body. When H^+ is exposed to a B_0, its magnetic moment precesses around the B_0 axis (i.e. the longitudinal axis of the MRI scanner) at a frequency equal to its gyromagnetic ratio (γ, 42,52 MHz/T) multiplied by the B_0 strength ($B_0 = 14T$, for the work performed in this thesis). This precession rate is called Larmor frequency (ω_L), and it defines the velocity at which H^+ precesses in a particular B_0 (**Equation 1**).

$$\omega_L = \gamma\, B_0$$

Equation 1. Larmor equation.

The sum of all the magnetic moments of all H^+ spins aligned with B0 results on a net longitudinal magnetization (M_0). H^+ spins that are precessing around the z axis (parallel to B_0) can be tilted towards the x-y plane by applying an on-resonance RF pulse, matching the Larmor frequency, perpendicular to B_0. The rotation of spins from z to x-y occurs with a particular flip angle (α) that is proportional to the amplitude and duration of the RF pulse. This results on a loss of M_0 and the generation of transverse magnetization (M_{xy}) immediately after each RF pulse. After excitation, M_0 tends to regrow and M_{xy} becomes smaller, due to spin-lattice relaxation and spin-spin relaxation, respectively. The time required for M_0 to recover 63% of its

16

original value, after the RF excitation, is characteristic of each tissue and is called *longitudinal relaxation time constant* (T_1), responsible for the T_1 contrast, which distinguishes bright white matter from dark cerebrospinal fluid, for instance. The time after which M_{xy} has reduced to 37% of its original value is defined as the *transverse relaxation time constant* (T_2), which reflects spin-spin interactions that are, again, specific for each tissue (although the *transverse relaxation* can also be affected by B_0 inhomogeneities, in such case the time constant is called T_2^*). T_2 contrast allows to detect, for example, cerebrospinal fluid or cytotoxic edema (*e.g.* after stroke) that appear hyperintense in the MR image [63-67]. This contrast was used to detect cerebral damage in the rats subjected to vasoconstriction of the brainstem (**_attached manuscript 1_**) and its validity was demonstrated with post-mortem histopathology. T_2^* contrast is the basis of BOLD fMRI (see next section).

The selection of a particular repetition time (TR, or the time between excitation pulses) and echo time (TE, or the time between the RF pulse and the readout of the signal) determines the weighting of the MR image towards T_1, T_2 or proton-density contrast.

Although more expensive, the safety of MRI (it does not use ionizing radiation) and its major capacity to detect brain lesions places it as the preferred modality to track brain lesions. Due to the complexity and the promising capabilities of MRI, a broad line of research is devoted to the improvement of MR sequences to achieve higher temporal and spatial resolution with better contrast, which is placing it as the gold standard soft-tissue imaging technique for diagnosis of brain-injured patients [68].

3.3. Assessing brain function

The living brain encompasses a wide variety of networks whose dynamic functional connectivity (*i.e.* temporal correlation) is believed to support specific neurological states. Resting-state functional MRI (rs-fMRI) emerges as a technique that allows visualization of neural activity from all voxels within the brain with relatively high spatial resolution. Its most common contrast is naturally given by the content of oxy- vs. deoxy-hemoglobin in the blood (Blood Oxygen Level Dependent signal (BOLD)). BOLD fMRI relies on the fact that more active neuronal populations receive more oxygenated blood, which translates into higher MRI signals (oxy-hemoglobin is diamagnetic and produces a signal without dropout, compared to the deoxy-hemoglobin, which is paramagnetic and exhibits a fast decay). The process by which neuronal activity triggers more oxygenated blood towards the active locus is called neuro-vascular coupling, and the exact mechanism behind it constitutes a very active area of research (astrocytes are promising players to mediate dilation of the microvasculature near active neurons [69, 70], although they are not the only candidates [71]).

Fluctuations of the fMRI signal observed in synchrony from different areas during a task-negative paradigm (*i.e.* rest) can be used to uncover resting-state networks (RSN) which connectivity may modulate particular brain functions [72]. Biswal implemented, for the first time, a temporal correlation analysis between the time course of voxels in the sensorimotor cortex and all other time courses in the rest of the brain to identify

components of the sensorimotor network (seed-based analysis of connectivity) [73]. The general assumption is that signals that co-fluctuate proceed from connected structures. The study of RSN is becoming particularly useful in the diagnosis of diverse neurological conditions [74]. Especially, the resting state default mode network (DMN) has been reliably observed to decrease its connectivity as a function of the DOC severity, disappearing completely in brain death [74-76]. Besides its usefulness to diagnose neurological conditions and distinguish between groups of study, rs-fMRI can be used in longitudinal studies to track recovery from a brain insult. In the ***attached manuscript 1***, a voxel-wise analysis of connectivity was performed from the rs-fMRI acquired in rats every hour after the onset of coma. This strategy allowed to build a slope map (by concatenating the individual connectivity maps acquired at different post-coma times) and identified key structures that exhibited a longitudinal increase of connectivity and that may hence participate in the recovery from coma (see ***Figure 5 of the attached manuscript 1***).

Due to the indirect link between the neuronal activity and the BOLD signal, one of the challenges when performing rs-fMRI is to correctly differentiate between the neural-driven oscillations and other potential sources that may contaminate the fMRI signal. fMRI is extremely sensitive to motion (especially in high magnetic field MRI systems), which makes it vulnerable to head movements and physiological noise (*i.e.* heart beating and respiration). To clean-up the fMRI data, methods to detect and remove potential artifacts have been developed for human fMRI [77]. In contrast, the rodent fMRI community has not carefully investigated the potential influence of the physiological noise on the fMRI signal and current preprocessing pipelines are limited to motion correction. One of the works performed during this PhD (***attached manuscript 3***) evaluated the influence of the respiration on rat fMRI. Spontaneous breathing in non-paralyzed anesthetized animals is accompanied by thoracic motion, which translates into chest and neck movements that alter the homogeneity of B_0 and hence, causes image distortions. Due to the low temporal resolution of the fMRI studies (a minimum TR of 0.5s for whole brain rat fMRI in a high field MR scanner), the respiratory signal of rats (~1Hz) cannot be appropriately sampled, and an aliased signal (respiration signal down-sampled at 1/TR) emerges in the data. In this work (***attached manuscript 3***), we demonstrated that the spectral bandwidth of this artefactual signal can be narrowed by imposing mechanical ventilation (*i.e.* forcing the respiratory cycle to be constant during the whole scan), which facilitates post-hoc filtering. Furthermore, by using mechanical ventilation, the artifacts can be deliberately shifted to a certain frequency by imposing a slightly different ventilatory rate in the animal. Ventilated paralyzed animals, in which only the lungs are inflated during the inspiration process (*i.e.* no accessory muscles are involved) show a significantly smaller influence of breathing on the fMRI signal, and therefore studies involving paralyzing agents benefit from cleaner fMRI data. Nevertheless, in occasions it is not possible to paralyze the animal due to specific experimental requirements (*e.g.* in awake studies). This was the case for the study performed in comatose rats (***attached manuscript 1***), in which no drug was added to the animals in order to avoid potential biological differences between groups. In this scenario, an alternative solution consisted on acquiring control data from healthy anesthetized animals with similar breathing-derived motion and

assess the extent to which the respiration artifacts contributed to the observed results (see *Supplementary Figure 7 of the attached manuscript 1*).

A less expensive (and consecutively more broadly available) imaging technique to inform about the brain function in DOC patients is positron emission tomography (**PET**). PET relies on the detection of specific compounds labeled with a radio-active tracer that are injected intravenously. The most typical tracer molecule is fluoro-deoxyglucose (2-deoxy-18fluoroglucose), which is a glucose analog labeled with the radionuclide fluorine-18 that allows tracking glucose consumption in the brain. In the field of DOC, fluoro-deoxyglucose has been used to demonstrate the lower brain metabolic activity in patients lacking awareness (*i.e.* coma or vegetative state) [78, 79]. Using a different tracer (Oxygen-labeled water (H2(15)O)), regional cerebral blood flow measured in vegetative state patients demonstrated how the deficient thalamocortical connectivity was regained after patients recovered consciousness [80]. The main disadvantage of PET is the involvement of radio-active compounds and its lower temporal resolution (minutes) compared to fMRI. On the other hand, it is considerably less expensive, and it allows tracking specific metabolic processes in a more direct way (*i.e.* avoiding the assumption of normal neurovascular coupling).

In humans, the most common form of recording neurological activity is scalp **EEG**. EEG directly measures the current generated upon neuronal firing with high temporal resolution in a relatively cheap and portable manner, but it presents the disadvantage of having a low spatial resolution. While cortical regions are reliably mapped with scalp EEG, the inference about the activity of deeper brain areas constitutes a major challenge (the specific sources of the recorded activity are unknown, what is called the "inverse problem"). In invasive animal studies, this problem is solved by using thin electrodes that can be directly lowered at the desired positions within the brain parenchyma, which allows recording the activity of the local neuronal population (Local Field Potentials (LFP)). Cortical activity measured from a single electrode can be reliable enough to track radical neurological changes. For example, in the study of coma in rats subjected to diffuse brainstem injury, a single electrode demonstrated the radical evolution of cortical activity from isoelectricity (upon the comatose insult) to burst-suppression patterns and to slow rhythms during early recovery from coma (***Figure 3 of the attached manuscript 1***). Modern electrophysiology systems include denser electrode arrays that allow recording from multiple brain sites, which has proven to be a successful way of mapping specific brain areas with higher spatial resolution [81].

In invasive animal studies, an optical fiber connected to a photomultiplier or a two-photon microscope can be used to image the fluorescent signal emitted by the calcium-sensitive protein GCaMP to track neural activity at a specific location. By choosing specific promoters, GCaMP can be expressed in different cell populations (*e.g.* in particular groups of neurons or astrocytes), which makes this technique much more specific than the electrophysiological counterpart, while granting similar temporal resolution. Neuronal calcium imaging was used in combination with LFP to better understand the cortical changes occurring during coma induction in rats (***attached manuscript 1***). The fact that calcium imaging does not produce

electromagnetic interference allows its merging with fMRI (***attached manuscripts 2 and 4***), which constitutes another advantage of this technique over the conventional electrophysiology, which inclusion in fMRI measurements requires complex manipulation of the hardware. Using the same technical approach, other molecules different from calcium can also be imaged by expressing proteins that report fluorescent signals upon binding to different target molecules (*e.g.* glutamate sensitive proteins).

3.4. Studying the brain response to stimulation (evoked studies)

Most functional imaging techniques can be merged with stimulation paradigms to assess the integrity of specific circuits or to infer conscious processing.

Median nerve stimulation combined with EEG allows detection of a two-components-response in the healthy brain: an early local response in primary somatosensory cortex and a late signal spreading towards parietal areas [82] [83]. During unconsciousness, only a local early response remains [83]. The prevalence of cortical activation in remote areas can be considered as cortico-cortical effective connectivity, and is disrupted in early stages of non-REM sleep [84] and during anesthesia-driven loss of consciousness [82]. Therefore, the extent and timing of the evoked EEG response serves as a marker of consciousness. Alternatively, the brain response to a given stimulus can be analyzed in terms of information content through different methods [83, 85-88]. Studies using these approaches demonstrate that cortical activity must retain a certain complexity level and integrate multi-site information to allow conscious processing in the awake brain [89].

In fMRI, task-based paradigms that involve active thinking of the subject are useful for the differential diagnosis of syndromes like vegetative state vs. locked-in. For instance, the premotor cortex activates when a conscious subject is asked to imagine himself playing a sport [90]. In contrast, when subjects lack awareness, no behavioral responses nor fMRI-discovered cortical activation are observed.

Multimodal studies involving fMRI and cell-specific stimulation in animals offer the possibility of investigating circuit-specific dynamics. One of the main stimulation techniques in modern animal experiments is optogenetics, which involves expression of channel-rhodopsin (ChR_2, a light-activated cation channel) in the target area followed by delivery of blue light pulses to produce cell depolarization [91]. In contrast to electrical stimulation, optogenetics allows a much more specific interaction with the neural components, as the expression of ChR_2 is controlled by specific promoters and, therefore, activation upon stimulation occurs in a particular cell population only. Stimulating and recording the activity of neurons in deep nuclei in parallel to whole brain fMRI constitutes a promising methodology to dissect neuronal circuits of arousal. The main challenge of deep-brain optogenetic stimulation is the fact that targeting deep brain structures remains poorly reliable. Although brain atlases exist that provide approximate coordinates of the nuclei, the size of the animal brain is variable, and so is the skull from which coordinates are referenced, which results in limited successful rates when targeting small deep brain nuclei. In order to minimize the targeting error (a limiting factor in deep brain studies), a robotic arm was developed (***attached manuscript 4***) that allows

remote positioning of fibers (or cannulas for injection) with real time MRI feedback. This newly-developed positioning tool leads to reliable targeting and, hence, precise activation of neural circuits that can be studied through fMRI during variable conscious states.

Despite all the available techniques to investigate the neural correlates of consciousness, critical information that is necessary for the design of a potential treatment of coma and other disorders of consciousness is not available yet. Nevertheless, important efforts have been made in the past 100 years that do provide certain insights into how the brain regains arousal and awareness, which are summarized in the following section.

4. NEURAL CORRELATES OF CONSCIOUSNESS

How does the brain support consciousness? Evidence from animal and human studies.

4.1. The brainstem

A number of experimental animal works performed in the 1930-1950's identified the pons and the midbrain as brain regions critical for arousal [92-96]. Transection studies in cats demonstrated cortical deactivation or slow wave rhythms upon disconnection of the brainstem from the diencephalon (first presented by Bremer as the "Cerveau isolé" preparation) [95, 97, 98]. In contrast, cortical activity remained almost unaffected when transections were performed below the medulla ("Encephale isolé") [95]. The reactivation of the cerebral cortex in anesthetized cats upon stimulation of the brainstem nuclei provided the first evidence of an activating system originated in the brainstem reticular formation [96]. Recent works involving pontine stimulation in anesthetized animals are also supportive of the role of the brainstem nuclei in arousal [99]. Additionally, traumatic brain injury human studies have detected disruption of the brainstem-thalamic and brainstem-basal forebrain connections in comatose patients, further demonstrating the role of the brainstem reticular formation in modulating consciousness [31].

The following nuclei within the brainstem tegmentum are candidates to support arousal: the cholinergic laterodorsal tegmental nucleus (LDT), the pedunculopontine tegmental nucleus (PPT), the serotonergic Raphe (R), the noradrenergic locus coeruleus (LC), the autonomic parabrachial nucleus (PB) and the periaqueductal gray matter (PAG), among others. Nevertheless, no bilateral lesion of any particular nucleus in isolation has been reported to cause coma. In contrast, impairment of a combination of these nuclei is observed in patients with brainstem coma [100], and in comatose rats subjected to diffuse brainstem damage (***attached manuscript 1***).

There is a growing evidence suggesting that the dopaminergic cells in the ventral tegmental area (VTA), in the rostral brainstem, could be a promising target to promote wakefulness from unconscious states. Electrical stimulation of this area, as well as optogenetic stimulation of its dopaminergic cells, produced arousal in rodents under general anesthesia [37, 101, 102]. The VTA receives inputs from cholinergic nuclei in the brainstem that have been repeatedly observed to be damaged in comatose patients [100, 103, 104]. Studies testing the effects of VTA stimulation in comatose patients or animal models of coma may shed light and the potential role of this nucleus in the recovery of consciousness after brain injury.

4.2. The cerebral cortex

Many studies have placed the cortical mantle (or more specifically, the connections within it) as the substrate of consciousness in the human brain [83, 85, 105]. Cortical activity by itself, measured with EEG, can reliably identify the depth of anesthesia [24]. A slow-wave recording indicates synchronous neuronal activity, which occurs upon deactivation of the reticular formation pathways, after excessive inhibition of the globus pallidus on the thalamus or upon cortical deafferentation (*e.g.* in coma) and it is chosen as the ideal

rhythm to produce unconsciousness during surgery [16, 24]. In contrast, a desynchronized EEG (low voltage fast activity waves) is typical of awake states.

Quiet wakefulness is commonly observed from human EEG as electrical activity oscillating at 8-13Hz (alpha), usually in occipital and parietal cortex while eyes are closed. Occipital alpha disappears and may be converted into frontal alpha (anteriorization) during transition to drowsiness, together with the emergence of slow waves [106-108].

EEG synchronization in the gamma band (30-80 Hz) has been reliably observed during visual studies performed in cats [109], and its power is decreased in patients under general anesthesia [110], which suggested a role of these fast oscillations in attentional processes. However, gamma synchronization has also been observed in NREM sleep or during seizures, implying that this rhythm might not be such a good indicator of attention.

As cortical activity may reflect both, thalamocortical processing (*e.g.* somatosensory processing) as well as conscious processing (*e.g.* attention to a given stimulus), several studies have opted to dichotomize conscious and unconscious perception conditions by exploring specific disorders like visual neglect, where a subject may process information of his visual field without being aware of it [111]. This kind of conditions demonstrate that the somatosensory cortex is not necessarily involved in consciousness (or, at least, its activation is not enough to allow conscious perception). Disruptions in the fronto-parietal network can result in visual neglect [112], suggesting a relevant participation of the frontal cortices in attentional processes. However, multiple literature references suggest that consciousness depends largely on the posterior rather than the anterior cortex. The frontal cortex loses communication with the posterior regions during anesthesia [86, 110, 113], and its activation is reduced during vivid imaginary experiences [114]. Besides, preservation of the parietal-occipital cortex, but not necessarily the frontal regions, is associated with better neurological function in DOC patients [74, 115, 116]. Based on the existing literature [117-120], it seems that the human prefrontal cortex is mainly associated to higher processing of the senses, while the occipital cortex may be more related to inner perceptions. For a review investigating the relevance of the anterior vs. posterior cortex in consciousness, see reference [105].

Within the cortex, layer 5 is likely to play a major role in the process of conscious perception, as indicated by animal behavioral studies with parallel calcium recordings in this layer [121-123], the fact that pyramidal cells in layer 5 are less active during slow wave sleep [124, 125] or the disrupted coupling between supra and infragranular layers during unconscious states [126].

Despite the multiple studies awarding conscious roles to the cerebral cortex, complete decerebration in animals did not cause permanent coma [92, 94]. Similarly, patients with hydranencephaly (almost inexistent cerebral cortex) can show signs of awareness [127], which questions the need of a cerebral cortex to perform conscious actions [128].

4.3. Subcortical structures outside the brainstem

Several reports have demonstrated the involvement of the thalamus in consciousness [129-132]. Intralaminar nuclei, connected to the fronto-parietal cortex, are activated during attention [133], and stimulation of the central thalamus improved behavioral responsiveness in a patient in a minimally conscious state [3] (potential mechanisms described elsewhere [131, 134]). Interestingly, it has been proposed that, while fronto-parietal connectivity during anesthesia relates to the concentration of anesthetic agent in blood, the thalamic connectivity could be a better indicator of the real level of consciousness [135]. In animals, electrical stimulation of the central thalamus produced an increase in arousal [131] and administration of a cholinergic agonist into this nucleus allowed rats to wake up from general anesthesia [136]. On the other hand, despite the potential benefits of thalamic stimulation [130, 131], massive thalamic dysfunction does not cause coma in animals [36] or humans [137, 138].

Neuronal populations of the lateral hypothalamus (LH) are involved in cortical arousal [139-142]. Consistently, several studies have identified damage to the orexinergic population of LH or to the histaminergic cells of the tuberomammillary nucleus in comatose patients [143], and suggested a dependency of coma recovery on the orexin levels of this nucleus [43, 144]. One of the main targets along the ascending circuits from LH are the cholinergic (but also GABAergic of glutamatergic) nuclei of the basal forebrain [145], which have been repeatedly reported to mediate wakefulness, attention and learning in humans and animals [146-152].
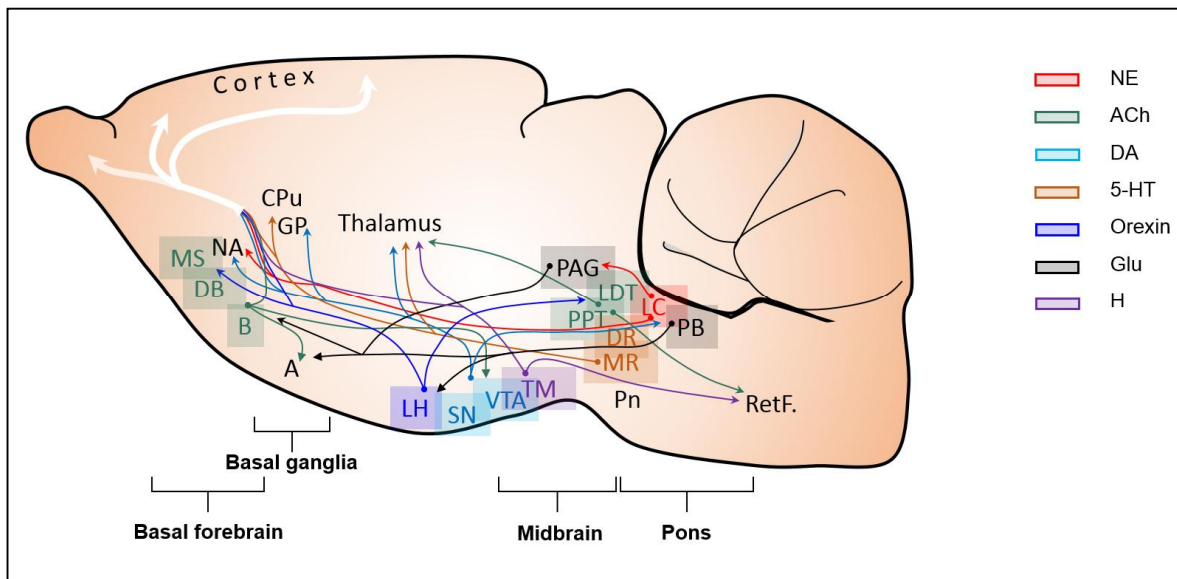
Figure 2*. **Arousal circuits in the rat brain**. NE: norepinephrine, Ach: acetyl-choline, DA: dopamine, 5-HT: serotonin, Glu: glutamate, H: histamine. A: amygdala, B: nucleus basalis of Meynert, CPu: caudate-putamen, D: diagonal band of Broca, GP: globus pallidus, LC: locus coeruleus, LDT: laterodorsal tegmental nucleus, LH: lateral hypothalamus, MS: medial septum, NA: Accumbens nucleus, PAG: periaqueductal grey, PB: parabrachial nucleus, PPT: penduculo-pontine tegmental nucleus, R: Raphe, Ret.F: other nuclei of the reticular formation, SN: substantia nigra, TM: tuberomammillary bodies, VTA: ventral tegmental area.*

In contrast to the historic relevance of the hypothalamic-basal forebrain activating system in consciousness, the role of the basal ganglia has been less considered and, in occasions, pieces of evidence have suggested their poor involvement in consciousness [153-155]. Nevertheless, several reports suggest that the dopaminergic system could play a role in arousal, as indicated by the behavior of dopamine-deficient mice [156, 157] and the fact that stimulation of the globus pallidus interna produced wakefulness in a human subject under anesthesia [158]. Besides, DOC patients show decreased connectivity between these nuclei, the thalamus and the frontal cortex [159], and the dorsal striatum decreases its connectivity in anesthetized animals [113]. The basal ganglia modulate thalamocortical connections, and thereby may be able of participating in conscious processing, which has been suggested as a possible mechanism by which hypnotic drugs like zolpidem [1] or midazolam [2] can affect the recovery of human consciousness after coma [160].

Other widely connected structures like the cerebellum are not believed to be necessary for consciousness, as demonstrated by cases where cerebellar agenesis did not impair cognitive functions significantly [161].

In general, loss of consciousness seems to imply functional clusterization at different brain levels, and often, it is an interplay between distant brain regions what seems to provide the propitious background for conscious processing to occur [116, 162, 163]. As pointed out above, the functionality of the fronto-posterior cortical axis is decreased during loss of consciousness [164], and the same occurs along the thalamo-cortical projections [165]. Similarly, as sleep transits from one stage to another, the connectivity between multiple regions in the brain changes [166]. The functional study conducted in the comatose rats with brainstem damage (***attached manuscript 1***) exemplifies the tendency of the neural networks to re-connect as the brain heals.

5. CONCLUSIONS AND FUTURE OF RESEARCH

The more we know, the more we realize that we might not be able of truly understanding the complexity of human consciousness. One of the reasons of such intricacy is the fact that consciousness, although partially measurable, is a subjective experience, and being able of isolating it from the whole variety of human behaviors might be unfeasible. However, experiments where the brain function can be tracked during the transition from unconscious to conscious states (*e.g.* from anesthesia or coma towards states of wakefulness) offer an opportunity to investigate the foundation of consciousness in relative isolation.

Although anesthesia provides a platform to reliably induce unconsciousness, we know that this state is different from the unconscious state that emerges after brain damage, and therefore, although valuable, anesthesia studies cannot provide enough information to set the basis of human natural loss or regaining of consciousness after brain injuries.

An additional problem is the fact that, in the same way that anesthesia and coma are not the same thing, the coma that emerges upon each subject-specific injury might also be different, and hence, it might not be feasible to build a robust understanding, from all different human cases, about how coma appears and how consciousness may be potentially resumed.

Animal models of coma offer the critical advantage of simplifying the clinical scenario focusing on one single cause of coma and, equally important, of allowing invasive procedures at every time-point during induction and recovery, which could provide detailed proof of the mechanisms behind each of the coma stages. Although a translation from animals to humans may not be direct, a series of coma models mimicking different human comas could certainly guide research towards better treatments to ameliorate the consequences of comatose insults in humans.

For the scientific community to better understand consciousness from animal models, new platforms need to be implemented that allow reliable detection of cell-specific subcortical function. Although whole-brain mapping can be achieved with fMRI, this imaging modality is not specific enough; therefore, fMRI reports should be complemented with other imaging techniques like calcium imaging from particular groups of neurons or with optogenetic stimulation of specific circuits.

This thesis provided several platforms to facilitate the study of consciousness. The first one is a model of brainstem coma, which allows inducing a human-like coma in the rat brain. The second one is the implementation of pupillometry in rodent fMRI, which allows adding an arousal index (equivalent to behavioral responses) to the functional images of the brain. This additional measure is particularly important in consciousness research because animals inside the MR scanner are isolated from the researcher and their behavioral state is unknown during the fMRI scan. The third one, is a tool for remote positioning of stimulation/recording fibers during MRI experiments, which copes with the problem of mistargeting deep brain nuclei and allows precise dissection of brain circuits.

Using the brainstem coma model, we identified a group of brain nuclei that re-connected during acute recovery from coma (in parallel to improved neurological function assessed with the Tübingen-Boston rat coma scale). This increase of connectivity in subcortical areas, assessed with fMRI, was associated to the re-activation of the cortex, which electrical activity was studied through LFPs. A future study should perform fMRI with parallel calcium imaging from the cerebral cortex, to investigate in detail the link between subcortical connectivity and cerebral function within the same animal as a function of the post-coma time. Additionally, this future study should take advantage of the here established MRI-compatible pupillometry (manuscript 2) to obtain a behavioral index during recording of brain function. Ideally, a separate group of animals would be assessed behaviorally outside the scanner with continuous pupillometry assessment during recovery from coma, the purpose being to find an equivalence between the scores obtained from the rat coma scale and the pupil dynamics. Pupillometry may additionally provide insights into the potential fluctuations of the brain state during coma (for instance, identifying certain time windows when the brain state is more susceptible to be altered). In this way, the results obtained from manuscript 1 should be reproduced at single subject level, which may allow a more exhaustive multi-modal analysis of the neural-behavioral re-configurations.

Given that the function of LH could not be reliably investigated due to certain limitations of fMRI (*i.e.*, non cell-specific, susceptible to artifacts), a future study should combine the fMRI with a more direct measure of neuronal activity in this region during recovery from coma. As LH is a deep brain nucleus, the MRI-compatible robotic arm (introduced here as manuscript 4) should be used to improve the reliability of the measurement. This experiment would help clarifying the role of LH on the early recovery from coma.

Last, the subcortical network here identified (basal-ganglia - basal-forebrain - thalamus) should be regarded as a promising target to modulate in future studies, either with optogenetic stimulation of the different components or by using pharmacological treatments to interfere with their function. This could constitute a new line of studies devoted at dissecting the subcortical circuit and, eventually, enabling a faster recovery from coma. The successful shortening of the recovery time in the rat brainstem coma model would translate into a potential treatment for human coma.

In summary, animal models are needed to reproduce human coma in a scenario that allows precise and multimodal investigation of the neural correlates of consciousness. The establishment and characterization of these models with newly available methodologies, could provide neurologists in critical care units with a guide to develop treatment strategies for comatose patients. This thesis aimed at initiating a step forward in this direction.

REFERENCES

1. Kim, C., et al., *Zolpidem-Induced Arousal by Paradoxical GABAergic Stimulation: A Case Report With F-18 Flumazenil Positron Emission Tomography and Single Photon Emission Computed Tomography Study.* Ann Rehabil Med, 2016. **40**(1): p. 177-81.
2. Carboncini, M.C., et al., *A case of post-traumatic minimally conscious state reversed by midazolam: Clinical aspects and neurophysiological correlates.* Restor Neurol Neurosci, 2014. **32**(6): p. 767-87.
3. Schiff, N.D., et al., *Behavioural improvements with thalamic stimulation after severe traumatic brain injury.* Nature, 2007. **448**(7153): p. 600-3.
4. Neumann, E., *Ursprungsgeschichte des Bewusstseins.* Rascher Verlag, 1949.
5. Gross, C.G., *Galen and the Squealing Pig.* The Neuroscientist, 1998. **4**(3): p. 216-221.
6. Crivellato, E. and D. Ribatti, *Soul, mind, brain: Greek philosophy and the birth of neuroscience.* Brain Res Bull, 2007. **71**(4): p. 327-36.
7. Pandya, S.K., *Understanding brain, mind and soul: contributions from neurology and neurosurgery.* Mens Sana Monogr, 2011. **9**(1): p. 129-49.
8. Haldane, E.S., *The Philosophical Works of Descartes.* Cambridge University Press, 1911.
9. Chambers, E., *Cyclopedia: An Universal Dictionary of Arts and Sciences.* 1728.
10. Thiel, U., *The Uses of Antiquity: Cudworth and seventeenth'century theories of consciousness.* Kluwer Academic Publishers, 1991: p. 79-99.
11. Browne, P., *The Procedure, Extent and Limits of Human Understanding.* Garland Pub, 1728.
12. Hennig, B., *Cartesian Conscientia.* British Journal for the History of Philosophy, 2007. **15**: p. 455-484.
13. Lewis, G., *Le Problème de lInconscient et la Cartésianisme.* Presses Universitaires de France, 1950.
14. Lewis, C.S., *Conscience and Conscious.* Studies in Words, Cambridge University Press, 1960.
15. Bruno, M.A., S. Laureys, and A. Demertzi, *Coma and disorders of consciousness.* Handb Clin Neurol, 2013. **118**: p. 205-13.
16. Koch, C., et al., *Neural correlates of consciousness: progress and problems.* Nat Rev Neurosci, 2016. **17**(5): p. 307-21.
17. Parvizi, J. and A. Damasio, *Consciousness and the brainstem.* Cognition, 2001. **79**(1-2): p. 135-60.
18. Laureys, S. and N.D. Schiff, *Coma and consciousness: paradigms (re)framed by neuroimaging.* Neuroimage, 2012. **61**(2): p. 478-91.
19. Guger, C., et al., *Complete Locked-in and Locked-in Patients: Command Following Assessment and Communication with Vibro-Tactile P300 and Motor Imagery Brain-Computer Interface Tools.* Front Neurosci, 2017. **11**: p. 251.
20. Kotchoubey, B. and M. Lotze, *Instrumental methods in the diagnostics of locked-in syndrome.* Restor Neurol Neurosci, 2013. **31**(1): p. 25-40.
21. Naci, L., et al., *Brain-computer interfaces for communication with nonresponsive patients.* Ann Neurol, 2012. **72**(3): p. 312-23.
22. Saper, C.B., T.E. Scammell, and J. Lu, *Hypothalamic regulation of sleep and circadian rhythms.* Nature, 2005. **437**(7063): p. 1257-1263.
23. Schwartz, M.D. and T.S. Kilduff, *The Neurobiology of Sleep and Wakefulness.* Psychiatr Clin North Am, 2015. **38**(4): p. 615-44.
24. Brown, E.N., R. Lydic, and N.D. Schiff, *General anesthesia, sleep, and coma.* N Engl J Med, 2010. **363**(27): p. 2638-50.
25. Weiss, N., et al., *Causes of coma and their evolution in the medical intensive care unit.* J Neurol, 2012. **259**(7): p. 1474-7.
26. Minert, A. and M. Devor, *Brainstem node for loss of consciousness due to GABA(A) receptor-active anesthetics.* Exp Neurol, 2016. **275 Pt 1**: p. 38-45.
27. Abulafia, R., V. Zalkind, and M. Devor, *Cerebral activity during the anesthesia-like state induced by mesopontine microinjection of pentobarbital.* J Neurosci, 2009. **29**(21): p. 7053-64.
28. Wilson, J.A. and H.J. Nordal, *EEG in connection with coma.* Tidsskr Nor Laegeforen, 2013. **133**(1): p. 53-7.
29. Sutter, R. and P.W. Kaplan, *Electroencephalographic patterns in coma: when things slow down.* Epileptologie, 2012. **29**: p. 201-208.
30. Horsting, M.W., et al., *The etiology and outcome of non-traumatic coma in critical care: a systematic review.* BMC Anesthesiol, 2015. **15**: p. 65.
31. Edlow, B.L., et al., *Disconnection of the ascending arousal system in traumatic coma.* J Neuropathol Exp Neurol, 2013. **72**(6): p. 505-23.

32.   Newcombe, V.F., et al., *Aetiological differences in neuroanatomy of the vegetative state: insights from diffusion tensor imaging and functional implications.* J Neurol Neurosurg Psychiatry, 2010. **81**(5): p. 552-61.

33.   Flores, F.J., et al., *Thalamocortical synchronization during induction and emergence from propofol-induced unconsciousness.* Proc Natl Acad Sci U S A, 2017. **114**(32): p. E6660-E6668.

34.   Li, D., V.S. Hambrecht-Wiedbusch, and G.A. Mashour, *Accelerated Recovery of Consciousness after General Anesthesia Is Associated with Increased Functional Brain Connectivity in the High-Gamma Bandwidth.* Front Syst Neurosci, 2017. **11**: p. 16.

35.   Guidera, J.A., et al., *Sevoflurane Induces Coherent Slow-Delta Oscillations in Rats.* Front Neural Circuits, 2017. **11**: p. 36.

36.   Fuller, P.M., et al., *Reassessment of the structural basis of the ascending arousal system.* J Comp Neurol, 2011. **519**(5): p. 933-56.

37.   Solt, K., et al., *Electrical stimulation of the ventral tegmental area induces reanimation from general anesthesia.* Anesthesiology, 2014. **121**(2): p. 311-9.

38.   Carter, M.E., et al., *Tuning arousal with optogenetic modulation of locus coeruleus neurons.* Nat Neurosci, 2010. **13**(12): p. 1526-33.

39.   Katayama, Y., et al., *Coma induced by cholinergic activation of a restricted region in the pontine reticular formation--a model of reversible forms of coma.* Neurol Med Chir (Tokyo), 1986. **26**(1): p. 1-10.

40.   Anaclet, C., et al., *The GABAergic parafacial zone is a medullary slow wave sleep-promoting center.* Nat Neurosci, 2014. **17**(9): p. 1217-24.

41.   Leung, L.S., et al., *Brain areas that influence general anesthesia.* Prog Neurobiol, 2014. **122**: p. 24-44.

42.   Shoykhet, M., et al., *Thalamocortical dysfunction and thalamic injury after asphyxial cardiac arrest in developing rats.* J Neurosci, 2012. **32**(14): p. 4972-81.

43.   Kang, Y.J., et al., *Recovery from Coma Post-Cardiac Arrest Is Dependent on the Orexin Pathway.* J Neurotrauma, 2017. **34**(19): p. 2823-2832.

44.   Katz, L., et al., *Outcome model of asphyxial cardiac arrest in rats.* J Cereb Blood Flow Metab, 1995. **15**(6): p. 1032-9.

45.   Xiong, Y., A. Mahmood, and M. Chopp, *Animal models of traumatic brain injury.* Nat Rev Neurosci, 2013. **14**(2): p. 128-42.

46.   Lee, D.E., et al., *Neural Correlates of Consciousness at Near-Electrocerebral Silence in an Asphyxial Cardiac Arrest Model.* Brain Connect, 2017. **7**(3): p. 172-181.

47.   Vieira, R.C., et al., *Diffuse Axonal Injury: Epidemiology, Outcome and Associated Risk Factors.* Front Neurol, 2016. **7**: p. 178.

48.   Ramiro, J.I. and A. Kumar, *Updates on management of anoxic brain injury after cardiac arrest.* Mo Med, 2015. **112**(2): p. 136-41.

49.   Greer, D., et al., *Serial MRI changes in comatose cardiac arrest patients.* Neurocrit Care, 2011. **14**(1): p. 61-7.

50.   Bekinschtein, T.A., et al., *Can electromyography objectively detect voluntary movement in disorders of consciousness?* J Neurol Neurosurg Psychiatry, 2008. **79**(7): p. 826-8.

51.   Xiao, J., et al., *An Auditory BCI System for Assisting CRS-R Behavioral Assessment in Patients with Disorders of Consciousness.* Sci Rep, 2016. **6**: p. 32917.

52.   Schaar, K.L., M.M. Brenneman, and S.I. Savitz, *Functional assessments in the rodent stroke model.* Exp Transl Stroke Med, 2010. **2**(1): p. 13.

53.   Fujimoto, S.T., et al., *Motor and cognitive function evaluation following experimental traumatic brain injury.* Neurosci Biobehav Rev, 2004. **28**(4): p. 365-78.

54.   Ting, W.K., J.L. Perez Velazquez, and M.D. Cusimano, *Eye movement measurement in diagnostic assessment of disorders of consciousness.* Front Neurol, 2014. **5**: p. 137.

55.   Reimer, J., et al., *Pupil fluctuations track fast switching of cortical states during quiet wakefulness.* Neuron, 2014. **84**(2): p. 355-62.

56.   Bradley, M.M., et al., *The pupil as a measure of emotional arousal and autonomic activation.* Psychophysiology, 2008. **45**(4): p. 602-7.

57.   Schneider, M., et al., *Spontaneous pupil dilations during the resting state are associated with activation of the salience network.* Neuroimage, 2016. **139**: p. 189-201.

58.   Teasdale, G. and B. Jennett, *Assessment of coma and impaired consciousness. A practical scale.* Lancet, 1974. **2**(7872): p. 81-4.

59.   Giacino, J.T., K. Kalmar, and J. Whyte, *The JFK Coma Recovery Scale-Revised: measurement characteristics and diagnostic utility.* Arch Phys Med Rehabil, 2004. **85**(12): p. 2020-9.

60.   Wijdicks, E.F., et al., *FOUR score and Glasgow Coma Scale in predicting outcome of comatose patients: a pooled analysis.* Neurology, 2011. **77**(1): p. 84-5.

61.   Mutch, C.A., J.F. Talbott, and A. Gean, *Imaging Evaluation of Acute Traumatic Brain Injury.* Neurosurg Clin N Am, 2016. **27**(4): p. 409-39.

62.   Lusic, H. and M.W. Grinstaff, *X-ray-computed tomography contrast agents.* Chem Rev, 2013. **113**(3): p. 1641-66.

63.   Toyoda, K., M. Ida, and K. Fukuda, *Fluid-attenuated inversion recovery intraarterial signal: an early sign of hyperacute cerebral ischemia.* AJNR Am J Neuroradiol, 2001. **22**(6): p. 1021-9.

64.   Wijdicks, E.F., N.G. Campeau, and G.M. Miller, *MR imaging in comatose survivors of cardiac resuscitation.* AJNR Am J Neuroradiol, 2001. **22**(8): p. 1561-5.

65.   Amin, O.S., et al., *Bilateral infarction of paramedian thalami: a report of two cases of artery of Percheron occlusion and review of the literature.* BMJ Case Rep, 2011. **2011**.

66.   Choi, S.P., et al., *Diffusion-weighted magnetic resonance imaging for predicting the clinical outcome of comatose survivors after cardiac arrest: a cohort study.* Crit Care, 2010. **14**(1): p. R17.

67.   Doelken, M., et al., *Differentiation of cytotoxic and vasogenic edema in a patient with reversible posterior leukoencephalopathy syndrome using diffusion-weighted MRI.* Diagn Interv Radiol, 2007. **13**(3): p. 125-8.

68.   Weiss, N., et al., *Clinical review: Prognostic value of magnetic resonance imaging in acute brain injury and coma.* Crit Care, 2007. **11**(5): p. 230.

69.   Wang, M., et al., *Brain-state dependent astrocytic Ca(2+) signals are coupled to both positive and negative BOLD-fMRI signals.* Proc Natl Acad Sci U S A, 2018. **115**(7): p. E1647-E1656.

70.   Petzold, G.C. and V.N. Murthy, *Role of astrocytes in neurovascular coupling.* Neuron, 2011. **71**(5): p. 782-97.

71.   Winkler, E.A., et al., *Pericytes Regulate Cerebral Blood Flow and Neuronal Health at a Capillary Level.* Neurosurgery, 2017. **81**(5): p. N37-N38.

72.   van den Heuvel, M.P. and H.E. Hulshoff Pol, *Exploring the brain network: a review on resting-state fMRI functional connectivity.* Eur Neuropsychopharmacol, 2010. **20**(8): p. 519-34.

73.   Biswal, B., et al., *Functional connectivity in the motor cortex of resting human brain using echo-planar MRI.* Magn Reson Med, 1995. **34**(4): p. 537-41.

74.   Vanhaudenhuyse, A., et al., *Default network connectivity reflects the level of consciousness in non-communicative brain-damaged patients.* Brain, 2010. **133**(Pt 1): p. 161-71.

75.   Norton, L., et al., *Disruptions of functional connectivity in the default mode network of comatose patients.* Neurology, 2012. **78**(3): p. 175-81.

76.   Boly, M., et al., *Functional connectivity in the default network during resting state is preserved in a vegetative but not in a brain dead patient.* Hum Brain Mapp, 2009. **30**(8): p. 2393-400.

77.   Murphy, K., R.M. Birn, and P.A. Bandettini, *Resting-state fMRI confounds and cleanup.* Neuroimage, 2013. **80**: p. 349-59.

78.   Rudolf, J., et al., *Cerebral glucose metabolism in acute and persistent vegetative state.* J Neurosurg Anesthesiol, 1999. **11**(1): p. 17-24.

79.   Phillips, C.L., et al., *"Relevance vector machine" consciousness classifier applied to cerebral metabolism of vegetative and locked-in patients.* Neuroimage, 2011. **56**(2): p. 797-808.

80.   Laureys, S., et al., *Restoration of thalamocortical connectivity after recovery from persistent vegetative state.* Lancet, 2000. **355**(9217): p. 1790-1.

81.   Chakrabarti, S. and C. Schwarz, *Cortical modulation of sensory flow during active touch in the rat whisker system.* Nat Commun, 2018. **9**(1): p. 3907.

82.   Ferrarelli, F., et al., *Breakdown in cortical effective connectivity during midazolam-induced loss of consciousness.* Proc Natl Acad Sci U S A, 2010. **107**(6): p. 2681-6.

83.   Supp, G.G., et al., *Cortical hypersynchrony predicts breakdown of sensory processing during loss of consciousness.* Curr Biol, 2011. **21**(23): p. 1988-93.

84.   Massimini, M., et al., *Breakdown of cortical effective connectivity during sleep.* Science, 2005. **309**(5744): p. 2228-32.

85.   Thul, A., et al., *EEG entropy measures indicate decrease of cortical information processing in Disorders of Consciousness.* Clin Neurophysiol, 2016. **127**(2): p. 1419-1427.

86.   Imas, O.A., et al., *Volatile anesthetics disrupt frontal-posterior recurrent information transfer at gamma frequencies in rat.* Neurosci Lett, 2005. **387**(3): p. 145-50.

87.   Kreuzer, M., et al., *Cross-approximate entropy of cortical local field potentials quantifies effects of anesthesia--a pilot study in rats.* BMC Neurosci, 2010. **11**: p. 122.

88.   Casali, A.G., et al., *A theoretically based index of consciousness independent of sensory processing and behavior.* Sci Transl Med, 2013. **5**(198): p. 198ra105.

89.	Tononi, G., *Integrated information theory of consciousness: an updated account.* Arch Ital Biol, 2012. **150**(4): p. 293-329.

90.	Owen, A.M., et al., *Detecting awareness in the vegetative state.* Science, 2006. **313**(5792): p. 1402.

91.	Britt, J.P., R.A. McDevitt, and A. Bonci, *Use of channelrhodopsin for activation of CNS neurons.* Curr Protoc Neurosci, 2012. **Chapter 2**: p. Unit2 16.

92.	Bignall, K.E. and L. Schramm, *Behavior of chronically decerebrated kittens.* Exp Neurol, 1974. **42**(3): p. 519-31.

93.	Bell, D.J., E.A. Horne, and H.E. Magee, *The decerebrate rat.* J Physiol, 1933. **78**(2): p. 196-207.

94.	Woods, J.W., *Behavior of Chronic Decerebrate Rats.* J Neurophysiol, 1964. **27**: p. 635-44.

95.	Lindsley, D.B., J.W. Bowden, and H.W. Magoun, *Effect upon the EEG of acute injury to the brain stem activating system.* Electroencephalogr Clin Neurophysiol, 1949. **1**(4): p. 475-86.

96.	Moruzzi, G. and H.W. Magoun, *Brain stem reticular formation and activation of the EEG.* Electroencephalogr Clin Neurophysiol, 1949. **1**(4): p. 455-73.

97.	Lindsley, D.B., et al., *Behavioral and EEG changes following chronic brain stem lesions in the cat.* Electroencephalogr Clin Neurophysiol, 1950. **2**(4): p. 483-98.

98.	Villablanca, J., *The electrocorticogram in the chronic cerveau isole cat.* Electroencephalogr Clin Neurophysiol, 1965. **19**(6): p. 576-86.

99.	Pillay, S., et al., *Brainstem stimulation increases functional connectivity of basal forebrain-paralimbic network in isoflurane-anesthetized rats.* Brain Connect, 2014. **4**(7): p. 523-34.

100.	Fischer, D.B., et al., *A human brain network derived from coma-causing brainstem lesions.* Neurology, 2016. **87**(23): p. 2427-2434.

101.	Taylor, N.E., et al., *Activation of D1 dopamine receptors induces emergence from isoflurane general anesthesia.* Anesthesiology, 2013. **118**(1): p. 30-9.

102.	Taylor, N.E., et al., *Optogenetic activation of dopamine neurons in the ventral tegmental area induces reanimation from general anesthesia.* Proc Natl Acad Sci U S A, 2016. **113**(45): p. 12826-12831.

103.	Dautan, D., et al., *Segregated cholinergic transmission modulates dopamine neurons integrated in distinct functional circuits.* Nat Neurosci, 2016. **19**(8): p. 1025-33.

104.	Oakman, S.A., et al., *Distribution of pontomesencephalic cholinergic neurons projecting to substantia nigra differs significantly from those projecting to ventral tegmental area.* J Neurosci, 1995. **15**(9): p. 5859-69.

105.	Boly, M., et al., *Are the Neural Correlates of Consciousness in the Front or in the Back of the Cerebral Cortex? Clinical and Neuroimaging Evidence.* J Neurosci, 2017. **37**(40): p. 9603-9613.

106.	Vijayan, S., et al., *Thalamocortical mechanisms for the anteriorization of alpha rhythms during propofol-induced unconsciousness.* J Neurosci, 2013. **33**(27): p. 11070-5.

107.	Feshchenko, V.A., R.A. Veselis, and R.A. Reinsel, *Propofol-induced alpha rhythm.* Neuropsychobiology, 2004. **50**(3): p. 257-66.

108.	Cimenser, A., et al., *Tracking brain states under general anesthesia by using global coherence analysis.* Proc Natl Acad Sci U S A, 2011. **108**(21): p. 8832-7.

109.	Roelfsema, P.R., et al., *Visuomotor integration is associated with zero time-lag synchronization among cortical areas.* Nature, 1997. **385**(6612): p. 157-61.

110.	John, E.R., et al., *Invariant reversible QEEG effects of anesthetics.* Conscious Cogn, 2001. **10**(2): p. 165-83.

111.	Driver, J. and J.B. Mattingley, *Parietal neglect and visual awareness.* Nat Neurosci, 1998. **1**(1): p. 17-22.

112.	Corbetta, M. and G.L. Shulman, *Spatial neglect and attention networks.* Annu Rev Neurosci, 2011. **34**: p. 569-99.

113.	Hudetz, A.G., X. Liu, and S. Pillay, *Dynamic repertoire of intrinsic brain states is reduced in propofol-induced unconsciousness.* Brain Connect, 2015. **5**(1): p. 10-22.

114.	Lou, H.C., et al., *A 15O-H2O PET study of meditation and the resting state of normal consciousness.* Hum Brain Mapp, 1999. **7**(2): p. 98-105.

115.	Stender, J., et al., *The Minimal Energetic Requirement of Sustained Awareness after Brain Injury.* Curr Biol, 2016. **26**(11): p. 1494-9.

116.	Demertzi, A., et al., *Intrinsic functional connectivity differentiates minimally conscious from unresponsive patients.* Brain, 2015. **138**(Pt 9): p. 2619-31.

117.	Pitts, M.A., A. Martinez, and S.A. Hillyard, *Visual processing of contour patterns under conditions of inattentional blindness.* J Cogn Neurosci, 2012. **24**(2): p. 287-303.

118.	Pitts, M.A., S. Metzler, and S.A. Hillyard, *Isolating neural correlates of conscious perception from neural correlates of reporting one's perception.* Front Psychol, 2014. **5**: p. 1078.

119.   Silverstein, B.H., et al., *P3b, consciousness, and complex unconscious processing.* Cortex, 2015. **73**: p. 216-27.
120.   Bagattini, C., C. Mazzi, and S. Savazzi, *Waves of awareness for occipital and parietal phosphenes perception.* Neuropsychologia, 2015. **70**: p. 114-25.
121.   Takahashi, N., et al., *Active cortical dendrites modulate perception.* Science, 2016. **354**(6319): p. 1587-1590.
122.   Phillips, W.A., et al., *The effects of arousal on apical amplification and conscious state.* Neurosci Conscious, 2016. **2016**(1): p. niw015.
123.   Lawrence, S.J.D., et al., *Laminar fMRI: Applications for cognitive neuroscience.* Neuroimage, 2017.
124.   Livingstone, M.S. and D.H. Hubel, *Effects of sleep and arousal on the processing of visual information in the cat.* Nature, 1981. **291**(5816): p. 554-61.
125.   Harris, K.D. and G.M. Shepherd, *The neocortical circuit: themes and variations.* Nat Neurosci, 2015. **18**(2): p. 170-81.
126.   Funk, C.M., et al., *Local Slow Waves in Superficial Layers of Primary Cortical Areas during REM Sleep.* Curr Biol, 2016. **26**(3): p. 396-403.
127.   Beshkar, M., *The presence of consciousness in the absence of the cerebral cortex.* Synapse, 2008. **62**(7): p. 553-6.
128.   Merker, B., *Consciousness without a cerebral cortex: a challenge for neuroscience and medicine.* Behav Brain Sci, 2007. **30**(1): p. 63-81; discussion 81-134.
129.   Van der Werf, Y.D., M.P. Witter, and H.J. Groenewegen, *The intralaminar and midline nuclei of the thalamus. Anatomical and functional evidence for participation in processes of arousal and awareness.* Brain Res Brain Res Rev, 2002. **39**(2-3): p. 107-40.
130.   Schiff, N.D., *Central thalamic deep-brain stimulation in the severely injured brain: rationale and proposed mechanisms of action.* Ann N Y Acad Sci, 2009. **1157**: p. 101-16.
131.   Shirvalkar, P., et al., *Cognitive enhancement with central thalamic electrical stimulation.* Proc Natl Acad Sci U S A, 2006. **103**(45): p. 17007-12.
132.   Baker, J.L., et al., *Robust modulation of arousal regulation, performance, and frontostriatal activity through central thalamic deep brain stimulation in healthy nonhuman primates.* J Neurophysiol, 2016. **116**(5): p. 2383-2404.
133.   Kinomura, S., et al., *Activation by attention of the human reticular formation and thalamic intralaminar nuclei.* Science, 1996. **271**(5248): p. 512-5.
134.   Liu, J., et al., *Frequency-selective control of cortical and subcortical networks by central thalamus.* Elife, 2015. **4**: p. e09215.
135.   Barttfeld, P., et al., *Factoring the brain signatures of anesthesia concentration and level of arousal across individuals.* Neuroimage Clin, 2015. **9**: p. 385-91.
136.   Alkire, M.T., et al., *Thalamic microinjection of nicotine reverses sevoflurane-induced loss of righting reflex in the rat.* Anesthesiology, 2007. **107**(2): p. 264-72.
137.   Lutkenhoff, E.S., et al., *Thalamic and extrathalamic mechanisms of consciousness after severe brain injury.* Ann Neurol, 2015. **78**(1): p. 68-76.
138.   Laureys, S., et al., *Cortical processing of noxious somatosensory stimuli in the persistent vegetative state.* Neuroimage, 2002. **17**(2): p. 732-41.
139.   Herrera, C.G., et al., *Hypothalamic feedforward inhibition of thalamocortical network controls arousal and consciousness.* Nat Neurosci, 2016. **19**(2): p. 290-8.
140.   Alam, M.A. and B.N. Mallick, *Glutamic acid stimulation of the perifornical-lateral hypothalamic area promotes arousal and inhibits non-REM/REM sleep.* Neurosci Lett, 2008. **439**(3): p. 281-6.
141.   Li, F.W., S. Deurveilher, and K. Semba, *Behavioural and neuronal activation after microinjections of AMPA and NMDA into the perifornical lateral hypothalamus in rats.* Behav Brain Res, 2011. **224**(2): p. 376-86.
142.   Venner, A., et al., *A Novel Population of Wake-Promoting GABAergic Neurons in the Ventral Lateral Hypothalamus.* Curr Biol, 2016. **26**(16): p. 2137-43.
143.   Valko, P.O., et al., *Damage to histaminergic tuberomammillary neurons and other hypothalamic neurons with traumatic brain injury.* Ann Neurol, 2015. **77**(1): p. 177-82.
144.   Feng, Z., et al., *Resuscitation therapy for traumatic brain injury-induced coma in rats: mechanisms of median nerve electrical stimulation.* Neural Regen Res, 2015. **10**(4): p. 594-8.
145.   Henny, P. and B.E. Jones, *Projections from basal forebrain to prefrontal cortex comprise cholinergic, GABAergic and glutamatergic inputs to pyramidal cells or interneurons.* Eur J Neurosci, 2008. **27**(3): p. 654-70.
146.   Everitt, B.J. and T.W. Robbins, *Central cholinergic systems and cognition.* Annu Rev Psychol, 1997. **48**: p. 649-84.

147. Lin, S.C., et al., *Optogenetic Dissection of the Basal Forebrain Neuromodulatory Control of Cortical Activation, Plasticity, and Cognition.* J Neurosci, 2015. **35**(41): p. 13896-903.
148. McLin, D.E., 3rd, A.A. Miasnikov, and N.M. Weinberger, *Induction of behavioral associative memory by stimulation of the nucleus basalis.* Proc Natl Acad Sci U S A, 2002. **99**(6): p. 4002-7.
149. Goard, M. and Y. Dan, *Basal forebrain activation enhances cortical coding of natural scenes.* Nat Neurosci, 2009. **12**(11): p. 1444-9.
150. Xu, M., et al., *Basal forebrain circuit for sleep-wake control.* Nat Neurosci, 2015. **18**(11): p. 1641-7.
151. Hangya, B., et al., *Central Cholinergic Neurons Are Rapidly Recruited by Reinforcement Feedback.* Cell, 2015. **162**(5): p. 1155-68.
152. Ballinger, E.C., et al., *Basal Forebrain Cholinergic Circuits and Signaling in Cognition and Cognitive Decline.* Neuron, 2016. **91**(6): p. 1199-1218.
153. Jain, S.K., et al., *Bilateral large traumatic basal ganglia haemorrhage in a conscious adult: a rare case report.* Brain Inj, 2013. **27**(4): p. 500-3.
154. Straussberg, R., et al., *Familial infantile bilateral striatal necrosis: clinical features and response to biotin treatment.* Neurology, 2002. **59**(7): p. 983-9.
155. Caparros-Lefebvre, D., A. Destee, and H. Petit, *Late onset familial dystonia: could mitochondrial deficits induce a diffuse lesioning process of the whole basal ganglia system?* J Neurol Neurosurg Psychiatry, 1997. **63**(2): p. 196-203.
156. Palmiter, R.D., *Dopamine signaling in the dorsal striatum is essential for motivated behaviors: lessons from dopamine-deficient mice.* Ann N Y Acad Sci, 2008. **1129**: p. 35-46.
157. Palmiter, R.D., *Dopamine signaling as a neural correlate of consciousness.* Neuroscience, 2011. **198**: p. 213-20.
158. Moll, C.K., et al., *Waking up the brain: a case study of stimulation-induced wakeful unawareness during anaesthesia.* Prog Brain Res, 2009. **177**: p. 125-45.
159. Weng, L., et al., *Abnormal structural connectivity between the basal ganglia, thalamus, and frontal cortex in patients with disorders of consciousness.* Cortex, 2017. **90**: p. 71-87.
160. Schiff, N.D., *Recovery of consciousness after brain injury: a mesocircuit hypothesis.* Trends Neurosci, 2010. **33**(1): p. 1-9.
161. Yu, F., et al., *A new case of complete primary cerebellar agenesis: clinical and imaging findings in a living patient.* Brain, 2015. **138**(Pt 6): p. e353.
162. Achard, S., et al., *Hubs of brain functional networks are radically reorganized in comatose patients.* Proc Natl Acad Sci U S A, 2012. **109**(50): p. 20608-13.
163. Monti, M.M., et al., *Dynamic change of global and local information processing in propofol-induced loss and recovery of consciousness.* PLoS Comput Biol, 2013. **9**(10): p. e1003271.
164. Boly, M., et al., *Connectivity changes underlying spectral EEG changes during propofol-induced loss of consciousness.* J Neurosci, 2012. **32**(20): p. 7082-90.
165. Akeju, O., et al., *Disruption of thalamic functional connectivity is a neural correlate of dexmedetomidine-induced unconsciousness.* Elife, 2014. **3**: p. e04499.
166. Tagliazucchi, E. and H. Laufs, *Decoding wakefulness levels from typical fMRI resting-state data reveals reliable drifts between wakefulness and sleep.* Neuron, 2014. **82**(3): p. 695-708.

PART II. OWN WORK

LIST OF APPENDED MANUSCRIPTS AND STATEMENTS OF CONTRIBUTIONS

1. Patricia Pais-Roldán, Brian L. Edlow, Yuanyuan Jiang, Johannes Stelzer, Ming Zou, and Xin Yu. **Multimodal Assessment of Recovery from Coma in a Rat Model of Diffuse Brainstem Tegmentum Injury**. Neuroimage. 2019 (Published)

   Contributions: I conducted all animal experiments, including surgeries, behavioral assessments, electrophysiology, (f)MRI and histopathology tests, guided by Dr. Xin Yu. Dr. Ming Zou provided feedback on the behavioral experiments. I analyzed all data, partially guided by Dr. Yuanyuan Jiang and Johannes Stelzer. Dr. Brian L. Edlow provided strong feedback from the clinical side to create the rat coma scale and on the discussion of the manuscript. I prepared all figures, wrote the manuscript (together with Dr. Brian L. Edlow and Dr. Xin Yu) and prepared all responses for the peer-review process of the article until its publication.

2. Patricia Pais-Roldán, Kengo Takahashi, Yi Chen, Yuanyuan Jiang, Hang Zheng, and Xin Yu. **Indexing arousal with multi-modal fMRI merging pupillometry and optical fiber calcium recording**. (Under review)

   Contributions: Yi Chen, Yuanyuan Jiang, Hang Zheng, Kengo Takahashi and I initiated an effort to acquire images from the pupil inside the MRI scanner in anesthetized rats, motivated by Dr. Xin Yu. I designed the final set-up to perform pupillometry in parallel to fMRI, performed all surgical procedures, and acquired and analyzed all data (assisted by Kengo Takahashi and Hang Zheng). I wrote the manuscript and prepared all figures. Dr. Xin Yu provided strong feedback for the interpretation of results and revised the manuscript.

3. Patricia Pais-Roldán, Bharat Biswal, Klaus Scheffler, and Xin Yu. **Identifying Respiration-Related Aliasing Artifacts in the Rodent Resting-State fMRI**. Front Neurosci. 2018 (Published)

   Contributions: I conducted all animal experiments, including surgeries and fMRI acquisitions. I designed and performed analysis of the data, prepared all figures and wrote a first version of the manuscript. Dr. Xin Yu provided strong guidance in the conceptualization, experimental feedback and manuscript corrections. Dr. Bharat Biswal and Prof. Dr. Klaus Scheffler suggested and reviewed particular experiments and analytical procedures. All authors revised the manuscript. I prepared and revised the responses for the peer-review process of the article until its publication.

4. Yi Chen, Patricia Pais-Roldán, Xu-ming Chen, Michael H. Frosz, and Xin Yu. **MRI-guided Robotic Arm drives optogenetic fMRI with concurrent Ca^{2+} recording**. Nat Comm. 2019 (Published)

   Contributions: I performed most animal surgeries and assisted the set-up of the robotic arm in the *in vivo* fMRI experiments. Yi Chen performed all *in vitro* tests with the robotic arm and acquired most of the *in vitro* and *in vivo* MRI data. Yi Chen analyzed the data and wrote a first version of the manuscript, which I revised together with Dr. Xin Yu.

SUMMARY TABLE

Scientific question	Methodology employed to answer the sci. question	Publi-cation	Novelty of the performed research (impact on the field of Neuroscience)
Can we reproduce brainstem coma in a rat?	Build a model of coma by causing brainstem ischemia	1	➢ 1st model for acute evaluation of brainstem coma in the rat ➢ 1st Rat Coma Scale ➢ 1st electrophysiological traces observed during brainstem-coma induction and hyper-acute recovery: transient burst suppression may be a hallmark of acute coma states ➢ 1st whole-brain fMRI longitudinal assessment during the acute coma recovery: basal ganglia, basal forebrain and thalamus re-connect during acute natural recovery of consciousness ➢ New methodology to track voxel-wise connectivity changes: Eigenvector Centrality Mapping Slope map
What are the potential nuclei mediating coma?	T2-weighted MRI		
Do rats improve their neurological function after this brainstem coma?	Design a scale to quantify neurological function from behavioral responses in the rat		
How does the brain recover from coma?	Longitudinal electrophysiology Longitudinal fMRI		
Can we obtain an arousal measure from rats undergoing fMRI?	Setup pupillometry inside the MRI scanner	2	➢ 1st pupil-fMRI setup in rodents and identification of first pupil-governed brain network in the anesthetized rat.
Which are the neural correlates of pupil spontaneous fluctuations in anesthetized rats?	Analyze the relationship between pupil size changes, calcium imaging from cingulate cortex and whole brain MRI		
How critical is the control of physiological noise (*e.g.* breathing) in rat fMRI? How can it be avoided or ameliorated?	Acquire and analyze fMRI data under different conditions (not paralyzed, paralyzed, with certain ventilatory rates, at certain TRs)	3	➢ 1st publication clarifying the respiration-related confounders in rat rs-fMRI
Can we remotely implant optical fibers on animals undergoing MRI with real time feedback?	Design, construct and adapt an MRI-compatible robotic arm Test *in vivo*	4	➢ 1st system available to control remotely the position of fibers for deep brain stimulation or recording for multimodal fMRI experiments in rats

1. Patricia Pais-Roldán, et al. **Multimodal Assessment of Recovery from Coma in a Rat Model of Diffuse Brainstem Tegmentum Injury**. Neuroimage. 2019

2. Patricia Pais-Roldán, et al. **Indexing arousal with multi-modal fMRI merging pupillometry and optical fiber calcium recording** (in submission process)

3. Patricia Pais-Roldán, et al. **Identifying Respiration-Related Aliasing Artifacts in the Rodent Resting-State fMRI**. Front Neurosci. 2018

4. Yi Chen, et al. **MRI-guided Robotic Arm drives optogenetic fMRI with concurrent Ca^{2+} recording**. Nat Comm. 2019

PART III. OWN SCIENTIFIC PUBLICATIONS RELATED TO THE PRESENTED THESIS
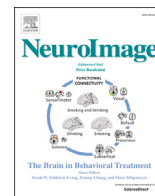
Multimodal assessment of recovery from coma in a rat model of diffuse brainstem tegmentum injury

Patricia Pais-Roldán [a,b], Brian L. Edlow [c,d], Yuanyuan Jiang [a], Johannes Stelzer [a], Ming Zou [e], Xin Yu [a,d,*]

[a] High-Field Magnetic Resonance Department, Max Planck Institute for Biological Cybernetics, Tuebingen, 72076, Germany
[b] Graduate Training Centre of Neuroscience, International Max Planck Research School, University of Tuebingen, Tuebingen, 72074, Germany
[c] Center for Neurotechnology and Neurorecovery, Massachusetts General Hospital, Boston, MA, 02114, USA
[d] Athinoula A. Martinos Center for Biomedical Imaging, Massachusetts General Hospital and Harvard Medical School, Charlestown, MA, 02129, USA
[e] Department of Geriatrics & Neurology, The 2nd Affiliated Hospital of Wenzhou Medical University, Wenzhou, Zhejiang, 325000, China

ABSTRACT

Despite the association between brainstem lesions and coma, a mechanistic understanding of coma pathogenesis and recovery is lacking. We developed a coma model in the rat mimicking human brainstem coma, which allowed multimodal analysis of a brainstem tegmentum lesion's effects on behavior, cortical electrophysiology, and global brain functional connectivity. After coma induction, we observed a transient period (~1h) of unresponsiveness accompanied by cortical burst-suppression. Comatose rats then gradually regained behavioral responsiveness concurrent with emergence of delta/theta-predominant cortical rhythms in primary somatosensory cortex. During the acute stage of coma recovery (~1–8h), longitudinal resting-state functional MRI revealed an increase in functional connectivity between subcortical arousal nuclei in the thalamus, basal forebrain, and basal ganglia and cortical regions implicated in awareness. This rat coma model provides an experimental platform to systematically study network-based mechanisms of coma pathogenesis and recovery, as well as to test targeted therapies aimed at promoting recovery of consciousness after coma.

1. Introduction

More than one million people worldwide experience a coma every year due to brainstem lesions caused by trauma, stroke, and other severe brain injuries (Maas et al., 2017; Edlow et al., 2014). Many die from their injuries or never recover consciousness, remaining in a vegetative state (Giacino et al., 2018). However, recovery of consciousness is possible in comatose patients who retain a sufficient number of subcortical projections to reactivate the cerebral cortex (Thengone et al., 2016; Katz et al., 2009; Giacino et al., 2014; Schiff et al., 2007). For these patients, the cortex remains quiescent until ascending neural activity from subcortical arousal nuclei in the brainstem, thalamus, hypothalamus, or basal forebrain is restored (Schiff et al., 2007; Laureys et al., 2000; Schiff, 2010). Yet, the relative contributions of the brainstem, thalamus, hypothalamus, and basal forebrain to the reemergence of consciousness after brainstem-lesion induced coma are unknown (Schiff, 2010). Animal coma models could provide critical experimental platforms to study the neural mechanisms

relevant to key brain state dynamic changes, which can help elucidate the neural basis for the reemergence of consciousness.

The neuroanatomic basis of consciousness has historically been studied using a lesional approach in which animal brains are examined under different surgical conditions. Removal of both cerebral hemispheres does not cause coma in rats, cats or dogs (Bignall and Schramm, 1974; Bell et al., 1933; Woods, 1964; Tonkovic-Capin et al., 1985), with animals being able to right themselves (return to the upright position), eat and even groom. These findings demonstrate the challenge of producing an animal coma model, while also highlighting the critical role of subcortical brain lesions for coma induction. Brainstem transection and stimulation studies further demonstrate that, although medullary nuclei modulate vital functions (Gromysz and Karczewski, 1981), it is the pontomesencephalic tegmentum that is most involved in arousal (Lindsley et al., 1949; Moruzzi and Magoun, 1949). Transections at this level result in cortical deactivation and the emergence of bursts (Lindsley et al., 1949), whereas stimulation of the pontomesencephalic tegmentum results in cortical excitability (Moruzzi and Magoun, 1949). Numerous

---

* Corresponding author. Max-Planck-Ring 11, 72076, Tuebingen, Germany.
  E-mail address: xin.yu@tuebingen.mpg.de (X. Yu).

animal studies have further verified that brainstem tegmentum lesions or inhibition are associated with altered consciousness (Fuller et al., 2011; Abulafia et al., 2009; Lindsley et al., 1950; Hayes et al., 1984; Webster and Jones, 1988; Jones et al., 1977; Hobson, 1965; Yang et al., 2018). For example, a rodent model involving chemical lesions of the parabrachial-precoeruleus complex created a coma-like brain state with sub-1 Hz cortical EEG (Fuller et al., 2011). Lesions involving the ponto-mesencephalic tegmentum have similarly been observed in human patients with coma (Parvizi and Damasio, 2003; Rosenblum, 2015; Edlow et al., 2013; Fischer et al., 2016).

Despite extensive animal and human evidence for the role of brainstem arousal nuclei in regulation of consciousness, few studies have investigated neurological state changes during coma induction or acute recovery of consciousness following brainstem lesions in patients or in animal models. A transient coma can be caused by administration of neuro-toxins (Sonobe et al., 2015; Sonobe and Haouzi, 2015; Tamaoki et al., 2016), anesthetics (Abulafia et al., 2009; Devor and Zalkind, 2001), or cholinergic agonists (Katayama et al., 1986), but the induced coma state is brief (*e.g.* 5–10 min) (Sonobe and Haouzi, 2015), dose-dependent, and associated with high fatality rates. Hypoxic-ischemic brain injury models in rats (Shoykhet et al., 2012; Manole et al., 2014; Katz et al., 1995; Jia et al., 2006; Kawai et al., 1992; Geocadin et al., 2000; Muthuswamy et al., 2002; Liachenko et al., 1998) and dogs (Leonov et al., 1990) can trigger coma, but the global neuronal injury precludes identification of specific brainstem nuclei whose lesioning causes coma and the subcortical circuits that are critical to recovery. Animal models of severe traumatic brain injury (Xiong et al., 2013) provide an opportunity to study coma but involve multifocal lesions and multiple pathophysiological processes (*e.g.* contusions and axonal shearing). Therefore, new animal models are needed to mimic clinical brainstem injury and to produce a coma of sufficient duration to study mechanisms of recovery.

Here, we describe a diffuse brainstem tegmentum lesion in the rat that reproducibly generates a coma of sufficient duration to enable comprehensive behavioral, electrophysiological, and radiological characterization of the comatose brain. A vasoconstrictor, endothelin-1 (ET-1), was injected into the brainstem to cause ischemic injury to the brainstem tegmentum, resulting in infarction of multiple brainstem arousal nuclei, but preserving diencephalic, basal forebrain and cortical structures, as confirmed by T2-weighted magnetic resonance imaging (MRI) and histopathology. After coma induction, behavioral recovery was tracked quantitatively using a newly developed and validated Tübingen-Boston Rat Coma Scale (RCS). Cortical function and network connectivity were measured using local field potential (LFP) recordings and resting-state functional MRI (rs-fMRI), respectively, for up to 6–8 h after induction. Using this multimodal approach, we aimed to answer the following questions: What are the initial electrophysiological signs of coma that occur in the cerebral cortex following brainstem injury? How do rats with brainstem coma behave immediately following the injury and during acute recovery? How do the electrophysiological properties of the cerebral cortex evolve in acute brainstem coma? Which subcortical and cortical networks reconnect as rats recover from brainstem coma?

2. Methods

2.1. Animal subjects

A total of 76 adult male Sprague Dawley rats (350 ± 50 g) underwent ET-1 injection (ET-1 injection group) into the mid-pons parenchyma (Fig. 1C), at approximate coordinates AP -11, ML ± 0.5, DV -1.3 mm from the ventral surface of the brainstem. The outcomes of these animals are reported in Fig. 1J. In summary, 68 rats entered the comatose state, whereas 8 did not, possibly due to technical failure during the injection. Of the 68 rats that entered the comatose state, 32 rats (47.1%) showed behavioral signs of recovery (*i.e.* the RCS score increased after coma induction) and were thus included in the present study: 6 in the behavior group, 6 in the LFP group, 14 in the rs-fMRI group, and 11 in the

anatomic MRI group (5 rats were common to the rs-fMRI and the anatomical MRI groups). Additionally, 3 animals underwent ET-1 injection and concurrent calcium and multi-unit activity (MUA) recording (Ca^{2+}-MUA group) to further characterize the phase of coma induction from a cortical level. In addition to the animals in the behavior group, behavioral RCS evaluations were performed in the LFP, rs-fMRI, and anatomic MRI groups (albeit at lower temporal resolution and without pupillary light reflex testing in the LFP group), which allowed confirmation of recovery in all animals included in our results.

Multiple additional groups of rats were studied as controls for comparison with the ET-1 injection group that exhibited the long-lasting coma. A cohort of adult male Sprague Dawly rats (350 ± 50 g) underwent a similar surgical procedure but with injection of phosphate buffered saline (PBS) instead of ET-1 to serve as a sham group for behavioral purposes (sham group, n = 4). A separate group of control animals was anesthetized with 2% isoflurane and scanned for a period of 6 h to serve as a control for the rs-fMRI group (rs-fMRI control group, n = 11). A subset of rats in the control rs-fMRI group were also used as controls for the anatomical MRI analysis (anatomic MRI control group, n = 9). Another group of rats underwent topical application of ET-1 to the surface of the brainstem without injection into the brainstem parenchyma (topical ET-1 control group, n = 4). Finally, a group of rats underwent basilar artery occlusion (BAO) during development of the ET-1 injection model, and these BAO data are reported here as another behavioral control group (BAO control group, n = 13). Table S1 provides a description of all groups and the number of animals used in each group.

2.2. Chemicals

ET-1 (E7764, SIGMA-ALDRICH) was used at a concentration of 400 μM (100 μg of ET-1 were diluted in 100 μL of PBS). Caution should be considered to store the diluted ET-1 in the $-80°$ freezer (the reported experiments use the ET-1 solution within less than 1 month storage). Also, the delivered ET-1 shows varied potency for vasoconstriction. Depending on the potency of the compound, a total volume ranging from 0.4 to 2 μL was injected into the brainstem through an infusion pump (every time a new batch of ET-1 was diluted, its efficacy was tested in 1 or 2 animals to calibrate the appropriate dosage). ET-1 is an endothelium-derived contracting factor (Yanagisawa et al., 1988a,b) that modifies the vascular tone, hence influencing local blood flow (Kramer et al., 1994). ET-1 has been used to reliably cause stroke (typically cortical) by means of focal cerebral ischemia in multiple animal species (Ansari et al., 2013; Virley et al., 2004; Roome et al., 2014).

2.3. Animal procedures

All animal procedures were approved by the Animal Protection Committee of Tübingen (Regierungspräsidium Tübingen).

2.3.1. Viral injections for GCaMP-mediated calcium imaging studies

4-weeks old animals were anesthetized with 5% isoflurane in chamber. A small amount of an ophthalmic ointment was placed over the eyes to protect from drying. The anesthetized animals were transferred to a stereotaxic frame and kept anesthetized with 1.5–2% isoflurane. The dorsal skull was exposed. The fissure Bregma was identified and used as a landmark to target the surface of the barrel cortex (AP-2.4, ML 4.9 mm). A ~0.8–1 mm diameter hole was drilled on the skull using an electric drill. A micro-injection pump was used to deliver 600 nL of the viral construct AAV5.Syn.GCaMP6f.WPRE.SV40 to the barrel cortex at a depth of 0.8–1.2 mm. After the surgery, animals were treated with a painkiller and antibiotic for 3 consecutive days, their weight was monitored and they were allowed to recover for 3–4 weeks, which corresponds to the time needed for the GCaMP to express in the target neuronal population (He et al., 2018; Wang et al., 2018). Calcium imaging and coma induction were conducted in the adult animals after this resting period.
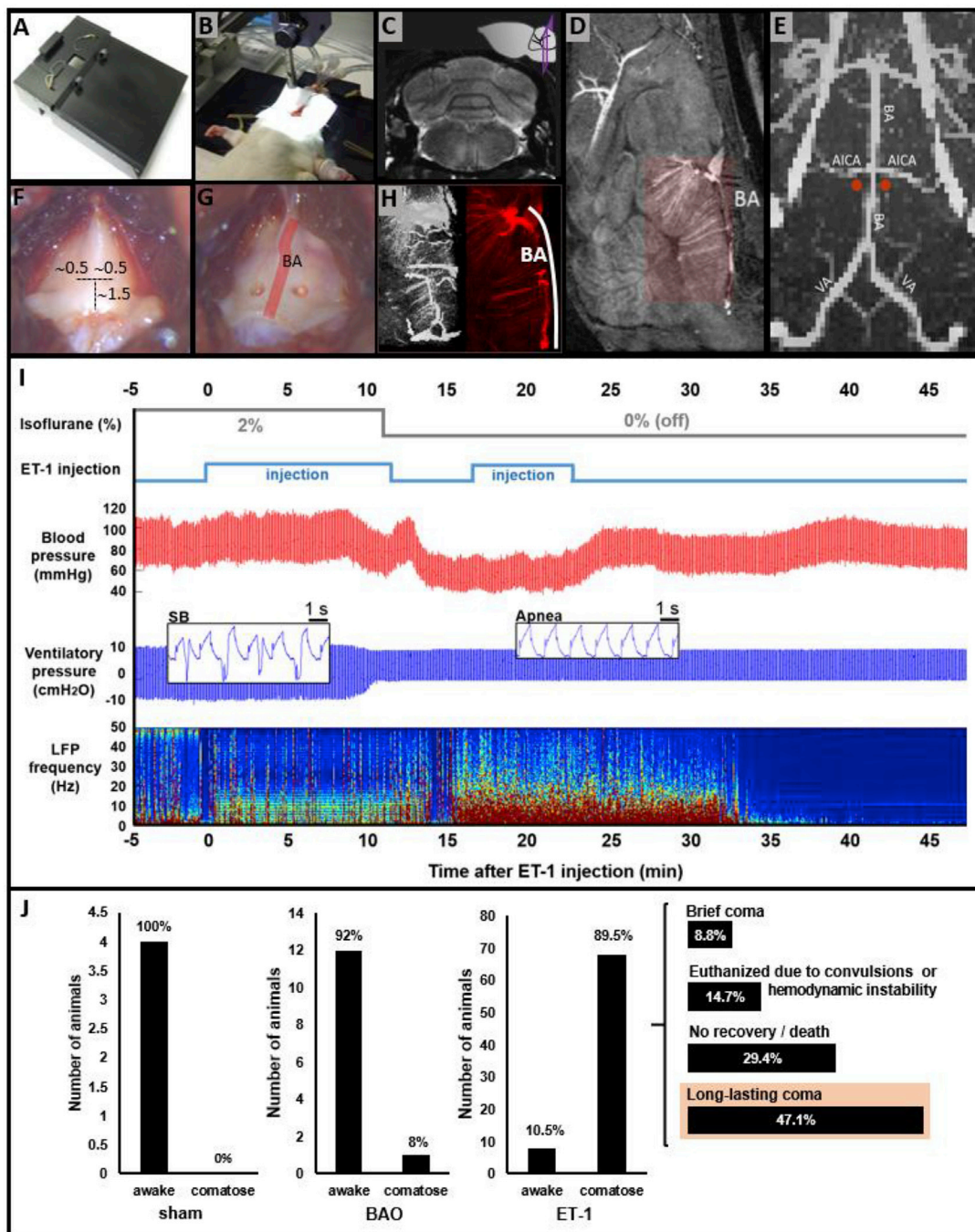
Fig. 1. Methodology of coma induction and outcome, compared to two control conditions. (A) Surgical bed designed for rats with dorsal implants and retractors to expose the basilar part of the occipital bone. **(B)** Typical setup of an anesthetized, mechanically ventilated rat during injection of endothelin-1 (ET-1) into the brainstem. **(C)** Approximate point of injection in a T2-weighted MRI image. **(D)** Sagittal view of an MRA of the rat brain highlighting the BA and penetrating branches. **(E)** 3D reconstruction of a high resolution MRA of the brainstem, indicating the approximate injection sites in relation to the BA (red dots). BA: basilar artery; AICA: anterior inferior cerebellar artery; VA: vertebral artery. **(F)** Approximate coordinates from the lower edge of the basioccipital (in mm) to drill the craniotomies for ET1 injection. **(G)** View of the craniotomy sites lateral to the BA, whose inferior-superior course along the midline is shown in schematic form as a red line superimposed on the bone. **(H)** 3D reconstruction of the MRA of the BA territory observed from different angles. BA: basilar artery. **(I)** Physiological monitoring during coma induction in a representative animal. Time 0 represents the beginning of injection of the vasoconstrictor ET-1 into the brainstem parenchyma. Anesthesia, provided with isoflurane, was switched off immediately following detection of apnea and hypotension, which occurred within the first 15 min after ET-1 injection. Apnea was detected based upon a change in shape and amplitude of the ventilatory pressure waveform (spontaneous breathing [SB] inset vs. apnea inset). Cortical activity, as measured by local field potentials (LFP), increased immediately after withdrawal of the anesthetic, then abruptly vanished approximately 35 min after ET-1 injection, resulting in an isoelectric line (see Fig. 3 for a more detailed description of the electrophysiological data). **(J)** Behavioral outcome of rats treated with sham surgery (injection of phosphate buffered saline (PBS) into the brainstem) ('sham', N = 4), BAO ('BAO', N = 13), or injection of ET-1 into the brainstem ('ET-1', N = 76), considered as either awake (fail to induce coma) or comatose. Sham rats showed a normal recovery; rats undergoing BAO awoke with certain abnormalities but not coma in ~92% of the cases; rats treated with ET-1 became comatose in ~90% of the cases (68 out of 76 animals). The long-term behavior of animals treated with ET-1 was variable, with 32 rats (~47% of 68) exhibiting a long-lasting coma with gradual recovery (named just "comatose animals" throughout the manuscript). 'Brief coma' defines absence of righting reflex for 1–2 h only, 'no recovery/death' defines rats not showing any recovery of the RCS score or dying within a period of 6 h; 'long-lasting coma' defines rats entering the coma state and exhibiting a gradual recovery of neurological function within a period of 6 h. BAO: basilar artery occlusion.

2.3.2. Animal preparation procedures prior to coma induction

Anesthesia was induced with 5% isoflurane in the adult animal in a chamber. Anesthetized animals were intubated with a 14 Gauge cannula inserted through the oral cavity to access the trachea. Rats were ventilated using an animal ventilator (CW-SAR-830/AP) at 60 ± 1 breaths per minute, with an inspired oxygen concentration of 30%. Anesthesia was maintained with 2–2.5% isoflurane for all surgical procedures until induction of coma. To monitor blood pressure, all animals underwent cannulation of the femoral artery with polyethylene tubing (PE-50, filled with heparin solution to prevent blood coagulation). Ventilatory pressure, end-tidal CO_2, arterial blood pressure, heart rate and temperature were monitored continuously throughout the experiments.

2.3.3. Procedure for electrode/fiber implantation

For electrophysiology studies, a $\sim 1\,M\Omega$ impedance and $\sim 100\,\mu m$ diameter tungsten electrode was implanted into the primary somatosensory cortex (S1, for forepaw or barrel cortex). The LFP recording in the S1 of rats has been routinely practiced with simultaneous fiber optic calcium recording (He et al., 2018; Wang et al., 2018). For combined electrophysiology-calcium imaging studies, an optical fiber of $\sim 200\,\mu m$ diameter was lowered together with a tungsten electrode into the primary somatosensory cortex (barrel cortex). Detailed procedure has been described previously (He et al., 2018; Wang et al., 2018). Briefly, the anesthetized rat was positioned in a stereotactic frame, the dorsal skull was exposed and a metal screw was placed on the occipital bone to serve both as reference and ground. The fissure Bregma was identified and used as a landmark to target the surface of the forepaw (AP 0.5, ML 4 mm), or barrel cortex (AP -2.4, ML 4.9 mm). A $\sim 1.5\,mm$ diameter burr hole was drilled on the skull and the dura mater was removed. The electrode (or the optical fiber + electrode) was lowered down to 0.9–1.2 mm from the brain surface (layer V of S1). An adhesive gel was used to fix the electrode to the skull and the skin was sutured around the implant.

2.3.4. Procedure for coma induction

The diffuse brainstem tegmentum coma model relies on vasoconstriction of the arteries irrigating the brainstem by means of injection of ET-1 (Fig. S1). Importantly, during development of this ET-1 injection model, we first performed a series of BAO experiments in rats (Supplementary Note 1). In contrast to BAO caused by thrombi in human patients (von Campe et al., 2003), which may result in a comatose state, we found that experimental BAO in rats does not reliably cause a comatose state (Fig. 1J and Fig. S2). Thus, for our ET-1 injection model, we aimed to target not only the basilar artery, but also its penetrating branches that irrigate the rostral brainstem (see Fig. 1D and E and H), producing a more diffuse brainstem tegmentum injury.

The procedure to induce coma through ET-1 injection was performed as follows. The anesthetized rat (2–2.5% isoflurane) was positioned in dorsal recumbence in a custom-made rat-surgery bed (Fig. 1A and B), which allowed surgical procedures to be performed from a ventral approach even in animals with implants on the dorsal skull. Eyes were covered with an eye ointment throughout the experiment to prevent drying (in animals subjected to behavioral tests the eyes were cleaned to test corneal reflex and the ointment was applied again until the next assessment). After shaving the ventral neck, a longitudinal incision was made on the skin, the thyrohyoid muscles were dissected, the trachea was retracted laterally from the midline and the basilar part of the occipital bone (basioccipital) was exposed (Fig. 1F and G). Two bilateral craniotomies of $\sim 0.5\,mm$ were performed on the basilar bone (Fig. 1G), at the level of the mid-pons (Fig. 1C). The stereotaxic coordinates were estimated based on the landmarks of the basilar bone (Fig. 1F) and high resolution MRI confirmed the injection point at the brain parenchyma with approximate coordinates AP -11/11.5, ML ± 0.5, DV 9 mm ($-1.3\,mm$ from the brain surface), based on the atlas of the rat brain (Paxinos and Watson, 2007). A 33 Gauge needle attached to a micro-syringe was lowered with a stereotaxic system between 0.5 and 1.5 mm

from the dura mater of the ventral surface of the brain, and a volume between 0.4 and $2\,\mu L$ of ET-1 solution was slowly injected into the brainstem (100–200 nL/min, using a micro-infusion pump). The needle was left in place for 8 min after injection and was carefully removed afterward. A small amount of dental wax was used to cover the craniotomies. The wound was sutured and the analgesic Ketoprofen was administered subcutaneously at 5 mg/kg. The entire procedure for coma induction is shown in Movie S1. The word "post-coma" is used in the text accompanied by the number of minutes or hours to refer to the time elapsing from the moment of coma induction (*i.e.* withdrawal of anesthesia after observing physiological changes upon injection of ET-1).

Supplementary video related to this article can be found at https://doi.org/10.1016/j.neuroimage.2019.01.060.

2.4. Behavioral analysis

We developed a coma scale to characterize rat behavior during coma induction and recovery. We aimed for the scale to resemble commonly used human coma scales (*i.e.* Glasgow Coma Scale (Teasdale and Jennett, 1974; Okamura, 2014), the FOUR Score (Wijdicks et al., 2011), and the Coma Recovery Scale-Revised (Giacino et al., 2004)) while incorporating behavioral observations made by our investigator team in the first subset (20 animals) of rats that underwent coma induction. We name this scale the "Tübingen-Boston Rat Coma Scale" (RCS). The purpose of this scale was to quantitatively discriminate between different neurological states in the rat, from the unconscious unresponsive state to the conscious and responsive state. The following reflexes, physiological responses, and behavioral domains are assessed in the RCS (Table 1): eye blink, motor function (reflexive and purposeful), brainstem reflexes (pupil, corneal and pinna reflex), respiration, righting reflex, auditory response, and whisker movement (detailed discussion in Supplementary Note 2).

A detailed characterization of behavioral coma recovery in the rat based on this scale, along with intra- and inter-rater reliability results, is provided in the Supplementary Note 2 and Fig. S3. The RCS total score ranges from 0, representing coma, loss of brainstem reflexes, loss of motor function, and apnea, to 16, reflecting a normal conscious rat (*i.e.* exhibiting all reflexes and voluntary movements observed in healthy animals). The RCS can be completed in 1 min by a trained investigator (Movie S2). For validation, we tested the RCS in healthy animals anesthetized at different isoflurane levels, the scores of which are reported in Fig. 2C and D. We used the Wilcoxon-Mann-Whitney test to assess for differences in RCS scores in different experimental groups (Fig. 2C). A comprehensive summary of behavioral observations made during development and validation of the RCS is provided in Supplementary Note 2.

Supplementary video related to this article can be found at https://doi.org/10.1016/j.neuroimage.2019.01.060.

In addition, to study stress levels in the animals, $300\,\mu L$ of blood were collected via the femoral catheter from 4 comatose animals at 3 h post-coma and from 4 control animals anesthetized with 1% isoflurane. The blood was centrifuged and plasma was separated and aliquoted in 2 samples ($50\,\mu L$ each) per animal for reproducibility testing purposes. Samples we stored at $-80\,^\circ C$ and sent to a steroid analysis laboratory (Steroidlabor im Analysenzentrum, Heidelberg, Germany), where a radioimmunoassay detection method was used to analyze the corticosterone content of the samples.

2.5. Acquisition and processing of electrophysiological (LFP and MUA) and calcium signals

LFPs were recorded with one of two electrophysiology systems (Biopac-Acknowledge or CED-Spike2), which showed similar results and confirmed the reliability of the recordings. When using Biopac (MP150, EEG100C module), the LFP signals were amplified 5000 times and recorded at 5000 samples per second, while with CED (1401), the LFP signals were pre-amplified 25 times at the headstage followed by a 20

Table 1

Tübingen-Boston Rat Coma Scale. Additional information can be found in Supplementary Information (in supplementary Note 2).

TÜBINGEN-BOSTON RAT COMA SCALE										
Subscales	**Minutes Post-Coma**									
	30	60	90	120	150	180	210	240	270	300
EYE BLINK SCALE										
2 - Blinks spontaneously[1]										
1 - Blinks upon stimulation[2]										
0 - No blinking (without directly touching the eye)										
MOTOR FUNCTION[3]										
4 - Voluntary walking										
3 - Isolated spontaneous movements (e.g. limbs or head)										
2 - Withdraws forepaw and/or hindpaw in response to noxious stimulation										
1 - Muscle contractions in response to noxious stimulation of the limbs										
0 - Absence of motor response to noxious stimulation										
BRAINSTEM REFLEXES										
3 - Pupil[4] AND corneal[5] AND pinna[6] reflexes present										
2 - Two of pupil/corneal/pinna reflexes present										
1 - Pupil OR corneal OR pinna reflex present										
0 - Absence of pupil, corneal and pinna reflexes										
RESPIRATION										
3 - Not intubated, breaths with a regular pattern										
2 - Not intubated, breaths with an irregular pattern										
1 - Breathes above ventilator rate (initiates spontaneous breaths)										
0 - Breathes at ventilator rate or apnea (no spontaneous breaths)										
RIGHTING REFLEX										
2 - Normal righting reflex[7]										
1 - Partial righting reflex										
0 - None										
AUDITORY RESPONSE										
1 - Auditory startle[8]										
0 - None										
WHISKER MOVEMENT										
1 - Spontaneous whisker movements[9]										
0 - None										
TOTAL SCORE										

Legend of the RCS:

[1] The observation time for assessment of spontaneous blink should be of around 3 min, in the absence of stimulation (in healthy rats it ranges from several seconds to 2–3 min).

[2] Stimulation to assess evoked blink consists of gently stimulating any part of the animal (without touching the eye –corneal reflex is assessed separately). Some rats blink easily in response to stimulation of the pinna (with or without parallel shaking of the head), therefore attention must be put on the eye response when testing the pinna reflex in order to score a positive evoked blink.

[3] Stimulation consists of pinching forepaw/hindpaw, applying a force of ~3 N for less than 0.5 s. Positive reactions may occur as muscle contractions or withdrawal of the limb.

[4] Pupil contraction is observed with optical microscope. The eye is subjected to different light intensities from darkness (eye is covered) to full brightness (increasing the intensity of the microscope light source). Pupil reflex is considered present if the eye exhibits a decrement in pupil diameter upon light intensification.

[5] The tip of a cotton swab is approached to the corneal epithelium, medial and lateral canthus of the eye. The reflex is considered present if a blink follows stimulation.

[6] A thin (~1 mm diameter) semi-flexible rod with blunt tip (to prevent damage) is used to lightly touch or tickle the pinna of the animal. The reflex is positive if the animal flicks ears or shakes head after stimulation.

[7] The test consists of bending the body of the animal to a side (taking it out of its normal upright position). Righting reflex is present if the animal is able to reorient itself (integrating movements of several muscles in head, trunk and limbs). Partial righting reflex is considered when only the upper or the lower body rotates to recover the upright position, in contrast to the synchronized whole-body re-positioning observed in a normal righting reflex.

[8] Stimulation is provided with hand clapping over the head of the animal. Startle reflex is considered present if the animal shows any reaction to the sound, *e.g.* body trembles.

[9] Natural whisker movement defined as a relatively high amplitude movement of all the whiskers in one pad.

Additional notes: Reflexes that can be tested on both sides (*e.g.* those concerning eyes, ears or paws) are considered present if one of the two (left or right) counterparts exhibits the positive response. If one reflex is tested several times, the best score counts.

times amplification using an MCP-PLUS Alpha Ohmega amplifier (total amplification = 500), and recorded at 16000 or 25000 samples per second. The GCaMP-dependent fluorescence signal was recorded using CED-Spike2 at 1000 samples per second. LFP signals were originally acquired on the whole spectrum allowed by the given sampling rate and record length (0.0016–2500 Hz), but were then filtered between 0.5 Hz and 49 Hz to avoid baseline and electrical noise, respectively. MUA was acquired through the WaveMark function in Spike2 using a high-pass filter time constant of 3.8 ms and a threshold of 0.1 mV.

An initial electrophysiological record was acquired prior to coma induction to ensure a stable signal. LFP/MUA/calcium recordings were acquired from 3 animals during coma induction (Fig. S4) and LFP was obtained from all animals in the electrophysiological study every hour post-coma in runs of 10 min. The behavioral state of the animal was assessed every 30 min with the RCS to test associations between behavioral scores and electrophysiological parameters at each post-coma time-point.

The LFP signals were processed using MATLAB (Natick, MA). A power spectrum of the whole LFP recording was computed for frequencies between 0.5 and 49 Hz using time-frequency decomposition (timefreq) based on wavelets with 2-second windows (van Vugt et al., 2007) (Fig. 3A and B). The power of the specific electrophysiological bands delta, theta, alpha, beta and gamma was calculated as frequencies between 0.5 and 4, 4 to 7, 7 to 15, 15 to 31, and 31–49 Hz, and plotted at different post-coma times (Fig. 3D). The raw LFP signal was additionally plotted to detect the electrical waveforms from the cortex (Fig. 3C). The correlation between the LFP power and the neurological score was computed using MATLAB (corr2 function) (Fig. 3E). The Hilbert transform was applied to specific LFP frequency bands to obtain the phase and the amplitude of the delta, theta and alpha bands. A graph showing the amplitude of theta or alpha at each phase of delta (phase-amplitude coupling) is shown in Fig. 3F and G. The delta phases at which the amplitude of theta and alpha were largest were used to extract the

delta/theta and delta/alpha phase-locked-amplitude coupling at each post-coma time. Finally, the phase-amplitude coupling values extracted from the different comatose animals were averaged at each post-coma time and the standard deviation of the mean was calculated (Fig. 3H).

2.6. Acquisition of magnetic resonance imaging (MRI) data

All images were acquired with a 14.1 T/26 cm magnet (Magnex, Oxford) interfaced to an Avance III console (Bruker, Ettlingen), and 12 cm diameter gradient capable of providing 100 G/cm with a rise time of 150 μs (Resonance Research). Trans-receiver surface coils with elliptical shape of ~2 × 2.7 cm minor and major axis, respectively, were used to acquire rs-fMRI images. Animals studied with MRI underwent an additional preparation step consisting on filling the ear canal with a fluoride paste to reduce the magnetic susceptibility artifacts at the air-tissue interface.

For quantitative analysis and localization of infarcted tissue, anatomical scans of the comatose animals were acquired between 4 and 6 h after coma induction. A T2-weighted Rapid Acquisition with Relaxation Enhancement (RARE) sequence was used to identify lesions (*i.e.* cytotoxic edema) in the brain, with the following parameters: effective echo time (TE), 38 ms; repetition time (TR), 2s; matrix size 128x128; in-plane resolution, 200 μm; slice thickness, 1 mm; RARE factor, 8. Typically, 42 times averaged 24 coronal slices were acquired in a scan time of 22 min 24 s.

A gradient-echo Fast Low Angle Shot (FLASH) sequence was used for visualization of the brain vasculature (MR angiography (MRA)) with the following parameters: flip angle, 50°; TE, 1.867 ms; TR, 20 ms.

To study brain connectivity changes during acute recovery from coma, a rs-fMRI scan was performed every ~60 min, starting at hour 1 and up to hour 8 after coma induction. A 3D-EPI sequence was used to map the T2*-weighted MRI signal with the following parameters: TE, 12.5 ms; TR, 1s; matrix size, 48x48x32; resolution, 400x400 × 600 μm
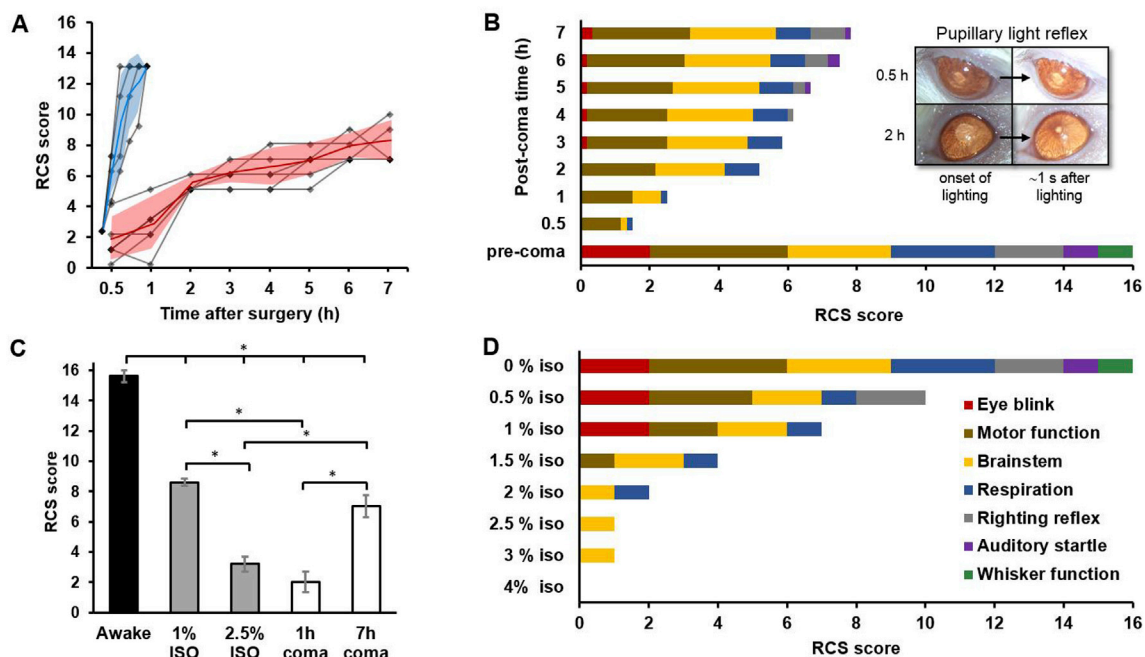
Fig. 2. Behavioral analysis. (**A**) The graph shows the individual (in gray/black) and averaged (in red or blue) RCS scores at different post-surgery times of rats after coma induction (n = 6; red color) or after sham surgery (n = 4; blue color). Note that all animals were ventilated, so the maximum RCS score possible was 14 (maximum Respiration score was 1). The shadowed areas represent the standard deviation of the data. (**B**) Averaged category-specific RCS scores before and after coma induction (n = 6). Insets show the microscopy-based assessment of pupillary light reflex (a brainstem reflex) at 0.5 and 2 h after coma induction. (**C**) RCS scores of rats under 5 different conditions: awake (n = 5), anesthesia with 1% isoflurane (1% ISO; n = 5), anesthesia with 2.5% isoflurane (2.5% ISO; n = 5), 1 h after coma induction (1h coma; n = 6), and 7 h after coma induction (7h coma, n = 6). Error bars represent standard error of the mean. (**D**) Category-specific RCS score of a representative anesthetized rat under different isoflurane concentrations.
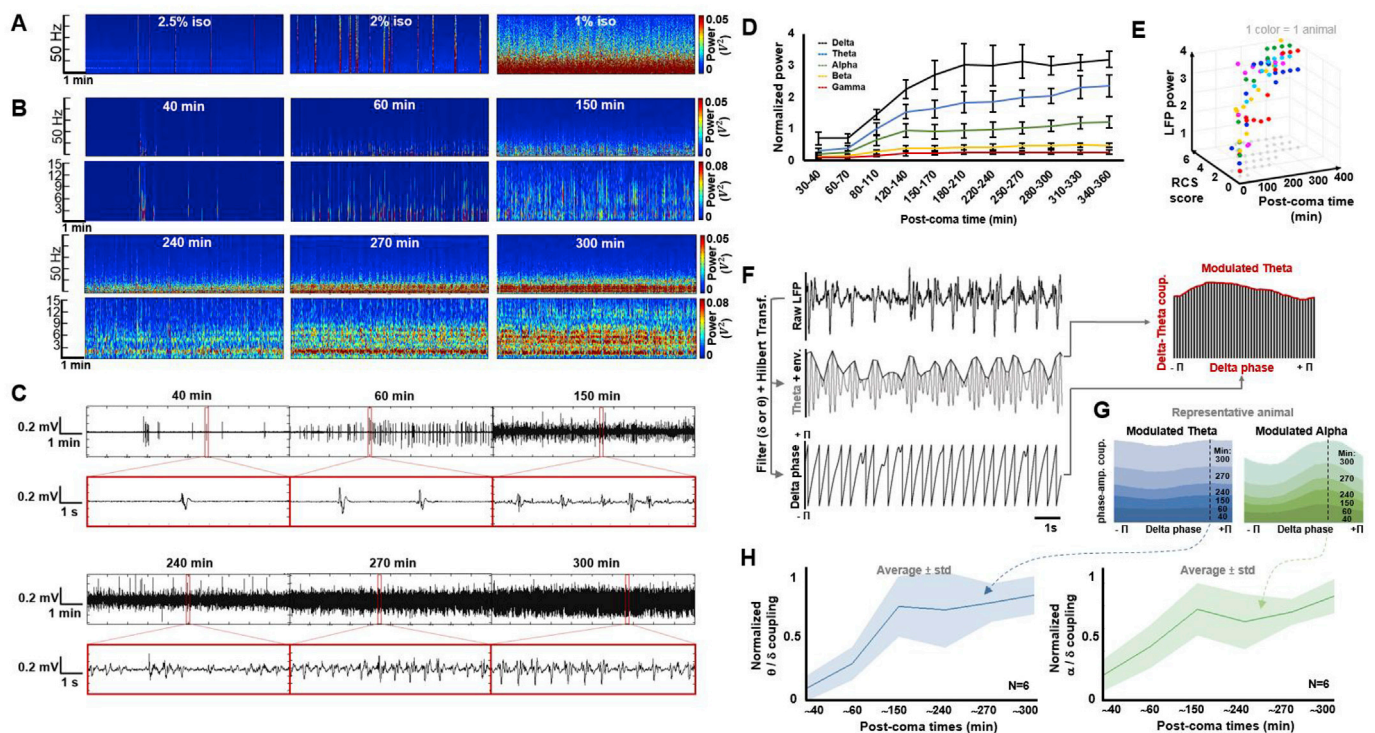
Fig. 3. Electrophysiological assessment of comatose rats. (**A**) Power spectra of cortical local field potential (LFP) recordings from a healthy anesthetized control rat at different isoflurane (iso) concentrations. (**B**) Representative LFP power spectra at different times after coma induction (without isoflurane). (**C**) LFP traces from a representative comatose rat (same as in B) at different times after coma induction. (**D**) Graph showing the mean LFP power at different frequency bands (delta: 0.5–4 Hz; theta: 4–7 Hz; alpha: 7–15Hz; beta: 15–31 Hz; gamma: 31–49 Hz) during coma recovery (n = 6). Error bars represent standard error of the mean. (**E**) 3-dimensional plot showing the relationship between LFP power, post-coma time and neurological score (different colors represent different animals). (**F**) Scheme exemplifying the acquisition of phase-amplitude coupling from the LFP data. (**G**) Phase-amplitude coupling (delta phase/theta amplitude (in blue) and delta phase/ alpha amplitude (in green)) at different post-coma times in a representative animal. (**H**) Group-level phase-coupling analysis along post-coma time. Shadowed areas in H represent standard deviation of the mean.

(600 μm slice thickness). Typically, the fMRI signal was recorded for 925 TRs in a scan time of 15 min 25 s. Additionally, an anatomic RARE image (TE, 9 ms; TR, 4000 ms; matrix size 128x128; in-plane resolution, 150 μm; slice thickness, 600 μm; RARE factor, 8) was acquired matching the geometry of the 3D-EPI for registration purposes.

2.7. Anatomic image processing and analysis

All anatomic images were registered to a template using AFNI software (3dAllineate). MATLAB software was used to quantitatively identify the infarcted regions from the anatomic MRI in the comatose versus anesthetized control rats based on T2 signal intensity. 14 regions of interest (ROIs) were defined based on a rat brain atlas (Paxinos and Watson, 2007), including 11 brainstem arousal nuclei (Fischer et al., 2016) (Okamura, 2014), 2 additional subcortical nuclei and 1 cortical region. Additionally, an ROI in the visual cortex served as reference or control ROI. Whole brain images (*i.e.* all slices grouped as a whole) were first normalized using the Matlab function mat2gray, and the average intensity of each ROI was calculated and divided by the intensity of the control ROI, for each individual rat. The final intensity values of each ROI were then averaged among the comatose and control groups to provide a comparative measure of ROI infarction between both conditions, and the standard error was calculated for both groups. Additionally, a percentage map was created by comparing mean MR images of the comatose and control groups. For visualization purposes, a 30% threshold was used on the overlay map (Fig. 4A, middle panel), which corresponds, approximately, to two times the standard deviation of the averaged T2-weighted MRI signal over the arousal nuclei in the comatose group (averaged standard deviation over arousal nuclei = 0.16). A 2-sample *t*-test was computed between the comatose and control animals to assess for significant infarcted areas. Correction for false discovery rate (FDR) included multiple comparisons analysis with randomization and permutation of 10,000 simulations (3dttest++ -Clustsim).

2.8. Histology

To confirm that T2-signal changes on the anatomic MR images represented infarction in the brain, the histopathologic stain TTC (2,3,5-triphenyltetrazolium chloride) was performed in the brains of 4 comatose rats from the anatomical MRI experimental group. Briefly, anesthetized rats were perfused with PBS only and the brain was removed and kept at −80 °C for 10 min, followed by 5 min at −20 °C. The brain was cut in 1 mm slices and exposed to 1% TTC (1g TTC in 100 mL PBS) at 37 °C for ∼20 min (until a reddish color was observed in the tissue). Slices were moved to 4% paraformaldehyde solution and a surgical microscope was used for photographing after 5–7 days.

2.9. Functional connectivity image processing and analysis

A combination of AFNI (Cox, 1996) and Lipsia (Lohmann et al., 2001) functions was used to process the rs-fMRI datasets. Two types of analysis were performed to identify the nuclei that potentially contributed to recovery from coma: eigenvector centrality mapping (ECM) and traditional region-based correlation analysis.

ECM calculates the degree of correlation between each voxel and every other voxel in the network, similar to degree centrality but additionally taking into account the hierarchy of each connection to assign higher values to those voxels that are connected to central hubs within
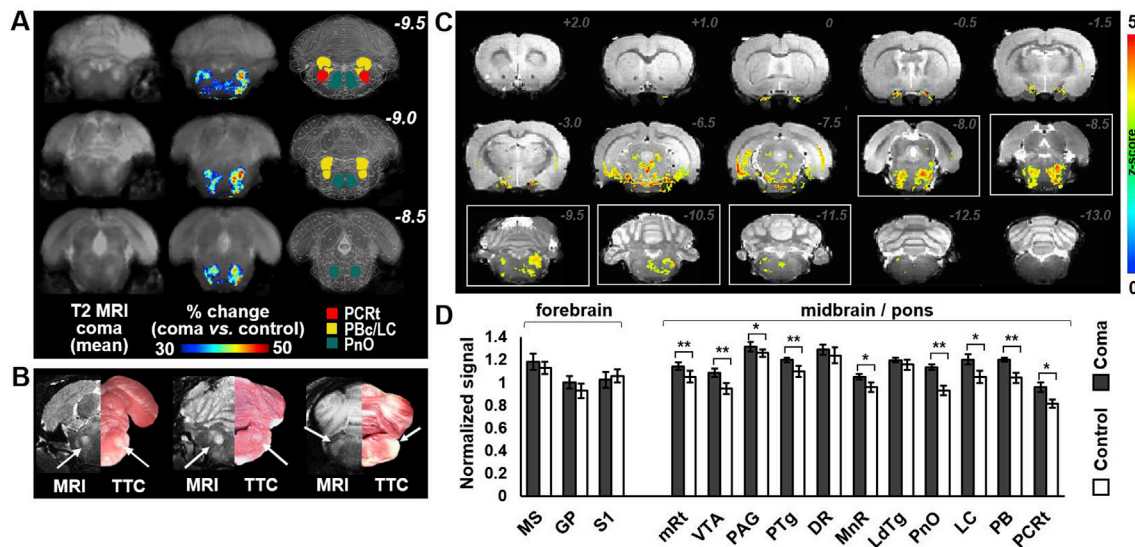
Fig. 4. Anatomic correlates of brainstem coma in the rat. (**A**) Averaged T2-weighted (T2) MRI of the coronal brainstem images from 11 comatose rats (left column); overlay showing areas with more than 30% T2 signal increase (*i.e.* infarcted areas, ≥ 2 x standard deviation) in the comatose rats, as compared to 9 healthy anesthetized controls (middle column); and regions of interest overlaid in the rat brain atlas for reference (right column). (**B**) TTC-stained brain slices of a representative comatose rat compared to its mirrored T2-weighted MRI (right and left panels respectively). Areas of histopathological infarction in the comatose animals correspond to regions of T2 signal increase (arrows). (**C**) Statistically thresholded overlay (visible voxels present a p-value <0.025, false discovery rate corrected), color-coded based on the Z-score from a 2-sample *t*-test between the T2-weighted intensity map of the comatose vs. control group. White boxes delineate slices with significant infarcts in arousal nuclei identified in comatose animals. (**D**) Normalized T2-weighted signal intensity within arousal nuclei of the pons and midbrain, as well as within regions of the forebrain, in comatose rats (n = 11) as compared to control rats (n = 9). Error bars represent standard error of the mean. Abbreviations: DR: dorsal raphe; GP: globus pallidus; LC: locus coeruleus; LDTg: latero-dorsal tegmental nucleus; MnR: median raphe; mRt: mesencephalic reticular formation; MS: medial septum; PAG: periaqueductal gray; PBc: parabrachial complex; PCRt: parvicellular reticular nucleus (~parafacial zone). PnO: pontis oralis (oral part); PTg: pedunculo-pontine tegmental nucleus; S1: primary somatosensory cortex; VTA: ventral tegmental area. **: p-value<0.005, *: p-value<0.01.

the network (Lohmann et al., 2010). From each rs-fMRI scan, ECM generates a map with the relative connectivity values of each voxel within the brain (Lohmann et al., 2010). The ECM analysis was performed on every rs-fMRI scan at each post-coma time (15 min rs-fMRI scans were generated every hour after coma induction), which identified several regions showing an increase in connectivity rank as the function of time (Fig. 5). First, all datasets were aligned using AFNI software (3dVolreg, 3dAllineate) and a mask was manually drawn for each slice to cover the midbrain, forebrain and all cortical regions (cerebellum and brainstem excluded). Next, Lipsia software was used to detect and correct motion artifacts (vmovcorrection, vcovariates, vresiduals). A despiking step was also included (vdespike), and time filtering was applied (vpreprocess) to keep frequencies between 0.1 and 0.01 Hz. After pre-processing, ECM was performed (vecm) to measure a relative correlation value of each voxel with the rest of the brain. A linear fitting of the time-dependent correlation values for each voxel was computed in AFNI (3dNLfim). The result was a brain map in which the intensity at each voxel depicted the slope of the concatenated correlation values of different post-coma times, indicating the recovery rate of functional connectivity, which constitutes a novel method to represent connectivity dynamic changes in a single brain map. Only voxels where the error of the fitting was below 5% were included in the future steps of analysis (*i.e.* averaging or statistical tests). Fig. S5 shows a schematic with all the (pre)processing functions used in AFNI and LIPSIA during rs-fMRI analysis. Fig. 5A and Fig. S5 show the main steps involved in the ECM analysis for acquisition of the slope map.

For region-based analysis of connectivity at different post-coma times, we analyzed the mean BOLD signal time-courses (pre-processed with motion correction, despiking and 0.1–0.01 Hz time-filtering) of 7 subcortical ROIs that were selected *a priori* based on the current literature in mammals arousal systems (Scammell et al., 2017): basal forebrain, striatum, globus pallidus, central thalamus, reticular thalamus and posterior lateral hypothalamus. We also performed region-based analysis on association cortical regions that are components of the rat default mode

network (cingulate and retrosplenial cortex) (Lu et al., 2012). Finally, we used primary somatosensory cortex to compare the connectivity changes of primary versus higher-order cortices. The corr2 MATLAB function was used to calculate the correlation between seeds for each animal at each time. The average correlation value in rats scanned at specific post-coma times was used to show the time-dependent degree of connectivity between specific ROIs. Fig. S6 shows a map with all the regions used during voxel-wise and seed-based rs-fMRI analysis presented in Fig. 6.

To analyze the motion profiles of the MRI scans, three rotational motion regressors (motion report output from the vmovcorrection function (Lipsia)) were used to acquire a final value representative of the degree of motion (Spisak et al., 2014) detected in each MRI scan. Briefly, the three column vectors ("regressors") were fitted into the following function using MATLAB:

$$Motion\ profile = \sum_t \sqrt{dx_1^2(t) + dx_2^2(t) + dx_3^2(t)}$$

where x_i = regressor$_i$ and d(x) (in MATLAB: diff(x)) returns a new vector of length = length(x)-1 that is the result of subtracting adjacent elements in x.

Control animals anesthetized with 2% isoflurane exhibited variable motion profiles at different scans along 5 h of scanning. After calculating the motion profile of each scan, the fMRI datasets were re-ordered in an increasing motion profile order, to mimic the motion profile trend of animals evolving from coma, and the slope map was acquired in the same way as for the comatose group (Fig. S7).

Finally, in order to test for differences between groups, a 2-tailed, 2-sample *t*-test was run on MATLAB (ttest2) for quantification and on AFNI (3dttest++) for visualization (*i.e.* statistic brain maps). Note that, while false discovery rate was corrected in the anatomical datasets using "–clustsim" (previous section), the functional connectivity slope maps were subjected to a different procedure to ensure reliability of the reported results: as the final measure is not connectivity but increase of
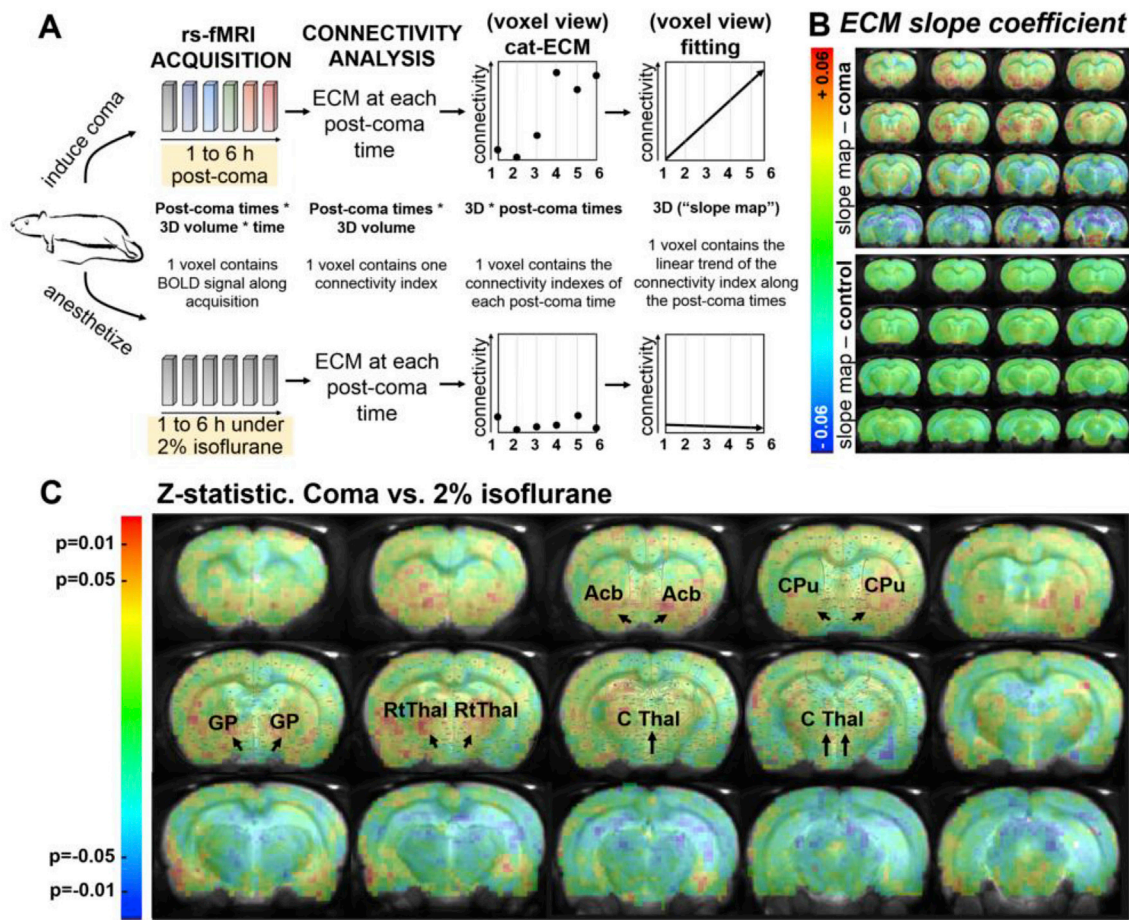
Fig. 5. Analysis of whole brain rs-fMRI in rats recovering from coma, compared to healthy anesthetized control animals. (**A**) Experimental design and general principle of the slope map. The text in the middle provides information about the dimensionality of the data and the meaning of the voxel at each step. (**B**) Averaged slope maps of the comatose rats (top panel) and the control rats (anesthetized with 2% isoflurane, bottom panel). (**C**) Brain map showing the z-statistic from the 2-tailed 2-sample *t*-test between coma and control (anesthetized with 2% isoflurane) slope maps.

connectivity (relative measure from one scan to the next), we masked out all voxels where the linear fitting of the concatenated connectivity values rendered an error above 5%. The final *t*-test was, therefore, applied to a set of volumes (slope maps) from which unreliable voxels across different scans had been screened out in a previous step.

3. Results

3.1. Diffuse injury to the brainstem tegmentum by ET-1 injection produces coma in the rat

Given the high neuroanatomic variability of infarcted areas in brainstem coma patients (Parvizi and Damasio, 2003; von Campe et al., 2003; Demel and Broderick, 2015; Kolukisa et al., 2015), we injected a vasoconstrictor, ET-1, into the parenchyma of the pontomedullary (PM) junction to alter the vascular network that irrigates the rostral brainstem tegmentum (Fig. 1D, E and H). The diffuse brainstem lesion induced coma in the animals. Fig. 1I shows physiological changes in blood pressure, ventilatory pressure and cortical activity observed during coma induction through ET-1 injection. In contrast to other strategies, ET-1-mediated brainstem injury caused coma in ~90% of the animals, with 47% of those exhibiting a long-lasting coma with possibilities of recovery (Fig. 1J).

Noteworthy is that all animals subjected to the procedure, independent of the long-term outcome, experienced a transient drop of blood pressure and cessation of spontaneous breathing. The fact that a

subgroup of these animals (~10% of a total n = 76) woke up within the next 5–15 min after withdrawal of isoflurane with focal infarcts in the medulla and caudal pons, but no infarcts in the rostral brainstem tegmentum (Fig. S2C), indicates that coma induction is not caused by ET-1 induced medulla/caudal pons infarcts, or the brief period of hypotension (Fig. 1I). A second control with topical application of ET-1 on the ventral brain surface (*i.e.*, more diffusible to the global cerebrovasculature via the CSF) caused transient vasoconstriction (10–20 min) of the major vessels (*e.g.*, basilar artery or anterior inferior cerebellar artery etc. Fig. S1G), and produced broad infarcts beyond the brainstem regions (Fig. S2D), but did not result in a long-lasting coma, with a much lower incidence of coma onset than the ET-1 injection cases. Also, we observed similar hypotension without causing coma in a subgroup of animals subjected to ET-1 injection that did not result in brainstem infarction (described above and in Supplementary Note 3), in rats undergoing BAO and, to an extent, in animals undergoing injection of PBS in similar coordinates (Figs. S2A–B). While these animals showed comparable hemodynamic changes during surgical manipulation of the brainstem, the behavioral recovery was unambiguously different from that of ET-1 treated rats (Fig. S2B and Fig. 1J), providing a negative control condition for this model to rule out a generalized hypoperfusion in the brain (similar to global ischemia) as the mechanism of coma. These results demonstrate that the ET-1 injection provides a reliable surgical procedure to induce coma in rats via diffuse injury of the rostral brainstem tegmentum.
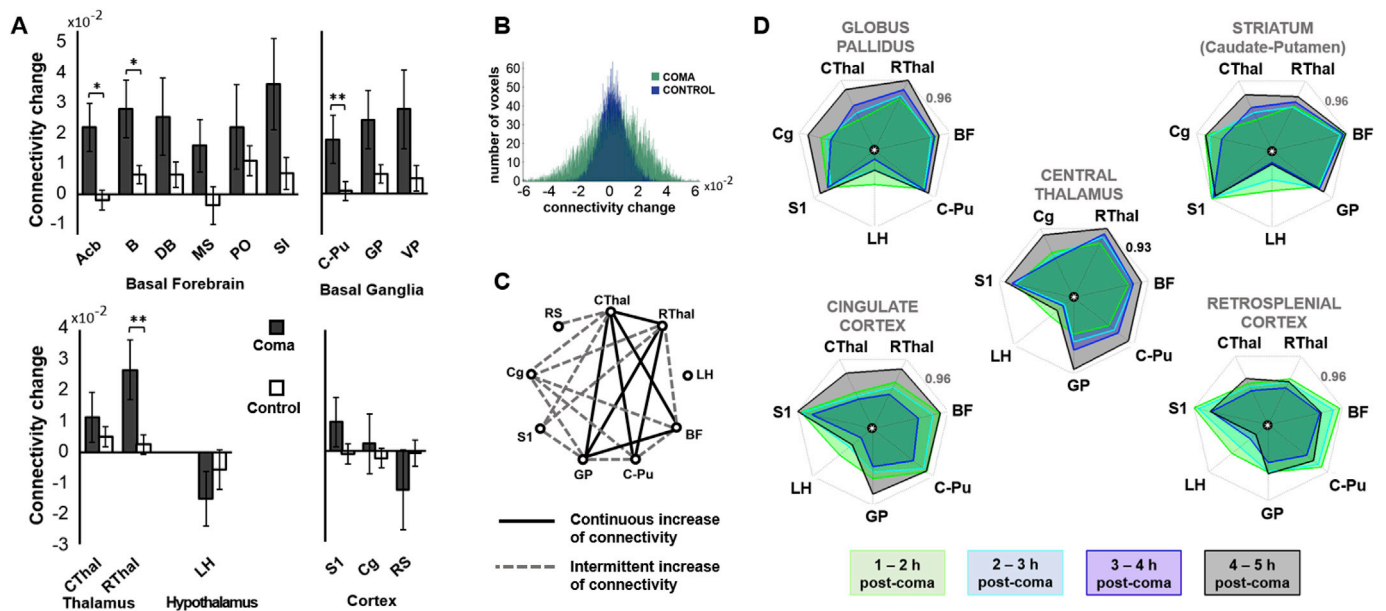
Fig. 6. Region-specific analysis of longitudinal changes in rs-fMRI connectivity. (**A**) Averaged slope (increase/decrease of connectivity during the 6-h study period) for regions of interest (ROIs) in basal forebrain, basal ganglia, thalamus, hypothalamus and cerebral cortex in rats recovering from coma (dark bars) and in control rats (white bars). (**B**) Histogram showing the distribution of voxels in the brain of comatose or healthy anesthetized control rats according to their connectivity change (slope value) during the 6-h study period. (**C**) Graph summarizing functional connections that increased continuously (solid black lines) and intermittently (dashed grey lines) during a 5-h period of coma recovery. (**D**) Seed-based connectivity results from 5 different seeds across 9 brain regions, at different post-coma times. The number at the top of each graph represents the maximum connectivity value observed during the seed-based study. Error bars represent standard error of the mean. Abbreviations: Acb: nucleus accumbens; B: nucleus basalis of Meynert; BF: basal forebrain; C-Pu: caudate-putamen; Cg: cingulate cortex; CThal: central thalamus; DB: diagonal band of Broca; GP: globus pallidus; LH: lateral hypothalamus; MS: medial septum; PO: preoptic nuclei; RS: retrosplenial cortex; RThal: reticular thalamus; SI: substantia innominata; S1: primary somatosensory cortex; VP: ventral pallidum. **: p-value<0.01, *: p-value<0.05.

3.2. Comatose animals gradually regain neurological function that is tracked by the Rat Coma Scale

To build upon prior efforts to characterize rat behavior during states of altered consciousness (Reed et al., 2013; Taylor et al., 2016), we developed a Rat Coma Scale (RCS) for quantitative assessment of rat behavior (Table 1). The RCS was designed to be similar to the human Glasgow Coma Scale (GCS) (Teasdale and Jennett, 1974), Full Outline of Unresponsiveness (FOUR) (Wijdicks et al., 2011) score, and Coma Recovery Scale-Revised (CRS-R) (Giacino et al., 2004), to optimize the translational relevance of the model (see Methods and Supplementary Material). It is important to acknowledge here that there is no current consensus regarding a definitive, gold-standard test that proves conscious awareness in the rat; hence, we anticipate that the RCS will need to be revised in the future as such evidence becomes available.

Rats in the behavioral study underwent repeated RCS assessments at each time post-coma starting at ~30 min after ET-1 injection and until at least 7 h post-coma, in intervals of 0.5–1 h. Prior to injection of ET-1, all rats had a maximal behavioral score on the RCS with clear exploratory whisking behavior. After injection of ET-1, the behavioral changes observed in rats were consistent with the absence of arousal and awareness, with apnea occurring in all rats entering the coma state (artificial ventilation provided continuously). At the time of the first RCS assessment, RCS scores ranged from 0 to 2 (median = 1), with rats showing, at most, motor reflexes (*i.e.* withdrawal of the limb in response to painful stimulation). The pupillary light reflex was typically absent during the first hour. Between 1 and 2 h after coma induction, rats recovered spontaneous breathing (but continued to receive mechanical ventilation). At this time, the pupil reflex also returned in most rats. During the following hours (typically at 2–3 h post-coma), the pinna reflex returned, as well as the corneal reflex in at least one eye. At hour 5–6 post-coma, some rats showed spontaneous movement of a limb or lifting up the head, which lasted for 1 or 2 s. Although recovery of the righting reflex was not observed in most rats during the first 8 h, in a few

cases it was possible to identify an attempt at keeping an upright posture, which was defined in the RCS as partial righting reflex, characterized by a slow righting movement of part of the body in response to bending the animal around its longitudinal axis. Fig. 2A shows RCS scores for comatose rats during the first 7 h post-coma and for sham animals, which fully recovered within one hour after the sham surgery. Fig. 2B shows category-specific RCS scores from 12 comatose rats, and Fig. 2D shows the corresponding category-specific RCS scores for a representative anesthetized rat under different anesthesia levels (0–4% isoflurane). At 7 h, the RCS score of the rats undergoing ET-1 injection was comparable to those of healthy rats anesthetized with 1% isoflurane, which is significantly higher than the RCS score of comatose rats at hour 1 post-coma, indicating a clear sign of recovery (Fig. 2C). Two animals were behaviorally assessed at 24 h, showing partial or complete righting reflex and weak attempts to initiate walking, suggesting ongoing recovery in neurological function. A video containing all reflexes tested in the RCS is provided as Movie S2. Movie S3 shows an example of a comatose rat recovering during the first 4 h.

Supplementary video related to this article can be found at https://doi.org/10.1016/j.neuroimage.2019.01.060.

Double-blinded analysis was performed to assess the RCS scores from multiple examiners to test the reliability of behavioral assessment (Fig. S3, details in methods section).

To assess the level of stress in the animals, the blood corticosterone content was measured at 3 h post-coma (RCS = 5–6), with levels comparable to those of the corticosterone measured in rats anesthetized with 1% isoflurane (125.4 ± 13.5 and 130.8 ± 9.7 ng/mL, respectively).

3.3. Cortical activity evolves from isoelectricity to slow wave-predominant rhythms during the first 4 h after coma induction

Cortical electrophysiological assessment was performed to confirm the comatose state and rule out the possibility of a locked-in state caused by damage to the descending motor pathways. Like the comatose state, a

locked-in state may be characterized by an absence of behavioral responses (Tsao et al., 2005). However, individuals who are locked-in retain arousal and awareness, and hence show normal or near-normal cortical electrophysiological features (Hawkes and Bryan-Smyth, 1974; Zeman, 2003). In the rats studied here, electrophysiological data recorded from S1 demonstrated profound cortical suppression, which rules out the possibility of a locked-in state. During surgery, prior to ET-1 injection, rats showed burst-suppression events (Fig. 1I, lower trace), typical of deep anesthesia. Approximately 10–15 min after ET-1 injection, the isoflurane was withdrawn (after blood pressure drop and cease of spontaneous breath), and cortical activity increased (Fig. 1I, lower trace), with a spectrum that resembled EEG patterns typical from awake or lightly anesthetized animals, although rats were completely unresponsive at this stage and had no spontaneous breathing with short-term hypotension (~15min, under ventilation and with sufficient O2 supplies). The paradoxical increase in cortical activity remained until approximately 20–35 min after ET-1 injection. At this moment, the cortex became isoelectric or transited to a burst-suppression pattern (Fig. 1I, lower trace and Fig. 3B and C). Cortical silence/inactivation was preceded by spreading depression/depolarization in 3 comatose animals that were subjected to recording of intracellular calcium and multi-unit activity (MUA) during the induction of coma (Fig. S4). Interestingly, iso-electrical lines were observed after cessation of the ET-1 vasoconstriction effect (Fig. S1G) and the return to baseline blood pressure (Fig. 1I), indicating a delayed coma onset following the immediate physiological state changes. The timing of cortical deactivation after injury to the tegmentum in this rat coma model is different from the fast onset of isoelectricity (in 2–3 min following insults) observed after global ischemia (i.e. occlusion of common carotid arteries (Pulsinelli and Brierley, 1979; Fortuna et al., 1997) or cardiac arrest (Jia et al., 2006; Geocadin et al., 2000; Bauer et al., 2013)). The initial period of isoelectricity (20–35 min after ET-1 injection) (Robert and Mumenthaler, 1977; Kroeger et al., 2013) was observed in 83% of the rats. In the other 17%, sparse bursting spikes (Lewis et al., 2013) were observed in the initial recordings, although a short period of isoelectricity might have occurred before starting the acquisition. The frequency of the bursting spikes increased as a function of post-coma time, similar to the burst-suppression pattern observed in rats anesthetized with 2–2.5% isoflurane (Fig. 3A), although the comatose burst spikes were smaller in amplitude. Within 2–4 h, this pattern evolved in most rats to a background of mainly delta and theta activity (Fig. 3D). Fig. 3C shows the LFP recordings of a representative rat (same animal as in Fig. 3B). Increased RCS scores correlated with LFP power during coma recovery, with a correlation coefficient of 0.73 ± 0.06 (Fig. 3E). Phase-coupling analysis (Fig. 3F) demonstrated an increase in the synchronization of the theta and alpha bands with delta phase as animals recovered behavioral responses during the first 6 h post-coma (Fig. 3G–H). These results demonstrate that cortical activity is regained in a gradual manner after brainstem coma, with the most pronounced changes occurring within the first 3–4 h.

3.4. Coma is associated with a diffuse brainstem tegmentum injury

To localize the brainstem lesions that caused coma, anatomical MRI was performed in comatose rats 4–6 h after the surgery (ET-1 long-lasting coma) and in healthy anesthetized control animals. Focal T2-hyperintense lesions were detected in the comatose animals in several pontine and midbrain arousal nuclei, including the mesencephalic reticular formation, pedunculopontine tegmental nucleus, locus coeruleus, parabrachial nuclear complex, parvicellular reticular nucleus (parafacial zone), ventral tegmental area and the pontis oralis (pontine reticular formation), among others (Fig. 4A and C). Fig. 4D shows the differences in T2-weighted signal in specific ROIs in the comatose rats as compared to healthy anesthetized animals. Histopathological stains of brainstem tissue with triphenyl tetrazolium chloride (TTC) in rats that had been scanned with MRI showed lesion patterns consistent with the

MRI findings (Fig. 4B), confirming the validity of the T2-weighted MR images for detection of infarcted brain tissue. In contrast to the brainstem injury, the basal forebrain, basal ganglia, thalamus, hypothalamus and cerebral cortex remained highly preserved (Fig. 4C and D), allowing these structures to be functionally studied during coma recovery. These results indicate that lesions involving arousal nuclei at the rostral brainstem tegmentum are crucial for the coma induction observed in the rat coma model.

3.5. Subcortical nuclei reconnect during the acute phase of coma recovery

Rs-fMRI was performed in the comatose animals at several post-coma times and in a healthy anesthetized control group at similar time intervals to track potential changes in brain connectivity during early recovery from coma. Longitudinal voxel-wise (ECM-based) and ROI-based connectivity analysis was performed on the acquired functional scans (see Methods).

Animals anesthetized with constant 2% isoflurane showed low global connectivity fluctuation over time. In contrast, rats recovering from coma showed several brain areas with a significant longitudinal increase in signal temporal correlation (i.e. connectivity) with the rest of the brain (Fig. 5C and Fig. 6A and B). This increase in connectivity was pronounced in the thalamus, the basal forebrain and the basal ganglia, with significant differences observed in the reticular thalamus, nucleus accumbens, nucleus basalis of Meynert and striatum (i.e. caudate-putamen) (Figs. 5C and 6A).

Similarly, in an ROI-specific seed-based analysis, a continuous increase of correlation was identified between the paired basal ganglia to central thalamus, or basal ganglia to reticular thalamic nuclei during the acute phase of coma recovery, suggesting a crucial involvement of the striato-pallidal-thalamic network (Fig. 6C and D). In addition, the central thalamus gradually connected with the basal forebrain and with the primary somatosensory cortex (S1) (Fig. 6C and D). The S1 and cingulate cortex experienced their most significant increase of correlation at 4–5 h post-coma with the thalamic nuclei and the globus pallidus. An increase in the correlation with the central thalamus at this time was also observed from the retrosplenial cortex, although the latter did not show net increases of connectivity with other regions. Notably, the posterior aspect of the lateral hypothalamus did not show an increase of connectivity with the other studied ROIs. All ROI-specific connectivity changes during acute coma recovery are summarized in Fig. 6C.

4. Discussion

We report a brainstem tegmentum lesion model in the rat that creates a comatose state of sufficient duration to enable longitudinal analysis of animal behavior, cortical electrophysiology, and brain network functional connectivity during coma recovery (a cost-benefit assessment of the model is provided as Supplementary Note 4). We developed and validated a behavioral scale, the Tübingen-Boston Rat Coma Scale, to quantitatively track coma recovery in the rat, analogous to coma scales that are commonly used in clinical practice to track recovery in humans. We found that increasing RCS scores were associated with increasing electrophysiological activity in the cerebral cortex, which evolved from transient isoelectricity to bursting spikes during the first hour post-coma, and to continuous slow wave (i.e. delta-theta) activity within the first 3 h of recording. Concurrently, we observed an increase in global functional connectivity in the thalamus, basal forebrain, and basal ganglia during coma recovery. Seed-based correlation analysis revealed a reemergence of connectivity between the central thalamus and the striato-pallidal complex, as well as between the thalamus, basal forebrain, cingulate cortex and retrosplenial cortex. These findings suggest an essential role of the thalamus, basal forebrain, and basal ganglia in reactivating the cerebral cortex and restoring behavioral responsiveness after ascending brainstem inputs are disrupted.

4.1. Relevance of a hyperacute model of coma and early electrophysiological changes

The brainstem tegmentum lesion model of coma described here provides a platform to elucidate mechanisms of coma pathogenesis and recovery within a hyperacute 6–8 h time window that has particular clinical-translational relevance. This is a time window during which therapeutic interventions aimed at mitigating neural network disruption and restoring consciousness are actively being investigated in patients with brainstem injuries (Smith et al., 2013). Yet little is known about acute changes in brain electrophysiology and functional connectivity in the immediate aftermath of brainstem coma, because electrophysiological and fMRI brain mapping studies are typically not feasible or safe to perform during the initial resuscitation and stabilization of a critically ill comatose patient (Edlow et al., 2017). This hyperacute time window (i.e. the first two hours) is particularly relevant to the interpretation of our electrophysiological recordings in the rat cortex, which revealed iso-electricity followed by burst spikes. These findings are uncommon in human comatose patients, except those whose coma is caused by global hypoxic-ischemic injury (Synek, 1988; Bagnato et al., 2010; Brenner, 2005). However, a few exceptional case reports support the hypothesis that a burst-suppression pattern may transiently occur after brainstem injury. In one case, a patient experienced recurrent coma that manifested electrophysiologically with a burst-suppression pattern and frontal intermittent rhythmic delta activity upon BA spasm and rostral brainstem ischemia (Frequin et al., 1991). It is also notable that a burst-suppression pattern can be observed when the cerebral cortex is intact but isolated from posterior structures in animals (Ingvar, 1955) and human subjects (Henry and Scoville, 1952; Kharoshankaya et al., 2014). It is possible that isoelectricity and bursting spikes have not been observed in human patients with brainstem coma because EEG data are not typically acquired during the hyperacute stage of injury. Alternatively, it is possible that our observations reflect species-specific electrophysiological dynamics within the rat brain in the setting of a brainstem lesion. EEG studies of human patients in the hyperacute stage of brainstem coma are needed to clarify whether the human cortex undergoes a similar progression from isoelectricity to burst-suppression before the emergence of a continuous delta-theta rhythm. The immediate transient period of cortical excitability following withdrawal of anesthesia after ET-1 injection (Fig. 1I) possibly reflects a delay in cortical deactivation upon a potential ischemic insult. Calcium imaging and multi-unit recording in three animals during coma induction showed increased MUA firing rate followed by spreading depression, and then full cortical silence (Fig. S4). The nature of this cortical deactivation with respect to the physiological changes that mark the onset of coma in our model will be further investigated.

4.2. Diffuse brainstem damage as the underlying cause of coma

The rat brainstem coma model is based upon injection of the vaso-constrictor ET-1 into the dorsomedial brainstem tegmentum, which leads to reduction in the diameter of pontine penetrator vessels branching from the BA (Fujii et al., 1991). The vasoconstriction effect of ET-1 is mediated by ET-1 receptors in the smooth muscle and endothelial cells of arteries (Dashwood et al., 1989; Loesch, 2005). The resulting ischemic insult is targeted to monoaminergic, cholinergic, and glutamatergic nuclei within the brainstem tegmentum that are known to mediate arousal, and hence consciousness, in animals and humans (Parvizi and Damasio, 2001). Importantly, neurons and astrocytes both express ET-1 receptors (Schi-nelli, 2006; Dashwood and Loesch, 2010), and therefore ET-1 interaction with the local neuro-glial network may contribute to neuronal dysfunction. Nevertheless, ischemic infarction of the brainstem tegmentum, as verified by radiological and histopathological analyses in this study, is believed to be the primary mechanism of coma induction. A transient period of global brain hypoperfusion cannot be ruled out in the present study, but, if present, it is not the source of coma, as a group of animals subjected to the same procedure and exhibiting the same hypotension but

without dorsal/rostral brainstem infarction did not enter the comatose state. Further supporting the brainstem-specific cause of coma is the fact that animals in which the ET-1 diffused from the brainstem to broader regions, causing massive injuries in the forebrain (Fig. S2D), had a lower incidence of coma or experienced a much faster recovery.

Using the ET-1 approach to disrupt the brainstem vasculature, we found that the neuroanatomic localization of the coma-causing lesion in our rat model was consistent with that of coma-causing brainstem lesions in prior animal and human studies, which have consistently highlighted the critical role of the brainstem tegmentum in consciousness (Fuller et al., 2011; Parvizi and Damasio, 2003; Fischer et al., 2016). Specifically, we found radiological and histopathological evidence of infarction within the mesencephalic reticular formation, ventral tegmental area, pedunculotegmental nucleus, median raphe, locus coeruleus, parabrachial nucleus, pontis oralis and parvocellular reticular nucleus (i.e. the parafacial zone (Anaclet et al., 2018; Anaclet et al., 2014)) (Supplementary Note 5). In contrast to the pathophysiological contribution of this diffuse brainstem tegmentum lesion to coma induction, the infarction observed ventrally near the point of ET-1 injection is not believed to contribute to coma induction, as animals subjected to ET-1 treatment but not entering the coma state (ET-1 control cases, Fig. 1J "awake") showed local infarction at the level where the vasoconstrictor was injected (i.e., the caudal pons, Fig. S2C and Supplementary Note 3). The specific contribution of each lesioned arousal nucleus to coma induction remains to be further investigated, which is why we refer to the model as a "diffuse brainstem tegmentum lesion" model of coma. In contrast to prior studies targeting individual arousal nuclei within the brainstem tegmentum, our coma model involves a large "diffuse" lesion that encompasses multiple arousal nuclei, which induced a robust comatose state verified by behavioral and electrophysiological tests. The fact that lesions involving individual arousal nuclei did not reliably cause coma in previous works (e.g. lesions of the ventral tegmental area, locus coeruleus, tuberomammillary nucleus, basal forebrain or suprachiasmatic nucleus caused alteration of the sleep-wake cycle but not coma (Blanco-Centurion et al., 2007; Gerashchenko et al., 2006; Tobler et al., 1983)) further suggests that a diffuse lesion involving multiple brainstem arousal nuclei may be key to the pathogenesis of a long-lasting comatose state. The similar anatomic boundaries of the infarcted brainstem region in this rat coma model to that of coma-causing brainstem lesions in humans (Parvizi and Damasio, 2003; Rosenblum, 2015; Edlow et al., 2013; Fischer et al., 2016) suggest that this animal model is well suited for use in future translational studies that will aim to identify the subcortical circuits that facilitate recovery of consciousness in rats and humans with coma-causing brainstem tegmentum lesions. Whether the diffuse topography of brainstem tegmentum lesions is necessary for the development of long-lasting coma will be investigated in future animal studies in which focal lesions to different combinations of individual arousal nuclei will be tested for their behavioral outcomes.

4.3. Connectivity changes during early recovery post-coma

Our rs-fMRI functional connectivity results provide compelling evidence of the neuroscientific and translational opportunities that are created by the new coma model. Specifically, our findings add to a growing body of evidence about the critical role of a striato-pallidal-thalamic-basal forebrain network in promoting recovery from coma. Consistent with the mesocircuit hypothesis (Schiff, 2010), rats recovering from coma experienced a continuous increase in connectivity between the striatum, globus pallidus and thalamus, accompanied by an increase in whole brain connectivity of these and basal forebrain nuclei. The contribution of the basal ganglia to recovery of consciousness has also been observed in humans emerging from anesthesia-induced coma (Mhuircheartaigh et al., 2010; Crone et al., 2017). In this work, the additional reconnection of the basal forebrain with the central thalamus suggests a potential role of basal forebrain arousal nuclei in coma recovery, particularly from the nucleus accumbens and nucleus basalis of

Meynert (although probably to a lesser extent than the thalamic-basal ganglia interactions, as reported by the ROI-based analysis, Fig. 6D: central thalamus graph). This observation is consistent with animal studies showing that the basal forebrain plays a crucial role in emergence from anesthesia (Zhang et al., 2016), in modulating sleep-wake circadian rhythms (Xu et al., 2015) and in the overall arousal level of the brain (Fuller et al., 2011; Anaclet et al., 2015).

In addition to reintegration of a striato-pallidal-thalamic-basal forebrain network, we also observed reintegration of a thalamocortical network (Steriade, 1999) during coma recovery in the rat. This finding builds upon prior studies showing that thalamocortical networks contribute to recovery of consciousness after severe brain injury and anesthesia (Laureys et al., 2000; White and Alkire, 2003; Ching et al., 2010). However, while thalamocortical networks are widely considered to be a substrate of consciousness (Laureys et al., 2000; Schiff, 2010; White and Alkire, 2003; Akeju et al., 2014), there is ongoing debate as to whether these networks are crucial for arousal or whether they primarily mediate higher-order cognition (Fuller et al., 2011; Mhuircheartaigh et al., 2010). Interestingly, we observed a longitudinal increase in cortical connectivity not only in the central thalamic nuclei, which are a key node of thalamocortical networks and whose electrical stimulation promotes cognitive enhancement in animals (Shirvalkar et al., 2006) and humans (Schiff et al., 2007; Monti et al., 2016), but also in the reticular thalamic nucleus, which encapsulates the thalamus and gates thalamocortical signaling (Steriade et al., 1986). Indeed, the reticular thalamic nucleus exhibited one of the most significant increases in connectivity during coma recovery of all the subcortical nodes that were studied (Fig. 6). Given that the reticular thalamic nucleus contains GABAergic inhibitory neurons whose optogenetic stimulation during the awake state results in a slow-wave EEG (Lewis et al., 2015), thalamic bursts and cortical spindles (Halassa et al., 2011), our observed correlation between reticular thalamic nucleus connectivity and coma recovery may seem counterintuitive. However, the reticular nucleus of the thalamus not only inhibits excitatory thalamocortical neurons during sleep, but also inhibits local inhibitory thalamic neurons during wakefulness, generating a net increase in cortical activity (Steriade et al., 1986). A circuit-based electrophysiological interpretation of our results is beyond the scope of the present study, but our connectivity results suggest that during cortical reactivation and coma recovery, inhibition of local inhibitory thalamic neurons by the thalamic reticular nucleus predominates over its inhibition of excitatory thalamocortical neurons. Also noteworthy is that the recovery of arousal during the acute post-coma stage may depend, to an extent, on thalamocortical connectivity changes. Multi-electrode recordings will be needed to further clarify the cortical neuronal synchronization and desynchronization patterns during post-coma recovery.

Unexpectedly, we did not detect an increase in connectivity between the hypothalamus and cerebral cortex during coma recovery. The hypothalamus is a key hub in the arousal network (Moruzzi and Magoun, 1949; Economo Cv, 1930; Nauta, 1946; Saper et al., 2001), a homeostatic control center (Saper et al., 2005), and has been shown to connect extensively with the cerebral cortex (Saper, 1985). One potential explanation for this reduced participation of the hypothalamus in recovery from brainstem tegmentum coma is the inhibitory inputs it receives from the reticular thalamus (Lewis et al., 2015) and the basal forebrain (Halassa et al., 2011). Alternatively, the hypothalamus is a large and heterogeneous region that contains diverse neuronal populations with broadly different homeostatic functions (Saper et al., 2005; Luthi, 2016; Leibowitz and Wortley, 2004). The challenges of imaging the hypothalamus in small animals have been previously reported (Van der Linden et al., 2007). The lack of spatial specificity in rs-fMRI global connectivity mapping may not allow to detect small clusters of hypothalamic neurons that contribute to coma recovery. It is also notable that the ventral location of the hypothalamus within the diencephalon is especially vulnerable to potential magnetic field inhomogeneities derived from the active breathing-induced resonance frequency offset (Van de Moortele et al., 2002; Pais-Roldán et al., 2018). Finally, it is possible that the

brainstem tegmentum lesion extended into the posterior aspect of the hypothalamus without being detected by the T2-weighted MRI scan. The use of more specific techniques, such as calcium imaging, that target specific neuronal populations (*e.g.* GABAergic or orexinergic neurons) and that are free of potential magnetic field artifacts may clarify the role of hypothalamic networks in rats recovering from brainstem coma.

An additional insight regarding brainstem coma recovery in the rat was generated by comparing the dynamic functional connectivity changes across the evaluation periods in subcortical arousal nuclei and different regions of the cerebral cortex. Whereas thalamic, basal forebrain, and striato-pallidal nuclei showed a continuous increase in connectivity during recovery, a consistent increase in connectivity between subcortical arousal nuclei with association cortices – particularly the cingulate cortex - was only observed after hour 4 post-coma, which corresponds to an epoch within the recovery period when more complex behavioral responses may become noticeable (*e.g.* righting reflex) and when background activity reappears in the electrophysiological recordings. Interestingly, a recent study reported a critical role of the prefrontal cortex (specifically the prelimbic cortex, an area immediately ventral to the cingulate cortex in the rat) on the transition to wakefulness from general anesthesia (Pal et al., 2018). Given that the cingulate cortex is an integrative hub for cognition (Newman et al., 2015; Lavin et al., 2013) and a key node of the rat default mode network (DMN) (Lu et al., 2012), our results suggest a link in the rat brain between reemergence of behavioral responses in the later phase of coma recovery and reintegration of subcortical and cortical networks that support arousal and awareness. Though the connectivity properties of the rat DMN are only beginning to be understood, there is compelling evidence in humans that reemergence of DMN connectivity is essential for recovery of consciousness after severe brain injury (Threlkeld et al., 2018; Norton et al., 2012). It is also notable that the region of association cortex that is believed to represent the hub node of the DMN differs in animals and humans. Whereas human rs-fMRI and diffusion MRI studies indicate that the posterior cingulate and precuneus (*i.e.* posteromedial complex) comprise the hub node of the DMN, it is the retrosplenial cortex in rats that is believed to play this role. The cingulate cortex has been identified as a region of association cortex that modulates cognition in rats (Ebitz and Platt, 2015; Joshi et al., 2016; Cao et al., 2016; Gompf et al., 2010; Wu et al., 2017), but evolutionary differences in the cingulate anatomy (*e.g.* rats do not possess Brodmann areas 23 and 31), and phenomenological differences between rodent and human consciousness (Boly et al., 2013) indicate that there are likely fundamental differences between the rat DMN and human DMN. Inferences pertaining to the translational human relevance of connectivity findings in the rat DMN must therefore be interpreted with caution. Nevertheless, our multimodal observations of cortical reactivation after brainstem coma provide evidence for a reintegration of subcortical arousal networks and the DMN in the rat brain. This cortical reactivation, and its accompanying behavioral improvement, appears to rely upon a constellation of subcortical arousal nodes within the thalamus, basal forebrain, and basal ganglia, along with cortical nodes within association regions of cerebral cortex.

5. Limitations and future directions

Several limitations pertaining to the multimodal analysis of brain function should be considered when interpreting the results of this study. Although the use of rs-fMRI to study brain function has been applied to rodents (Pawela et al., 2008; Shim et al., 2013), it remains challenging to account for potential artifacts associated with spontaneous breathing in non-anesthetized animals. This spontaneous breathing could lead to B_0 field inhomogeneity, such as the voluntary respiration-induced resonance offset, and special care is needed to dampen these motion artifacts (Van de Moortele et al., 2002; Pais-Roldán et al., 2018). Although several regression steps were used to acquire a reliable analysis, motion artifact remains an issue in the acquisition of rs-fMRI once the animal recovers spontaneous breathing. To investigate the degree of interference between

motion and the observed results, we calculated the motion profiles of the fMRI scans acquired from the comatose rats and from control rats anesthetized with 2% isoflurane. The varying motion profile observed in the control rats was in a range similar to that observed in the comatose rats, which allowed us to re-order the scans in a way that the motion content at each time matched that observed during coma recovery. The slope map for the re-ordered control scans was then re-calculated, which provided a "motion reference" map (Fig. S7). This motion reference map was substantially different from the coma recovery slope map, diminishing concern about motion interference in our data.

It is also important to emphasize that the network-based connectivity results reported here are based upon macroscale measurements of large groups of neurons. Circuit-based insights into the connectivity and functional dynamics of individual subcortical neurons within the arousal network will require future studies with neuron-specific techniques. This limitation is particularly relevant to the interpretation of our hypothalamic connectivity results, which unexpectedly did not show an increase in global connectivity during coma recovery, as discussed above. With regard to the rs-fMRI analysis of brain network function, it should also be noted that the whole-brain ECM-based connectivity was a relative measure among brain voxels. The highlighted voxels in the slope connectivity map are the ones in which the dynamic connectivity degree increased the most in comparison with others (the ECM analysis provides a rank, not an absolute value). Thus, functional nuclei that contribute to coma recovery might not have been readily identified here if they were overshadowed by the more significant connectivity changes observed in the thalamus, basal forebrain, and basal ganglia (see Supplementary Note 6 for a more detailed discussion about the interpretation of the ECM analysis).

Although converging evidence from our control studies suggests that coma induction is attributable to the diffuse brainstem tegmentum lesion, we acknowledge that a pathophysiologic contribution to coma induction from global cerebral hypoperfusion cannot be definitively ruled out. Future studies should clarify the potential existence and extent of such injury in the present model. Nevertheless, the observation that 10% of the ET-1 treated cases (*i.e.* waking animals) experienced similar systemic hypotension and even, in some cases, diffuse ET-1-induced infarcts through the brain, demonstrates that an episode of global hypoperfusion, if present, is not the main cause of coma in this rat coma model.

6. Conclusion

We developed a method to induce coma via a diffuse brainstem tegmentum lesion in adult rats and provided verification of brainstem lesion anatomy, behavioral assessment and examination of brain electrophysiology and network connectivity. Unlike other approaches, this animal model makes it possible to perform multimodal analysis longitudinally during the hyperacute phase (first 6–8 h) of natural coma recovery in the rat, which is currently not feasible in human patients in the clinical environment. The rs-fMRI connectivity analysis identified a crucial interaction between the thalamus, basal forebrain, and basal ganglia in reactivating the cerebral cortex during coma recovery. Future lines of study dedicated to stimulating specific thalamic, basal forebrain, and basal ganglionic subcortical arousal nuclei will aim to clarify their relative contributions to coma recovery. Establishing a reliable coma model in the rat may ultimately facilitate the development of targeted therapies aimed at promoting recovery of consciousness in humans with brainstem injuries.

Author contributions

Conceptualization, X.Y., P.P. and B.L.E.,; Methodology, X.Y. P.P. and M.Z.; Writing-original draft, X.Y., P.P. and B.L.E.; Writing-review & editing, X.Y., P.P. and B.L.E; Supervision, X.Y; Software, P.P., Y.J. and J.S.; Formal analysis, P.P.

Appendix A. Supplementary data

Supplementary data to this article can be found online at https://doi.org/10.1016/j.neuroimage.2019.01.060.

References

Abulafia, R., Zalkind, V., Devor, M., 2009. Cerebral activity during the anesthesia-like state induced by mesopontine microinjection of pentobarbital. J. Neurosci. 29 (21), 7053–7064.

Akeju, O., Loggia, M.L., Catana, C., Pavone, K.J., Vazquez, R., Rhee, J., et al., 2014. Disruption of thalamic functional connectivity is a neural correlate of dexmedetomidine-induced unconsciousness. Elife 3, e04499.

Anaclet, C., Ferrari, L., Arrigoni, E., Bass, C.E., Saper, C.B., Lu, J., et al., 2014. The GABAergic parafacial zone is a medullary slow wave sleep-promoting center. Nat. Neurosci. 17 (9), 1217–1224.

Anaclet, C., Pedersen, N.P., Ferrari, L.L., Venner, A., Bass, C.E., Arrigoni, E., et al., 2015. Basal forebrain control of wakefulness and cortical rhythms. Nat. Commun. 6, 8744.

Anaclet, C., Griffith, K., Fuller, P.M., 2018. Activation of the GABAergic parafacial zone maintains sleep and counteracts the wake-promoting action of the psychostimulants armodafinil and caffeine. Neuropsychopharmacology 43 (2), 415–425.

Ansari, S., Azari, H., Caldwell, K.J., Regenhardt, R.W., Hedna, V.S., Waters, M.F., et al., 2013. Endothelin-1 induced middle cerebral artery occlusion model for ischemic stroke with laser Doppler flowmetry guidance in rat. J. Vis. Exp. 72.

Bagnato, S., Boccagni, C., Prestandrea, C., Sant'Angelo, A., Castiglione, A., Galardi, G., 2010. Prognostic value of standard EEG in traumatic and non-traumatic disorders of consciousness following coma. Clin. Neurophysiol. 121 (3), 274–280.

Bauer, G., Trinka, E., Kaplan, P.W., 2013. EEG patterns in hypoxic encephalopathies (post-cardiac arrest syndrome): fluctuations, transitions, and reactions. J. Clin. Neurophysiol. 30 (5), 477–489.

Bell, D.J., Horne, E.A., Magee, H.E., 1933. The decerebrate rat. J. Physiol. 78 (2), 196–207.

Bignall, K.E., Schramm, L., 1974. Behavior of chronically decerebrated kittens. Exp. Neurol. 42 (3), 519–531.

Blanco-Centurion, C., Gerashchenko, D., Shiromani, P.J., 2007. Effects of saporin-induced lesions of three arousal populations on daily levels of sleep and wake. J. Neurosci. 27 (51), 14041–14048.

Boly, M., Seth, A.K., Wilke, M., Ingmundson, P., Baars, B., Laureys, S., et al., 2013. Consciousness in humans and non-human animals: recent advances and future directions. Front. Psychol. 4, 625.

Brenner, R.P., 2005. The interpretation of the EEG in stupor and coma. Neurol. 11 (5), 271–284.

Cao, B., Wang, J., Shahed, M., Jelfs, B., Chan, R.H., Li, Y., 2016. Vagus nerve stimulation alters phase synchrony of the anterior cingulate cortex and facilitates decision making in rats. Sci. Rep. 6, 35135.

Ching, S., Cimenser, A., Purdon, P.L., Brown, E.N., Kopell, N.J., 2010. Thalamocortical model for a propofol-induced alpha-rhythm associated with loss of consciousness. Proc. Natl. Acad. Sci. U. S. A. 107 (52), 22665–22670.

Cox, R.W., 1996. AFNI: software for analysis and visualization of functional magnetic resonance neuroimages. Comput. Biomed. Res., Int. J. 29 (3), 162–173.

Crone, J.S., Lutkenhoff, E.S., Bio, B.J., Laureys, S., Monti, M.M., 2017. Testing proposed neuronal models of effective connectivity within the cortico-basal ganglia-thalamo-cortical loop during loss of consciousness. Cerebr. Cortex 27 (4), 2727–2738.

Dashwood, M.R., Loesch, A., 2010. Endothelin-1 as a neuropeptide: neurotransmitter or neurovascular effects? J. Cell Commun. Signal 4 (1), 51–62.

Dashwood, M., Turner, M., Jacobs, M., 1989. Endothelin-1: contractile responses and autoradiographic localization of receptors in rabbit blood vessels. J. Cardiovasc. Pharmacol. 13 (Suppl. 5), S183–S185.

Demel, S.L., Broderick, J.P., 2015. Basilar occlusion syndromes: an update. Neurohospitalist 5 (3), 142–150.

Devor, M., Zalkind, V., 2001. Reversible analgesia, atonia, and loss of consciousness on bilateral intracerebral microinjection of pentobarbital. Pain 94 (1), 101–112.

Ebitz, R.B., Platt, M.L., 2015. Neuronal activity in primate dorsal anterior cingulate cortex signals task conflict and predicts adjustments in pupil-linked arousal. Neuron 85 (3), 628–640.

Economo Cv, 1930. Sleep as a problem of localization. J. Nerv. Ment. Dis. 71 (3).

Edlow, B.L., Haynes, R.L., Takahashi, E., Klein, J.P., Cummings, P., Benner, T., et al., 2013. Disconnection of the ascending arousal system in traumatic coma. J. Neuropathol. Exp. Neurol. 72 (6), 505–523.

Edlow, J.A., Rabinstein, A., Traub, S.J., Wijdicks, E.F., 2014. Diagnosis of reversible causes of coma. Lancet 384 (9959), 2064–2076.

Edlow, B.L., Chatelle, C., Spencer, C.A., Chu, C.J., Bodien, Y.G., O'Connor, K.L., et al., 2017. Early detection of consciousness in patients with acute severe traumatic brain injury. Brain 140 (9), 2399–2414.

Fischer, D.B., Boes, A.D., Demertzi, A., Evrard, H.C., Laureys, S., Edlow, B.L., et al., 2016. A human brain network derived from coma-causing brainstem lesions. Neurology 87 (23), 2427–2434.

Fortuna, S., Pestalozza, S., Lorenzini, P., Bisso, G.M., Morelli, L., Michalek, H., 1997. Transient global brain hypoxia-ischemia in adult rats: neuronal damage, glial proliferation, and alterations in inositol phospholipid hydrolysis. Neurochem. Int. 31 (4), 563–569.

Frequin, S.T., Linssen, W.H., Pasman, J.W., Hommes, O.R., Merx, H.L., 1991. Recurrent prolonged coma due to basilar artery migraine. A case report. Headache 31 (2), 75–81.

Fujii, K., Heistad, D.D., Faraci, F.M., 1991. Role of the basilar artery in regulation of blood flow to the brain stem in rats. Stroke 22 (6), 763–767.

Fuller, P.M., Sherman, D., Pedersen, N.P., Saper, C.B., Lu, J., 2011. Reassessment of the structural basis of the ascending arousal system. J. Comp. Neurol. 519 (5), 933–956.

Geocadin, R.G., Muthuswamy, J., Sherman, D.L., Thakor, N.V., Hanley, D.F., 2000. Early electrophysiological and histologic changes after global cerebral ischemia in rats. Mov. Disord. 15 (Suppl. 1), 14–21.

Gerashchenko, D., Blanco-Centurion, C.A., Miller, J.D., Shiromani, P.J., 2006. Insomnia following hypocretin2-saporin lesions of the substantia nigra. Neuroscience 137 (1), 29–36.

Giacino, J.T., Kalmar, K., Whyte, J., 2004. The JFK Coma Recovery Scale-Revised: measurement characteristics and diagnostic utility. Arch. Phys. Med. Rehabil. 85 (12), 2020–2029.

Giacino, J.T., Fins, J.J., Laureys, S., Schiff, N.D., 2014. Disorders of consciousness after acquired brain injury: the state of the science. Nat. Rev. Neurol. 10 (2), 99–114.

Giacino, J.T., Katz, D.I., Schiff, N.D., Whyte, J., Ashman, E.J., Ashwal, S., et al., 2018. Practice guideline update recommendations summary: disorders of consciousness: report of the guideline development, dissemination, and implementation subcommittee of the American academy of neurology; the American congress of rehabilitation medicine; and the national Institute on disability, independent living, and rehabilitation research. Neurology 91 (10), 450–460.

Gompf, H.S., Mathai, C., Fuller, P.M., Wood, D.A., Pedersen, N.P., Saper, C.B., et al., 2010. Locus ceruleus and anterior cingulate cortex sustain wakefulness in a novel environment. J. Neurosci. 30 (43), 14543–14551.

Gromysz, H., Karczewski, W.A., 1981. The effects of brainstem transection on respiratory activity in the rabbit. Acta Neurobiol. Exp. 41 (2), 225–235.

Halassa, M.M., Siegle, J.H., Ritt, J.T., Ting, J.T., Feng, G., Moore, C.I., 2011. Selective optical drive of thalamic reticular nucleus generates thalamic bursts and cortical spindles. Nat. Neurosci. 14 (9), 1118–1120.

Hawkes, C.H., Bryan-Smyth, L., 1974. The electroencephalogram in the "locked-in" syndrome. Neurology 24 (11), 1015–1018.

Hayes, R.L., Pechura, C.M., Katayama, Y., Povlishock, J.T., Giebel, M.L., Becker, D.P., 1984. Activation of pontine cholinergic sites implicated in unconsciousness following cerebral concussion in the cat. Science 223 (4633), 301–303.

He, Y., Wang, M., Chen, X., Pohmann, R., Polimeni, J.R., Scheffler, K., et al., 2018. Ultra-slow single-vessel BOLD and CBV-based fMRI spatiotemporal dynamics and their correlation with neuronal intracellular calcium signals. Neuron 97 (4), 925–939 e5.

Henry, C.E., Scoville, W.B., 1952. Suppression-burst activity from isolated cerebral cortex in man. Electroencephalogr. Clin. Neurophysiol. 4 (1), 1–22.

Hobson, J.A., 1965. The effects of chronic brain-stem lesions on cortical and muscular activity during sleep and waking in the cat. Electroencephalogr. Clin. Neurophysiol. 19, 41–62.

Ingvar, D.H., 1955. Electrical activity of isolated cortex in the unanesthetized cat with intact brain stem. Acta Physiol. Scand. 33 (2–3), 151–168.

Jia, X., Koenig, M.A., Shin, H.C., Zhen, G., Yamashita, S., Thakor, N.V., et al., 2006. Quantitative EEG and neurological recovery with therapeutic hypothermia after asphyxial cardiac arrest in rats. Brain Res. 1111 (1), 166–175.

Jones, B.E., Harper, S.T., Halaris, A.E., 1977. Effects of locus coeruleus lesions upon cerebral monoamine content, sleep-wakefulness states and the response to amphetamine in the cat. Brain Res. 124 (3), 473–496.

Joshi, S., Li, Y., Kalwani, R.M., Gold, J.I., 2016. Relationships between pupil diameter and neuronal activity in the locus coeruleus, colliculi, and cingulate cortex. Neuron 89 (1), 221–234.

Katayama, Y., Tsubokawa, T., Abekura, M., Hayes, R.L., Becker, D.P., 1986. Coma induced by cholinergic activation of a restricted region in the pontine reticular formation–a model of reversible forms of coma. Neurol. Med.-Chir. 26 (1), 1–10.

Katz, L., Ebmeyer, U., Safar, P., Radovsky, A., Neumar, R., 1995. Outcome model of asphyxial cardiac arrest in rats. J. Cerebr. Blood Flow Metabol. 15 (6), 1032–1039.

Katz, D.I., Polyak, M., Coughlan, D., Nichols, M., Roche, A., 2009. Natural history of recovery from brain injury after prolonged disorders of consciousness: outcome of patients admitted to inpatient rehabilitation with 1-4 year follow-up. Prog. Brain Res. 177, 73–88.

Kawai, K., Nitecka, L., Ruetzler, C.A., Nagashima, G., Joo, F., Mies, G., et al., 1992. Global cerebral ischemia associated with cardiac arrest in the rat: I. Dynamics of early neuronal changes. J. Cerebr. Blood Flow Metabol. 12 (2), 238–249.

Kharoshankaya, L., Filan, P.M., Bogue, C.O., Murray, D.M., Boylan, G.B., 2014. Global suppression of electrocortical activity in unilateral perinatal thalamic stroke. Dev. Med. Child Neurol. 56 (7), 695–698.

Kolukisa, M., Ozdemir Gultekin, T., Eryigit Baran, G., Aralasmak, A., Kocaman, G., Gursoy, A.E., et al., 2015. One-year follow-up in patients with brainstem infarction due to large-artery atherothrombosis. Neuropsychiatric Dis. Treat. 11, 379–384.

Kramer, B.K., Ackermann, M., Kohler, S.M., Riegger, G.A., 1994. Role of endothelin in hypertension. Clin. Invest. 72 (2), 88–93.

Kroeger, D., Florea, B., Amzica, F., 2013. Human brain activity patterns beyond the isoelectric line of extreme deep coma. PLoS One 8 (9), e75257.

Laureys, S., Faymonville, M.E., Luxen, A., Lamy, M., Franck, G., Maquet, P., 2000. Restoration of thalamocortical connectivity after recovery from persistent vegetative state. Lancet 355 (9217), 1790–1791.

Lavin, C., Melis, C., Mikulan, E., Gelormini, C., Huepe, D., Ibanez, A., 2013. The anterior cingulate cortex: an integrative hub for human socially-driven interactions. Front. Neurosci. 7, 64.

Leibowitz, S.F., Wortley, K.E., 2004. Hypothalamic control of energy balance: different peptides, different functions. Peptides 25 (3), 473–504.

Leonov, Y., Sterz, F., Safar, P., Radovsky, A., Oku, K., Tisherman, S., et al., 1990. Mild cerebral hypothermia during and after cardiac arrest improves neurologic outcome in dogs. J. Cerebr. Blood Flow Metabol. 10 (1), 57–70.

Lewis, L.D., Ching, S., Weiner, V.S., Peterfreund, R.A., Eskandar, E.N., Cash, S.S., et al., 2013. Local cortical dynamics of burst suppression in the anaesthetized brain. Brain 136 (Pt 9), 2727–2737.

Lewis, L.D., Voigts, J., Flores, F.J., Schmitt, L.I., Wilson, M.A., Halassa, M.M., et al., 2015. Thalamic reticular nucleus induces fast and local modulation of arousal state. Elife 4, e08760.

Liachenko, S., Tang, P., Hamilton, R.L., Xu, Y., 1998. A reproducible model of circulatory arrest and remote resuscitation in rats for NMR investigation. Stroke 29 (6), 1229–1238 discussion 38-9.

Lindsley, D.B., Bowden, J.W., Magoun, H.W., 1949. Effect upon the EEG of acute injury to the brain stem activating system. Electroencephalogr. Clin. Neurophysiol. 1 (4), 475–486.

Lindsley, D.B., Schreiner, L.H., Knowles, W.B., Magoun, H.W., 1950. Behavioral and EEG changes following chronic brain stem lesions in the cat. Electroencephalogr. Clin. Neurophysiol. 2 (4), 483–498.

Loesch, A., 2005. Localisation of endothelin-1 and its receptors in vascular tissue as seen at the electron microscopic level. Curr. Vasc. Pharmacol. 3 (4), 381–392.

Lohmann, G., Muller, K., Bosch, V., Mentzel, H., Hessler, S., Chen, L., et al., 2001. LIPSIA–a new software system for the evaluation of functional magnetic resonance images of the human brain. Comput. Med. Imag. Graph. 25 (6), 449–457.

Lohmann, G., Margulies, D.S., Horstmann, A., Pleger, B., Lepsien, J., Goldhahn, D., et al., 2010. Eigenvector centrality mapping for analyzing connectivity patterns in fMRI data of the human brain. PLoS One 5 (4), e10232.

Lu, H., Zou, Q., Gu, H., Raichle, M.E., Stein, E.A., Yang, Y., 2012. Rat brains also have a default mode network. Proc. Natl. Acad. Sci. U. S. A. 109 (10), 3979–3984.

Luthi, A., 2016. Sleep: switching off the off-switch. Curr. Biol. 26 (16), R765–R767.

Maas, A.I.R., Menon, D.K., Adelson, P.D., Andelic, N., Bell, M.J., Belli, A., et al., 2017. Traumatic brain injury: integrated approaches to improve prevention, clinical care, and research. Lancet Neurol. 16 (12), 987–1048.

Manole, M.D., Kochanek, P.M., Bayir, H., Alexander, H., Dezfulian, C., Fink, E.L., et al., 2014. Brain tissue oxygen monitoring identifies cortical hypoxia and thalamic hyperoxia after experimental cardiac arrest in rats. Pediatr. Res. 75 (2), 295–301.

Mhuircheartaigh, R.N., Rosenorn-Lanng, D., Wise, R., Jbabdi, S., Rogers, R., Tracey, I., 2010. Cortical and subcortical connectivity changes during decreasing levels of consciousness in humans: a functional magnetic resonance imaging study using propofol. J. Neurosci. 30 (27), 9095–9102.

Monti, M.M., Schnakers, C., Korb, A.S., Bystritsky, A., Vespa, P.M., 2016. Non-invasive ultrasonic thalamic stimulation in disorders of consciousness after severe brain injury: a first-in-man report. Brain Stimul. 9 (6), 940–941.

Moruzzi, G., Magoun, H.W., 1949. Brain stem reticular formation and activation of the EEG. Electroencephalogr. Clin. Neurophysiol. 1 (4), 455–473.

Muthuswamy, J., Kimura, T., Ding, M.C., Geocadin, R., Hanley, D.F., Thakor, N.V., 2002. Vulnerability of the thalamic somatosensory pathway after prolonged global hypoxic-ischemic injury. Neuroscience 115 (3), 917–929.

Nauta, W.J., 1946. Hypothalamic regulation of sleep in rats; an experimental study. J. Neurophysiol. 9, 285–316.

Newman, L.A., Creer, D.J., McGaughy, J.A., 2015. Cognitive control and the anterior cingulate cortex: how conflicting stimuli affect attentional control in the rat. J. Physiol. Paris 109 (1–3), 95–103.

Norton, L., Hutchison, R.M., Young, G.B., Lee, D.H., Sharpe, M.D., Mirsattari, S.M., 2012. Disruptions of functional connectivity in the default mode network of comatose patients. Neurology 78 (3), 175–181.

Okamura, K., 2014. Glasgow Coma Scale flow chart: a beginner's guide. Br. J. Nurs. 23 (20), 1068–1073.

Pais-Roldán, P., Biswal, B., Scheffler, K., Yu, X., 2018. Identifying respiration-related aliasing artifacts in the rodent resting-state fMRI. Front. Neurosci. 12, 788.

Pal, D., Dean, J.G., Liu, T., Li, D., Watson, C.J., Hudetz, A.G., et al., 2018. Differential role of prefrontal and parietal cortices in controlling level of consciousness. Curr. Biol. 28 (13), 2145–2152 e5.

Parvizi, J., Damasio, A., 2001. Consciousness and the brainstem. Cognition 79 (1–2), 135–160.

Parvizi, J., Damasio, A.R., 2003. Neuroanatomical correlates of brainstem coma. Brain 126 (Pt 7), 1524–1536.

Pawela, C.P., Biswal, B.B., Cho, Y.R., Kao, D.S., Li, R., Jones, S.R., et al., 2008. Resting-state functional connectivity of the rat brain. Magn. Reson. Med. 59 (5), 1021–1029.

Paxinos, G., Watson, C., 2007. The Rat Brain in Stereotaxic Coordinates, sixth ed. Academic Press/Elsevier, Amsterdam ; Boston.

Pulsinelli, W.A., Brierley, J.B., 1979. A new model of bilateral hemispheric ischemia in the unanesthetized rat. Stroke 10 (3), 267–272.

Reed, S.J., Plourde, G., Tobin, S., Chapman, C.A., 2013. Partial antagonism of propofol anaesthesia by physostigmine in rats is associated with potentiation of fast (80-200 Hz) oscillations in the thalamus. Br. J. Anaesth. 110 (4), 646–653.

Robert, F., Mumenthaler, M., 1977. [Criteria of brain death. Spinal reflexes in 45 personal studies]. Schweiz. Med. Wochenschr. 107 (10), 335–341.

Roome, R.B., Bartlett, R.F., Jeffers, M., Xiong, J., Corbett, D., Vanderluit, J.L., 2014. A reproducible Endothelin-1 model of forelimb motor cortex stroke in the mouse. J. Neurosci. Methods 233, 34–44.

Rosenblum, W.I., 2015. Immediate, irreversible, posttraumatic coma: a review indicating that bilateral brainstem injury rather than widespread hemispheric damage is essential for its production. J. Neuropathol. Exp. Neurol. 74 (3), 198–202.

Saper, C.B., 1985. Organization of cerebral cortical afferent systems in the rat .2. Hypothalamocortical projections. J. Comp. Neurol. 237 (1), 21–46.

Saper, C.B., Chou, T.C., Scammell, T.E., 2001. The sleep switch: hypothalamic control of sleep and wakefulness. Trends Neurosci. 24 (12), 726–731.

Saper, C.B., Scammell, T.E., Lu, J., 2005. Hypothalamic regulation of sleep and circadian rhythms. Nature 437 (7063), 1257–1263.

Scammell, T.E., Arrigoni, E., Lipton, J.O., 2017. Neural circuitry of wakefulness and sleep. Neuron 93 (4), 747–765.

Schiff, N.D., 2010. Recovery of consciousness after brain injury: a mesocircuit hypothesis. Trends Neurosci. 33 (1), 1–9.

Schiff, N.D., Giacino, J.T., Kalmar, K., Victor, J.D., Baker, K., Gerber, M., et al., 2007. Behavioural improvements with thalamic stimulation after severe traumatic brain injury. Nature 448 (7153), 600–603.

Schinelli, S., 2006. Pharmacology and physiopathology of the brain endothelin system: an overview. Curr. Med. Chem. 13 (6), 627–638.

Shim, W.H., Baek, K., Kim, J.K., Chae, Y., Suh, J.Y., Rosen, B.R., et al., 2013. Frequency distribution of causal connectivity in rat sensorimotor network: resting-state fMRI analyses. J. Neurophysiol. 109 (1), 238–248.

Shirvalkar, P., Seth, M., Schiff, N.D., Herrera, D.G., 2006. Cognitive enhancement with central thalamic electrical stimulation. Proc. Natl. Acad. Sci. U. S. A. 103 (45), 17007–17012.

Shoykhet, M., Simons, D.J., Alexander, H., Hosler, C., Kochanek, P.M., Clark, R.S., 2012. Thalamocortical dysfunction and thalamic injury after asphyxial cardiac arrest in developing rats. J. Neurosci. 32 (14), 4972–4981.

Smith, D.H., Hicks, R., Povlishock, J.T., 2013. Therapy development for diffuse axonal injury. J. Neurotrauma 30 (5), 307–323.

Sonobe, T., Haouzi, P., 2015. H2S induced coma and cardiogenic shock in the rat: effects of phenothiazinium chromophores. Clin. Toxicol. 53 (6), 525–539.

Sonobe, T., Chenuel, B., Cooper, T.K., Haouzi, P., 2015. Immediate and long-term outcome of acute H2S intoxication induced coma in unanesthetized rats: effects of methylene blue. PLoS One 10 (6), e0131340.

Spisak, T., Jakab, A., Kis, S.A., Opposits, G., Aranyi, C., Berenyi, E., et al., 2014. Voxel-wise motion artifacts in population-level whole-brain connectivity analysis of resting-state FMRI. PLoS One 9 (9), e104947.

Steriade, M., 1999. Brainstem activation of thalamocortical systems. Brain Res. Bull. 50 (5–6), 391–392.

Steriade, M., Domich, L., Oakson, G., 1986. Reticularis thalami neurons revisited - activity changes during shifts in states of vigilance. J. Neurosci. 6 (1), 68–81.

Synek, V.M., 1988. Prognostically important eeg coma patterns in diffuse anoxic and traumatic encephalopathies in adults. J. Clin. Neurophysiol. 5 (2), 161–174.

Tamaoki, S., Suzuki, H., Okada, M., Fukui, N., Isobe, M., Saito, T., 2016. Development of an experimental rat model of hyperammonemic encephalopathy and evaluation of the effects of rifaximin. Eur. J. Pharmacol. 779, 168–176.

Taylor, N.E., Van Dort, C.J., Kenny, J.D., Pei, J., Guidera, J.A., Vlasov, K.Y., et al., 2016. Optogenetic activation of dopamine neurons in the ventral tegmental area induces reanimation from general anesthesia. Proc. Natl. Acad. Sci. U. S. A. 113 (45), 12826–12831.

Teasdale, G., Jennett, B., 1974. Assessment of coma and impaired consciousness. A practical scale. Lancet 2 (7872), 81–84.

Thengone, D.J., Voss, H.U., Fridman, E.A., Schiff, N.D., 2016. Local changes in network structure contribute to late communication recovery after severe brain injury. Sci. Transl. Med. 8 (368), 368re5.

Threlkeld, Z.D., Bodien, Y.G., Rosenthal, E.S., Giacino, J.T., Nieto-Castanon, A., Wu, O., et al., 2018. Functional networks reemerge during recovery of consciousness after acute severe traumatic brain injury. Cortex 106, 299–308.

Tobler, I., Borbely, A.A., Groos, G., 1983. The effect of sleep deprivation on sleep in rats with suprachiasmatic lesions. Neurosci. Lett. 42 (1), 49–54.

Tonkovic-Capin, M., Krolo, M., Stuth, E.A., Hopp, F.A., Zuperku, E.J., 1985. Improved method of canine decerebration. J. Appl. Physiol. 85 (2), 747–750, 1998.

Tsao, J.W., Hemphill 3rd, J.C., Johnston, S.C., Smith, W.S., Bonovich, D.C., 2005. Initial Glasgow Coma Scale score predicts outcome following thrombolysis for posterior circulation stroke. Arch. Neurol. 62 (7), 1126–1129.

Van de Moortele, P.F., Pfeuffer, J., Glover, G.H., Ugurbil, K., Hu, X., 2002. Respiration-induced B0 fluctuations and their spatial distribution in the human brain at 7 Tesla. Magn. Reson. Med. 47 (5), 888–895.

Van der Linden, A., Van Camp, N., Ramos-Cabrer, P., Hoehn, M., 2007. Current status of functional MRI on small animals: application to physiology, pathophysiology, and cognition. NMR Biomed. 20 (5), 522–545.

van Vugt, M.K., Sederberg, P.B., Kahana, M.J., 2007. Comparison of spectral analysis methods for characterizing brain oscillations. J. Neurosci. Methods 162 (1–2), 49–63.

Virley, D., Hadingham, S.J., Roberts, J.C., Farnfield, B., Elliott, H., Whelan, G., et al., 2004. A new primate model of focal stroke: endothelin-1-induced middle cerebral artery occlusion and reperfusion in the common marmoset. J. Cerebr. Blood Flow Metabol. 24 (1), 24–41.

von Campe, G., Regli, F., Bogousslavsky, J., 2003. Heralding manifestations of basilar artery occlusion with lethal or severe stroke. J. Neurol. Neurosurg. Psychiatry 74 (12), 1621–1626.

Wang, M., He, Y., Sejnowski, T.J., Yu, X., 2018. Brain-state dependent astrocytic Ca(2+) signals are coupled to both positive and negative BOLD-fMRI signals. Proc. Natl. Acad. Sci. U. S. A. 115 (7), E1647–E1656.

Webster, H.H., Jones, B.E., 1988. Neurotoxic lesions of the dorsolateral pontomesencephalic tegmentum-cholinergic cell area in the cat. II. Effects upon sleep-waking states. Brain Res. 458 (2), 285–302.

White, N.S., Alkire, M.T., 2003. Impaired thalamocortical connectivity in humans during general-anesthetic-induced unconsciousness. Neuroimage 19 (2 Pt 1), 402–411.

Wijdicks, E.F., Rabinstein, A.A., Bamlet, W.R., Mandrekar, J.N., 2011. FOUR score and Glasgow Coma Scale in predicting outcome of comatose patients: a pooled analysis. Neurology 77 (1), 84–85.

Woods, J.W., 1964. Behavior of chronic decerebrate rats. J. Neurophysiol. 27, 635–644.

Wu, D., Deng, H., Xiao, X., Zuo, Y., Sun, J., Wang, Z., 2017. Persistent neuronal activity in anterior cingulate cortex correlates with sustained attention in rats regardless of sensory modality. Sci. Rep. 7, 43101.

Xiong, Y., Mahmood, A., Chopp, M., 2013. Animal models of traumatic brain injury. Nat. Rev. Neurosci. 14 (2), 128–142.

Xu, M., Chung, S., Zhang, S., Zhong, P., Ma, C., Chang, W.C., et al., 2015. Basal forebrain circuit for sleep-wake control. Nat. Neurosci. 18 (11), 1641–1647.

Yanagisawa, M., Kurihara, H., Kimura, S., Tomobe, Y., Kobayashi, M., Mitsui, Y., et al., 1988. A novel potent vasoconstrictor peptide produced by vascular endothelial cells. Nature 332 (6163), 411–415.

Yanagisawa, M., Kurihara, H., Kimura, S., Goto, K., Masaki, T., 1988. A novel peptide vasoconstrictor, endothelin, is produced by vascular endothelium and modulates smooth muscle Ca2+ channels. J. Hypertens. Suppl. 6 (4), S188–S191.

Yang, S.R., Hu, Z.Z., Luo, Y.J., Zhao, Y.N., Sun, H.X., Yin, D., et al., 2018. The rostromedial tegmental nucleus is essential for non-rapid eye movement sleep. PLoS Biol. 16 (4), e2002909.

Zeman, A., 2003. What is consciousness and what does it mean for the persistent vegetative state? Adv. Clin. Neurosci. Rehabil. 3, 12–14.

Zhang, L.N., Yang, C., Ouyang, P.R., Zhang, Z.C., Ran, M.Z., Tong, L., et al., 2016. Orexin-A facilitates emergence of the rat from isoflurane anesthesia via mediation of the basal forebrain. Neuropeptides 58, 7–14.
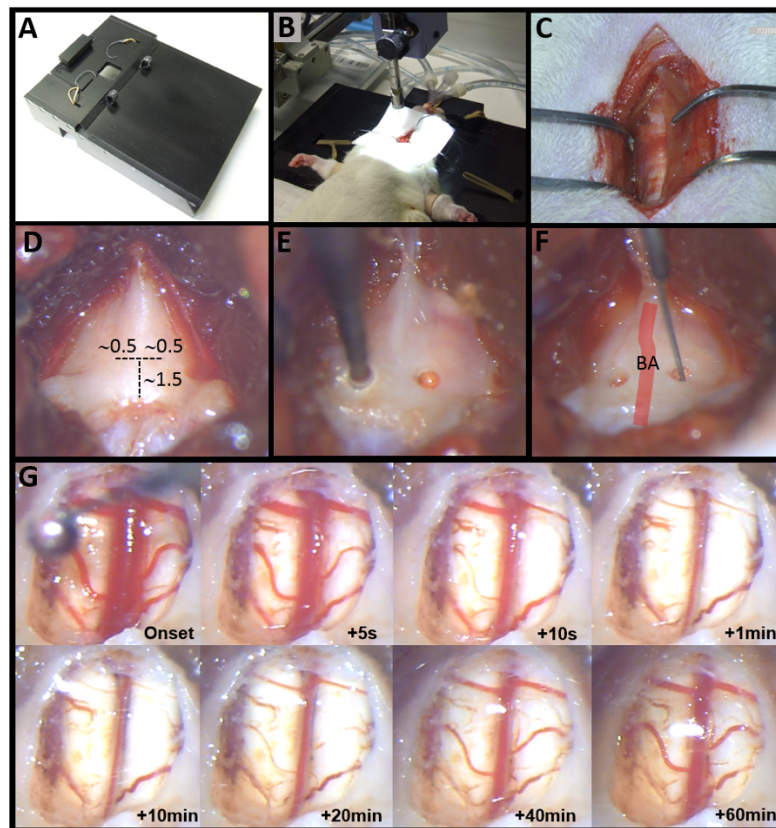
SUPPLEMENTARY MATERIAL

Multimodal Assessment of Recovery from Coma in a Rat Model of

Diffuse Brainstem Tegmentum Injury

Patricia Pais-Roldán[1,2], Brian L. Edlow[3,4], Yuanyuan Jiang[1], Johannes Stelzer[1], Ming Zou[5], Xin Yu[1,4]

Figure S1

Fig S1. Surgical procedure and vasoconstriction effect of ET-1. (**A**) Surgical bed designed for rats with dorsal implants and retractors to expose the basilar part of the occipital bone. (**B**) Typical setup of an anesthetized, mechanically ventilated rat during injection of endothelin-1 (ET-1) into the brainstem. (**C**) Beginning of the surgery from the ventral aspect of the neck. In the picture the Thyrohyoid muscles were dissected and the trachea could be observed. (**D**) Exposure of the basioccipital (under the trachea) and approximate coordinates from the lower edge of the bone (in mm) to drill the craniotomies. (**E**) Craniotomy drilling. (**F**) View of the craniotomy sites lateral to the basilar artery (BA), whose inferior-superior course along the midline is shown in schematic form as a red line superimposed on the bone, during injection of ET-1. (**G**) View of the BA and its branches with a craniotomy performed over the whole basioccipital in an anesthetized rat, at different times after delivery of 800 nL of 400 µM ET-1.
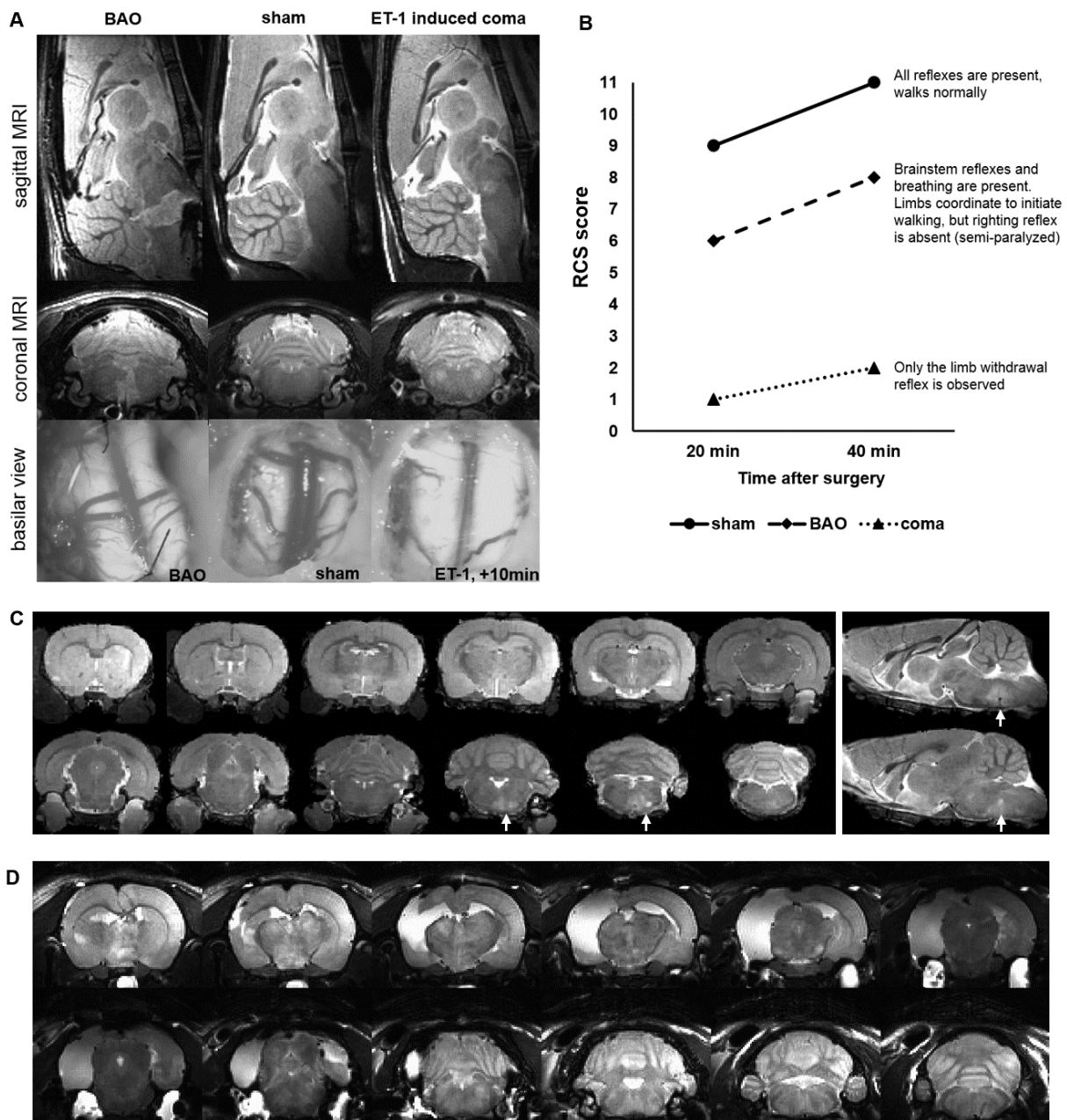
Fig S2. Anatomical and behavioral outcome of 3 different experimental conditions. (**A**) Anatomical T2-weighted MRI and view of the ventral brainstem vasculature in an animal with BAO, sham surgery or ET-1 mediated vasoconstriction. (**B**) Representative neurological score of differently treated animals at 2 times after surgery. (**C**) T2-weighted MRI showing infarction limited to the injection point in a rat subjected to ET-1 injection that did not enter coma (rat belonging to the "no coma induction" group of ET-1 treated animals -see **Fig 1J-**). (**D**) T2-weighted MRI showing massive infarction in different brain regions in a rat subjected to ET-1 injection that did not enter the long-lasting coma state (rat belonging to the "brief coma" group of ET-1 treated animals -see **Fig 1J-**).
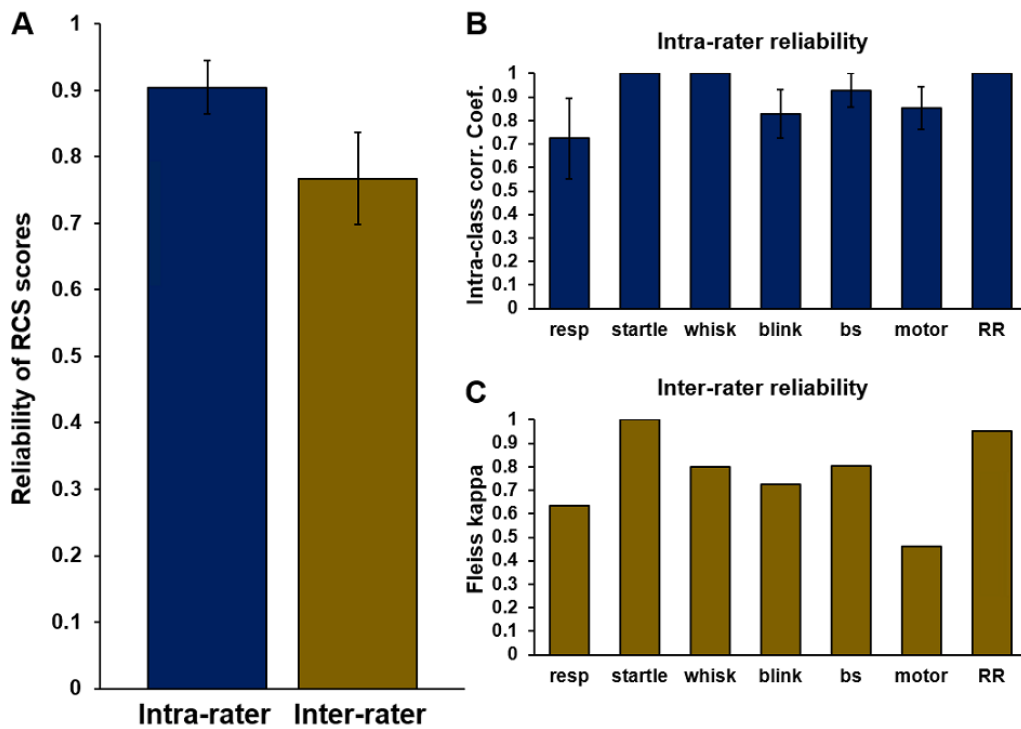
Fig S3. Reliability of the RCS. (**A**) Overall inter- and intra- reliability of the RCS. (**B**) Intra-rater reliability (intra-class correlation coefficient) of each category of the RCS. (**C**) Inter-rater reliability (Fleiss kappa) of each category of the RCS. Abbreviations: bs: brainstem reflexes; resp: respiration; RR: righting reflex; whisk: whisker function. Error bars represent the standard error of the mean.

Figure S4
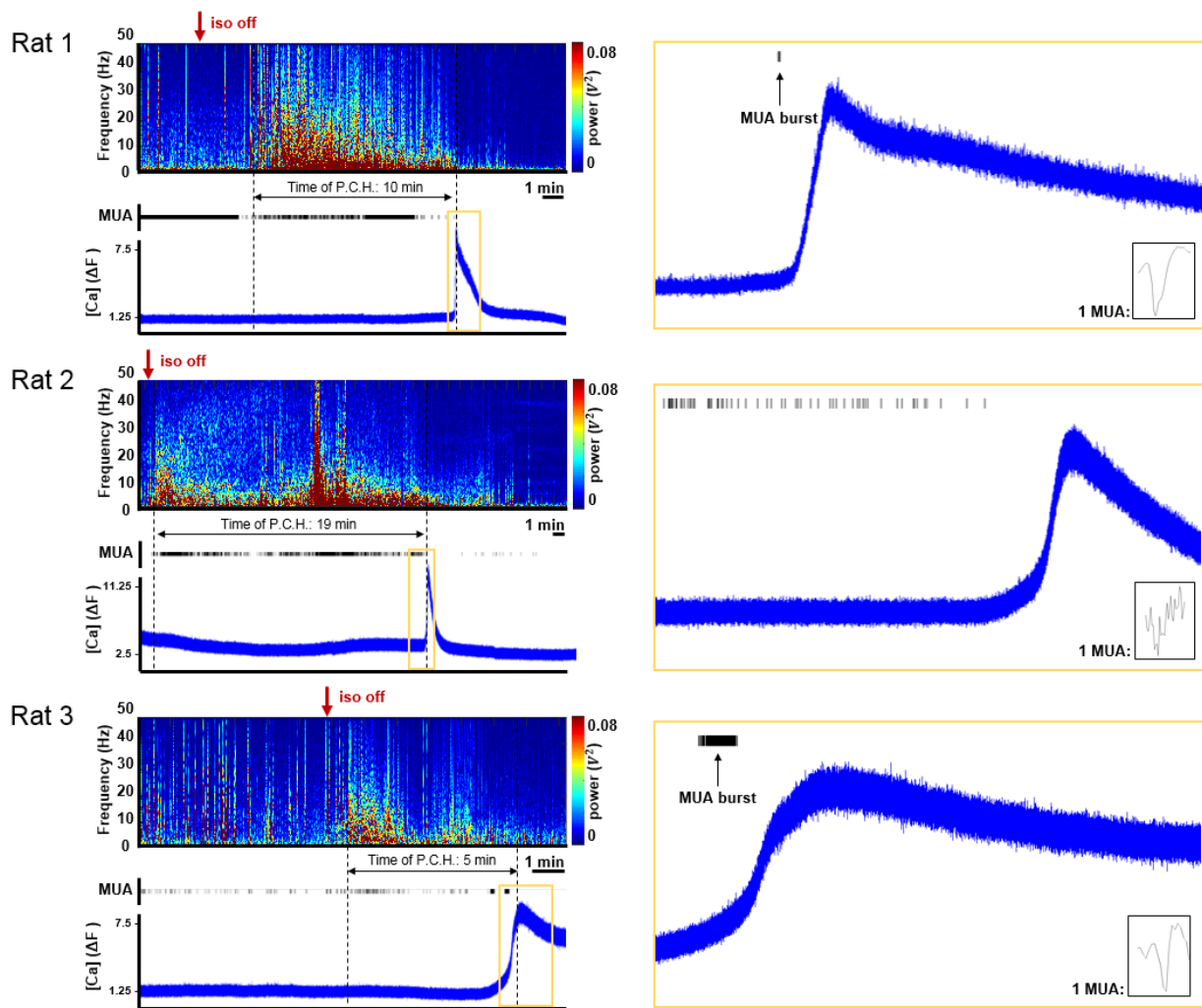
Fig S4. Electrophysiological and calcium-related changes during coma induction. The figure shows the LFP spectral decomposition, multiunit activity (MUA, small black vertical lines) and intracellular calcium concentration (blue trace) from layer V of the barrel cortex in 3 different animals subjected to the procedure of coma induction through ET-1 injection. At first, animals are anesthetized with 2-2.5% isoflurane during injection of ET-1, then the anesthesia is withdrawn (red arrows). The animal will only have spinal motor reflexes during the next ~60 minutes, and the cortical activity will exhibit only burst-suppression patterns during the first 1-2 hours post-coma, but an initial period of cortical hyper-excitability is observed for a short amount of time after withdrawal of the anesthetic, followed by a massive wave of calcium internalization, denoting cortical spreading depression/depolarization. Multiunit activity exhibits burst firing at the onset of the depolarization wave, which marks the beginning of isoelectricity/burst suppression patterns. Note the different durations of the paradoxical cortical hyper-excitability period (P.C.H.) in the different animals. Insets at the right bottom of each plot show the representative shape of one multi-unit.

5
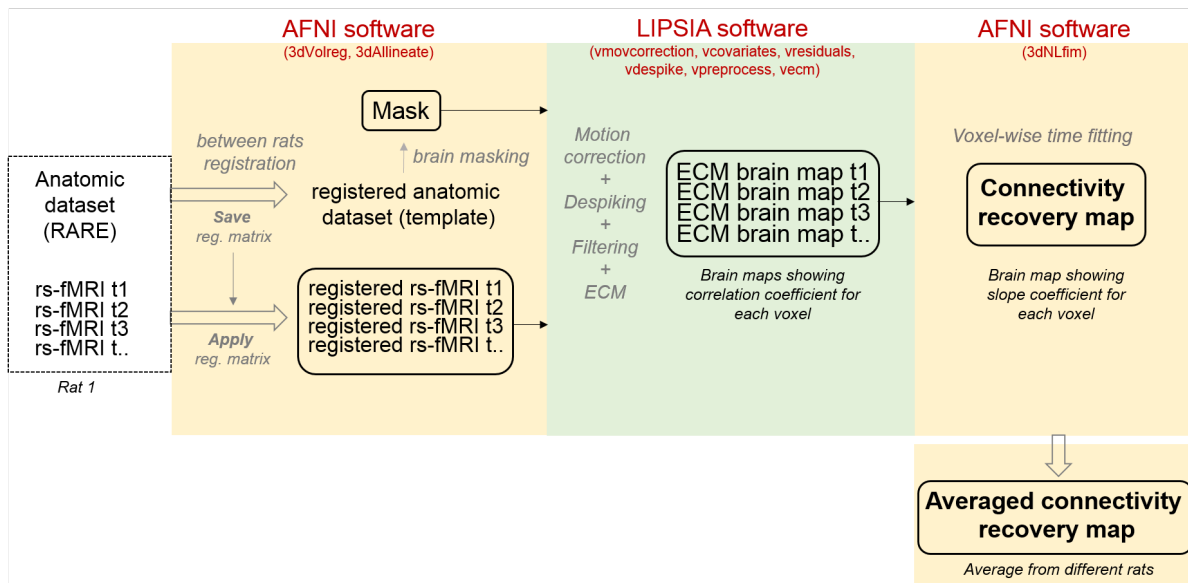
Fig S5. Methodology for rs-fMRI processing for acquisition of the slope (recovery) map. Abbreviations: reg: registration; ECM: eigenvector centrality mapping.
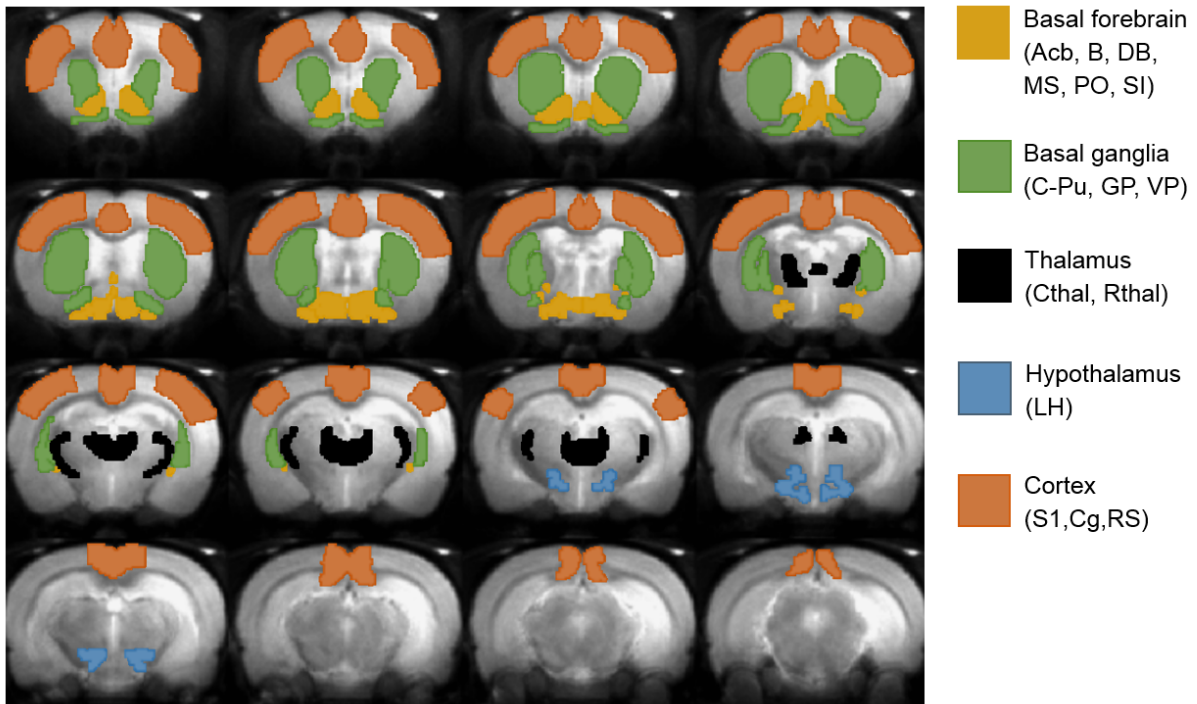
Fig S6. ROIs selected for rs-fMRI analysis. Abbreviations: Acb: nucleus accumbens; B: nucleus basilis of Meynert; BF: basal forebrain; C-Pu: caudate-putamen; Cg: cingulate cortex; CThal: central thalamus; DB: diagonal band of Broca; GP: globus pallidus; LH: lateral hypothalamus; MS: medial septum; PO: preoptic nuclei; RS: retrosplenial cortex; RThal: reticular thalamus; SI: substantia innominata; S1: primary somatosensory cortex; VP: ventral pallidum.
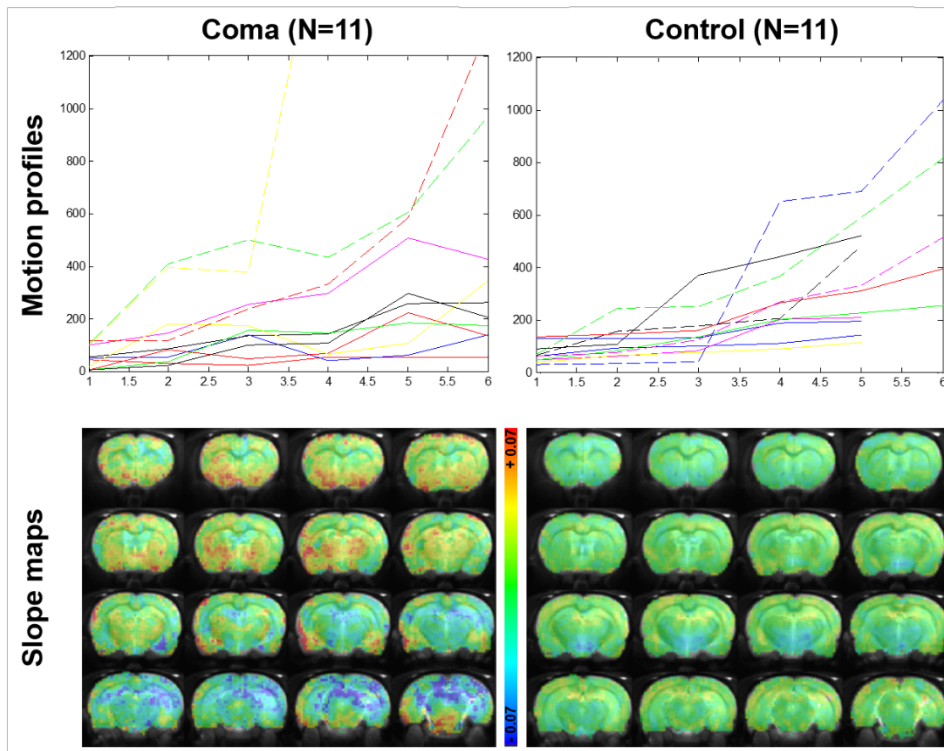
Fig S7. Validation of the rs-fMRI regarding the potential motion interference. The slope map of a control group of healthy anesthetized rats with similar motion profile is provided. Different colors and line types in the motion profile graphs represent different animals of the same group.

SUPPLEMENTARY VIDEOS:

Movie S1. Surgical procedure for brainstem coma induction.

Movie S2. RCS tested in the rat.

Movie S3. Behavioral progression of a comatose rat.

SUPPLEMENTARY NOTES:

SUPPLEMENTARY NOTE 1

Surgical procedure for basilar artery occlusion (BAO)

The anesthetized rat (2-2.5% isoflurane) was positioned in dorsal recumbence. After shaving the ventral neck, a longitudinal incision was made on the skin, the Thyrohyoid muscles were dissected, the trachea was left to a side and the basilar aspect of the basilar bone was exposed. An electric drill was used to delineate and remove a skull window or approximately 2 x 3 mm to expose the basilar artery (BA). The dura mater was removed. 6-0 silk suture was used to occlude the BA at 2 to 4 points, above and below the anterior inferior cerebellar artery. The wound was closed, painkiller was provided and isoflurane was switched off to assess behavior of the animal.

SUPPLEMENTARY NOTE 2

Behavioral assessment of coma recovery with the Tübingen-Boston Rat Coma Scale (RCS)

Similar to the clinical practice of using behavioral scales to categorize states of altered consciousness in brain-injured patients, we developed a Rat Coma Scale (RCS) to provide standard and reproducible behavioral assessments across different animals. A variety of rodent neurological examination scales have been proposed for the assessment of neurological function after different models of brain injury such as stroke (Schaar, Brenneman et al. 2010) or recovery from general anesthesia (Reed, Plourde et al. 2013, Taylor, Van Dort et al. 2016). Nevertheless, none of them was intended to be used during the acute comatose state. Human coma scales such as Glasgow Coma Scale (GCS), Full Outline of UnResponsiveness (FOUR), and Coma Recovery Scale-Revised (CRS-R) provide a method to measure human behaviors and reflexes in coma and related states (Avezaat, Braakman et al. 1977, Wijdicks, Bamlet et al. 2005, Di Perri, Thibaut et al. 2014). Nevertheless, these human scales cannot be directly translated to rats, as certain behaviors cannot be reliably tested in small animals. For instance, the GCS, FOUR, and CRS-R all include an analysis of patient responses to verbal commands, which cannot be applied in an assessment of rodent behavior. The design of a rat-specific coma scale was, therefore, necessary to investigate coma in a rat model.

We aimed for the RCS to be an adaptation of the commonly used GCS, FOUR, and CRS-R human scales to the rat. Behaviors and reflexes that could be reliably measured in rats, as in humans, were included in the RCS. These included brainstem reflexes, respiratory function, and eye responses. We also incorporated several rat-specific behaviors into the RCS, based upon prior studies demonstrating the utility of tracking these behaviors during

transitions in states of consciousness. These included whisker function and the righting reflex, which has been used as an analog of human loss of consciousness (Hallam, Floyd et al. 2004, Alkire, McReynolds et al. 2007, Sukhotinsky, Zalkind et al. 2007, Nguyen, Li et al. 2009, Taylor, Van Dort et al. 2016). Another important difference between the human and rat scales pertains to the opening and closing of the eyes. Although rats close their eyes during sleep, their eyes remain open under anesthesia, and most of the rats undergoing the coma-induction procedure remained with eyes open during the entire study (despite eye ointment being placed over the cornea to prevent eye drying). Therefore, the condition defined by Eyes Closed, scoring low in humans, needed to be modified in rats, as open eyes are compatible with an unconscious state in these animals (*e.g.* during anesthesia).

At early times (less than one hour after surgery), most animals exhibited exclusively motor withdrawal reflex, consistent with acute coma (Schott and Rossor 2003). Unlike the human coma scales, for which volitional behavioral responses reliably indicate cerebral cortical function, we relied on an additional method to detect cortical activity (LFP) in the rat. Identification of a cortical isoelectric line or spike-bursting pattern supported a comatose diagnosis and excluded other paralyzed but conscious states such as locked-in syndrome.

Importantly, a new measure that may indicate pain localization was observed in some healthy animals. Specifically, we observed that when the examiner pinches the left or right ear of the animal, the animal may turn its head toward the site of stimulation, suggesting a pain localization response. This behavioral measure was not included in the RCS described here because it is not a test for which there is prior evidence and because it was not tested in all the animals of this study. Nevertheless, this measure should be considered as part of a revised RCS in future studies, as it could improve the sensitivity of the scale for differentiating behavioral states in the rat.

Some animals were observed to develop certain behavioral abnormalities after injection of ET-1, not considered in the RCS, including momentary tremors of the head, ears, and whiskers, tongue swelling, proptosis, or convulsions (Saposnik and Caplan 2001). Animals experiencing convulsions were euthanized and not included in subsequent analyses.

Intra-rate and Inter-rater reliability of the RCS:

To assess the inter-subject and intra-reliability of the RCS, 5 raters (4 of them unrelated to the project and one co-author, but not the main investigator) were trained on the RCS with **Movie S2**. For assessment of the inter-rater reliability, 23 videos containing the assessment of the animal were shown to 5 blind raters, who were asked to score each of the videos following the RCS criteria. Fleiss kappa was calculated using MATLAB at a significance level of $\alpha = 0.05$. The final inter-rater reliability value was calculated as the averaged Fleiss kappa from each category of the

RCS. For assessment of the intra-rater reliability, 10 pairs of videos were shown to 5 blind raters. Each paired video was either a duplicated video or a different video recorded within 5 minutes after its correlate in the same animal. The intra-class correlation coefficient (ICC) was calculated using MATLAB at a significance level of $\alpha = 0.05$. The ICC was calculated for each category, based on all raters' paired scores, with the final intra-rater reliability value calculated as the averaged ICC for all categories. The overall intra-rater reliability of the RCS based on the audio-visual material resulted in an ICC of 0.9. The overall and subscale reliability of the RCS can be found in **Fig S3**.

SUPPLEMENTARY NOTE 3

Control studies in relation to a potential contribution of hypopnea and hypotension in the development of coma

The transient drop of blood pressure and loss of spontaneous breath observed during injection of ET-1 in rats that entered the coma state might be regarded as potential factors underlying coma induction. It is worth noting that sham animals subjected to injection of PBS in the same coordinates also experienced transient hypotension, presumably in relation to the interference with the medullary centers that control blood pressure near the site of injection. Importantly, a subset of animals in which ET-1 injection was performed did not enter the coma state or did so for a very short period of time ("no coma induction" and "brief coma", **Figure 1J**: ET-1 and **Table S1**). These animals serve a valuable control to understand the extent to which hyponea and hypotension influence the coma state in the reported model. In these animals that could awake after injection of ET-1 , the blood pressure dropped and the spontaneous breath was lost during injection (all animals were ventilated), similar to what is observed in the comatose animals. However, these ET-1 control animals with brief or no coma induction woke up several minutes after withdrawal of the isoflurane. Anatomically, the MRI of some ET-1-treated animals with no coma induction showed infarcts focused on the area of injection (AP ~ -11 mm), which implies that lesion of the nuclei at the level of the injection point is not the cause of coma. Diversified infarcts in the forebrain were occasionally observed in ET-1-treated animals that experienced only a brief coma, indicating that a diffuse injury produced by ET-1 does not trigger coma in rats. Notably, all rats showed normal SpO2 values during and after induction of coma. The physiological and anatomical findings observed in the "ET-1 + no coma induction" and "ET-1 + brief coma" control groups indicate that hypotension and respiratory depression are not the main cause of coma in the rats.

12

SUPPLEMENTARY NOTE 4

Cost benefit of the rat brainstem coma model

Although ~90% of the animals subjected to the procedure entered a coma state, only ~50% of the animals showed an initial deep comatose state with subsequent gradual recovery (the other ~50% died before regaining neurological function, developed seizures or exhibited a short period of coma only). It is possible that most animals that did not enter the coma state (or did so for a very short time) were not subjected to the optimal dose of ET-1. The potency of ET-1 has been observed to differ from one batch to another, and therefore, determination of the optimal volume is subjected to preliminary tests (involving additional animals). We would expect a much higher success rate (*i.e.,* more comatose animals that can be used to track recovery from coma) under conditions of controlled drug efficacy (*e.g.* by testing the potency of ET-1 before each animal experiment).

An important consideration is that some animals developed tremors or convulsions shortly after coma induction, which hinders identification of the neural correlates specific to coma and may constitute an end-point in animal experiments (although it is also notable that human coma is often associated with convulsions as well (Mauguiere, Blanc et al. 1979, Hannawi, Abers et al. 2016)).

An additional challenge emerges from the way in which this surgery is performed (dorsal recumbency, in contrast to the common stereotaxic-based procedures), which requires customized rat beds (see **Fig 1A**). Theoretically, the same results could be achieved by injecting the compound from the dorsal surface of the skull (common cerebral injection), but due to the depth of the target site, this alternative may present other disadvantages (*e.g.,* damage to the 4th ventricle and larger targeting errors -the BA is a clear landmark in the ventral surface of the brainstem-).

Despite the complexity of this procedure, it is worth emphasizing that, unlike previous attempts at producing a brainstem coma model, our ET-1 approach creates a sustained comatose state, which enables multimodal analysis of brain physiology during coma recovery. Approaches acting at the neurotransmitter level without causing brainstem infarction, like GABA agonists, may produce a global brain dysfunction that is transient and readily reversible. Similarly, pentobarbital delivered directly to the brainstem causes an anesthesia-like state lasting only 12-15 minutes (Devor and Zalkind 2001, Abulafia, Zalkind et al. 2009). Sodium channel blockers like lidocaine injected into the subarachnoid space in rats likewise produce a transient unresponsive state that is reversed after stopping the infusion of the drug (Yamada, Kaga et al. 1994). The ET-1-induced brainstem tegmentum lesion, on the other hand, successfully yields a comatose state of sufficient duration to study the physiology and mechanisms of coma recovery.

The brainstem coma model can be applied to an adult rat in less than 2h, including preparation of the animal (*e.g.* catheter placing) and until withdrawal of the anesthesia, and it can be merged with other techniques such as electrophysiology, optic fiber-mediated calcium imaging or optogenetic stimulation. Thus, this work creates opportunities for novel insights into acute recovery from coma, a subject that has not been possible to study with prior models.

SUPPLEMENTARY NOTE 5

Anatomical verification of brainstem lesion in the rat coma model

The anatomical findings are concordant with recent optogenetic rodent studies targeting the adrenergic neurons in the locus coeruleus (LC) and electrophysiological studies focused on the cholinergic and orexinergic neurons of the pedunculopontine tegmental nucleus (PPT) and laterodorsal tegmental nucleus (LDT), which demonstrated their role in regulating the brain state in favor of arousal (Xi, Morales et al. 2001, Petrovic, Ciric et al. 2013). Besides LC, PPT and LDT, the parabrachial complex (PB) and the parafacial zone (PZ, including the parvicellular reticular nucleus) were also infarcted in this model. The cell-specific lesion of the PB-precoeruleus complex in rats leads to a sub 1Hz EEG signal, mimicking a coma-like physiological state when a large region of the basal forebrain is lesioned (Fuller, Sherman et al. 2011). Meanwhile, the GABAergic neurons in PZ were reported to promote slow wave sleep through their inhibitory projection to PB (Anaclet, Ferrari et al. 2014), which send glutamatergic projections to the basal forebrain to maintain cortical activation and wakefulness (Anaclet, Lin et al. 2012, Kaur, Pedersen et al. 2013). Due to the ET-1 mediated ischemic insult of the pons, the rat brainstem coma model also showed lesions located at the mesopontine area covering the nucleus pontis oralis, in which focal injection of cholinergic agonists (Katayama, Tsubokawa et al. 1986) or anesthetic (Devor and Zalkind 2001, Reiner, Sukhotinsky et al. 2007, Abulafia, Zalkind et al. 2009) could lead to drug-dependent loss of consciousness or anesthesia induction. The ET-1 induced vasoconstriction could spread to the midbrain area and produce infarcts to the raphe nuclei (mainly the medial aspect), the ventral tegmental area (VTA), and the mesencephalic reticular formation. Direct optogenetic stimulation or focal injection of calcium chloride to the dorsal raphe promoted wakefulness in rodents, which was reduced during chemogenetic inhibition of the raphe neurons (Cui, Li et al. 2016, Cho, Treweek et al. 2017). A recent study also showed that electrical or optogenetic stimulation of VTA shortened the recovery time from general anesthesia (Solt, Van Dort et al. 2014, Taylor, Van Dort et al. 2016).

SUPPLEMENTARY NOTE 6

Interpretation of the ECM-analysis

The ECM-based connectivity analysis of the rs-fMRI provided a normalized measure of whole brain connectivity that was relative among brain voxels and not an absolute value. For instance, a negative value in the recovery map would not necessarily mean that the voxel connectivity decreases, but only that its connectivity does not increase as much as others' (it could just not change, or increase at a lower extent). That said, the negative connectivity slope observed in the caudal brain (occipital cortex/superior colliculus/caudal hippocampus, **Figure 5B** and **5C**) might reflect a delay in the regaining of functional connectivity with respect to other brain areas, potentially due to a special susceptibility of this region to the ischemic insult. For the same technical reason, areas that might appear overshadowed in the ECM-based analysis could as well contribute to brain recovery, although their tendency to connect with other brain areas as the post-coma period progresses was not as evident as in the reported nuclei.

SUPPLEMENTARY TABLE 1:

Animal group	N. of animals	Use of the group	Data obtained
ET-1 injection + long-lasting coma (n=32 total)	6	Main behavior results	Comatose rats show low neurological scores and gradually recover neurological function over the next 8 hours
	6	Main electrophysiology results (LFP) (behavior tracked, although without pupil reflex testing)	Comatose rats suffer a short period of isoelectricity followed by burst suppression pattern and enter a slow wave-predominant rhythm after 2-4 hours
	14 (5 used in the anatomic MRI group)	Main rs-fMRI results (behavior tested before and after rs-fMRI)	Certain nuclei in basal forebrain, basal ganglia and thalamus increase their connectivity along recovery from coma, potentially mediating reactivation of the cerebral cortex
	11 (5 used in the rs-fMRI group)	Main anatomic MRI results (behavior tracked, although at lower time resolution)	Several nuclei within the brainstem suffer ischemia after injection of ET-1 and are potentially responsible for the behavioral unresponsiveness
ET-1 injection + no recovery + death	20	Not used for any analysis (most died before MRI was obtained or during MRI acquisition)	
ET-1 injection + developed seizures	10	Euthanized upon apparition of seizures, not included in analysis	Seizures are a potential side effect of coma induction in this model (13% of treated animals)
ET-1 injection + brief coma	6	Imaged (depending on scanner availability) to be used as control	Technical failures (e.g. during injection) and lesions outside the brainstem do not cause long-lasting coma in the rat
ET-1 injection + no coma induction	8	Imaged (depending on scanner availability) to be used as control	
ET-1 injection + coma induction recording	3	Used to investigate the process of coma induction with parallel LFP and calcium imaging	Cortical spreading depression marks the onset of isoelectricity after injection of ET-1
Sham surgery	4	Used as healthy control group for behavioral analysis	Animals injected with PBS instead of ET-1 wake up during the first 40min after surgery. The effects observed in comatose animals must be due to the vasoconstriction and not to the surgical procedure *per se*
Anesthetized	11 (2 undergoing rs-fMRI and 9 belonging to both rs-fMRI and anatomical MRI control groups)	Used as reference for assessment of anatomical and functional MRI from comatose animals	
Basilar artery occlusion	13	Behavioral control	A focal lesion to the basilar artery does not produce coma in the rat
Topical application of ET-1	4	Behavioral control	Topical application of ET-1 does not produce an injury focused on the brainstem nuclei or a reliable coma

Table S1. Use of all animals included in this study. "Long-lasting coma" refers to animals that gradually recovered neurological function during the first 6-8 hours, in contrast to "brief coma", where animals recovered neurological function within 1-2 hours. "No recovery + death", where animals died without showing neurological recovery.

REFERENCES RELEVANT TO SUPPLEMENTARY MATERIAL

Abulafia, R., et al. (2009). "Cerebral activity during the anesthesia-like state induced by mesopontine microinjection of pentobarbital." J Neurosci **29**(21): 7053-7064.

Alkire, M. T., et al. (2007). "Thalamic microinjection of nicotine reverses sevoflurane-induced loss of righting reflex in the rat." Anesthesiology **107**(2): 264-272.

Amzica, F. (2009). "Basic physiology of burst-suppression." Epilepsia **50 Suppl 12**: 38-39.

Anaclet, C., et al. (2014). "The GABAergic parafacial zone is a medullary slow wave sleep-promoting center." Nat Neurosci **17**(9): 1217-1224.

Anaclet, C., et al. (2012). "Identification and characterization of a sleep-active cell group in the rostral medullary brainstem." J Neurosci **32**(50): 17970-17976.

Avezaat, C. J., et al. (1977). "[A scoring device for the level of consciousness: the Glasgow "coma" scale]." Ned Tijdschr Geneeskd **121**(53): 2117-2121.

Borjigin, J., et al. (2013). "Surge of neurophysiological coherence and connectivity in the dying brain." Proc Natl Acad Sci U S A **110**(35): 14432-14437.

Ching, S., et al. (2013). "Real-time closed-loop control in a rodent model of medically induced coma using burst suppression." Anesthesiology **119**(4): 848-860.

Ching, S., et al. (2012). "A neurophysiological-metabolic model for burst suppression." Proc Natl Acad Sci U S A **109**(8): 3095-3100.

Cho, J. R., et al. (2017). "Dorsal Raphe Dopamine Neurons Modulate Arousal and Promote Wakefulness by Salient Stimuli." Neuron **94**(6): 1205-1219 e1208.

Cui, S. Y., et al. (2016). "Ca(2+) in the dorsal raphe nucleus promotes wakefulness via endogenous sleep-wake regulating pathway in the rats." Mol Brain **9**(1): 71.

Devor, M. and V. Zalkind (2001). "Reversible analgesia, atonia, and loss of consciousness on bilateral intracerebral microinjection of pentobarbital." Pain **94**(1): 101-112.

Di Perri, C., et al. (2014). "Measuring consciousness in coma and related states." World J Radiol **6**(8): 589-597.

Fuller, P. M., et al. (2011). "Reassessment of the structural basis of the ascending arousal system." J Comp Neurol **519**(5): 933-956.

Geocadin, R. G., et al. (2000). "Early electrophysiological and histologic changes after global cerebral ischemia in rats." Mov Disord **15 Suppl 1**: 14-21.

Geocadin, R. G., et al. (2002). "Neurological recovery by EEG bursting after resuscitation from cardiac arrest in rats." Resuscitation **55**(2): 193-200.

Hallam, T. M., et al. (2004). "Comparison of behavioral deficits and acute neuronal degeneration in rat lateral fluid percussion and weight-drop brain injury models." J Neurotrauma **21**(5): 521-539.

Hannawi, Y., et al. (2016). "Abnormal movements in critical care patients with brain injury: a diagnostic approach." Crit Care **20**: 60.

Katayama, Y., et al. (1986). "Coma induced by cholinergic activation of a restricted region in the pontine reticular formation--a model of reversible forms of coma." Neurol Med Chir (Tokyo) **26**(1): 1-10.

Kaur, S., et al. (2013). "Glutamatergic signaling from the parabrachial nucleus plays a critical role in hypercapnic arousal." J Neurosci **33**(18): 7627-7640.

Kroeger, D., et al. (2013). "Human brain activity patterns beyond the isoelectric line of extreme deep coma." PLoS One **8**(9): e75257.

Mauguiere, F., et al. (1979). "[Significance of epileptic seizures occurring during the first week of traumatic coma (author's transl)]." Rev Electroencephalogr Neurophysiol Clin **9**(2): 149-155.

Nguyen, H. T., et al. (2009). "Behavior and cellular evidence for propofol-induced hypnosis involving brain glycine receptors." Anesthesiology **110**(2): 326-332.

Petrovic, J., et al. (2013). "Lesion of the pedunculopontine tegmental nucleus in rat augments cortical activation and disturbs sleep/wake state transitions structure." Exp Neurol **247**: 562-571.

Reed, S. J., et al. (2013). "Partial antagonism of propofol anaesthesia by physostigmine in rats is associated with potentiation of fast (80-200 Hz) oscillations in the thalamus." Br J Anaesth **110**(4): 646-653.

Reiner, K., et al. (2007). "Mesopontine tegmental anesthesia area projects independently to the rostromedial medulla and to the spinal cord." Neuroscience **146**(3): 1355-1370.

Robert, F. and M. Mumenthaler (1977). "[Criteria of brain death. Spinal reflexes in 45 personal studies]." Schweiz Med Wochenschr **107**(10): 335-341.

Saposnik, G. and L. R. Caplan (2001). "Convulsive-like movements in brainstem stroke." Arch Neurol **58**(4): 654-657.

Schaar, K. L., et al. (2010). "Functional assessments in the rodent stroke model." Exp Transl Stroke Med **2**(1): 13.

Schott, J. M. and M. N. Rossor (2003). "The grasp and other primitive reflexes." J Neurol Neurosurg Psychiatry **74**(5): 558-560.

Solt, K., et al. (2014). "Electrical stimulation of the ventral tegmental area induces reanimation from general anesthesia." Anesthesiology **121**(2): 311-319.

Sukhotinsky, I., et al. (2007). "Neural pathways associated with loss of consciousness caused by intracerebral microinjection of GABA A-active anesthetics." Eur J Neurosci **25**(5): 1417-1436.

Taylor, N. E., et al. (2016). "Optogenetic activation of dopamine neurons in the ventral tegmental area induces reanimation from general anesthesia." Proc Natl Acad Sci U S A.

Wijdicks, E. F., et al. (2005). "Validation of a new coma scale: The FOUR score." Ann Neurol **58**(4): 585-593.

Wilson, J. A. and H. J. Nordal (2013). "EEG in connection with coma." Tidsskr Nor Laegeforen **133**(1): 53-57.

Xi, M. C., et al. (2001). "Effects on sleep and wakefulness of the injection of hypocretin-1 (orexin-A) into the laterodorsal tegmental nucleus of the cat." Brain Res **901**(1-2): 259-264.

Yamada, K., et al. (1994). "Analysis of auditory brain stem response with lidocaine injection into the cerebrospinal fluid in rats." Ann Otol Rhinol Laryngol **103**(10): 796-800.

Title:

Indexing arousal with multi-modal fMRI merging pupillometry and optical fiber calcium recording

Authors:

Patricia Pais-Roldán[1,2], Kengo Takahashi[1,2], Yi Chen[1,2], Hang Zeng[1,2], Yuanyuan Jiang[1] and Xin Yu[*1,3]

Affiliations:

1. High-Field Magnetic Resonance Department, Max Planck Institute for Biological Cybernetics, Tuebingen, 72076, Germany.

2. Graduate Training Centre of Neuroscience, International Max Planck Research School, University of Tuebingen, Tuebingen, 72074, Germany.

3. Athinoula A. Martinos Center for Biomedical Imaging Massachusetts General Hospital and Harvard Medical School, Charlestown, MA, 02129, USA

Lead corresponding author:
Dr. Xin Yu
Email: xin.yu@tuebingen.mpg.de
Address: Max-Planck-Ring 11, 72076, Tuebingen, Germany
Phone: +49 7071 601-740
Fax: +49 7071 601-701

Classification: BIOLOGICAL SCIENCES: Neuroscience

Keywords: brain state, rat, anesthesia, multimodal imaging

ABSTRACT

Pupillometry, a non-invasive measure of arousal, complements human functional magnetic resonance imaging (fMRI) to detect periods of variable cognitive processing and identify networks that relate to particular attentional states. Despite the crucial role of animal models to link brain function to behavior, e.g., the investigation of the neuronal correlates of pupil dynamics in rodents, a cross-scale view of the brain state dynamics related to their behavioral output remains lacking. Here, we complemented whole-brain resting-state fMRI in adult rats with cortical calcium recording (GCaMP-mediated) and pupillometry to tackle the linkage between neurovascular coupling dynamics and arousal markers across different scales. This multimodal platform allowed us to identify a global brain network that co-varied with pupil size changes, which served to generate an index indicative of the brain state fluctuation during anesthesia. Besides the global fMRI correlation with pupil dynamics and neuronal calcium oscillation, a specific correlation pattern was detected in the brainstem, at a location consistent with the noradrenergic cell group 5 (A5), which appeared dependent on the specific coupling between different frequencies of the calcium signal fluctuation from the cingulate cortex, possibly indicating particular brain states. The rat fMRI adapted to holding calcium recordings and pupillometry serves a fundamental tool to track brain state changes across different scales, which also opens the possibility of performing controlled behavioral research inside the MR scanner.

Significance statement:

Resting-state fMRI (rs-fMRI) performed in animals allows investigating the spatial correlation patterns of the brain function, which presents oscillatory features according to varied brain states, even under anesthesia. However, the link between particular global fMRI signal oscillations and fluctuations in the level of arousal, which can be indexed by spontaneous pupil dilations, is seldom investigated in rodent brains. Here, we established pupillometry with rs-fMRI and concurrent cortical calcium recordings in anesthetized rats, enabling the arousal fluctuation analysis across multiple scales. A unique positive correlation with pupil dilations was detected at the noradrenergic-cell-group 5 (A5) in the ventral brainstem, which was associated with specific coupling between spectrally different calcium waves measured from the cingulate cortex, possibly indicating a unique brain state.

INTRODUCTION

The brain state varies at low frequencies (<0.1 Hz) to mediate arousal or attentional states during rest ([1](#), [2](#)). Studying such resting-state fluctuations at different scales makes it possible to identify the neuromodulatory schemes underlying the spontaneous transitions between different brain states ([3-5](#))([6](#)). Functional Magnetic Resonance Imaging performed during rest (rs-fMRI) can be used to extract the temporal dynamics from different neuronal populations across the brain ([7-9](#)). The temporal correlation between remote areas can be used to map baseline functional connectivity patterns that portray so-called resting-state networks, which have been associated with particular neuropsychological states and have a potential prognostic value in clinical disorders ([10-12](#)). Alternatively, transitions between distinct brain states (e.g., sleep or attention) can be tracked as direct changes in the global fMRI signal. Several human and non-human primate studies have demonstrated that the global fMRI signal accurately reflects the momentary level of attention or arousal ([1](#), [13](#), [14](#)), suggesting a critical role of the ubiquitous spontaneous oscillations in orchestrating the transition between brain states. Additionally, human experiments where pupillometry was added to the fMRI measurement have identified some potential neural correlates of arousal ([15-17](#)), yet the mechanisms underlying spontaneous transitions towards varying brain states remain only partially understood.

Recently, experiments performed in rats have revealed key global signatures that precede brain state changes during anesthesia by measuring the fMRI signal in parallel to the calcium-dependent neuronal and astrocytic activity ([4](#)). The results obtained from these rodent experiments add to growing evidence demonstrating the relevance of the fMRI global signal change within the framework of tracking brain state fluctuations ([1](#), [14](#)). Neuron-vessel interactions underlying blood oxygen level dependent (BOLD) contrast in fMRI have been investigated across scales using the multimodal fMRI platform in anesthetized and awake animals ([4](#), [18](#)), demonstrating its great potential to be applied in behaving rodents to track different brain states. Despite the ongoing efforts to set up an awake rodent multimodal fMRI platform ([19-21](#)), the potential stress and motion-related artifacts lead to significant confounders that draw reliable functional correlation features of the fMRI signal and harden its interpretation ([22](#), [23](#)). In addition, a robust behavioral arousal measurement is still missing for rodents inside the MRI scanner to correlate with the fMRI fluctuation, which could be further used to elucidate the linkage between function and behavior at multiple scales. Here, as an intermediate step to the awake rodent multimodal fMRI, we first aimed at adding pupillometry, an index of physiological arousal, to the existing multimodal platform of anesthetized rodents, allowing for a detailed investigation of the dynamic correlation that exists between the brain function and the pupil size-based arousal changes.

Eye blinks, unconscious eye movements and pupil size variations can report the level of arousal ([1](#)), condition task performance and reflect the level of cognition processing ([24](#)), attention ([25](#)), fear ([26](#)) or reward anticipation ([27](#)). Animal experiments performed on bench (e.g. electrophysiological studies) have allowed to accurately test the relationship between pupil dilations and neural activity specific to particular brain areas. Pupil fluctuations have been repeatedly linked to the activity of neurons in the noradrenergic locus coeruleus (LC) ([28](#), [29](#)), and mark cortical state changes ([30-34](#)), which places the

pupil as an affordable arousal indicator to merge with other brain imaging schemes. These studies have linked pupil dilations to desynchronized cortical activity ([30]) and depolarized states during walking-related arousal ([35]). Pupillometry can be especially informative during anesthesia, where motor-driven behavioral measurements are not accessible to the experimenter. Kum et al. showed that anesthetic wash out (i.e. emergence from anesthesia) is accompanied by burst activity and mydriasis in rats ([32]), suggesting that lighter unconscious states during anesthesia could be tracked by measuring the pupil size.

Despite the existing rodent studies combining electrophysiological measurements with pupillometry, to date there are no studies merging the pupil dynamics with the activity of neuronal populations and concurrent whole-brain fMRI in rats. The goal of this work was to merge the bench measures with fMRI to create a platform that allows investigating the link between the spatiotemporal changes in brain activity and the transitory brain states that can be tracked with pupillometry. Here, GCaMP-mediated recordings of neuronal activity from the cingulate cortex were acquired in parallel to whole-brain fMRI in anesthetized rats subjected to concurrent pupillometry. Based on the rs-fMRI signal and its correlation with the pupil dilations, we identified the presence of oscillatory brain states, which were specifically represented by GCaMP-based neuronal calcium dynamics from the cingulate cortex. Besides tackling the technical challenge of performing pupillometry in small animal MR scanners, we demonstrate the potential of this platform to investigate arousal mechanisms at multiple scales.

RESULTS

Concurrent fMRI, neuronal calcium and pupil dynamics track brain state changes in the anesthetized rat.

We used a small MRI-compatible camera to track the pupil dynamics from the rat eye in parallel to fMRI and obtain a measure of arousal fluctuation during anesthesia (**Sup. Fig. 1**). The measure of pupil size changes was introduced in a multi-scale analysis workflow as illustrated in **Figure 1**. Three main recordings were obtained in parallel: 1) video recording of the pupil, 2) optical fiber calcium recording (in the cingulate cortex, as well as in the barrel cortex in some rats), and 3) whole-brain fMRI imaging. First, the vector representing the pupil size fluctuation was generated from the acquired video (see *Methods* for details). This vector of the pupil dynamics was correlated to each fMRI voxel time course to obtain a pupil-fMRI correlation map. In addition, another correlation map was created by comparing the fMRI time courses with the 1st derivative of the pupil size (i.e. pupil dilations). Second, the pupil dilations-fMRI correlation map, considered as a pupil-relevant spatial template, was correlated with the original 4D fMRI (i.e. a time-varying volume) to create a specific spatiotemporal correlation time course that provided an fMRI index of arousal, similar to what has been shown in previous rs-fMRI arousal studies on non-human primates ([1]). Third, the pupil dynamics were studied in relation to the calcium signal fluctuation from the cingulate cortex, in particular the 2-3Hz activity band, which showed the strongest power throughout the calcium spectrum (the spectral analysis of the calcium signals is explained in the *Methods* section) ([4], [36]). Finally, the time course of the fMRI arousal index was

4

compared with the calcium dynamics from the cingulate cortex. **Supplementary Figure 2** shows a summary pipeline with the main steps used in this work. The relationship between the fMRI signal and its arousal index time course, as well as the pupil and calcium dynamics, is exemplified in **Supplementary video 1**.

Figure 2 shows the brain state fluctuation detected with the multimodal platform in a representative animal under anesthesia. Alternation between brain states was clearly linked to the transition from constricted to dilated pupil or vice-versa (**Fig. 2, top trace**, and **Sup. Fig. 3**), which showed a strong correlation with the whole-brain fMRI signal fluctuation and with the neuronal calcium signal oscillation (**Fig. 2, middle and bottom traces**). It is noteworthy that the brain state dynamics varied across different trials. This dynamicity can be presented by the index of pupillary unrest (PUI), which measured the variability in pupil size per run (see *Methods*) ([37](#)). The PUI was positively correlated with the standard deviation of the pupil size, showing 43% of the total trails (n=71 of 10 rats) with a PUI above 1000 with salient low-frequency oscillatory patterns (**Sup. Fig. 4**). Together, this multimodal measurement makes it possible to perform cross-scale correlation analysis to investigate the largely varying arousal fluctuation in the anesthetized state.

Correlation analysis of whole-brain fMRI with pupil dynamics in the anesthetized rats.

Simultaneous fMRI and pupillometry allowed us to compute two pupil-correlated fMRI maps during the anesthetized state. **Fig. 3A** shows the correlation map of the pupil size changes with the whole-brain fMRI, presenting negative correlation to most of the cerebral cortex, thalamus, septal nuclei and the superior colliculus, some of which have been previously identified as neural correlates of pupil dilations during wakefulness (i.e. cingulate cortex or superior colliculus ([38](#), [39](#))). While the change in pupil size correlates with periods of arousal fluctuation during wakefulness ([15](#)), specific brain regions relevant to the switch between arousal states can be potentially assessed by correlating the fMRI signal with the derivative of the pupil size dynamic time course ([16](#), [27](#), [40](#)); therefore we also performed correlation analysis between BOLD-fMRI and the 1st order derivative of the pupil size (i.e. pupil dilation/constriction velocity, e.g., the purple trace in **Fig. 2**). Besides the negative correlation observed through most of the brain, similar to the pupil-size correlation map (**Fig. 3A&C**), a positively correlated area was observed in the brainstem region, which was not detected in the pupil-size correlation map (**Fig. 3B&D**). The positively correlated brainstem nucleus overlapped with the rostral A5 area (**Fig. 3D**), which contains primarily noradrenergic cells and projects to the major subcortical arousal nuclei through the reticular formation pathway ([41](#)). It is worth noting that no significant positive correlation was observed in other subcortical nuclei involved in arousal regulation, e.g. the LC ([28](#)), or the central and mediodorsal thalamic nuclei ([4](#), [42](#)), which may be due to the highly variable brain state dynamics across the multiple trials.

Validation of a pupil-fMRI derived index of arousal.

As shown in **Figure 4**, the momentary pupil-linked arousal can be inferred from each acquired rs-fMRI volume by calculating its spatial correlation with the pupil-fMRI map. Consecutive spatial correlation values can be concatenated to produce a vector of the time-varying fMRI arousal index ([1](#)). To specify the neuronal correlates of the inferred arousal fluctuation, the power profile of the concurrent neuronal

calcium signal was assessed in relation to the global fMRI arousal index and the pupil dynamic changes, showing strong correlation features with both signals (**Fig. 4E&G**). The fMRI arousal index was positively correlated with the pupil dynamics (**Fig. 4B&C**) but showed a negative correlation with the power of the calcium 2-3Hz oscillation (**Fig. 4D&E**). In addition, the neuronal calcium recordings from cingulate and barrel cortex in our anesthetized rats co-varied (negatively) with pupil size changes, showing a decrease of the 2-3Hz power during dilations (**Sup. Fig. 2** and **Fig. 4G&H**), consistent with the negative correlation observed from the same cortical region in the pupil-fMRI correlation map. The salient correlation features observed across multiple trials between the fMRI arousal index, the calcium oscillation from the cingulate cortex and the pupil dynamics present a generalized three-way interaction scheme to elucidate the arousal state changes in anesthetized rats (**Fig. 4F**).

Neurophysiological correlates of the pupil dilation-relevant brainstem activation.
Besides the power profile of the 2-3Hz band, investigations concerning the low-frequency calcium oscillation (i.e. the baseline fluctuation at <0.1Hz) provided an additional dynamic feature to depict the neurophysiological state of animals (**Fig. 5**) (36, 43). To better categorize the neurophysiological states of the anesthetized rats, cross-correlation analysis of the baseline fluctuation and the 2-3Hz power amplitude changes was performed, which identified a subset of trials with strong cross-frequency coupling (**Fig. 5B**). However, approximately 60% of the trials demonstrated poor correlation or uncoupled cross-frequency calcium dynamics (**Fig. 5B**), similar to the dissociation of phase and amplitude coupling observed in previous EEG studies (44). We performed cluster analysis to sort trials into two different groups according to their cross-frequency coupling features and compared the group-pupil-fMRI correlation maps resulting from both neurophysiological states (**Fig. 5C**). Similar to the pupil-fMRI correlation map acquired with all trials considered as part of the same set (**Fig. 3A**), a negative correlation through most of the brain was observed from both groups (i.e. regardless of the neurophysiological coupling), with no statistically significant difference observed between them (**Fig. 5D**, upper bar plot). However, the positive correlation between pupil dilations and A5 (brainstem) was found significantly higher in the calcium-uncoupled group (**Fig. 5D**, lower bar plot). This result suggests that, under anesthesia, the cortical neurophysiological state (determined as coupled or uncoupled calcium signals) is specifically linked to the activation of A5 during pupil dilations.

Interestingly, the uncoupled trials exhibited higher pupil standard deviation than that of the coupled trials (**Fig. 5E**, marked in the red box), i.e. the pupil was more dynamic when baseline and 2-3Hz calcium fluctuations were uncoupled. However, no apparent relationship existed between the pupil standard deviation and the pupil-fMRI correlation coefficients of A5 or the global brain area (**Fig. 5F**, $R^2 < 0.2$ in all cases). The noradrenergic cell group A5 in the brainstem is involved in the regulation of the cardiovascular system (41, 45, 46), which could support a potential role of this nucleus in the modulation of the pupil dynamics and the global fMRI signal fluctuation through sympathetic regulation. Nevertheless, the fact that the degree of pupil dynamicity appeared independent from the level of pupil-A5 correlation suggests that A5 itself is not a sole driver of the pupil dynamics or the global pupil-fMRI correlation patterns. The cross-spectral calcium analysis in the context of the correlation between pupil

and whole-brain fMRI demonstrated that, under anesthesia, the cortical neurophysiological state is specifically linked to the activation of A5 during pupil dilations.

DISCUSSION

In this work, simultaneous whole-brain fMRI and optical fiber-mediated neuronal calcium recording were complemented with concurrent measurements of the pupil size to identify transitional brain states in anesthetized rats. The pupil dynamics-whole-brain rs-fMRI correlation map demonstrated an overall negative signal throughout the cortical and subcortical regions, but with specific positive correlation on the noradrenergic cell group A5 located in the brainstem, which seemed particularly relevant to the uncoupling between high and low frequency oscillations of the neuronal calcium signal and, possibly, the standard deviation (i.e. dynamicity) of the pupil size (**Fig. 5**). Overall, the correlation found between the pupil dynamics, the fMRI arousal index and the neuronal activity (recorded as GCaMP fluorescent signal from the cingulate cortex, as well as in the barrel cortex) indicates reliable tracking of the brain state fluctuation by the multimodal fMRI platform.

Despite the large variability of the brain state fluctuation among different trials during anesthesia (see the diverse pupil dynamics observed from different animals on **Sup. Fig. 4**), robust negative correlation was observed globally between the fMRI and the pupil dynamics across different animals (**Sup. Fig. 5**), even when trials were sorted in two different groups based on their neuronal calcium oscillatory features (**Fig. 5C**) (which did affect the detection of the positive signal on the brainstem). Our results suggest that the pupil dynamics observed during anesthesia in rats are directly linked to the global fMRI signal fluctuation, as well as to the alternating population activity observed as neuronal calcium transient oscillations; in particular, the 2-3Hz power fluctuation (**Fig. 2** and **Sup. Fig. 3**). A relationship between pupil size and cortical activity, presumably linked to changes in arousal, has been reliably observed in mice during wakefulness and during Non-REM sleep (30, 33, 34). These animals also transited between periods of high amplitude and low-frequency neuronal firing coupled to constricted pupils and periods of low population activity (i.e. more desynchronized states) linked to pupil dilations, in agreement with our observations (**Fig. 4G&H** and **Sup. Fig. 3**). Also, the switch from desynchronized (low amplitude fast activity) to synchronized (high amplitude slow waves) EEG in rats anesthetized with isoflurane (47) or urethane (48) has been previously associated to the transition from pupil dilation to constriction. By altering the concentrations of isoflurane, Kum et al. reported that changes of pupil size serve as a precedent sign of the emergence from anesthesia, demonstrating a linkage between pupil dynamics and transitions between brain arousal states (32).

We report two findings based on the pupil dynamics-fMRI correlation analysis in rats under anesthesia. One is the global negative fMRI signal related to the pupil dilations (**Fig. 3B**). The observation of cortical regions anti-correlated with the pupil dynamics is in agreement with the arousal-based rs-fMRI signal correlation patterns obtained from un-anesthetized non-human primates with eye-opening/closing tracking (1). The reduced BOLD signal observed during pupil dilations in our anesthetized animals coincided with suppressed calcium transient activity from the cortex (**Fig. 4D**), which is in agreement

with previous reports of lightly anesthetized rats (36). However, in contrast to the previously reported anti-correlation between cortical and subcortical functional dynamics during vigilant brain states (1, 49-52), the pupil-based fMRI correlation maps in our study show a rather global negative correlation feature spread over both, cortical and subcortical regions (**Fig. 3**). In particular, the anti-correlation of the cortex and thalamus observed by rs-fMRI at varied arousal states (53, 54) has not been revealed in the anesthetized rats. Wang et al. have previously reported a positive BOLD response in the midline thalamic nuclei preceding a massing global negative BOLD signal coupled to specific astrocytic calcium transients in anesthetized rats (4). The lack of detection of this fast-positive thalamic BOLD signal from the pupil-based fMRI correlation map may be caused by the largely varied indices of pupil unrest across the different trials (**Sup. Fig. 4**). In addition, the massive global negative BOLD signal may overshadow the phasic positive contribution from the thalamus. A future study integrating concurrent astrocytic calcium signal recording into the multimodal fMRI platform will attempt to further investigate the anti-correlation features of the cortex and the thalamus relevant to the brain state.

The second finding is the robust positive correlation observed in the A5 noradrenergic cell group from the pupil dilations-fMRI correlation map (**Fig. 3D**). The neurons of this pontine nucleus send projections to several midbrain areas involved in arousal and vital functions, including the periaqueductal gray and the parabrachial nucleus (41, 55), and are suppressed during REM-like states induced by the acetylcholine agonist carbachol and the alpha-2 receptor clonidine (56), which supports its potential role related to arousal state fluctuation and pupil size regulation. Similar to the LC, the A5 noradrenergic area may play an alternative regulatory role on arousal, as suggested from the multiple studies associating noradrenaline to brain state modulation (57-59). Although brain state fluctuation and pupil dynamics have been reported to be regulated through the noradrenergic projections from LC (28, 29), we observed no significant positive correlation patterns in LC or their projection areas. This fact may indicate that the temporal features of pupil dynamics did not serve as a strong linear regressor to fit the neuronal activity-coupled fMRI signal particular to LC in the anesthetized brain (60, 61). Importantly, to date, the existence of a causal link between LC and pupil modulation remains to be clarified (40). Further strategies (e.g. noradrenergic specific cell targeting) will be needed to confirm and characterize the unexplored relationship between the A5 group and the pupil dynamics. Additionally, similar to the specific astrocytic-dependent fMRI activation pattern deciphered in anesthetized rats (4), knowledge about the specific dynamic signaling underlying pupil dilations may be needed to identify functional nuclei that may modulate pupil dynamics with particular firing and neurovascular coupling patterns. Also noteworthy is that the A5 area is mostly positively correlated with the 1st order derivative rather than the direct pupil size (**Fig. 3C**), indicating that the activation of A5 is more relevant to the change than to the maintenance of the brain state.

Besides specifying the neural correlates of the pupil dynamics (i.e. decreased population activity in the cortex and generalized negative BOLD signal linked to pupil dilations), the concurrent neuronal calcium signal fluctuating at ultra-low frequency allowed us to consider additional features to characterize the brain state. The cross-correlation of the calcium baseline fluctuation and the 2-3Hz power profile changes (similar to the phase-amplitude coupling described in EEG recordings (44, 62)), revealed two

distinguishable states in the anesthetized brain across multiple trials in our study (**Fig. 5B**). Besides the highly correlated ultra-slow baseline with higher frequency components of the calcium signal, as previously reported in anesthetized rats ([36]), we also identified cross-frequency uncorrelated features, indicating a dissociated amplitude-phase coupling ([44]). In contrast to the robust global negative pupil-fMRI correlation under both coupled and uncoupled neurophysiological states, the positive correlation in A5 was only significant in the uncoupled calcium dynamic state, which was paired with a higher standard deviation of the pupil dynamics (**Fig. 5E**). Given the role of A5 on the regulation of the cardiovascular system, it could be hypothesized that activation of A5 potentially leads to bottom-up impact on the cerebrovascular hemodynamic signals and the pupil dynamics ([41]), which could strengthen the global negative fMRI correlation feature observed here. However, the negative pupil-global fMRI correlation values did not appear linearly dependent on the pupil-A5 correlation, neither seemed the pupil dynamicity (i.e. pupil size standard deviation) reliant on the pupil-A5 relationship (**Fig. 5F**). Thus, A5 activation may represent a potent indicator of specific brain states under particular cross-frequency uncoupling conditions in the anesthetized brain, but it does not serve as the major driver, or at least not the essential factor, to modulate the brain state fluctuation. The mechanism behind the A5-activation-related brain state fluctuation will be further investigated with circuit specific methods in future studies.

CONCLUSION

Here, we merged pupillometry, as a marker of arousal, with whole-brain fMRI and calcium recordings from the cingulate cortex in anesthetized rats. We identified a quasi-global negative fMRI spatial pattern that was correlated with pupil size changes and served as a template to produce an arousal fMRI index during anesthesia. The neurobiological relevance of the inferred pupil-fMRI-based arousal index was verified with the detection of closely coupled neuronal calcium oscillations in the cingulate cortex. In addition, cross-correlation analysis of the low-frequency calcium baseline and the 2-3Hz power fluctuation identified two distinguishable neurophysiological states, defined based on the coupling or uncoupling of the calcium signals. While the global negative pupil-fMRI correlation was present under both states, the positive correlation on the A5 noradrenergic group of the pons was mainly linked to the neurophysiological state characterized by uncoupled neuronal calcium dynamics. The multimodal platform (fMRI combined with optical fiber calcium recording and pupillometry) allows investigating the pupil-dependent arousal state of the brain, which opens the possibility to link brain function and behavior inside the MRI scanner and further enriches multimodal brain mapping to facilitate consciousness research.

 METHODS

10 adult Sprague Dawley rats were used to acquire the results of the current study (n=71 trials). All animals were subjected to intracortical viral injection at 4 weeks of age to express the genetically

encoded calcium indicator, GCaMP6f, allowed to recover for one month and then subjected to a terminal fMRI study under anesthesia, with parallel measures of the pupil size and of the calcium signals. In 8 of the 10 animals, the barrel cortex was additionally targeted to record calcium signals from a region of the primary somatosensory cortex. All animal procedures were approved by the Animal Protection Committee of Tübingen (Regierungspräsidium Tübingen).

Analysis of the multimodal data included temporal correlation between the pupil dynamics and the fMRI signals, spatial correlation between each fMRI volume and the pupil-fMRI correlation map and cross-correlation measures between the whole brain fMRI, the calcium signal at 2-3Hz or baseline and the pupil size/pupil dilations. A scheme summarizing the main analysis pipeline can be found as Supplementary Figure 2.

For details concerning surgical procedures, calcium signal acquisition, fMRI sequence and pupil measures see **Supplementary Methods**.

ACKNOWLEDGMENTS

REFERENCES

1. Chang C*, et al.* (2016) Tracking brain arousal fluctuations with fMRI. *Proc Natl Acad Sci U S A* 113(16):4518-4523.
2. Watson BO (2018) Cognitive and Physiologic Impacts of the Infraslow Oscillation. *Front Syst Neurosci* 12:44.
3. Lee SH & Dan Y (2012) Neuromodulation of brain states. *Neuron* 76(1):209-222.
4. Wang M, He Y, Sejnowski TJ, & Yu X (2018) Brain-state dependent astrocytic Ca(2+) signals are coupled to both positive and negative BOLD-fMRI signals. *Proc Natl Acad Sci U S A* 115(7):E1647-E1656.
5. Zagha E & McCormick DA (2014) Neural control of brain state. *Curr Opin Neurobiol* 29:178-186.
6. Liu X*, et al.* (2015) Arousal transitions in sleep, wakefulness, and anesthesia are characterized by an orderly sequence of cortical events. *Neuroimage* 116:222-231.
7. Biswal B, Yetkin FZ, Haughton VM, & Hyde JS (1995) Functional connectivity in the motor cortex of resting human brain using echo-planar MRI. *Magn Reson Med* 34(4):537-541.
8. Raichle ME*, et al.* (2001) A default mode of brain function. *Proc Natl Acad Sci U S A* 98(2):676-682.
9. Jonckers E, Shah D, Hamaide J, Verhoye M, & Van der Linden A (2015) The power of using functional fMRI on small rodents to study brain pharmacology and disease. *Front Pharmacol* 6:231.
10. Dacosta-Aguayo R*, et al.* (2014) Prognostic value of changes in resting-state functional connectivity patterns in cognitive recovery after stroke: A 3T fMRI pilot study. *Hum Brain Mapp* 35(8):3819-3831.
11. Fox MD & Greicius M (2010) Clinical applications of resting state functional connectivity. *Front Syst Neurosci* 4:19.

12. Kiviniemi V, *et al.* (2009) Functional segmentation of the brain cortex using high model order group PICA. *Hum Brain Mapp* 30(12):3865-3886.
13. Scholvinck ML, Maier A, Ye FQ, Duyn JH, & Leopold DA (2010) Neural basis of global resting-state fMRI activity. *Proc Natl Acad Sci U S A* 107(22):10238-10243.
14. Turchi J, *et al.* (2018) The Basal Forebrain Regulates Global Resting-State fMRI Fluctuations. *Neuron* 97(4):940-952 e944.
15. Murphy PR, Vandekerckhove J, & Nieuwenhuis S (2014) Pupil-linked arousal determines variability in perceptual decision making. *PLoS Comput Biol* 10(9):e1003854.
16. Schneider M, *et al.* (2016) Spontaneous pupil dilations during the resting state are associated with activation of the salience network. *Neuroimage* 139:189-201.
17. Yellin D, Berkovich-Ohana A, & Malach R (2015) Coupling between pupil fluctuations and resting-state fMRI uncovers a slow build-up of antagonistic responses in the human cortex. *Neuroimage* 106:414-427.
18. Gao YR, *et al.* (2017) Time to wake up: Studying neurovascular coupling and brain-wide circuit function in the un-anesthetized animal. *Neuroimage* 153:382-398.
19. Ferenczi EA, *et al.* (2016) Prefrontal cortical regulation of brainwide circuit dynamics and reward-related behavior. *Science* 351(6268):aac9698.
20. Stenroos P, *et al.* (2018) Awake Rat Brain Functional Magnetic Resonance Imaging Using Standard Radio Frequency Coils and a 3D Printed Restraint Kit. *Front Neurosci* 12:548.
21. Desai M, *et al.* (2011) Mapping brain networks in awake mice using combined optical neural control and fMRI. *J Neurophysiol* 105(3):1393-1405.
22. Pais-Roldan P, Biswal B, Scheffler K, & Yu X (2018) Identifying Respiration-Related Aliasing Artifacts in the Rodent Resting-State fMRI. *Front Neurosci* 12:788.
23. Hoyer C, Gass N, Weber-Fahr W, & Sartorius A (2014) Advantages and challenges of small animal magnetic resonance imaging as a translational tool. *Neuropsychobiology* 69(4):187-201.
24. Knapen T, *et al.* (2016) Cognitive and Ocular Factors Jointly Determine Pupil Responses under Equiluminance. *PLoS One* 11(5):e0155574.
25. Wainstein G, *et al.* (2017) Pupil Size Tracks Attentional Performance In Attention-Deficit/Hyperactivity Disorder. *Sci Rep* 7(1):8228.
26. Leuchs L, Schneider M, Czisch M, & Spoormaker VI (2017) Neural correlates of pupil dilation during human fear learning. *Neuroimage* 147:186-197.
27. Schneider M, Leuchs L, Czisch M, Samann PG, & Spoormaker VI (2018) Disentangling reward anticipation with simultaneous pupillometry / fMRI. *Neuroimage* 178:11-22.
28. Joshi S, Li Y, Kalwani RM, & Gold JI (2016) Relationships between Pupil Diameter and Neuronal Activity in the Locus Coeruleus, Colliculi, and Cingulate Cortex. *Neuron* 89(1):221-234.
29. Murphy PR, O'Connell RG, O'Sullivan M, Robertson IH, & Balsters JH (2014) Pupil diameter covaries with BOLD activity in human locus coeruleus. *Hum Brain Mapp* 35(8):4140-4154.
30. Reimer J, *et al.* (2014) Pupil fluctuations track fast switching of cortical states during quiet wakefulness. *Neuron* 84(2):355-362.
31. Reimer J, *et al.* (2016) Pupil fluctuations track rapid changes in adrenergic and cholinergic activity in cortex. *Nat Commun* 7:13289.
32. Kum JE, Han HB, & Choi JH (2016) Pupil Size in Relation to Cortical States during Isoflurane Anesthesia. *Exp Neurobiol* 25(2):86-92.
33. Yuzgec O, Prsa M, Zimmermann R, & Huber D (2018) Pupil Size Coupling to Cortical States Protects the Stability of Deep Sleep via Parasympathetic Modulation. *Curr Biol* 28(3):392-400 e393.
34. McGinley MJ, *et al.* (2015) Waking State: Rapid Variations Modulate Neural and Behavioral Responses. *Neuron* 87(6):1143-1161.
35. McGinley MJ, David SV, & McCormick DA (2015) Cortical Membrane Potential Signature of Optimal States for Sensory Signal Detection. *Neuron* 87(1):179-192.
36. He Y, *et al.* (2018) Ultra-Slow Single-Vessel BOLD and CBV-Based fMRI Spatiotemporal Dynamics and Their Correlation with Neuronal Intracellular Calcium Signals. *Neuron* 97(4):925-939 e925.
37. Ludtke H, Wilhelm B, Adler M, Schaeffel F, & Wilhelm H (1998) Mathematical procedures in data recording and processing of pupillary fatigue waves. *Vision Res* 38(19):2889-2896.
38. Ebitz RB & Platt ML (2015) Neuronal activity in primate dorsal anterior cingulate cortex signals task conflict and predicts adjustments in pupil-linked arousal. *Neuron* 85(3):628-640.
39. Wang CA, Boehnke SE, White BJ, & Munoz DP (2012) Microstimulation of the monkey superior colliculus induces pupil dilation without evoking saccades. *J Neurosci* 32(11):3629-3636.
40. Costa VD & Rudebeck PH (2016) More than Meets the Eye: the Relationship between Pupil Size and Locus Coeruleus Activity. *Neuron* 89(1):8-10.
41. Byrum CE & Guyenet PG (1987) Afferent and efferent connections of the A5 noradrenergic cell group in the rat. *J Comp Neurol* 261(4):529-542.

42. Baker JL*, et al.* (2016) Robust modulation of arousal regulation, performance, and frontostriatal activity through central thalamic deep brain stimulation in healthy nonhuman primates. *J Neurophysiol* 116(5):2383-2404.

43. Du C, Volkow ND, Koretsky AP, & Pan Y (2014) Low-frequency calcium oscillations accompany deoxyhemoglobin oscillations in rat somatosensory cortex. *Proc Natl Acad Sci U S A* 111(43):E4677-4686.

44. Siems M & Siegel M (2018) Dissociated cortical- and amplitude-coupling patterns in the human brain. *[bioRxiv]*.

45. Huangfu DH, Koshiya N, & Guyenet PG (1991) A5 noradrenergic unit activity and sympathetic nerve discharge in rats. *Am J Physiol* 261(2 Pt 2):R393-402.

46. Kanbar R, Depuy SD, West GH, Stornetta RL, & Guyenet PG (2011) Regulation of visceral sympathetic tone by A5 noradrenergic neurons in rodents. *J Physiol* 589(Pt 4):903-917.

47. Takahashi H, Tokushige H, Shiramatsu TI, Noda T, & Kanzaki R (2015) Covariation of pupillary and auditory cortical activity in rats under isoflurane anesthesia. *Neuroscience* 300:29-38.

48. Blasiak T, Zawadzki A, & Lewandowski MH (2013) Infra-slow oscillation (ISO) of the pupil size of urethane-anaesthetised rats. *PLoS One* 8(4):e62430.

49. Feige B*, et al.* (2005) Cortical and subcortical correlates of electroencephalographic alpha rhythm modulation. *J Neurophysiol* 93(5):2864-2872.

50. Goldman RI, Stern JM, Engel J, Jr., & Cohen MS (2002) Simultaneous EEG and fMRI of the alpha rhythm. *Neuroreport* 13(18):2487-2492.

51. Poudel GR, Innes CR, Bones PJ, Watts R, & Jones RD (2014) Losing the struggle to stay awake: divergent thalamic and cortical activity during microsleeps. *Hum Brain Mapp* 35(1):257-269.

52. Liu Z*, et al.* (2012) Finding thalamic BOLD correlates to posterior alpha EEG. *Neuroimage* 63(3):1060-1069.

53. Killgore WD*, et al.* (2015) Daytime sleepiness is associated with altered resting thalamocortical connectivity. *Neuroreport* 26(13):779-784.

54. Zou Q*, et al.* (2009) Functional connectivity between the thalamus and visual cortex under eyes closed and eyes open conditions: a resting-state fMRI study. *Hum Brain Mapp* 30(9):3066-3078.

55. Bruinstroop E*, et al.* (2012) Spinal projections of the A5, A6 (locus coeruleus), and A7 noradrenergic cell groups in rats. *J Comp Neurol* 520(9):1985-2001.

56. Fenik V, Marchenko V, Janssen P, Davies RO, & Kubin L (2002) A5 cells are silenced when REM sleep-like signs are elicited by pontine carbachol. *J Appl Physiol (1985)* 93(4):1448-1456.

57. Ding F*, et al.* (2013) alpha1-Adrenergic receptors mediate coordinated Ca2+ signaling of cortical astrocytes in awake, behaving mice. *Cell Calcium* 54(6):387-394.

58. Paukert M*, et al.* (2014) Norepinephrine controls astroglial responsiveness to local circuit activity. *Neuron* 82(6):1263-1270.

59. Kenny JD, Taylor NE, Brown EN, & Solt K (2015) Dextroamphetamine (but Not Atomoxetine) Induces Reanimation from General Anesthesia: Implications for the Roles of Dopamine and Norepinephrine in Active Emergence. *PLoS One* 10(7):e0131914.

60. Song AH*, et al.* (2017) Pharmacological Modulation of Noradrenergic Arousal Circuitry Disrupts Functional Connectivity of the Locus Ceruleus in Humans. *J Neurosci* 37(29):6938-6945.

61. Devilbiss DM & Waterhouse BD (2011) Phasic and tonic patterns of locus coeruleus output differentially modulate sensory network function in the awake rat. *J Neurophysiol* 105(1):69-87.

62. Jensen O & Colgin LL (2007) Cross-frequency coupling between neuronal oscillations. *Trends Cogn Sci* 11(7):267-269.

63. Siegle GJ, Steinhauer SR, Stenger VA, Konecky R, & Carter CS (2003) Use of concurrent pupil dilation assessment to inform interpretation and analysis of fMRI data. *Neuroimage* 20(1):114-124.
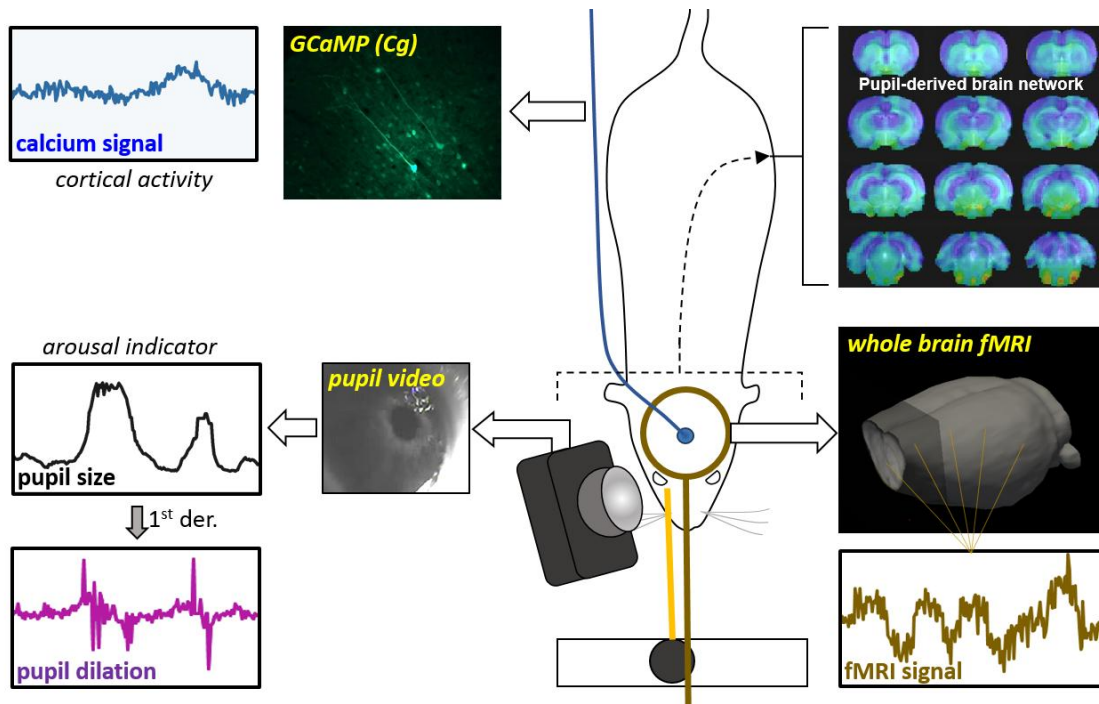
Figure 1. Multimodal GCaMP-pupil-fMRI platform. The scheme shows the setup used to acquire concurrent neuronal calcium signals from the cingulate cortex (GCaMP-based), pupillometry and whole-brain fMRI, which allowed building a pupil-fMRI correlation map and study the relationship between whole-brain patterns, neurophysiological features and arousal states.
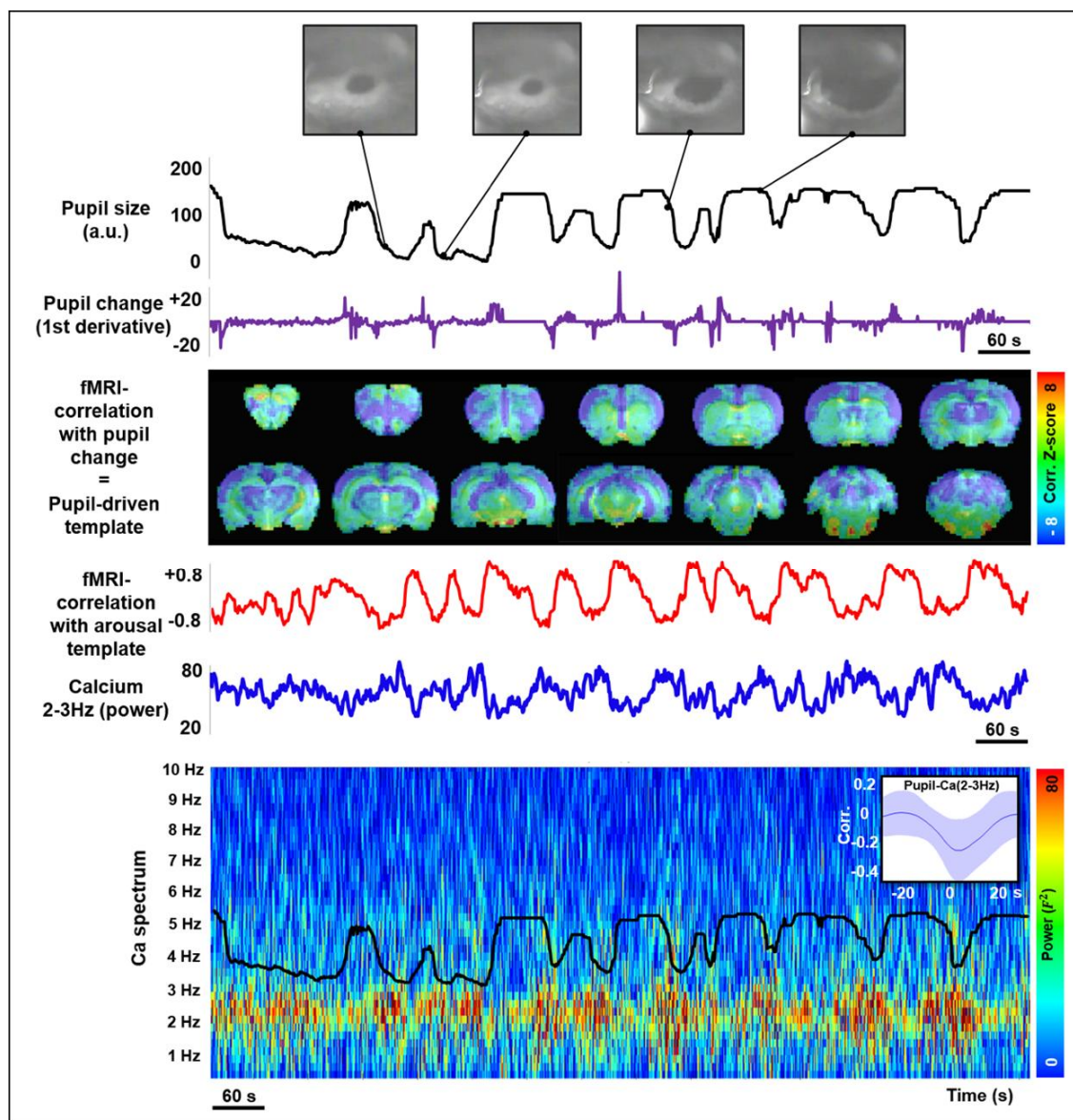
Figure 2. Tracking brain state changes with pupillometry, fMRI and calcium imaging. The traces, map and spectrum in this figure show an example of the measures obtained concurrently during a 15min scan in an anesthetized rat. The top trace (black) shows the variable pupil size during the scan time (higher values represent bigger pupils). The purple trace was computed by acquiring the 1st derivative of the pupil size, and it tracks periods of pupil dilations (positive values) or constrictions (negative values). The brain map shows, on its overlay, the correlation values between the fMRI time-course of each voxel and the pupil change vector (a more detailed version of the correlation map can be found in **Fig 3**). The red trace represents the time-varying similarity between the brain configuration at each TR and the pupil-driven template, indicative of the degree to which the brain state is governed by pupil-fluctuations. The blue trace shows the power fluctuations of the 2-3Hz band of intraneuronal calcium from the cingulate cortex, and below, the frequency content of the calcium signal is shown in bins of 2s windows during the whole scan time. The black trace over the spectral decomposition of the calcium signal shows again the fluctuations in the pupil size. Note the negative correlation between the pupil and the power of the 2-3Hz calcium band. The averaged±standard deviation cross-correlation measure between these two signals across 71 trials from 10 animals is plotted in the upper right inset within this subplot.

14
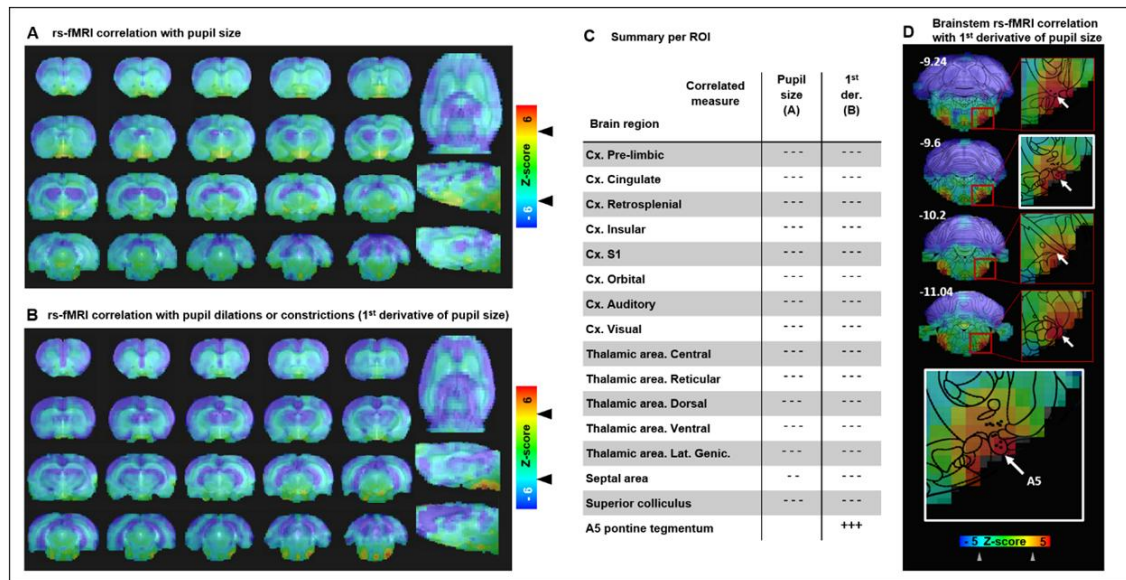
Figure 3. Co-variability of the fMRI signals with the pupil dynamics. **A**. Statistic map of the fMRI correlation with the pupil size. **B**. Statistic map of the fMRI correlation with the 1st derivative of the pupil size. N=71 trials from 10 animals. The black arrowheads in the color bars identify a p-value of ±0.01. **C**. Region-specific correlation analysis for each of the two conditions (A and B). [- - -] / [+ + +]= p-value<0.001. **D**. Statistic 1st derivative map focused on the brainstem region to show the positive correlation detected on the noradrenergic group A5. Coordinates on the top left of each slice indicate the distance in the anterior-posterior axis from bregma in mm. White arrows identify the A5 region. Arrowheads next to the color bar identify a p-value of ±0.01.
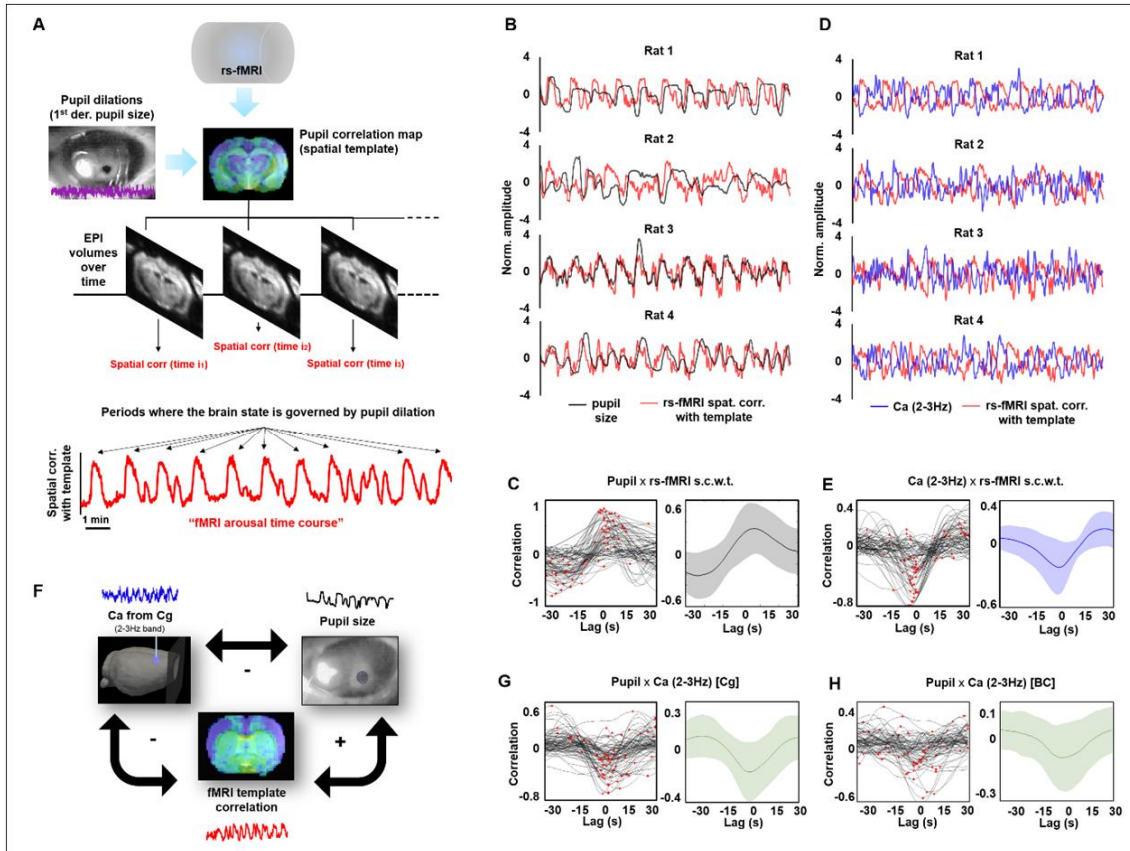
Figure 4. Acquisition and properties of the pupil-governed brain state time course. A. Schematic showing how the pupil-governed time course (rs-fMRI spatial correlation with template) was computed for each fMRI scan. **B**. Four pairs of time-courses from different animals are shown to exemplify the similarity between the fluctuations in the pupil size (black traces) and the fluctuations in the fMRI spatial correlation with template (red traces). **C**. Cross correlation between the pupil size and the rs-fMRI spatial correlation with the template ("fMRI sc"). **D**. Four pairs of time-courses from different animals are shown to exemplify the strong inverse relationship between the fMRI sc reflecting time-varying pupil-governed brain states (red traces) and the population activity at 2-3Hz from the cingulate cortex (blue traces). **E**. Cross correlation between the fMRI sc and the power of the calcium fluctuations in the 2-3Hz frequency band. **F.** Schematic summarizing the relationships between the 2-3Hz calcium signal, pupil size changes, and fMRI spatial correlation with the template. **G, H**. Cross correlation between the pupil size and the calcium signal (2-3Hz power) from the cingulate cortex (G) or the barrel cortex (H). Red dots on the left graphs in C,E, G and H identify the maximum correlation value from each trial within a ±30s lag. Right graphs represent the average±standard deviation.
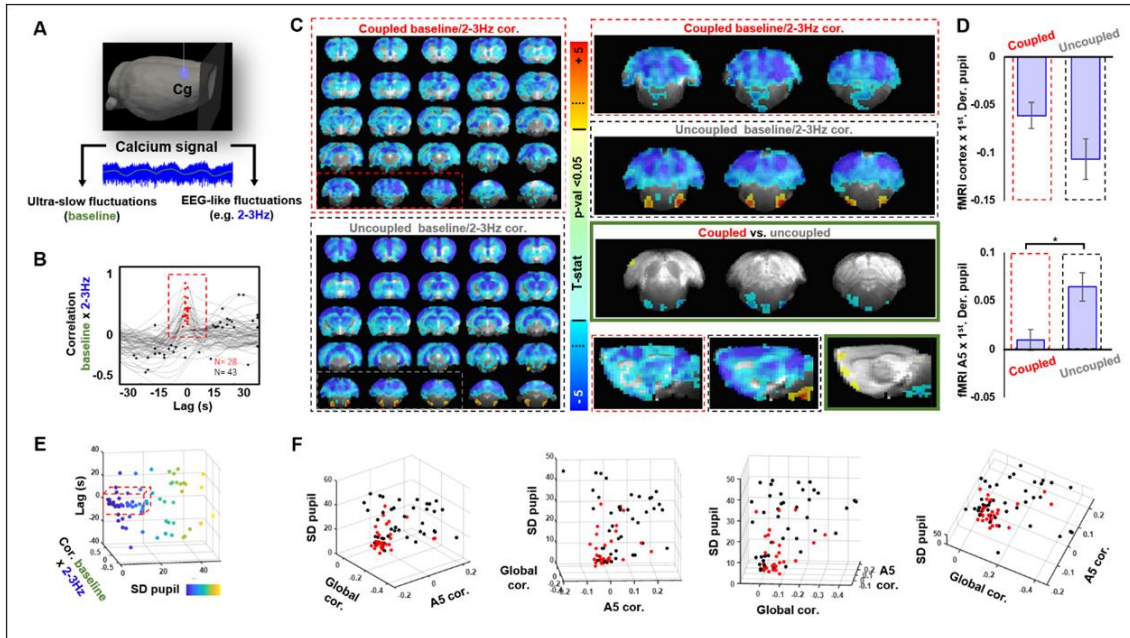
Figure 5. Neurophysiological state associated to the activation of A5 during pupil dilations. A. The calcium signal can be decomposed in slow (baseline) or relatively fast fluctuations (e.g. 2-3Hz). **B.** The graph shows the cross-correlation between the 2-3Hz band and the baseline –red/black dots: coupled/uncoupled trials-). **C**. The maps show the voxel-wise t-statistic for a one-sample t-test run on the fMRI correlation map with the 1st derivative of the pupil, for trials with coupled (upper map) or uncoupled (bottom map) calcium signals. On the right, three coronal slices covering the brainstem are magnified from both maps to show the differences in the A5 correlation values between both groups. The 3rd row shows the results of a t-test between both groups (note the significant differences encountered in the A5). At the bottom, a sagittal slice from each group of the above maps is shown for further verification. Maps are thresholded at p-value < 0.05 (FDR correction of 0.99) **D**. The two bar plots quantify the averaged correlation values shown on C from the coupled (left bars) or uncoupled (right bars) groups extracted from an ROI covering the whole cortex (upper graph –negatively correlated with the 1st derivative of the pupil size) or an ROI covering the A5 (lower graph –positively correlated with the 1st derivative of the pupil size). Note the statistically significant difference found on the A5 between the coupled and the uncoupled group. **E**. 3D scatter plot showing the relationship between baseline/2-3Hz correlation, lag of the maximum correlation value and standard deviation of the pupil (SD pupil, also coding for the color in this figure). **F**. Scatter plots showing the pupil-correlation values from the whole cortex ("global cor.") and the A5 ("A5 cor.") against the pupil standard deviation, color coded based on the baseline/2-3Hz coupling. The coefficient of determination (R squared) was calculated for each pair of data: R^2(SD pupil–A5) = 0.04; R^2(SD pupil–global signal) = 0.14; R^2(A5-global signal = 0.08).

SUPPLEMENTARY METHODS:

Procedure of viral injection

Anesthesia was induced in 4 weeks old animals with 5% isoflurane in the chamber. Anesthetized animals were placed on a stereotaxic frame with ears and teeth fixed, where they breathed a mixture of air and oxygen with vaporized 1.5-2% isoflurane through a mask. An eye ointment was placed over the eyes to prevent from drying. The scalp was shaved and disinfected, a middle cut was made and the skull was exposed. The fissure Bregma was identified and the right cingulate cortex was marked at coordinates +1.2 mm AP and +0.5 mm ML (area 24b). For injections in the barrel cortex, the coordinates were -2.4 mm AP and 4.9 mm ML. A pneumatic drill was used to make a ~0.8 mm diameter craniotomy on the target coordinates. A 33G micro-syringe connected to a microinjection pump was lowered down to a depth of -1.8 mm from the brain surface for injections in the cingulate cortex or -1.2 for injections in the barrel cortex, and 600 nL of the viral vector AAV5.Syn.GCaMP6f.WPRE.SV40 were infused at a rate of 200 nL/min. After injection, the needle was left in place for 8 min to avoid leaking and then it was carefully removed. The craniotomy was covered with sterile wax, the skin was sutured, and animals were treated with painkiller and antibiotic for 3 consecutive days to prevent infection.

fMRI preparation procedures

Adult rats were anesthetized with 5% isoflurane in the chamber and orally intubated with a 14G cannula. A small animal ventilator (CW-SAR-830/AP) was used from this moment to ventilate animals at 60±1 breaths per minute with a mixture of 70% air and 30% oxygen. Surgical anesthesia was maintained at 2-2.5% isoflurane. The femoral artery and vein were cannulated with polyethylene tubing (PE-50, filled with heparin to prevent coagulation), to monitor blood pressure and to serve as intravenous infusion line, respectively. Animals were then positioned into a stereotaxic frame to proceed with the implantation of the optical fiber for calcium imaging. The scalp was shaved and disinfected. A middle cut was made to expose the skull and a ~1mm diameter blur hole was made over the coordinates +1.2 mm AP and +0.5 mm ML to target the cingulate cortex, or -2.4 mm AP and +4.9 mm ML to target the barrel cortex. A 200μm optical fiber was carefully lowered 1.9 or 1.2 mm DV for cingulate or barrel cortex respectively and fixed to the skull with cement. The implant was allowed to dry for 30-40 min. To avoid air-tissue interfaces artifacts in the fMRI images, the ear canal of anesthetized animals was filled with a fluoride paste. At the end of the surgeries, a bolus of ~80mg/kg alpha-chloralose anesthesia was infused intravenously and isoflurane was discontinued. The animal was moved to the MRI bore and the venous catheter was connected to an infusion pump that injected a mixture of alpha-chloralose (~25mg/kg/h) and the paralyzer agent pancuronium (~2mg/ks/h) for the duration of the experiment. Rectal temperature, ventilatory pressure, end-tidal CO_2, arterial blood pressure and heart rate were constantly monitored. Anesthetized animals were euthanized after the last fMRI scan following the approved protocols.

Acquisition and pre-processing of calcium signals

The GCaMP fluorescence signal was detected through optical fibers by a photomultiplier, amplified, and recorded using an analog to digital converter (Biopac -Goleta, CA-) at a sampling rate of 5000

samples per second. Matlab (Natick, MA) code was used to read and synchronize the signals with the fMRI data. Calcium signals were normalized by subtracting and dividing by mean $((F-\bar{F})/\bar{F})$ to report the level of GCaMP-mediated fluorescence signal change. In multimodal correlation analysis, all signals were detrended and normalized to 1 for comparison purposes. Spectral analysis was performed on Matlab using wavelet decomposition (2s sliding windows to map a frequency range between 0.5 and 10 Hz every second during the whole scan) and the power of the most salient frequency band (2-3 Hz) was extracted.

Acquisition and pre-processing of fMRI

All MRI images were acquired on a 14.1T / 26cm magnet (Magnex, Oxford) with an Avance III console (Bruker, Ettlingen) and a 12cm diameter gradient providing 100G/cm with 150µs rise time (Resonance Research). An elliptic trans-receiver surface coil (~2x2.7cm) was used in all experiments. Functional scans were acquired using a 3D EPI sequence providing whole-brain coverage, with the following parameters: 1s TR, 12.5ms TE, 48x48x32 matrix size, 400x400x600µm resolution. Each scan was run for 925 TRs (15 min 25 s). An anatomical RARE image was additionally acquired within each session for registration purposes with the following parameters: 4s TR, 9ms TE, 128x128 matrix size, 32 slices, 150µm in-plane resolution, 600µm slice thickness, 8x RARE factor. During analysis, anatomical scans from different animals were first registered to a template (a RARE scan from one of the animals) using 3dAllineate in AFNI, and the registration matrix was then applied to the EPI scans to align all the data to the same coordinates. Co-registered volumes were then blurred by applying a 0.8 mm FWHM Gaussian filter, normalized by mean and temporally filtered (0.005 to 0.15Hz).

Acquisition and pre-processing of pupil data

A customized MRI-compatible camera (dimensions: 25 mm x 25 mm x 15 mm + a lens of 10 mm diameter x 20 mm) with the following features was used to acquire one video during each fMRI scan: 24 bits per pixel, 240x352 pixels, 29.97 frames/s, RGB24 format. **Supplementary Figure 1A** shows the spatial configuration of all the components used for video acquisition of the pupil during the multimodal fMRI experiment. The camera was held on an adjustable rat bed made in-house, with the lens approximately 0.5 to 1 cm apart from the right eye of the animal (**Sup. Fig. 1B**). A movable infrared LED light source (peak wavelength = 850nm) was additionally positioned on the rat bed to provide a good contrast of the pupil. 925 frames (corresponding to the fMRI acquisition volumes) were read and processed using a customized Matlab script. Contrast enhancement and threshold-based image binarization were performed in all frames. Different approaches were taken in subsequent steps to detect the pupil depending on the contrast of the acquired video: 1. Images where the pupil got isolated by simple contrast-threshold binarization were subjected to automatic object decomposition using "regionprops" and the pupil was identified as the region closer to the center that was calculated in the previous frame (the first approximate center was always pre-defined manually). An additional step to ensure correct identification of the pupil following automatic segmentation involved checking that the area of the candidate region lied within a pre-defined expected range (minimum and maximum diameter pre-defined manually in the first frame of each video). 2. A second approach was used when the pupil

exhibited a good contrast only in a portion of its circumference (i.e. the whole circle could not be isolated automatically after binarization). This approach consisted of detecting intensity changes in the binary images along 3 chosen directions, starting from an approximate pre-defined center, to identify 3 points of the circle that represents the pupil. 3. Frames where none of the previous two methods succeeded to correctly identify the pupil were processed manually by defining 3 points along the pupil circumference. Once the pupil was identified as a circle on a video frame, its diameter was calculated and stored in a vector of length equal to the number of TRs. An additional step consisted of saving each one of the processed video-frames as an image file with the identified pupil overlaid on it (using "viscircles" over each original image). This step served to confirm the correct identification of the pupil. Incorrect detections observed as outliers along the diameter vector were solved by interpolation of the neighbor frames. If incorrect detection occurred in more than 2 consecutive frames, the script was run again with adjusted parameters or manual detection to recalculate the pupil diameter in the missing frames. Editable parameters included: contrast threshold for image binarization, center coordinates in the first frame, minimum and maximum expected diameter of the pupil (in pixels) and the 3 directions to build the gradient vectors that detect intensity changes in the binary image.

<u>Pupillary unrest index (PUI)</u>

Adapted from Lüdtke et al. ([37](#)), we produced a measure of the variability of the pupil size by summing up the cumulative differences between consecutive points of the smoothed pupil diameter vector (for each trial, $PUI = sum(abs(diff(smooth([Pupil\ diameter\ vector]))))$). This measure provided a way to quantify the dynamicity of the pupil during each fMRI scan (similar to the standard deviation of the pupil size).

Multimodal analysis of the data

<u>Acquisition of correlation maps</u>

The pupil diameter vector (indicative of the pupil size at each time point) and its 1st derivative (indicative of whether the pupil was suffering dilation or constriction at a given moment) were used as reference vectors to generate fMRI correlation maps. For each trial, the 2 vectors were converted to 1d files and read in AFNI by the function 3dTcor to calculate the correlation value between each 1d file and each time course in the 3D fMRI scan. This produced 2 correlation maps per trial: one pupil size - fMRI correlation map and one 1st derivative of the pupil - fMRI correlation map. One-sample t-tests were performed on the correlation maps from 71 trials of 10 different animals to report significantly correlated brain voxels with the pupil size or the 1st derivative of pupil size.

An additional step was taken to quantify the degree to which specific regions of the brain reflect pupil dynamics by averaging the correlation values of voxels within 16 ROIs. This was done using the AFNI function 3dmaskave. The selected ROIs (3 primary cortices (somatosensory, auditory and visual), 5 different association cortices (orbitofrontal, pre-limbic, cingulate, insular and restrosplenial), 5 thalamic areas (central, reticular, dorsal, ventral and lateral geniculate), septal area, superior colliculus and pontine noradrenergic group V) were chosen based on the previous literature ([1](#), [16](#), [17](#), [29](#), [63](#)) and on

the previously acquired voxel-wise correlation maps. The correlation value for each ROI was subjected to a one-sample t-test and the results were reported at 3 different significance levels (0.05, 0.01 and 0.001).

Acquisition of the pupil-governed brain state vector

Following a modified strategy from Chang et al. ([1]), a vector containing the momentary spatial correlation between each TR acquisition volume and the averaged 1st derivative-pupil correlation map (template) was computed from each fMRI scan using 3ddot in AFNI. In Chang et al., this vector is believed to extract the time-varying level of arousal from an fMRI scan. Due to our experimental conditions (anesthetized animals), this vector is simply called throughout the text "fMRI spatial correlation with template", also referred as the "pupil-governed brain state vector" or the "fMRI arousal time-course". A video showing the relationship between this time course and the multimodal fMRI data for one representative trial is provided as **Sup. Video. 1**.

Cross correlation analysis.

Cross correlation analysis was performed between the measures from different modalities using the xcorr function in Matlab with a maximum lag of ±30s. Results of the cross-correlation analysis are reported as averaged correlation ± standard deviation.
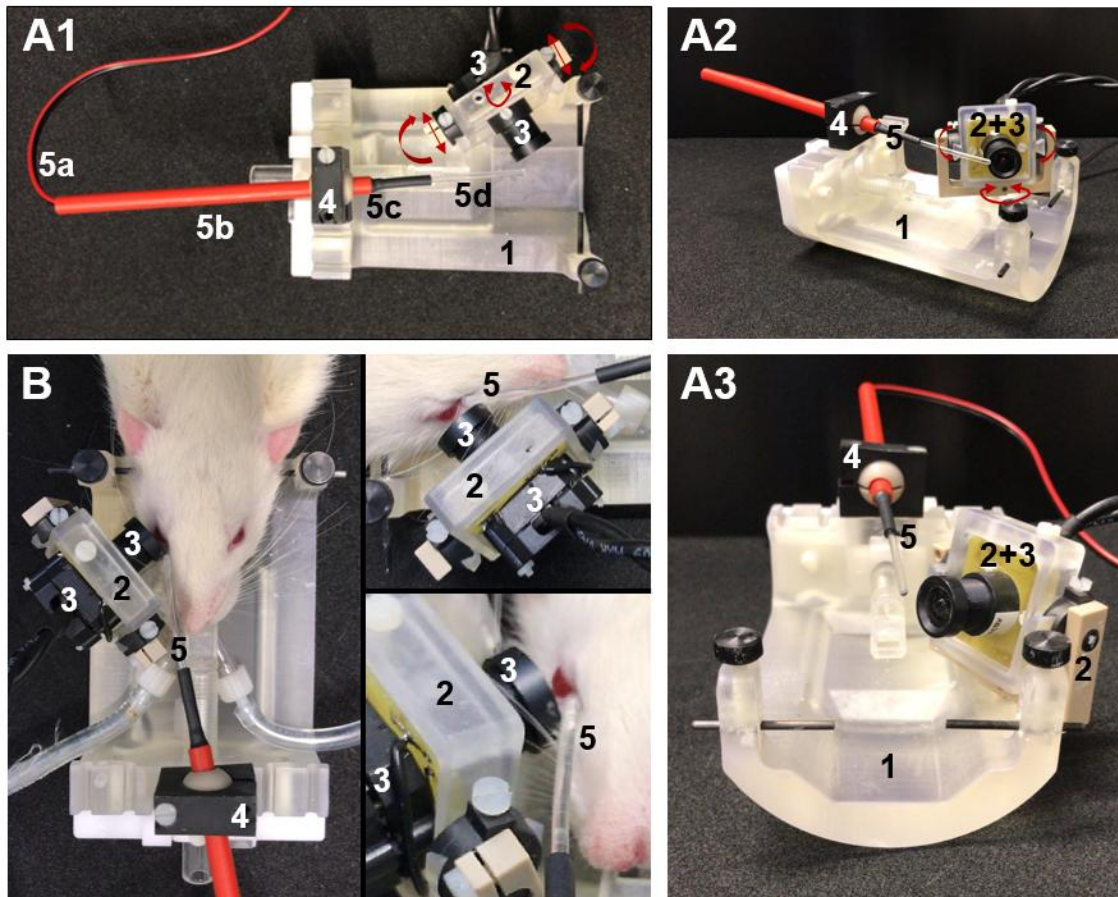
Supplementary Figure 1. Adapted MRI rat bed for pupillometry measurements. A1, A2, A3. Images show three different views of the camera holder (**2**), camera (**3**), light source holder (**4**) and light source (**5**) assembled into the MRI rat bed (**1**; the basic MRI rat bed contains two ear bars and one teeth bar). The light source consists of a power-supplied LED (**5a**-**5c**) and a polycarbonate tube used as a light guide, attached to it (**5d**). In the pictures, the LED is hidden at the end of the red tube (**5b**-**5c**; the black part is a shrinking tube surrounding the LED and building the connection with the extension light guide). **5a** is the cable that extends from outside the MRI room to supply power to the LED and **5b** is a rigid plastic cover to better control the positioning of the LED. The light guide is attached to the LED to conduct the infrared light towards the eye of the animal (the LED would cause artifacts in the MRI image if positioned near the head). The camera holder (**2**) allows to rotate the camera around a vertical and a horizontal axis and to slide it front or backward. The light source holder (**4**) allows to control the position of the light source through a modified ball-and-socket joint that enables rotation and sliding front or backward. **B.** Images show how the camera and light source are positioned to perform pupillometry in a living rat. The position of the light source needs to be finely adjusted to acquire good contrast of the pupil within the eye.
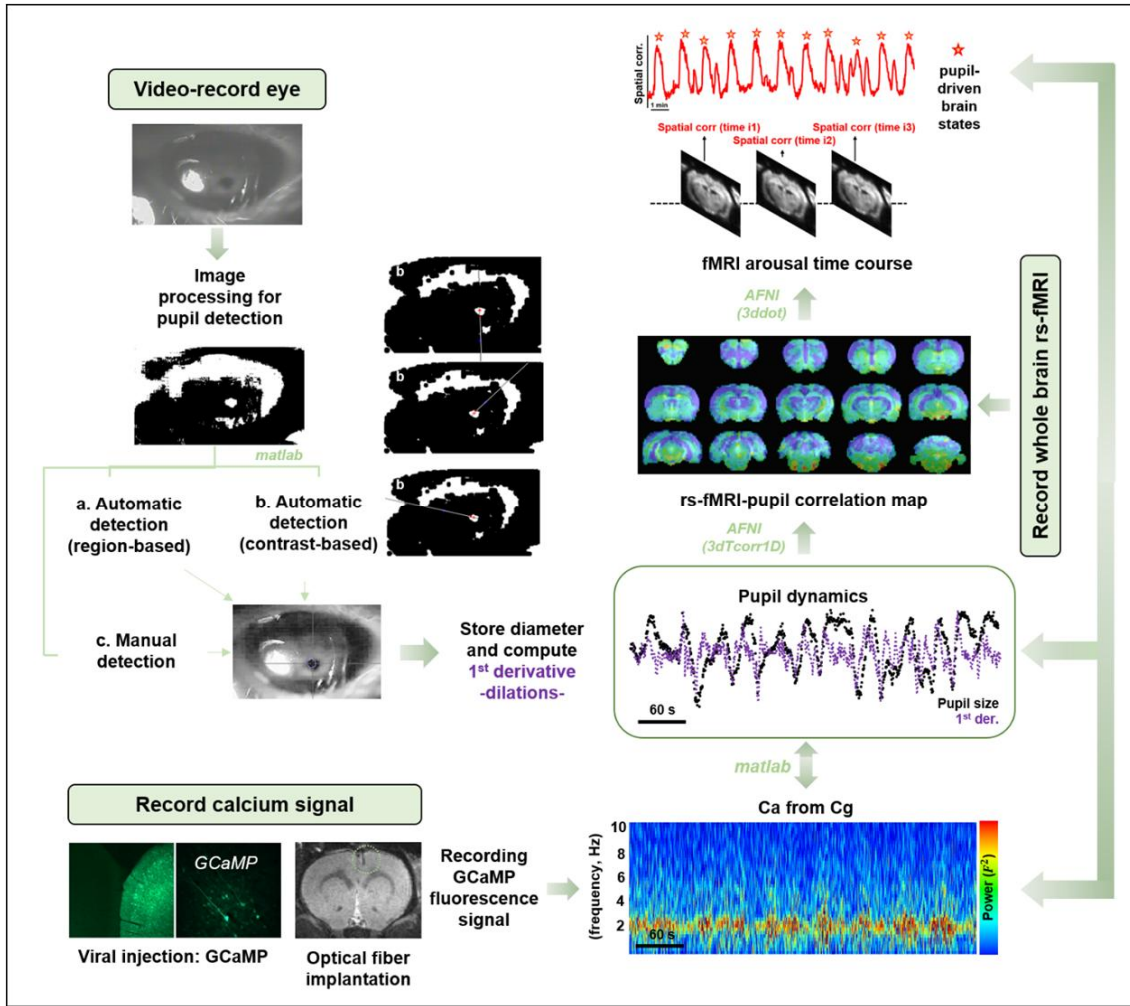
Supplementary Figure 2. Schematic showing the main steps carried out during the analysis of the multimodal pupil-calcium-fMRI data. Eye videos were processed using Matlab to extract the diameter of the pupil at each scan time point (see Methods). AFNI was used to compute the fMRI correlation maps with the vector of the pupil size or the 1st derivative of the pupil size (i.e. pupil dilations). The map resulting from the correlation between the fMRI signals and the 1st derivative vector was considered as template. A new vector was generated from the spatial correlation values between each acquisition volume and the template. Matlab was used for all cross-correlation analysis with the calcium signals.
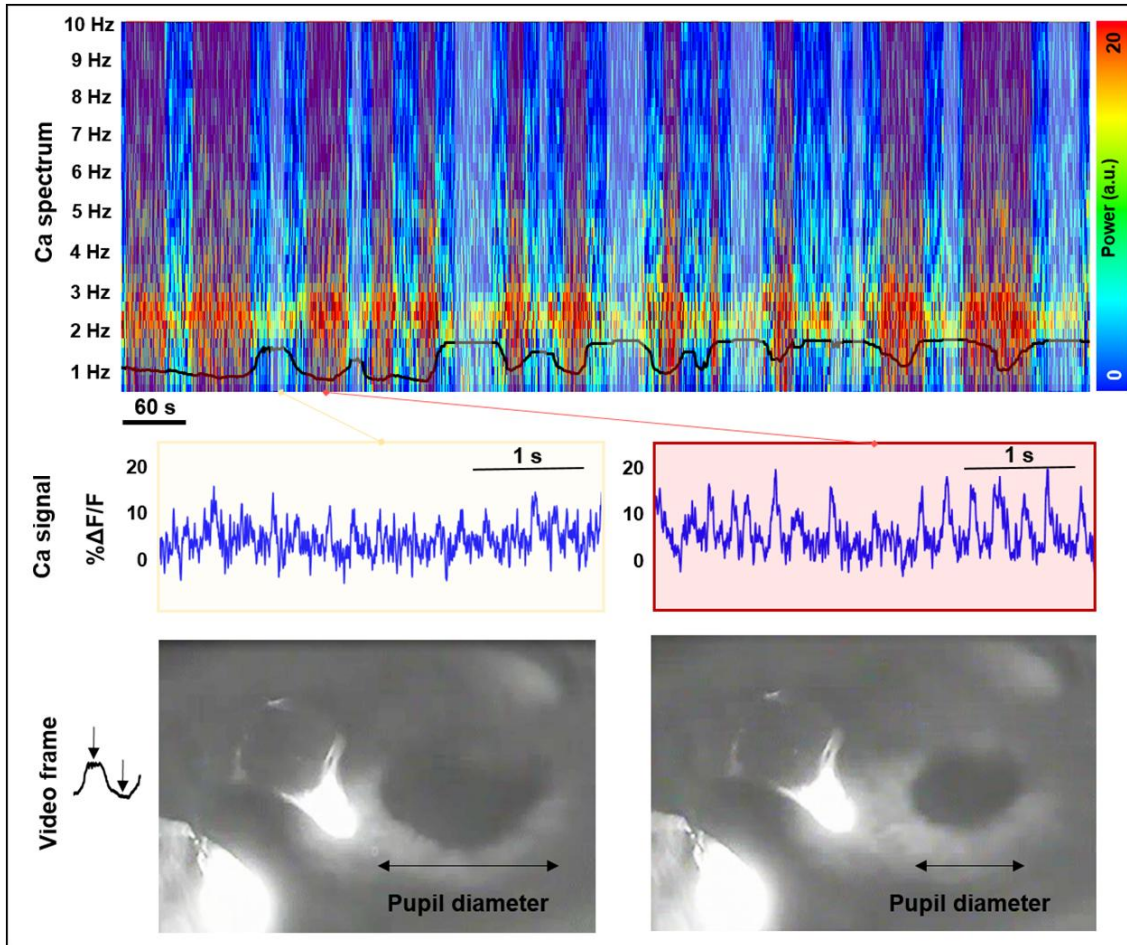
Supplementary Figure 3. Relationship between pupil size and calcium dynamics in a representative animal. The figure shows the different states encountered during a 15 minutes trial, characterized by higher or lower amplitude of the calcium signals and subsequent changes in the pupil size.
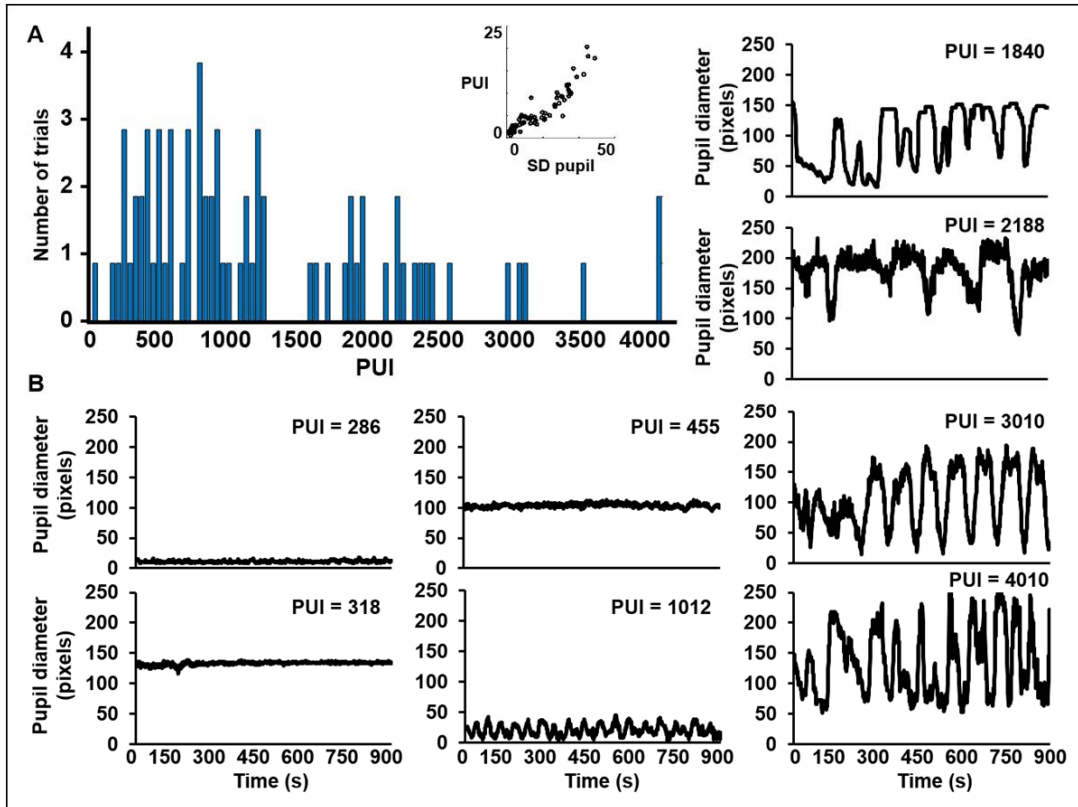
Supplementary Figure 4. Variability of the pupil dynamics across trials. A. Histogram of the pupillary unrest index (PUI) of all trials acquired throughout the study. The inset shows the relationship between the PUI and the standard deviation of the pupil size. Different points represent different trials. **B.** Pupil diameter vectors of different trials and their corresponding PUI.
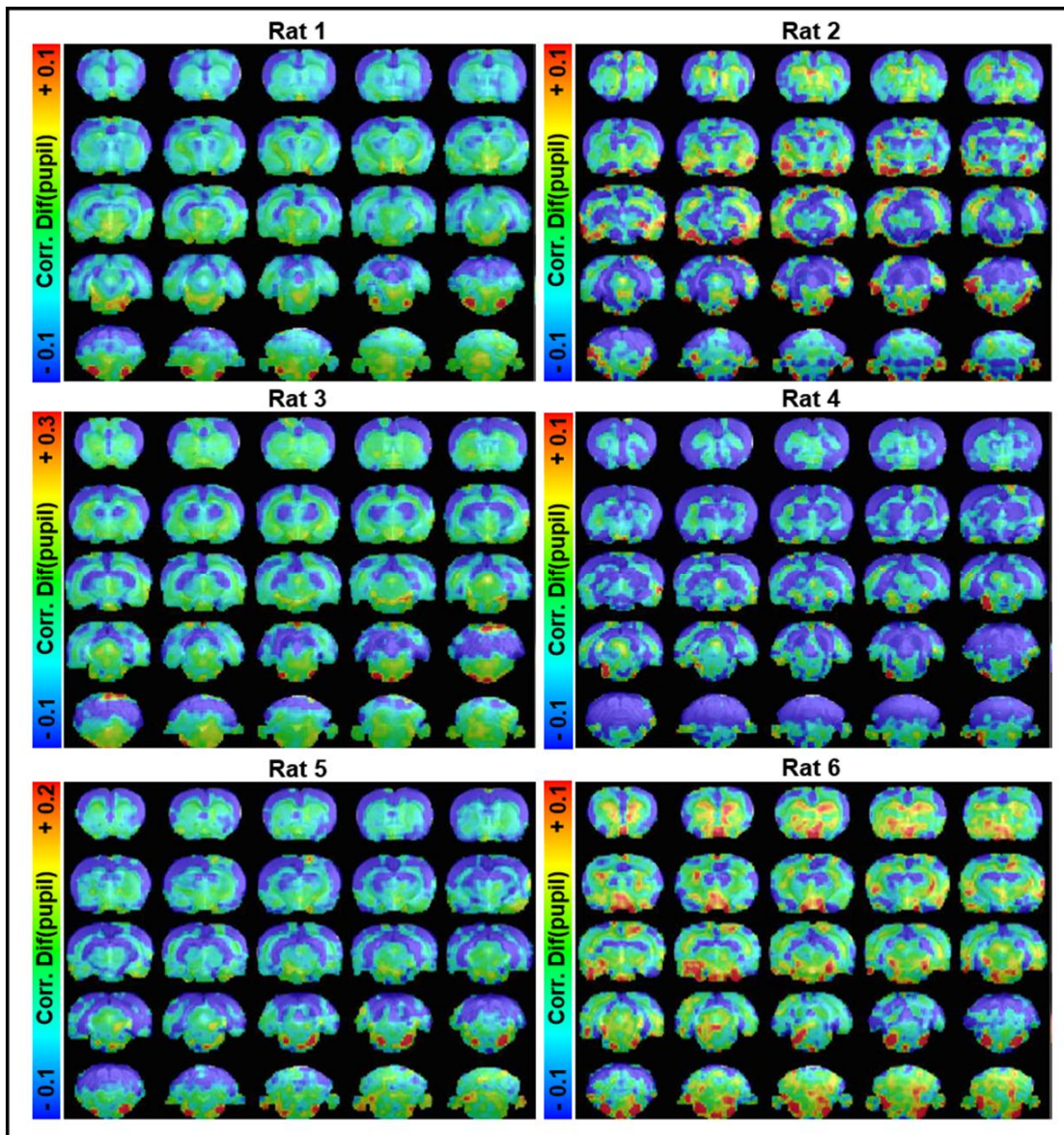
Supplementary Figure 5. Pupil dynamics-fMRI correlation maps from 6 different animals. The color on each voxel represents the correlation coefficient between the fMRI time course and the time-varying 1st derivative of the pupil size. Note the robustness of the negative correlation, especially on cortical regions, and the positive correlation on the A5 group in the brainstem. The statistic map can be found on **Figure 3B** of this manuscript.

SUPPLEMENTARY VIDEO 1:

https://www.dropbox.com/s/bns0f5m3d8s69y1/supVideo_multimodal_bigP.mp4?dl=0

frontiers
in Neuroscience

Identifying Respiration-Related Aliasing Artifacts in the Rodent Resting-State fMRI

Patricia Pais-Roldán[1,2], Bharat Biswal[3], Klaus Scheffler[1,4] and Xin Yu[1,5]*

[1] High-Field Magnetic Resonance Department, Max Planck Institute for Biological Cybernetics, Tuebingen, Germany,
[2] Graduate Training Centre of Neuroscience, International Max Planck Research School, University of Tuebingen, Tuebingen, Germany, [3] Department of Biomedical Engineering, New Jersey Institute of Technology, Newark, NJ, United States,
[4] Department for Biomedical Magnetic Resonance, University of Tuebingen, Tuebingen, Germany, [5] Athinoula A. Martinos Center for Biomedical Imaging, Massachusetts General Hospital and Harvard Medical School, Charlestown, MA, United States

Resting-state functional magnetic resonance imaging (rs-fMRI) combined with optogenetics and electrophysiological/calcium recordings in animal models is becoming a popular platform to investigate brain dynamics under specific neurological states. Physiological noise originating from the cardiac and respiration signal is the dominant interference in human rs-fMRI and extensive efforts have been made to reduce these artifacts from the human data. In animal fMRI studies, physiological noise sources including the respiratory and cardiorespiratory artifacts to the rs-fMRI signal fluctuation have typically been less investigated. In this article, we demonstrate evidence of aliasing effects into the low-frequency rs-fMRI signal fluctuation mainly due to respiration-induced B0 offsets in anesthetized rats. This aliased signal was examined by systematically altering the fMRI sampling rate, i.e., the time of repetition (TR), in free-breathing conditions and by adjusting the rate of ventilation. Anesthetized rats under ventilation showed a significantly narrower frequency bandwidth of the aliasing effect than free-breathing animals. It was found that the aliasing effect could be further reduced in ventilated animals with a muscle relaxant. This work elucidates the respiration-related aliasing effects on the rs-fMRI signal fluctuation from anesthetized rats, indicating non-negligible physiological noise needed to be taken care of in both awake and anesthetized animal rs-fMRI studies.

Keywords: rat fMRI, physiological noise, EPI, ventilation rate, repetition time, resting state networks

INTRODUCTION

Low-frequency (< 0.1 Hz) fMRI signal fluctuation (LFF) related to spontaneous brain dynamic signaling has been observed using a number of different brain imaging modalities (Biswal et al., 1995; Obrig et al., 2000). Applying a series of data analysis including correlation, coherence and independent component analysis of LFF during resting state scans has revealed distinct "resting-state" networks (RSN) that represent potential functional connectivity across regions in the brain (De Luca et al., 2005; Fox et al., 2009). The "default mode" network (DMN) is one of the RSNs that has been reliably identified from resting-state fMRI (rs-fMRI) in the human brain (Raichle et al., 2001; Greicius et al., 2003). Similar DMN spatial correlation patterns have been detected in both anesthetized monkeys and rodents, using fMRI (Vincent et al., 2007; Mantini et al., 2011;

Lu et al., 2012; Cabral et al., 2014; Stafford et al., 2014; Paasonen et al., 2018). This has allowed translational studies to specify the potential neuronal basis/underpins of the RSNs detected by fMRI in animal models. Animal fMRI has played a critical role in mapping the brain dynamics across multiple scales (Logothetis, 2002; Airaksinen et al., 2010; Hyder and Rothman, 2010; Mishra et al., 2011; Pan et al., 2011; Schulz et al., 2012; Yu et al., 2016; Yu, 2017; Albers et al., 2018; Wang et al., 2018). Multi-modal animal fMRI platform has been developed by merging fMRI with optogenetics (Lee et al., 2010; Liang et al., 2015; Yu et al., 2016; Albers et al., 2018), for cell/circuit specific activation, and with concurrent electrophysiological recordings (Goense and Logothetis, 2008; Shmuel and Leopold, 2008; Scholvinck et al., 2010; Pan et al., 2013). Also, fMRI brain mapping has been performed with parallel fiber optic measurements of the brain dynamic signals through genetically encoded sensors (e.g., detection of calcium with GCaMP or even of glutamate with GluSnRf) for identification of the LFF neural correlates (Schulz et al., 2012; Xie et al., 2016; Schwalm et al., 2017; Albers et al., 2018; He et al., 2018; Jiang et al., 2018; Wang et al., 2018). Thus, the multi-modal animal fMRI offers the possibility of studying the multi-site neural components underlying the RSNs.

Extensive efforts have been made to elucidate the confounding issues of LFF in the human brain, especially in the correction of motion artifacts from varied sources (Biswal et al., 1996; Welvaert and Rosseel, 2012; Murphy et al., 2013; Chen et al., 2015a; Jorge et al., 2015; Bright and Murphy, 2017). Besides the head motion-caused artifacts (Yang et al., 2005), the cardiorespiratory (CR) interference, e.g., the respiration-induced B0 field offset and cardiac pulsation etc., are the most dominant physiological noise source to a broad frequency range of the fMRI signal fluctuation (Hu et al., 1995; Noll et al., 1998; Van de Moortele et al., 2002; Razavi et al., 2008; Birn et al., 2008a; Starck et al., 2010; Birn, 2012; Murphy et al., 2013; Cordes et al., 2014). The CR-relevant parameters including arteriole CO2 (Wise et al., 2004), respiratory volume per time (RVT) (Birn et al., 2006, 2008b), and heart rate variability (HRV) (Shmueli et al., 2007), oscillate at frequencies < 0.1 Hz and directly interfere with the rs-fMRI signal correlation features. In addition, the slow sampling rate of fMRI could alias the high-frequency oscillation of the cardiac signal, and even the respiration artifacts at TR > 2 s, which can contaminate the low frequency range in human rs-fMRI studies (Biswal et al., 1996; Lowe et al., 1998; Noll et al., 1998; Dagli et al., 1999; Frank et al., 2001; De Luca et al., 2006). To solve the aliasing problem, high sampling rate imaging schemes or fMRI with specific TRs are needed to avoid the aliased oscillatory signals in the < 0.1 Hz low frequency range (Frank et al., 2001; De Luca et al., 2006; Posse et al., 2013; Cordes et al., 2014; Tong et al., 2014; Reynaud et al., 2017). Advanced imaging schemes and signal denoising methods have been developed to reduce these artifacts in human rs-fMRI studies (Biswal et al., 1996; Kiviniemi et al., 2003, 2005; Feinberg et al., 2010; Murphy et al., 2013; Feinberg and Setsompop, 2013; Liu, 2016; Abreu et al., 2017; Bright and Murphy, 2017; Caballero-Gaudes and Reynolds, 2017).

The CR-relevant confounding issues have been less concerned in animal rs-fMRI studies, especially in anesthetized animals with head-fixation to remove a large portion of the motion-relevant artifacts that are usually observed in awake human subjects (Kannurpatti et al., 2008; Zhao et al., 2008; Biswal and Kannurpatti, 2009; Pawela et al., 2010; Williams et al., 2010; Majeed et al., 2011). The respiratory rates of animals at different anesthesia vary largely, which can alter the respiration-related neck/chest motion patterns across different cases (Zhao et al., 2008; Williams et al., 2010; Bukhari et al., 2017). In many rs-fMRI studies using 2D-EPI sequences with different TRs (0.1 s -single slice- to 2 s), the CR-relevant aliasing effect was either reported negligible, or could be filtered out from the < 0.1 Hz LFF (Zhao et al., 2008; Biswal and Kannurpatti, 2009; Williams et al., 2010). Under the same anesthesia (e.g., medetomidine), the respiration-relevant motion artifacts have been reported to have different spatial patterns by different studies, either located only at the brain edge voxels using 300 ms TR (Magnuson et al., 2015), or to spread through the whole brain structure with severe aliasing interference at 3 s TR (Kalthoff et al., 2011). To better interpret the RSNs in animal rs-fMRI studies, the potential aliasing effect needs to be characterized carefully to avoid confounding the < 0.1 Hz LFF (Kalthoff et al., 2011). This is particularly critical for multi-modal fMRI studies that adopt 3D-EPI sequences to achieve even higher spatiotemporal resolution, so that more refined functional patterns from smaller brain nuclei can be matched with other imaging modalities in multi-scales (e.g., Wang et al., 2018) or even in awake animal fMRI studies (Ferenczi et al., 2016). Thus, for the implementation of a multi-modal fMRI methodology, a quality control to prevent or correct the physiological-related noise in the animal rs-fMRI signal is crucial to reliably investigate the neural basis of the RSNs detected in the animal brain.

In this study, we focused on deciphering the confounding rs-fMRI signal oscillation due to the respiration-related artifacts in anesthetized rats freely breathing or under ventilation with or without a muscle relaxant. By systematically varying the TR and the ventilation rates during the rs-fMRI acquisition, we characterized the aliasing effects, showing altered interference at different conditions. In addition, the frequency-specific power map demonstrated the voxel-specific sensitivity to the respiration-related motion artifacts with unique spatiotemporal dynamic interference. Because the ventilation mechanism enforces sinusoidal signals at very specific frequencies, it helps narrow the broad respiratory bandwidth of the free-breathing conditions, providing an efficient solution to avoid the overlap of the aliased oscillation to the < 0.1 Hz fMRI signal fluctuation. Furthermore, the muscle relaxant can significantly reduce the respiratory-induced B0 distortion and its corresponding aliasing artifacts to the LFF. In summary, this work provides a detailed view on aliasing effects of the rs-fMRI signal fluctuation from anesthetized rats, indicating a crucial CR interference issue needed to be taken care of in both awake and anesthetized animal rs-fMRI studies.

MATERIALS AND METHODS

Simulations of the Physiological Noise Sampling at Different TR for fMRI

In order to simulate the aliasing effect of the respiratory motion in the fMRI signal acquired at a certain TR, a cosine wave oscillating at frequencies near the common rat ventilatory rate was created using Matlab (Mathworks, Natick, MA, United States). The generated signal was then down-sampled at frequencies equivalent to potential volume acquisition times (TR). The resulting waves were plotted to illustrate the effect of sampling an intruder ventilatory-driven signal at a certain TR.

Mathematical Explanation of the Observed Aliasing Effects

The function $f(TR)$ calculates the frequency $freqS$ of a signal S that results from sampling an original signal $S0$ at a given TR.

$$f(TR) = abs(freqS0 - k^* \frac{1}{TR}) = freqS$$

with $k = 1,2,3 \ldots$.

Supplementary Figure S1B shows an example of how a signal (e.g., motion from breathing at 60.1 breaths per minute) can be aliased by using typical TRs (i.e., TR > 0.5 s). When using a sampling frequency equal to the peak frequency S0, the resampled signal (S) is flat (frequency = 0) (see Supplementary Figure S1A middle inferior panel). In the practice, complete cancelation of the signal is often not possible, when dealing with analog devices, but by getting very close to the peak frequency, an extremely slow aliased signal can remain, which would lie out of the rs-fMRI analysis ($freqS <<< 0.01$ Hz, Supplementary Figure S1B). By knowing the specific rate at which the animals breathe (e.g., by imposing a respiration rate with ventilatory support) it is possible to choose an appropriate TR that minimizes the interference of the aliased signal with the spectrum of interest (e.g., 0.01–0.1 Hz).

Animal Subjects, Procedures, and Experimental Design

In order to test whether aliasing occurs in the fMRI signal upon spontaneous breathing, nine adult (300–400 g) male Sprague Dawley rats were included in the study and their fMRI signal was assessed under anesthesia at three different conditions: (1) spontaneous breathing through a mask; (2) ventilated, not paralyzed; and (3) ventilated and paralyzed. All animal procedures were approved by the Animal Protection Committee of Tübingen (Regierungspräsidium Tübingen).

All animals were initially anesthetized with 5% isoflurane in chamber. In order to track changes in the blood pressure, the femoral artery was catheterized and connected to a blood pressure transducer (Biopac, Goleta, CA, United States). As in further steps the effect of a muscle relaxant was to be assessed, the femoral vein was also catheterized and connected to an infusion pump. The inner ear cavity was filled with paste to avoid air-tissue interfaces near the brain. A closed-loop heating system was used to keep the rectal temperature at 37°C during the entire

experiment, ensuring stable physiological conditions. The end-tidal CO2 was also controlled throughout the experiment using a Respironics-Novametric monitor. A chest transducer was placed under the chest of the animal and constantly used to monitor breathing through a Biopac acquisition system, at 5000 samples per second.

During acquisition of the fMRI, 6 animals were kept anesthetized with 1.5–2% isoflurane, 1 animal was anesthetized with alpha-chloralose (25 mg/Kg·h), 1 with urethane (1 dose of 1–2 g/Kg) and 1 with medetomidine (0.05–0.5 mg/Kg·h), to rule out the contribution of a specific anesthetic to the observed effects. First, the not-yet-intubated animals were transferred to the 12 cm horizontal bore of a 14T MRI scanner and breathed oxygen-enhanced air (~30% oxygen) through a mask. In the second part of the study, animals were intubated and maintained at a constant ventilatory rate that could be varied between scans. A last study was carried out in animals anesthetized with isoflurane with concurrent intravenous infusion (~1–2 mg/Kg·h) of the muscle paralyzer agent Pancuronium (typical fMRI setup). All animals were euthanized right after the fMRI study based on the termination procedure from the approved protocols.

fMRI Acquisition

To detect the BOLD signal in the anesthetized animals, 2D and 3D Echo Planar Imaging (EPI) sequences were used, covering a field of view (FOV) of 2.24 cm × 1.92 cm × 1.92 cm with a matrix size of 56 × 48 × 32, achieving a resolution of 400 µm × 400 µm × 600 µm (all the data shown in the main figures correspond to 3D EPI, unless stated otherwise - Supplementary Figure S7 is an example of a 2D EPI-). In order to determine whether different TRs modified the frequency of the aliased signal, the TR was varied between scans (TE was kept at 9.75 ms). A phantom containing Phosphate Buffered Saline (PBS) was located over the animal's head to compare the signal detected inside the brain with a signal experiencing similar motion in an inert tissue. A surface coil of diameter 2.2 cm was used to transmit and receive the RF signals. For anatomical registration purposes, RARE images were also acquired using a TR of 4000 ms, TE of 9.025 ms, FOV of 2.24 × 1.92 × 1.92 and matrix size of 128x128x32 (resolution of 175 µm × 150 µm × 600 µm). Table 1 summarizes the conditions and fMRI parameters used in our study.

Analysis of the Data

The purpose of the analysis was to determine the influence of the respiration in the fMRI time course. Therefore, both signals (i.e., the chest–derived motion trace and the fMRI time-course), were considered for analysis.

Assessment of the Spatial Distribution of the Interference

The amplitude of the fluctuations in the BOLD signal was considered as an indicator of the level of contamination in the data. In order to detect the brain areas most vulnerable to the respiration-related interference, a power map was created in AFNI (Cox, 1996), by calculating the BOLD signal change at

TABLE 1 | Experimental conditions.

TR (s)	No V	V-54	V-56	V-58	V-59	V-60	V-61	V-62	V-64	V-66
0.5	wo P					w & o P				
0.8	wo P					w & o P				
0.9	wo P					w & o P				
1	wo P	wo P	wo P	wo P	wo P	w & o P	w & o P	w & o P	w & o P	w & o P
1.1	wo P					w & o P				
1.2	wo P					w & o P				
1.5	wo P					w & o P				
2	wo P					w & o P				

The table summarizes the parameters used in our study in terms of ventilatory frequency (in beats per minute), TR, and the use of a muscle relaxant (Pancuronium). No V, not ventilated (using mask); V-N, Ventilated (at the rate N, in breaths per minute); P, Pancuronium (wo: without, w & o, with and without).

each voxel. The function 3dPeriodogram was used to obtain 1024 frequency components and their corresponding power in each functional scan. 3dTstat was used to average the power of the frequencies in the range of 0.005 to 0.4 Hz in each voxel, resulting in a color-coded power map. In order to compare different animals and to average maps together, all scans were registered to a template using 3dAllineate. First, the anatomical datasets were aligned, and later the registration matrix was applied to the functional scans.

Comparative Analysis Between Chest Motion and fMRI Signal

In order to compare the respiratory-driven chest motion and the fMRI time-course, both signals were plotted in temporal and frequency domains. fMRI time courses were extracted by manually drawing a mask of 4 voxels from inside the brain and from a phantom placed over the animal's head. The AFNI function 3dMaskave was used to compute the average of the 4 voxels and output a 1D file. To extract single voxel time courses, the AFNI function 3dmaskdump was implemented. The time courses were then read in matlab using dlmread. In order to create a signal that simulates the chest motion detected from the fMRI, chest movement traces were down-sampled to 1/TR for each fMRI acquisition and included in the analysis. The fast Fourier transform (fft) function of matlab was used to calculate the power spectral density (PSD) from the original chest movement trace, from the down-sampled chest trace, and from the fMRI time courses. The full width at half maximum (FWHF) of the peak aliased frequency was calculated on the enveloped chest and fMRI spectra using matlab, to assess their similarity in terms of bandwidth and differentiate between mask and ventilation conditions. A two-tailed not-paired t-test was performed to assess the differences between groups. Errors in figures represent standard error of the mean.

Analysis of the Variance

To quantify the degree of variability that is incorporated to a group of scans solely based on the aliasing effect (i.e., variability of the fMRI signal upon using different ventilatory rates or TRs), spectral signal similarity was evaluated for each pair of conditions (e.g., time course acquired at TR = 1 vs. TR = 1.2 s, or time course acquired from the animal ventilated at 60 bpm

vs. 61 bpm) by using the corr2 function in matlab applied to the PSDs. Correlation matrices were built to visualize the effect across all different conditions. Signal amplitude (i.e., BOLD signal change) was calculated as the standard deviation within the time course. A two-tailed not-paired t-test was performed to assess the difference in averaged signal amplitude (indicative of signal contamination) between fMRI time courses from spontaneously breathing animals vs. paralyzed animals. Errors in figures represent standard error of the mean.

Power Spectrum Characterization

In order to have a measure of the spectral specificity of the respiration-induced interference at different conditions (i.e., how wide the contaminated frequency range is or how much it spreads from a center frequency in an animal breathing through mask or mechanically ventilated), a map showing the fractional amplitude of low frequency fluctuations (fALFF) at specific frequency bands was generated using the function 3dRSFC (Zou et al., 2008), to cover a bandwidth of 0.01 Hz at the peak aliased frequency and the immediate lower and higher spectral components. To further verify the effect of ventilating the animals on the width of the frequency range subjected to respiratory-driven interference, the matlab function bandpower was used to calculate the average power within a 0.01 Hz bandwidth centered at the peak aliased frequency or the immediate superior and inferior neighbors. A two-tailed paired t-test was performed to assess the difference in power between the peak and the neighbor frequencies. Errors in figures represent standard error of the mean.

Table 2 provides the p-values obtained from the different t-tests performed during analysis.

RESULTS

Identification of the Aliased Respiration-Driven Artifact in Anesthetized Rats

A 3D EPI-fMRI method was used to study the potential interference between the animal respiration and the rs-fMRI signal in anesthetized rats. **Figure 1** illustrates the potential disruption of B0 field homogeneity due to the respiration-induced movement of the chest/neck, which results in distorted

TABLE 2 | *p*-values.

Figure 2E	Mask chest	Mask brain	Vent,noP chest	Vent,no P brain	
Mask chest		0.70	2.52*10^−8		
Mask brain	0.70			7.00*10^−6	
Vent, noP chest	2.52*10^−8			0.015	
Vent, no P brain		7.00*10^−6	0.015		

Figure 2F	Mask-peak	Mask-neigh	Vent,noP-peak	Vent,noP-neigh	Vent,P-peak	Vent,P-neigh
Mask- Peak		2.5*10^−2	0.90		4.02*10^−12	
Mask- neigh	2.5*10^−2			9.68*10^−11		2.83*10^−14
Vent,noP-peak	0.90			8.91*10^−4	2.97*10^−4	
Vent,noP-neigh		9.68*10^−11	8.91*10^−4			1.10*10^−3
Vent,P-peak	4.02*10^−12		2.97*10^−4			4.40*10^−4
Vent,P-neigh		2.83*10^−14		1.10*10^−3	4.40*10^−4	

Figure 5D	noP	P
noP		1.13*10^−5
P	1.13*10^−5	

The table summarizes the p-values obtained from the t-tests performed during analysis, organized by figures.

EPI images with characteristic periodic patterns in ventilated rats without muscle relaxant. It is worth noting that the periodic motion artifacts can be detected in animals under different anesthesia (e.g., medetomidine, urethane, isoflurane, and alpha-chloralose) (**Supplementary Figure S2**). Since muscle relaxants avoid the movement of the chest/neck, they reduce the respiration-induced B0 offset during fMRI acquisition, therefore, 3D EPI images show little distortion in paralyzed rats under ventilation (**Figure 1C**).

To specify the aliasing effect that occurs when the respiratory cycle is sampled at a given TR (see simulated data in **Supplementary Figure S1**), the respiratory signal (i.e., the chest movement) was recorded simultaneously with the rs-fMRI signal in anesthetized rats under three conditions: (1) not-ventilated, spontaneously breathing through mask, (2) ventilated, without muscle relaxant (i.e., not paralyzed), and (3) ventilated, with muscle relaxant (i.e., paralyzed). In **Figure 2**, the TR of the 3D EPI-fMRI was 1.2 s, i.e., 0.83 Hz. As shown in the PSD of the respiratory signal, the freely breathing rat (i.e., not ventilated -breathing through mask-) exhibits a broad frequency peak centered at ~1 Hz ("chest", **Figure 2A**). The FWHM of this broad peak in non-ventilated rats is ~0.06 Hz ± 0.004 Hz (**Figure 2E**). The aliasing effect of this respiratory signal at a sampling rate of 0.83 Hz causes a slow oscillatory signal at the 0.17 Hz ± 0.03 Hz, which is observed in both, brain voxels and phantom voxels positioned at the top of the rat head (**Figure 2A**). A strong correlation between the peak frequency observed from the aliased (i.e., down-sampled) chest motion and the fMRI time course of both, brain and phantom voxels, suggests that the artifacts originate from the respiratory-induced B0 offset and not from brain functional dynamic signals. Similarly, the fMRI signal from rats ventilated at 1 Hz shows clear aliasing effect at 0.17 Hz, but the bandwidth of the aliased signal, assessed as the FWHM of the aliased peak, is much sharper than the observed in not-ventilated animals

(**Figure 2E**, *p*-value = $7*10^{-6}$), in both brain and phantom voxels (**Figure 2B**). The aliased signal is significantly reduced in paralyzed ventilated rats (**Figures 2C,F**).

Prevalence and Characteristics of the Aliased Signal Across Different Ventilatory Conditions

To specify the spatial distribution of the respiration-related motion artifacts on the 3D EPI images, the mean voxel-wise power map (0.005–0.4 Hz) was calculated for each group (**Figure 2D**), showing that dorsal cortical areas and ventral brain regions are more sensitive to the motion artifacts. However, no generalized spatial patterns of motion artifacts can be achieved; instead, the respiratory-related motion and, hence, the interferential signal, varies across animals (**Supplementary Figure S3**). The significantly lower power estimate at the peak frequency in the paralyzed group (*p*-value = $2.9*10^{-4}$, compared to the non-paralyzed ventilated condition) suggests a reduced aliasing effect in animals without spontaneous breathing (**Figure 2D**, bottom map, and **Figure 2F**). **Figure 2F** and **Supplementary Figure S4** demonstrate the differences in power between the aliased center frequency and the collateral frequency bands at three conditions (mask, ventilated and ventilated paralyzed). **Figure 2F** shows the averaged power within a bandwidth of 0.01 Hz calculated at the peak and the neighbor frequencies across different animals, showing a significantly sharper effect (i.e., less contribution of the neighbor frequencies) in ventilated animals, compared to freely breathing rats (*p*-value = $9.68*10^{-11}$). **Supplementary Figure S4** provides the fALFF maps specific for the peak and neighbor frequency bands in a representative animal. The power estimates in the adjacent frequency bands are much lower when the animal is ventilated, in comparison to the free-breathing condition. This indicates that ventilation can prevent the spread of respiratory-motion aliasing

FIGURE 1 | Effect of the spontaneous respiration on the B0 field. **(A,B)** The schemes illustrate the B0 field at the iso-center of the MR bore in the presence of a paralyzed **(A)** or a non-paralyzed animal **(B)**. Note how the B0 is relatively homogeneous when a paralyzed animal is passively ventilated due to the lack of large body motion and how B0 inhomogeneities emerge upon active breathing involving diaphragm, intercostal and neck muscle movement during the respiration **(B)**. **(C,D)** Coronal sections from a 3D EPI sequence acquired at 1.2 s TR, showing the effect of the B0 (in)homogeneity in a paralyzed **(C)** and spontaneously breathing animal **(D)**. Note the distortions in the images acquired from the non-paralyzed animal, compared to the paralyzed condition.

effects along a broader frequency bandwidth (**Figures 2E,F** and **Supplementary Figure S4**). This is particularly important when the conventional TR at 1s is used, which causes the aliasing oscillatory effect at < 0.1 Hz to directly interfere with the low-frequency rs-fMRI signal fluctuation (**Supplementary Figure S5**). This result demonstrates that ventilation can be used to confine the aliasing oscillatory effect to a sharp frequency range.

Characterization of the Spatial and Temporal Patterns of the Respiration-Driven Aliasing Effects on rs-fMRI: Influence of the TR and the Ventilatory Rate

The features of the aliased oscillation were evaluated in non-paralyzed animals at multiple voxels across different parts of the brain and a phantom located over the animal's head. Different voxels exhibited different signal interference, in both, mask-breathing and non-paralyzed ventilated animals (**Figures 3B,C, 4A,B**), which demonstrates a highly varied effect of the respiration on the rat fMRI signal. In order to reduce the potential interference of the aliased respiration on the LFF (< 0.1 Hz), different TRs were used (0.5 s to 2 s), demonstrating that the aliasing oscillation can be shifted along the spectrum in non-ventilated animals (e.g., to be out of the < 0.1 Hz low-frequency

range) (**Figure 3D** and **Supplementary Figures S1B**, **S5**). Similarly, to avoid the interference to the < 0.1 Hz rs-fMRI signal fluctuation, the ventilation rate could be altered in mechanically ventilated animals with fixed TR (1 s, **Figure 4C** and **Supplementary Figure S1A**), as an alternative strategy for anesthetized animal rs-fMRI studies without employing muscle relaxant agents.

Examination of the Variability and Magnitude of the Aliasing Effect on the rs-fMRI in Ventilated Rats: Influence of Muscle Relaxants

The fMRI signal is an indirect measure of neuronal activation and therefore, any variability introduced by external sources is undesired and should be minimized. In order to assess the degree of variability between data acquired under different ventilatory rates or different TRs (i.e., different aliasing effects), and to determine whether the use of a paralyzer agent could reduce the differences across scans, fMRI time courses were acquired at different sampling and ventilatory conditions with and without the muscle relaxant Pancuronium (**Figure 5**). In ventilated rats anesthetized with constant 2% isoflurane and without muscle relaxant, the fMRI time courses acquired at different TRs exhibited a large between-scan spectral variability, compared to groups of scans performed during infusion of the
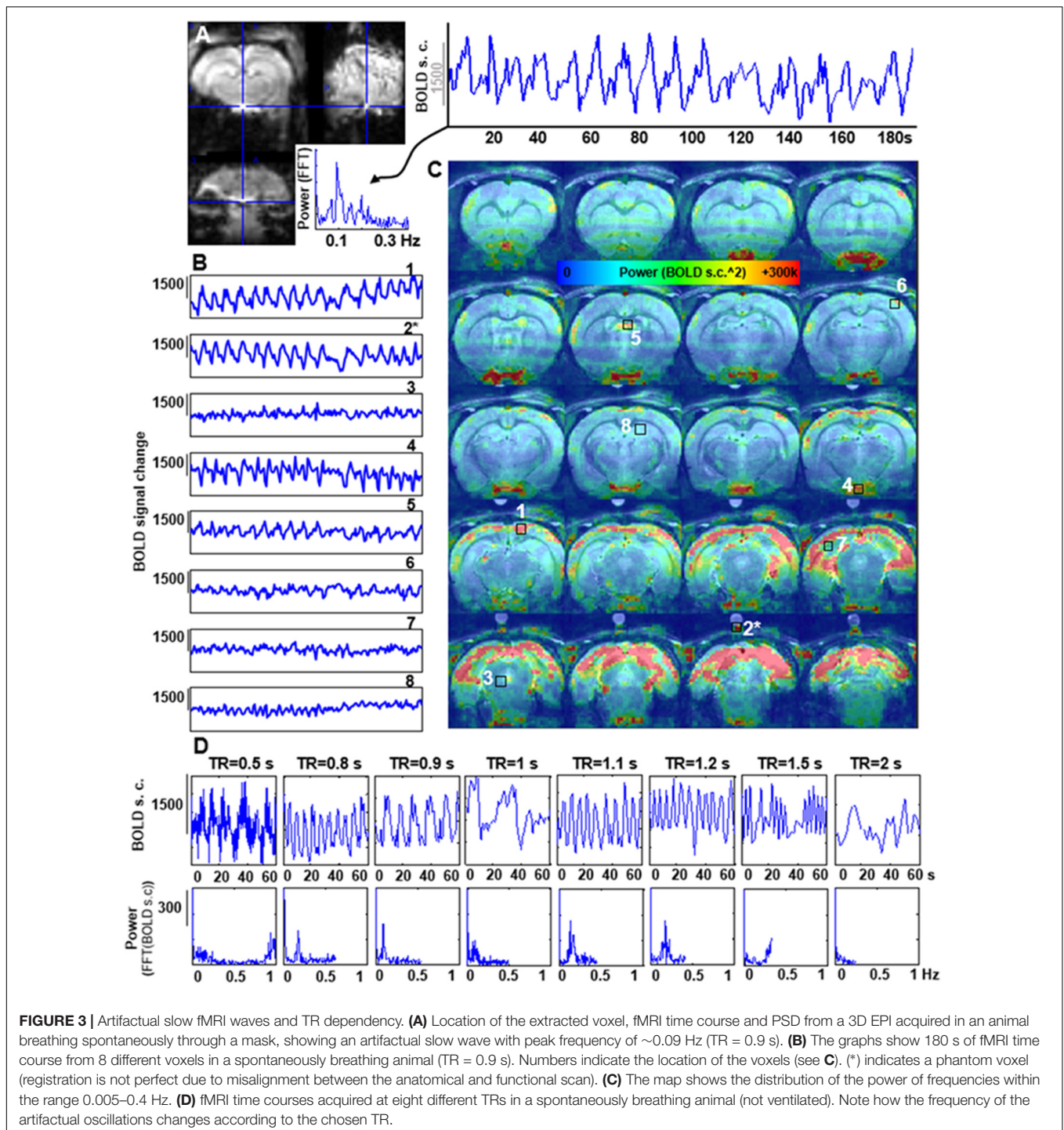
FIGURE 2 | Spectral and spatial characterization of the respiratory interference at 3 conditions: spontaneously breathing through a mask, ventilated and ventilated while paralyzed. **(A,B,C)** The original chest movement recorded at a sampling rate of 5000 is shown as a black trace. The down-sampled chest-motion (resampled at 1/TR) is shown in red. Note the smaller amplitude of this signal in the paralyzed condition **(C**, vs. **A** or **B)**. The fMRI time course of a voxel in the brain or in a phantom (over the animal's head) is shown in blue. The frequency decomposition of the signals is shown on the right. Note the similarity between the spectra of the aliased chest and fMRI signal. **(D)** The power maps show the distribution of the interference for each condition (averaged from 5 different animals). Note the low power scale in paralyzed animals. **(E)** The graph shows the spectral FWHM (i.e., spreading) of the peak breathing frequency and the aliased signal in the fMRI time course for non-intubated (mask, $N = 26$) and ventilated non-paralyzed animals ($N = 17$). **(F)** The graphs show the averaged power calculated within a frequency range that contains either the peak frequency (i.e. aliased from chest motion) or the limiting/neighbor frequency bands. N(Mask) = 16 trials from 4 animals, N(Vent,noP) = 16 trials from 3 animals, N(Vent,P) = 14 trials from 4 animals. Statistical test within conditions: two-tailed paired t-test. Statistical test between conditions: two-tailed not-paired t-test. (*): p-value < 0.005.

paralyzer agent (**Figure 5B**). Similarly, the spectral correlation between scans acquired at different ventilatory rates was lower in spontaneously breathing animals (**Figure 5F**). The magnitude of the aliased-motion artifact, estimated as the standard deviation within the fMRI time course, was calculated across animals, revealing a significantly lower contamination of the fMRI signal in the paralyzed condition (**Figure 5E**, p-value = $1.13*10^{-5}$). These experiments demonstrate that the respiration-induced interference on the fMRI signal and the subsequent inter-scan variability can be ameliorated by providing a muscle relaxant during the fMRI study. In agreement with this, the seed-based correlation analysis of rs-fMRI acquired from ventilated rats without muscle relaxant (no denoising procedure) showed highly varied correlation patterns throughout the brain, in contrast to the more specific correlation pattern observed from rats ventilated and paralyzed with a muscle relaxant, which identifies RSNs more reliably (**Supplementary Figure S6**), as previously reported (Williams et al., 2010; Lu et al., 2012; Hsu et al., 2016; Bajic et al., 2017).

DISCUSSION

In this study, the aliasing effect due to respiration-induced B0 distortion was systematically characterized in the rs-fMRI of anesthetized rats at varied fMRI imaging and respiratory controlling conditions: different TRs, altered respiration rates, free-breathing vs. ventilation (with or without muscle relaxant). The ventilation scheme was found to significantly narrow the broad respiratory frequency bandwidth of the free-breathing anesthetized rats (from FWHM≅0.06 Hz to FWHM≅0.01 Hz) and reduce the potential aliasing interference on the < 0.1 Hz fMRI signal fluctuation, which can be further reduced by the muscle relaxant. The characterization of the spatial and temporal dynamic features of the aliasing effects due to B0 distortion from individual animals allows choosing appropriate TRs or ventilation rates to avoid the aliased oscillation within the 0.01–0.1 Hz range of the fMRI signal. This may be particularly useful in fMRI studies intended to study brain dynamics in awake animals, which are becoming a common platform to investigate

FIGURE 3 | Artifactual slow fMRI waves and TR dependency. **(A)** Location of the extracted voxel, fMRI time course and PSD from a 3D EPI acquired in an animal breathing spontaneously through a mask, showing an artifactual slow wave with peak frequency of ~0.09 Hz (TR = 0.9 s). **(B)** The graphs show 180 s of fMRI time course from 8 different voxels in a spontaneously breathing animal (TR = 0.9 s). Numbers indicate the location of the voxels (see **C**). (*) indicates a phantom voxel (registration is not perfect due to misalignment between the anatomical and functional scan). **(C)** The map shows the distribution of the power of frequencies within the range 0.005–0.4 Hz. **(D)** fMRI time courses acquired at eight different TRs in a spontaneously breathing animal (not ventilated). Note how the frequency of the artifactual oscillations changes according to the chosen TR.

neurological processes without the potential confounder effects from general anesthetics. Despite the benefit of being anesthetic-free, imaging the awake brain involves the need of coping with other sources of confusion variables like potential stress or spontaneous voluntary movement of the limbs or body and, inevitably, spontaneous breathing. While the stress and voluntary motion can be avoided by exhaustive training with the animal, the last one is a factor inherent to and inseparable

of the awake condition. Therefore, faced the unfeasibility of applying a muscle relaxant to these animals, it is critical to understand the implications of imaging a spontaneously breathing rodent before acquiring rs-fMRI data and, if possible, choose adequate parameters that allow an easy discrimination between neurological and artifactual signals (e.g., deviating the aliased signal from the spectral range intended for analysis by choosing a convenient TR). Given the physiological noise of the

FIGURE 4 | Effect of the rate of artificial ventilation on the fMRI time-course. **(A)** The graphs show 300 s of fMRI time course from 8 different voxels, extracted from a 3D EPI in an animal ventilated at 59 bpm (0.96 Hz) (TR = 1 s). Numbers indicate the location of the voxels (see C). (*) indicates a phantom voxel (registration is not perfect due to misalignment between the anatomical and functional scan). **(B)** The map shows the distribution of the power of frequencies in the range 0.005–0.4 Hz. **(C)** fMRI time courses acquired with TR = 1s in a non-paralyzed animal ventilated at seven different rates.

rs-fMRI detected from anesthetized rats, this work suggests that the denoising methods developed for human fMRI (Hu et al., 1995; Glover et al., 2000; Birn et al., 2014; Caballero-Gaudes and Reynolds, 2017) should be adapted and implemented in the routine rs-fMRI animal studies.

Divergence Between the Aliasing Interference in Humans and Rodents

Human cardiovascular and respiratory signals in the young adult fluctuate at 0.66–1.66 Hz and 0.16–0.33 Hz, respectively (Fleming et al., 2011). Human respiration can, therefore, be sampled if relatively short TRs are used (< 1.5 s), preventing aliasing. In contrast, the cardiovascular oscillations constitute a clear source of aliasing in human fMRI (TR needs to be ~0.3 s to sample the human heart rate appropriately) (Hu et al., 1995; Kiviniemi

et al., 2005; Feinberg et al., 2010; Hugger et al., 2011). Despite the similarity between the neurological signals of human and rodents (e.g., EEG spectrum), the heart and respiratory rates are approximately 5 times faster in the rat (5–8 Hz and 0.9–1.5 Hz, respectively), with their respiratory cycle matching the human cardiac cycle (Zhao et al., 2008; Williams et al., 2010). The spectral features of the rat cardio-respiratory signals imply the need of correction methods to avoid aliasing in the 0.01–0.1 Hz fMRI signal. Here, we have shown how the respiratory interference can be detected and shifted away from the rs-fMRI analysis by changing the ventilatory rate or the rate of fMRI sampling (i.e., TR). This is possible due to the fact that the aliased frequency depends on the frequency of the interference (i.e., the respiratory rate) and on the sampling rate (i.e., the TR), which is a consequence of the Nyquist Sampling Theorem, stating that if the rate of sampling is less than twice the signal frequency,
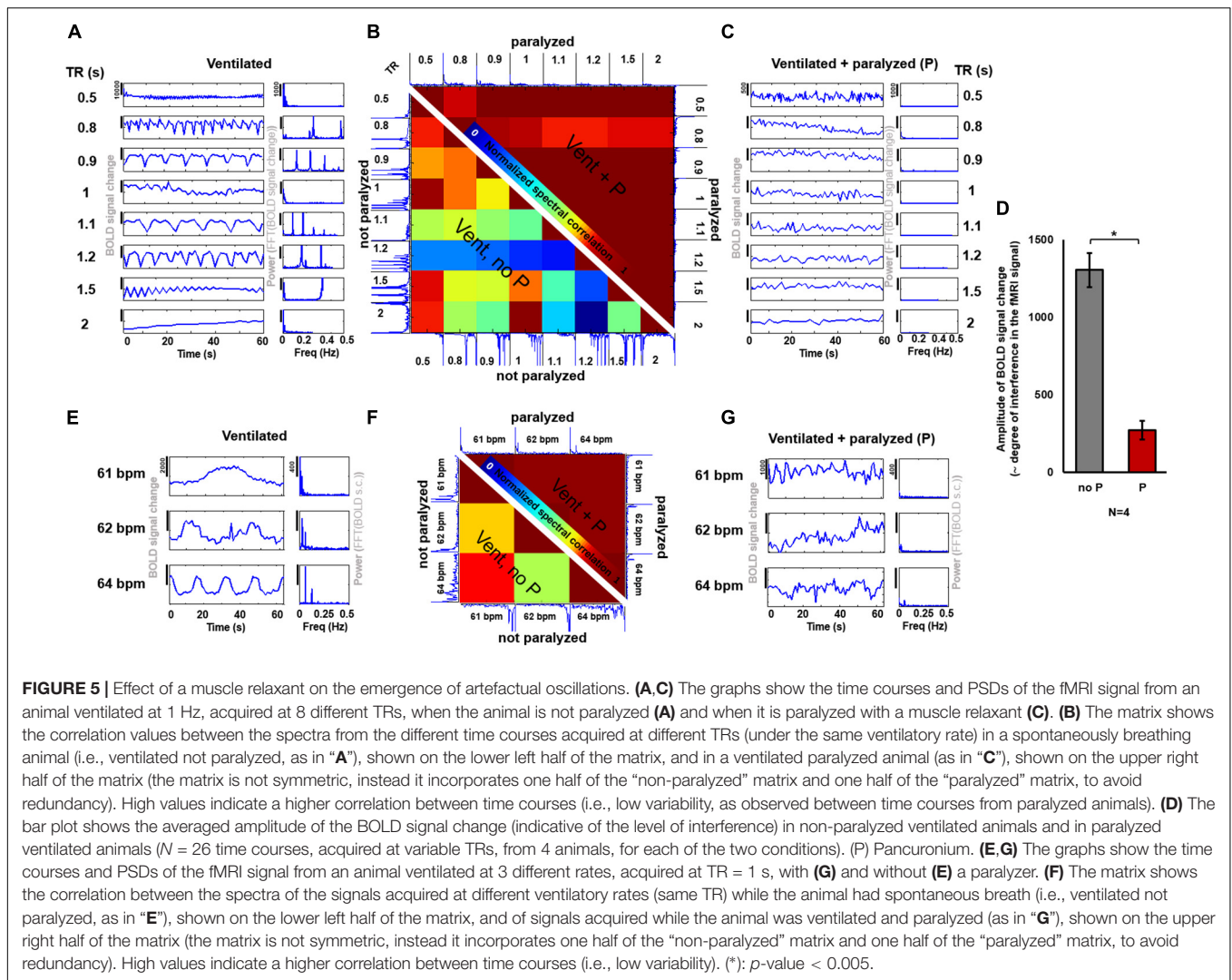
FIGURE 5 | Effect of a muscle relaxant on the emergence of artefactual oscillations. **(A,C)** The graphs show the time courses and PSDs of the fMRI signal from an animal ventilated at 1 Hz, acquired at 8 different TRs, when the animal is not paralyzed **(A)** and when it is paralyzed with a muscle relaxant **(C)**. **(B)** The matrix shows the correlation values between the spectra from the different time courses acquired at different TRs (under the same ventilatory rate) in a spontaneously breathing animal (i.e., ventilated not paralyzed, as in "**A**"), shown on the lower left half of the matrix, and in a ventilated paralyzed animal (as in "**C**"), shown on the upper right half of the matrix (the matrix is not symmetric, instead it incorporates one half of the "non-paralyzed" matrix and one half of the "paralyzed" matrix, to avoid redundancy). High values indicate a higher correlation between time courses (i.e., low variability, as observed between time courses from paralyzed animals). **(D)** The bar plot shows the averaged amplitude of the BOLD signal change (indicative of the level of interference) in non-paralyzed ventilated animals and in paralyzed ventilated animals ($N = 26$ time courses, acquired at variable TRs, from 4 animals, for each of the two conditions). (P) Pancuronium. **(E,G)** The graphs show the time courses and PSDs of the fMRI signal from an animal ventilated at 3 different rates, acquired at TR = 1 s, with **(G)** and without **(E)** a paralyzer. **(F)** The matrix shows the correlation between the spectra of the signals acquired at different ventilatory rates (same TR) while the animal had spontaneous breath (i.e., ventilated not paralyzed, as in "**E**"), shown on the lower left half of the matrix, and of signals acquired while the animal was ventilated and paralyzed (as in "**G**"), shown on the upper right half of the matrix (the matrix is not symmetric, instead it incorporates one half of the "non-paralyzed" matrix and one half of the "paralyzed" matrix, to avoid redundancy). High values indicate a higher correlation between time courses (i.e., low variability). (*): p-value < 0.005.

aliasing occurs, with $f_{alias} = | f_{resp} - n * f_{sample} |$, $n = 1, 2, \ldots$, $f_{sample} = 1/TR$ (Holst, 1996; Kiviniemi et al., 2005). Future studies using fast imaging schemes (e.g., line scanning with 50 ms TR Yu et al., 2014) could be used to characterize the cardiovascular contributions to the fMRI signal in rodent studies.

3D vs. 2D EPI fMRI Methods

In this work, we demonstrated the aliasing effect of the respiratory-driven artifacts in the rat rs-fMRI acquired as 3D EPI, which is a highly efficient sequence to acquire whole-brain fMRI signal. Nevertheless, a significant portion of the animal and human fMRI studies are performed with multi-slice (2D) EPI (Keilholz et al., 2004; Bruno et al., 2010; Magnuson et al., 2010; Williams et al., 2010; Lu et al., 2012; D'Arceuil et al., 2013; Chen et al., 2015b), which is less sensitive to physiological noise than its 3D counterpart (Lutti et al., 2013). While 2D EPI slices are acquired consecutively within ∼30 ms, with each slice sensing a different dynamic B0 field during a small portion of the respiratory cycle, 3D EPI schemes sample the whole brain slab in an additional phase encoding step,

which incorporates the B0 field distortion through the whole respiratory cycle. This difference will certainly make the 3D EPI method more sensitive to the B0 field distortions due to respiration. To account for the potential differences between both imaging schemes, multi-slice 2D EPI was acquired in animals to demonstrate the presence of a similar aliased respiratory signal in both rs-fMRI paradigms (**Supplementary Figure S7**). Although the abovementioned aliased signals could be detected in both imaging schemes, the aliased signal interference remains but is reduced in the 2D EPI method in comparison to the 3D EPI [a more exhaustive comparison between the sensitivity of both methodologies is beyond the purpose of the current study, for a discussion on the topic see: (Goerke et al., 2005)]. While physiological noise can be regressed out retrospectively from 2D EPI datasets by slice-selective correction methods (Glover et al., 2000; Hutton et al., 2011), other strategies, e.g., ICA-based artifact removal (Griffanti et al., 2014), may be applied to 3D EPIs to diminish the noise generated by the aliased cardiorespiratory interference (Caballero-Gaudes and Reynolds, 2017).

Complexity of the Respiration-Induced B0 Distortion Aliased Signal Throughout the Brain

The B0 offset induced by respiration-related motion causes dynamic B0 spatial distortion through the respiratory phasic cycles. **Figures 2D**, **3C**, **4B** show how the oscillatory signals due to motion-related artifacts dominate the fMRI signal fluctuation of the cerebellum, cortex and hypothalamic area across a frequency bandwidth (0.005–0.4Hz). Despite a major susceptibility of the dorsal, occipital and ventral regions, the distribution of the artifactual signals can vary between animals with different respiratory motion (**Supplementary Figure S3**), which shows the challenges of the generalized correction method. Paralysis of the ventilated animal resulted in a significantly reduced interference, as passive ventilation does not involve recruitment of accessory muscles in the chest or neck of the animal, which are the major contributors to the B0 inhomogeneities (Raj et al., 2001; Van de Moortele et al., 2002). However, other physiological variables not coupled to motion, such as the arterial CO2 signal (Wise et al., 2004), can change with each respiratory cycle and its direct vascular interference can be aliased into the rs-fMRI signal, even in paralyzed animals. The aliasing of these signals would cause a strong correlation between large vessels (Dagli et al., 1999). Besides the breathing-related physiological variables, an enveloped blood pressure signal of frequency ∼0.01–0.04 Hz (Meyer waves, dependent on sympathetic activity) may also appear and contaminate the BOLD signal near large vessels (Diehl et al., 1995; Pfurtscheller et al., 2017). Importantly these signals would not be a consequence of aliasing (e.g., generated due to insufficient sampling) but may be caused by real cardiac-induced slow fluctuations (Bhattacharyya and Lowe, 2004). The ventral area (i.e., near the circle of Willis) highlighted in the power map of **Figures 3**, **4** may also potentially indicate a contribution of an aliased cardiorespiratory signal in the rs-fMRI data.

Spontaneous vs. Imposed Ventilation

Free-breathing subjects may exhibit a broad respiratory frequency bandwidth (FWHM≅0.06 Hz) along the acquisition time (**Figures 2A,E** and **Supplementary Figures S5**, **S7**, black and red traces of the mask condition). This produces an equally broad bandwidth of frequencies aliased into the fMRI signal (**Figures 2A,E** and **Supplementary Figures S5**, **S7**, blue traces of the mask condition). In 2D EPI, different slices within the volume may be acquired at different phases of the varied respiratory cycles along the scan time, which leads to mild aliasing periodic patterns that could be diminished with slice-selective denoising methods (Glover et al., 2000; Hutton et al., 2011). In 3D EPI, the B0-offset throughout the varied respiratory cycles may produce artifacts along the second phase encoding direction that is harder to be corrected using the existing regression methods. Ventilation of animals at constant rates during scans forces the respiratory cycle to remain unvaried, therefore avoiding phase difference between cycles and sharpening the spectrum of the respiratory-derived motion within functional

scans (**Figure 2E** and **Supplementary Figure 4b**). By providing ventilation at specific rates, the process of identification of the aliased frequency is optimized, allowing to exclude the given spectral components with band-stop filters. Furthermore, paralyzer agents could be used to further dampen the respiratory interference.

CONCLUSION

Here, we present evidence for an interference in the rs-fMRI signal fluctuation from the respiration-related motion in animals breathing through mask or artificially ventilated, which can be observed as waves within a large frequency range depending on the length of the particular respiratory cycle and on the TR used to sample the fMRI signal (i.e., aliasing effect). The artifacts can be significantly dampened by using muscle paralyzers like Pancuronium for anesthesied animals of terminal studies. For the chronic or longitudinal studies, post-processing methods with retrospective regression (Hu et al., 1995; Glover et al., 2000), e.g., RETROICOR, can be used to attenuate the respiration-induced artifacts, as has been routinely used for human fMRI studies. Additionally, the use of a convenient TR may further simplify the cleaning process by shifting the aliased respiratory-driven artifacts to a specific frequency range that can be filtered out from the analysis. Our observations suggest that recording of respiratory cycles and blood pressure in parallel to fMRI and data cleaning (i.e., removal of physiological noise) constitutes a necessary step in small animal fMRI as well, especially in awake or non-paralyzed anesthetized rodent studies.

AUTHOR CONTRIBUTIONS

XY led the research. XY, KS, and PP-R designed the experiments. PP-R and XY performed the experiments. PP-R XY and BB guided the analysis. PP-R performed the analysis. XY, PP-R, and BB wrote the manuscript. All authors reviewed the manuscript.

SUPPLEMENTARY MATERIAL

The Supplementary Material for this article can be found online at: https://www.frontiersin.org/articles/10.3389/fnins.2018.00788/full#supplementary-material

REFERENCES

Abreu, R., Nunes, S., Leal, A., and Figueiredo, P. (2017). Physiological noise correction using ECG-derived respiratory signals for enhanced mapping of spontaneous neuronal activity with simultaneous EEG-fMRI. *Neuroimage* 154, 115–127. doi: 10.1016/j.neuroimage.2016.08.008

Airaksinen, A. M., Niskanen, J. P., Chamberlain, R., Huttunen, J. K., Nissinen, J., Garwood, M., et al. (2010). Simultaneous fMRI and local field potential measurements during epileptic seizures in medetomidine-sedated rats using raser pulse sequence. *Magn. Reson. Med.* 64, 1191–1199. doi: 10.1002/mrm.22508

Albers, F., Wachsmuth, L., Van Alst, T. M., and Faber, C. (2018). multimodal functional neuroimaging by simultaneous BOLD fMRI and fiber-optic calcium recordings and optogenetic control. *Mol. Imaging Biol.* 20, 171–182. doi: 10.1007/s11307-017-1130-6

Bajic, D., Craig, M. M., Mongerson, C. R. L., Borsook, D., and Becerra, L. (2017). Identifying rodent resting-state brain networks with independent component analysis. *Front. Neurosci.* 11:685. doi: 10.3389/fnins.2017.00685

Bhattacharyya, P. K., and Lowe, M. J. (2004). Cardiac-induced physiologic noise in tissue is a direct observation of cardiac-induced fluctuations. *Magn. Reson. Imaging* 22, 9–13. doi: 10.1016/j.mri.2003.08.003

Birn, R. M. (2012). The role of physiological noise in resting-state functional connectivity. *Neuroimage* 62, 864–870. doi: 10.1016/j.neuroimage.2012.01.016

Birn, R. M., Cornejo, M. D., Molloy, E. K., Patriat, R., Meier, T. B., Kirk, G. R., et al. (2014). The influence of physiological noise correction on test-retest reliability of resting-state functional connectivity. *Brain Connect.* 4, 511–522. doi: 10.1089/brain.2014.0284

Birn, R. M., Diamond, J. B., Smith, M. A., and Bandettini, P. A. (2006). Separating respiratory-variation-related neuronal-activity-related fluctuations in fluctuations from fMRI. *Neuroimage* 31, 1536–1548. doi: 10.1016/j.neuroimage.2006.02.048

Birn, R. M., Murphy, K., and Bandettini, P. A. (2008a). The effect of respiration variations on independent component analysis results of resting state functional connectivity. *Hum. Brain Mapp.* 29, 740–750. doi: 10.1002/hbm.20577

Birn, R. M., Smith, M. A., Jones, T. B., and Bandettini, P. A. (2008b). The respiration response function: the temporal dynamics of fMRI signal fluctuations related to changes in respiration. *Neuroimage* 40, 644–654. doi: 10.1016/j.neuroimage.2007.11.059

Biswal, B., Deyoe, E. A., and Hyde, J. S. (1996). Reduction of physiological fluctuations in fMRI using digital filters. *Magn. Reson. Med.* 35, 107–113. doi: 10.1002/mrm.1910350114

Biswal, B., Yetkin, F. Z., Haughton, V. M., and Hyde, J. S. (1995). Functional connectivity in the motor cortex of resting human brain using echo-planar MRI. *Magn. Reson. Med.* 34, 537–541. doi: 10.1002/mrm.1910340409

Biswal, B. B., and Kannurpatti, S. S. (2009). Resting-state functional connectivity in animal models: modulations by exsanguination. *Methods Mol. Biol.* 489, 255–274. doi: 10.1007/978-1-59745-543-5_12

Bright, M. G., and Murphy, K. (2017). Cleaning up the fMRI time series: Mitigating noise with advanced acquisition and correction strategies. *Neuroimage* 154, 1–3. doi: 10.1016/j.neuroimage.2017.03.056

Bruno, M. A., Soddu, A., Demertzi, A., Laureys, S., Gosseries, O., Schnakers, C., et al. (2010). Disorders of consciousness: moving from passive to resting state and active paradigms. *Cogn. Neurosci.* 1, 193–203. doi: 10.1080/17588928.2010.485677

Bukhari, Q., Schroeter, A., Cole, D. M., and Rudin, M. (2017). Resting state fMRI in mice reveals anesthesia specific signatures of brain functional networks and their interactions. *Front. Neural Circuits* 11:5. doi: 10.3389/fncir.2017.00005

Caballero-Gaudes, C., and Reynolds, R. C. (2017). Methods for cleaning the BOLD fMRI signal. *Neuroimage* 154, 128–149. doi: 10.1016/j.neuroimage.2016.12.018

Cabral, J., Kringelbach, M. L., and Deco, G. (2014). Exploring the network dynamics underlying brain activity during rest. *Prog. Neurobiol.* 114, 102–131. doi: 10.1016/j.pneurobio.2013.12.005

Chen, L., Beckett, A., Verma, A., and Feinberg, D. A. (2015a). Dynamics of respiratory and cardiac CSF motion revealed with real-time simultaneous multi-slice EPI velocity phase contrast imaging. *Neuroimage* 122, 281–287. doi: 10.1016/j.neuroimage.2015.07.073

Chen, L., Vu, A. T., Xu, J., Moeller, S., Ugurbil, K., Yacoub, E., et al. (2015b). Evaluation of highly accelerated simultaneous multi-slice EPI for fMRI. *Neuroimage* 104, 452–459. doi: 10.1016/j.neuroimage.2014.10.027

Cordes, D., Nandy, R. R., Schafer, S., and Wager, T. D. (2014). Characterization and reduction of cardiac- and respiratory-induced noise as a function of the sampling rate (TR) in fMRI. *Neuroimage* 89, 314–330. doi: 10.1016/j.neuroimage.2013.12.013

Cox, R. W. (1996). AFNI: software for analysis and visualization of functional magnetic resonance neuroimages. *Comput. Biomed. Res.* 29, 162–173. doi: 10.1006/cbmr.1996.0014

Dagli, M. S., Ingeholm, J. E., and Haxby, J. V. (1999). Localization of cardiac-induced signal change in fMRI. *Neuroimage* 9, 407–415. doi: 10.1006/nimg.1998.0424

D'Arceuil, H., Coimbra, A., Triano, P., Dougherty, M., Mello, J., Moseley, M., et al. (2013). Ferumoxytol enhanced resting state fMRI and relative cerebral blood volume mapping in normal human brain. *Neuroimage* 83, 200–209. doi: 10.1016/j.neuroimage.2013.06.066

De Luca, M., Beckmann, C. F., De Stefano, N., Matthews, P. M., and Smith, S. M. (2006). fMRI resting state networks define distinct modes of long-distance interactions in the human brain. *Neuroimage* 29, 1359–1367. doi: 10.1016/j.neuroimage.2005.08.035

De Luca, M., Smith, S., De Stefano, N., Federico, A., and Matthews, P. M. (2005). Blood oxygenation level dependent contrast resting state networks are relevant to functional activity in the neocortical sensorimotor system. *Exp. Brain Res.* 167, 587–594. doi: 10.1007/s00221-005-0059-1

Diehl, R. R., Linden, D., Lucke, D., and Berlit, P. (1995). Phase relationship between cerebral blood flow velocity and blood pressure. A clinical. test of autoregulation. *Stroke* 26, 1801–1804. doi: 10.1161/01.STR.26.10.1801

Feinberg, D. A., Moeller, S., Smith, S. M., Auerbach, E., Ramanna, S., Gunther, M., et al. (2010). Multiplexed echo planar imaging for sub-second whole brain FMRI and fast diffusion imaging. *PLoS One* 5:e15710. doi: 10.1371/journal.pone.0015710

Feinberg, D. A., and Setsompop, K. (2013). Ultra-fast MRI of the human brain with simultaneous multi-slice imaging. *J. Magn. Reson.* 229, 90–100. doi: 10.1016/j.jmr.2013.02.002

Ferenczi, E. A., Zalocusky, K. A., Liston, C., Grosenick, L., Warden, M. R., Amatya, D., et al. (2016). Prefrontal cortical regulation of brainwide circuit dynamics and reward-related behavior. *Science* 351:aac9698. doi: 10.1126/science.aac9698

Fleming, S., Thompson, M., Stevens, R., Heneghan, C., Pluddemann, A., Maconochie, I., et al. (2011). Normal ranges of heart rate and respiratory rate in children from birth to 18 years of age: a systematic review of observational studies. *Lancet* 377, 1011–1018. doi: 10.1016/S0140-6736(10)62226-X

Fox, M. D., Zhang, D., Snyder, A. Z., and Raichle, M. E. (2009). The global signal and observed anticorrelated resting state brain networks. *J. Neurophysiol.* 101, 3270–3283. doi: 10.1152/jn.90777.2008

Frank, L. R., Buxton, R. B., and Wong, E. C. (2001). Estimation of respiration-induced noise fluctuations from undersampled multislice fMRI data. *Magn. Reson. Med.* 45, 635–644. doi: 10.1002/mrm.1086

Glover, G. H., Li, T. Q., and Ress, D. (2000). Image-based method for retrospective correction of physiological motion effects in fMRI: RETROICOR. *Magn. Reson. Med.* 44, 162–167. doi: 10.1002/1522-2594(200007)44:1<162::AID-MRM23>3.0.CO;2-E

Goense, J. B., and Logothetis, N. K. (2008). Neurophysiology of the BOLD fMRI signal in awake monkeys. *Curr. Biol.* 18, 631–640. doi: 10.1016/j.cub.2008.03.054

Goerke, U., Moller, H. E., Norris, D. G., and Schwarzbauer, C. (2005). A comparison of signal instability in 2D and 3D EPI resting-state fMRI. *NMR Biomed.* 18, 534–542. doi: 10.1002/nbm.987

Greicius, M. D., Krasnow, B., Reiss, A. L., and Menon, V. (2003). Functional connectivity in the resting brain: a network analysis of the default mode hypothesis. *Proc. Natl. Acad. Sci. U.S.A.* 100, 253–258. doi: 10.1073/pnas.0135058100

Griffanti, L., Salimi-Khorshidi, G., Beckmann, C. F., Auerbach, E. J., Douaud, G., Sexton, C. E., et al. (2014). ICA-based artefact removal and accelerated fmri acquisition for improved resting state network imaging. *Neuroimage* 95, 232–247. doi: 10.1016/j.neuroimage.2014.03.034

He, Y., Wang, M., Chen, X., Pohmann, R., Polimeni, J. R., Scheffler, K., et al. (2018). Ultra-Slow Single-Vessel BOLD and CBV-Based fMRI spatiotemporal dynamics and their correlation with neuronal intracellular calcium signals. *Neuron* 97, 925–939.e5. doi: 10.1016/j.neuron.2018.01.025

Holst, G. C. (1996). Sampling, aliasing, and target appearance. *Infrared Phys. Technol.* 37, 627–634. doi: 10.1016/S1350-4495(97)80356-8

Hsu, L. M., Liang, X., Gu, H., Brynildsen, J. K., Stark, J. A., Ash, J. A., et al. (2016). Constituents and functional implications of the rat default mode network. *Proc. Natl. Acad. Sci. U.S.A.* 113, E4541–E4547. doi: 10.1073/pnas.1601485113

Hu, X. P., Le, T. H., Parrish, T., and Erhard, P. (1995). Retrospective estimation and correction of physiological fluctuation in functional Mri. *Magn. Reson. Med.* 34, 201–212. doi: 10.1002/mrm.1910340211

Hugger, T., Zahneisen, B., Levan, P., Lee, K. J., Lee, H. L., Zaitsev, M., et al. (2011). Fast undersampled functional magnetic resonance imaging using nonlinear regularized parallel image reconstruction. *PLoS One* 6:e28822. doi: 10.1371/journal.pone.0028822

Hutton, C., Josephs, O., Stadler, J., Featherstone, E., Reid, A., Speck, O., et al. (2011). The impact of physiological noise correction on fMRI at 7 T. *Neuroimage* 57, 101–112. doi: 10.1016/j.neuroimage.2011.04.018

Hyder, F., and Rothman, D. L. (2010). Neuronal correlate of BOLD signal fluctuations at rest: err on the side of the baseline. *Proc. Natl. Acad. Sci. U.S.A.* 107, 10773–10774. doi: 10.1073/pnas.1005135107

Jiang, Y., Chen, X., and Yu, X. (2018). Fiber optic mediated extracellular glutamate and intracellular calcium recording with simultaneous fMRI. *Int. Soc. Magn. Reson. Med.*

Jorge, J., Grouiller, F., Ipek, O., Stoermer, R., Michel, C. M., Figueiredo, P., et al. (2015). Simultaneous EEG-fMRI at ultra-high field: artifact prevention and safety assessment. *Neuroimage* 105, 132–144. doi: 10.1016/j.neuroimage.2014.10.055

Kalthoff, D., Seehafer, J. U., Po, C., Wiedermann, D., and Hoehn, M. (2011). Functional connectivity in the rat at 11.7T: Impact of physiological noise in resting state fMRI. *Neuroimage* 54, 2828–2839. doi: 10.1016/j.neuroimage.2010.10.053

Kannurpatti, S. S., Biswal, B. B., Kim, Y. R., and Rosen, B. R. (2008). Spatio-temporal characteristics of low-frequency BOLD signal fluctuations in isoflurane-anesthetized rat brain. *Neuroimage* 40, 1738–1747. doi: 10.1016/j.neuroimage.2007.05.061

Keilholz, S. D., Silva, A. C., Raman, M., Merkle, H., and Koretsky, A. P. (2004). Functional MRI of the rodent somatosensory pathway using multislice echo planar imaging. *Magn. Reson. Med.* 52, 89–99. doi: 10.1002/mrm.20114

Kiviniemi, V., Kantola, J. H., Jauhiainen, J., Hyvarinen, A., and Tervonen, O. (2003). Independent component analysis of nondeterministic fMRI signal sources. *Neuroimage* 19, 253–260. doi: 10.1016/S1053-8119(03)00097-1

Kiviniemi, V., Ruohonen, J., and Tervonen, O. (2005). Separation of physiological very low frequency fluctuation from aliasing by switched sampling interval fMRI scans. *Magn. Reson. Imaging* 23, 41–46. doi: 10.1016/j.mri.2004.09.005

Lee, J. H., Durand, R., Gradinaru, V., Zhang, F., Goshen, I., Kim, D. S., et al. (2010). Global and local fMRI signals driven by neurons defined optogenetically by type and wiring. *Nature* 465, 788–792. doi: 10.1038/nature09108

Liang, Z., Watson, G. D., Alloway, K. D., Lee, G., Neuberger, T., and Zhang, N. (2015). Mapping the functional network of medial prefrontal cortex by combining optogenetics and fMRI in awake rats. *Neuroimage* 117, 114–123. doi: 10.1016/j.neuroimage.2015.05.036

Liu, T. T. (2016). Noise contributions to the fMRI signal: an overview. *Neuroimage* 143, 141–151. doi: 10.1016/j.neuroimage.2016.09.008

Logothetis, N. K. (2002). The neural basis of the blood-oxygen-level-dependent functional magnetic resonance imaging signal. *Philos. Trans. R. Soc. Lond. B Biol. Sci.* 357, 1003–1037. doi: 10.1098/rstb.2002.1114

Lowe, M. J., Mock, B. J., and Sorenson, J. A. (1998). Functional connectivity in single and multislice echoplanar imaging using resting-state fluctuations. *Neuroimage* 7, 119–132. doi: 10.1006/nimg.1997.0315

Lu, H., Zou, Q., Gu, H., Raichle, M. E., Stein, E. A., and Yang, Y. (2012). Rat brains also have a default mode network. *Proc. Natl. Acad. Sci. U.S.A.* 109, 3979–3984. doi: 10.1073/pnas.1200506109

Lutti, A., Thomas, D. L., Hutton, C., and Weiskopf, N. (2013). High-resolution functional MRI at 3 T: 3D/2D echo-planar imaging with optimized

physiological noise correction. *Magn. Reson. Med.* 69, 1657–1664. doi: 10.1002/mrm.24398

Magnuson, M., Majeed, W., and Keilholz, S. D. (2010). Functional connectivity in blood oxygenation level-dependent and cerebral blood volume-weighted resting state functional magnetic resonance imaging in the rat brain. *J. Magn. Reson. Imaging* 32, 584–592. doi: 10.1002/jmri.22295

Magnuson, M. E., Thompson, G. J., Schwarb, H., Pan, W. J., Mckinley, A., Schumacher, E. H., et al. (2015). Errors on interrupter tasks presented during spatial and verbal working memory performance are linearly linked to large-scale functional network connectivity in high temporal resolution resting state fMRI. *Brain Imaging Behav.* 9, 854–867. doi: 10.1007/s11682-014-9347-3

Majeed, W., Magnuson, M., Hasenkamp, W., Schwarb, H., Schumacher, E. H., Barsalou, L., et al. (2011). Spatiotemporal dynamics of low frequency BOLD fluctuations in rats and humans. *Neuroimage* 54, 1140–1150. doi: 10.1016/j.neuroimage.2010.08.030

Mantini, D., Gerits, A., Nelissen, K., Durand, J. B., Joly, O., Simone, L., et al. (2011). Default mode of brain function in monkeys. *J. Neurosci.* 31, 12954–12962. doi: 10.1523/JNEUROSCI.2318-11.2011

Mishra, A. M., Ellens, D. J., Schridde, U., Motelow, J. E., Purcaro, M. J., Desalvo, M. N., et al. (2011). Where fMRI and electrophysiology agree to disagree: corticothalamic and striatal activity patterns in the WAG/Rij rat. *J. Neurosci.* 31, 15053–15064. doi: 10.1523/JNEUROSCI.0101-11.2011

Murphy, K., Birn, R. M., and Bandettini, P. A. (2013). Resting-state fMRI confounds and cleanup. *Neuroimage* 80, 349–359. doi: 10.1016/j.neuroimage.2013.04.001

Noll, D. C., Genovese, C. R., Vazquez, A. L., O'brien, J. L., and Eddy, W. F. (1998). Evaluation of respiratory artifact correction techniques in multishot spiral functional MRI using receiver operator characteristic analyses. *Magn. Reson. Med.* 40, 633–639. doi: 10.1002/mrm.1910400417

Obrig, H., Neufang, M., Wenzel, R., Kohl, M., Steinbrink, J., Einhaupl, K., et al. (2000). Spontaneous low frequency oscillations of cerebral hemodynamics and metabolism in human adults. *Neuroimage* 12, 623–639. doi: 10.1006/nimg.2000.0657

Paasonen, J., Stenroos, P., Salo, R. A., Kiviniemi, V., and Grohn, O. (2018). Functional connectivity under six anesthesia protocols and the awake condition in rat brain. *Neuroimage* 172, 9–20. doi: 10.1016/j.neuroimage.2018.01.014

Pan, W. J., Thompson, G., Magnuson, M., Majeed, W., Jaeger, D., and Keilholz, S. (2011). Broadband local field potentials correlate with spontaneous fluctuations in functional magnetic resonance imaging signals in the rat somatosensory cortex under isoflurane anesthesia. *Brain Connect.* 1, 119–131. doi: 10.1089/brain.2011.0014

Pan, W. J., Thompson, G. J., Magnuson, M. E., Jaeger, D., and Keilholz, S. (2013). Infraslow LFP correlates to resting-state fMRI BOLD signals. *Neuroimage* 74, 288–297. doi: 10.1016/j.neuroimage.2013.02.035

Pawela, C. P., Biswal, B. B., Hudetz, A. G., Li, R., Jones, S. R., Cho, Y. R., et al. (2010). Interhemispheric neuroplasticity following limb deafferentation detected by resting-state functional connectivity magnetic resonance imaging (fcMRI) and functional magnetic resonance imaging (fMRI). *Neuroimage* 49, 2467–2478. doi: 10.1016/j.neuroimage.2009.09.054

Pfurtscheller, G., Schwerdtfeger, A., Brunner, C., Aigner, C., Fink, D., Brito, J., et al. (2017). Distinction between neural and vascular BOLD oscillations and intertwined heart rate oscillations at 0.1 Hz in the resting state and during movement. *PLoS One* 12:e0168097. doi: 10.1371/journal.pone.0168097

Posse, S., Ackley, E., Mutihac, R., Zhang, T., Hummatov, R., Akhtari, M., et al. (2013). High-speed real-time resting-state FMRI using multi-slab echo-volumar imaging. *Front. Hum. Neurosci.* 7:479. doi: 10.3389/fnhum.2013.00479

Raichle, M. E., Macleod, A. M., Snyder, A. Z., Powers, W. J., Gusnard, D. A., and Shulman, G. L. (2001). A default mode of brain function. *Proc. Natl. Acad. Sci. U.S.A.* 98, 676–682. doi: 10.1073/pnas.98.2.676

Raj, D., Anderson, A. W., and Gore, J. C. (2001). Respiratory effects in human functional magnetic resonance imaging due to bulk susceptibility changes. *Phys. Med. Biol.* 46, 3331–3340. doi: 10.1088/0031-9155/46/12/318

Razavi, M., Eaton, B., Paradiso, S., Mina, M., Hudetz, A. G., and Bolinger, L. (2008). Source of low-frequency fluctuations in functional MRI signal. *J. Magn. Reson. Imaging* 27, 891–897. doi: 10.1002/jmri.21283

Reynaud, O., Jorge, J., Gruetter, R., Marques, J. P., and Van Der Zwaag, W. (2017). Influence of physiological noise on accelerated 2D and 3D resting state
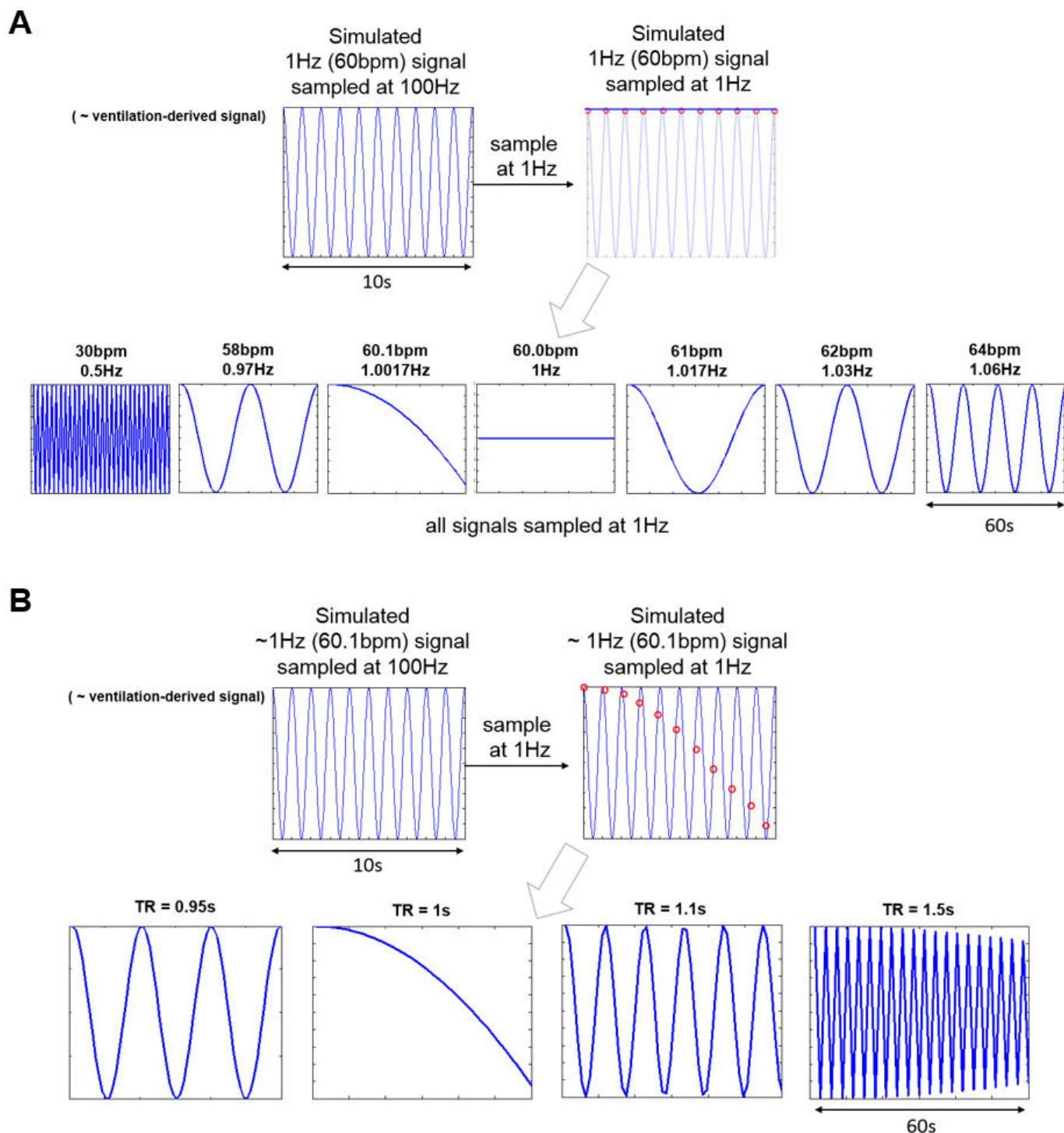
functional MRI data at 7 T. *Magn. Reson. Med.* 78, 888–896. doi: 10.1002/mrm.
26823

Scholvinck, M. L., Maier, A., Ye, F. Q., Duyn, J. H., and Leopold, D. A. (2010).
Neural basis of global resting-state fMRI activity. *Proc. Natl. Acad. Sci. U.S.A.*
107, 10238–10243. doi: 10.1073/pnas.0913110107

Schulz, K., Sydekum, E., Krueppel, R., Engelbrecht, C. J., Schlegel, F., Schroter, A.,
et al. (2012). Simultaneous BOLD fMRI and fiber-optic calcium recording in rat
neocortex. *Nat. Methods* 9, 597–602. doi: 10.1038/nmeth.2013

Schwalm, M., Schmid, F., Wachsmuth, L., Backhaus, H., Kronfeld, A., Aedo
Jury, F., et al. (2017). Cortex-wide BOLD fMRI activity reflects locally-recorded
slow oscillation-associated calcium waves. *Elife* 6:e27602. doi: 10.7554/eLife.
27602

Shmuel, A., and Leopold, D. A. (2008). Neuronal correlates of spontaneous
fluctuations in fMRI signals in monkey visual cortex: Implications for
functional connectivity at rest. *Hum. Brain Mapp.* 29, 751–761. doi: 10.1002/
hbm.20580

Shmueli, K., Van Gelderen, P., De Zwart, J. A., Horovitz, S. G., Fukunaga, M.,
Jansma, J. M., et al. (2007). Low-frequency fluctuations in the cardiac rate as
a source of variance in the resting-state fMRI BOLD signal. *Neuroimage* 38,
306–320. doi: 10.1016/j.neuroimage.2007.07.037

Stafford, J. M., Jarrett, B. R., Miranda-Dominguez, O., Mills, B. D., Cain, N.,
Mihalas, S., et al. (2014). Large-scale topology and the default mode network
in the mouse connectome. *Proc. Natl. Acad. Sci. U.S.A.* 111, 18745–18750.
doi: 10.1073/pnas.1404346111

Starck, T., Remes, J., Nikkinen, J., Tervonen, O., and Kiviniemi, V. (2010).
Correction of low-frequency physiological noise from the resting state BOLD
fMRI–Effect on ICA default mode analysis at 1.5 *T. J. Neurosci. Methods* 186,
179–185. doi: 10.1016/j.jneumeth.2009.11.015

Tong, Y., Hocke, L. M., and Frederick, B. (2014). Short repetition time multiband
echo-planar imaging with simultaneous pulse recording allows dynamic
imaging of the cardiac pulsation signal. *Magn. Reson. Med.* 72, 1268–1276.
doi: 10.1002/mrm.25041

Van de Moortele, P. F., Pfeuffer, J., Glover, G. H., Ugurbil, K., and Hu, X. (2002).
Respiration-induced B0 fluctuations and their spatial distribution in the human
brain at 7 Tesla. *Magn. Reson. Med.* 47, 888–895. doi: 10.1002/mrm.10145

Vincent, J. L., Patel, G. H., Fox, M. D., Snyder, A. Z., Baker, J. T., Van Essen,
D. C., et al. (2007). Intrinsic functional architecture in the anaesthetized monkey
brain. *Nature* 447, 83–86. doi: 10.1038/nature05758

Wang, M., He, Y., Sejnowski, T. J., and Yu, X. (2018). Brain-state dependent
astrocytic Ca(2 +) signals are coupled to both positive and negative BOLD-
fMRI signals. *Proc. Natl. Acad. Sci. U.S.A.* 115, E1647–E1656. doi: 10.1073/pnas.
1711692115

Welvaert, M., and Rosseel, Y. (2012). How ignoring physiological noise can bias the
conclusions from fMRI simulation results. *J. Neurosci. Methods* 211, 125–132.
doi: 10.1016/j.jneumeth.2012.08.022

Williams, K. A., Magnuson, M., Majeed, W., Laconte, S. M., Peltier, S. J., Hu, X.,
et al. (2010). Comparison of alpha-chloralose, medetomidine and isoflurane
anesthesia for functional connectivity mapping in the rat. *Magn. Reson. Imaging*
28, 995–1003. doi: 10.1016/j.mri.2010.03.007

Wise, R. G., Ide, K., Poulin, M. J., and Tracey, I. (2004). Resting fluctuations in
arterial carbon dioxide induce significant low frequency variations in BOLD
signal. *Neuroimage* 21, 1652–1664. doi: 10.1016/j.neuroimage.2003.11.025

Xie, Y., Chan, A. W., Mcgirr, A., Xue, S., Xiao, D., Zeng, H., et al. (2016).
Resolution of high-frequency mesoscale intracortical maps using the genetically
encoded glutamate sensor iglusnfr. *J. Neurosci.* 36, 1261–1272. doi: 10.1523/
JNEUROSCI.2744-15.2016

Yang, S., Ross, T. J., Zhang, Y., Stein, E. A., and Yang, Y. (2005). Head motion
suppression using real-time feedback of motion information and its effects on
task performance in fMRI. *Neuroimage* 27, 153–162. doi: 10.1016/j.neuroimage.
2005.02.050

Yu, X. (2017). "When photons meet protons: Optogenetics, Calcium signal
detection, and fMRI in small animals," in *Small Animal Imaging Basics and
Practical Guide*, eds F. Kiessling, B. Pichler, and P. Hauff (Berlin: Springer
International Publishing).

Yu, X., He, Y., Wang, M., Merkle, H., Dodd, S. J., Silva, A. C., et al. (2016). Sensory
and optogenetically driven single-vessel fMRI. *Nat. Methods* 13, 337–340.
doi: 10.1038/nmeth.3765

Yu, X., Qian, C., Chen, D. Y., Dodd, S. J., and Koretsky, A. P. (2014). Deciphering
laminar-specific neural inputs with line-scanning fMRI. *Nat. Methods* 11,
55–58. doi: 10.1038/nmeth.2730

Zhao, F., Zhao, T., Zhou, L., Wu, Q., and Hu, X. (2008). BOLD study
of stimulation-induced neural activity and resting-state connectivity
in medetomidine-sedated rat. *Neuroimage* 39, 248–260. doi: 10.1016/j.
neuroimage.2007.07.063

Zou, Q. H., Zhu, C. Z., Yang, Y., Zuo, X. N., Long, X. Y., Cao, Q. J., et al.
(2008). An improved approach to detection of amplitude of low-frequency
fluctuation (ALFF) for resting-state fMRI: fractional ALFF. *J. Neurosci. Methods*
172, 137–141. doi: 10.1016/j.jneumeth.2008.04.012

Supplementary Figure 1. **Simulation of the aliasing effect.**

(**A**) The graphs show the signal that would be observed after sampling a periodic movement (e.g. respiratory-driven movement) at 1 s TR. Examples of different ventilatory rates are provided. If the ventilatory rate matches the sampling frequency (1/TR), the resulting signal has frequency = 0, therefore it can be canceled out. By using different ventilatory rates, the frequency of the recorded oscillation varies.
(**B**) Effect of the TR on the aliasing of a periodic signal (e.g. respiratory-driven movement) of frequency 1.0017 Hz (60.1 breaths per minute). If the signal was sampled at its exact frequency, a flat line would remain (signal cancellation). By sampling it at a rate close to the ventilatory frequency (sampling the 1.0017 Hz respiratory signal at 1 Hz), a slow wave appears. The waveforms that result from down-sampling the original signal vary their frequency depending on the chosen TR.

Supplementary Figure 2. **Aliased ventilation in the fMRI time course observed under different anesthetics.**
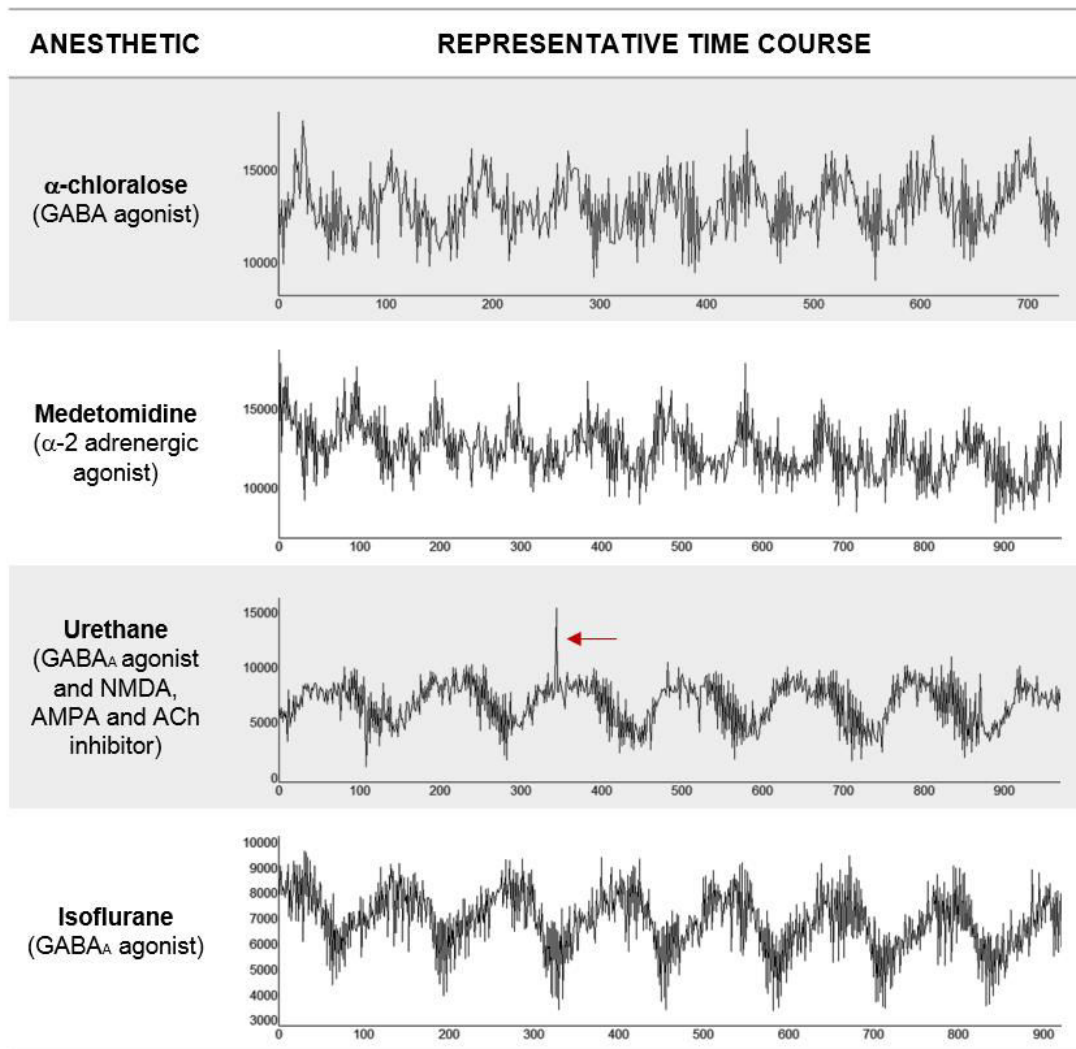
The ultraslow waves can be observed under different anesthetics when the muscle relaxant is not present. The red arrow indicates motion, identified in the time course as a fast change of the BOLD signal, in contrast to the slow aliased signal. TR = 1 s, ventilatory rate near 1 Hz (around 60 bpm).

Supplementary Figure 3. **The power map from individual animals.**
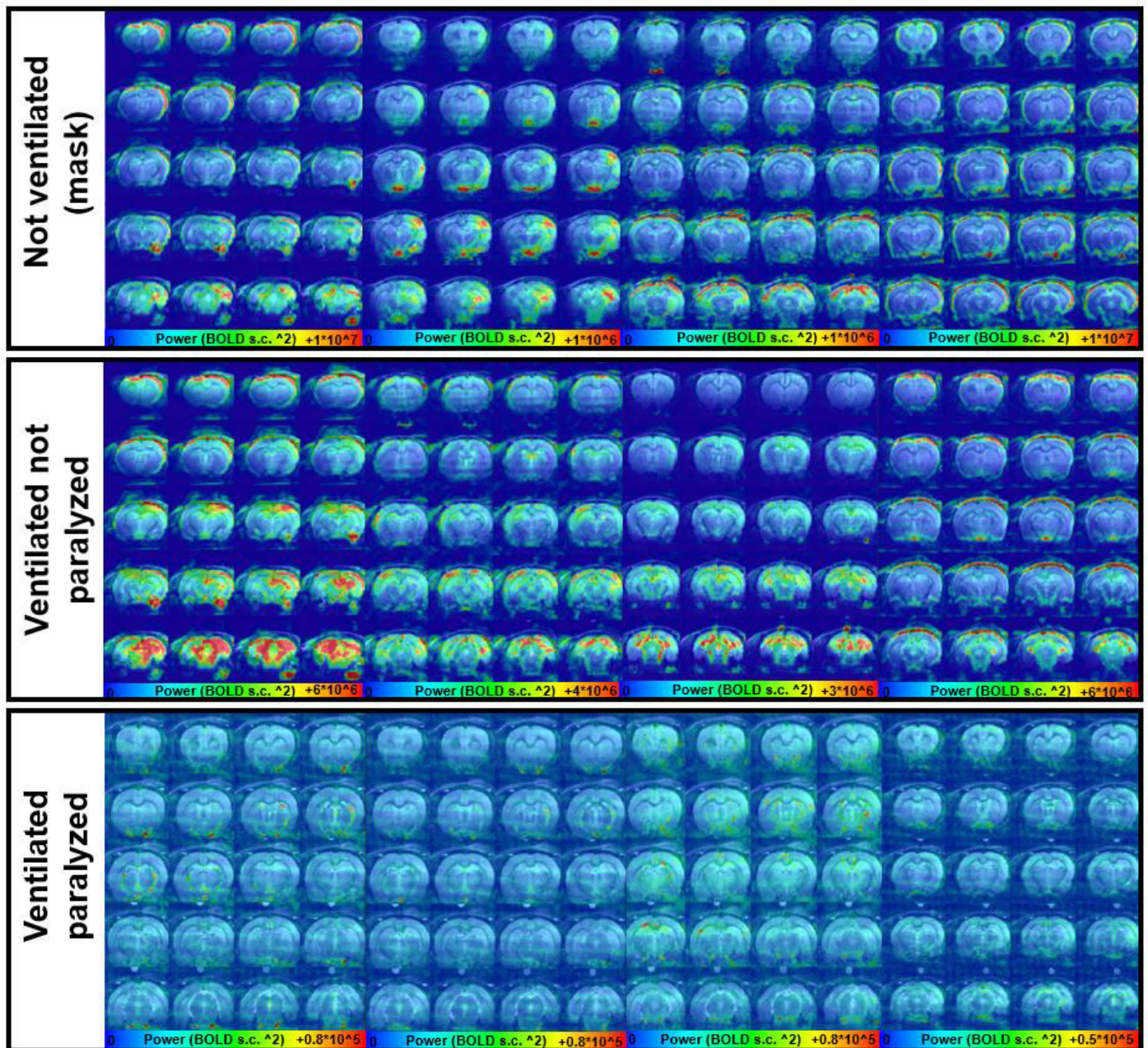
The figure shows 4 individual examples of the power map acquired from animals under 3 different conditions (breathing through a mask -up-, ventilated -middle-, or ventilated and paralyzed -down-). Note how the power of the artifactual oscillations is higher in areas of the periphery, ventral aspect of the brain and occipital lobe/cerebellum, although different patterns can be observed in different animals. When the animal is paralyzed, a more homogeneous pattern is observed, which occurs at a much lower power compared to the non-paralyzed conditions.

Supplementary Figure 4. Spectral resolution of the aliased respiration assessed with fALFF from mask vs. ventilated non-paralyzed vs. paralyzed animals.
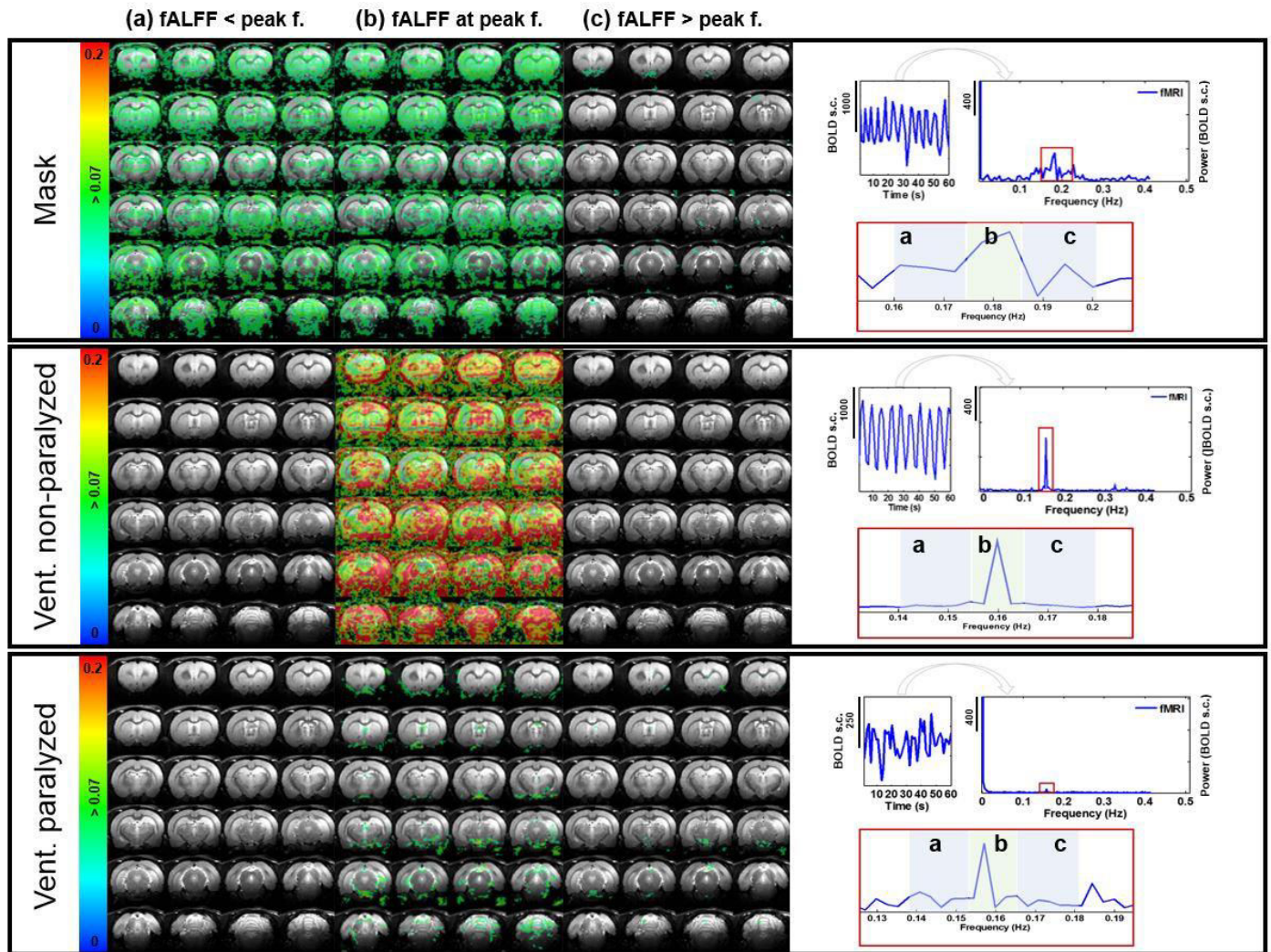
The maps on the left show, for each condition, the fraction of the spectra within the peak frequency range (b), frequency range below the peak (a) and frequency range above the peak (c), with respect to the whole spectrum. On the right, the fMRI time course and PSD of a brain voxel are shown. TR = 1.2 s, ventilatory rate = 1 Hz (60 bpm) in the ventilated conditions.

Supplementary Figure 5. **Aliasing of the respiration in the spontaneously breathing animal.**
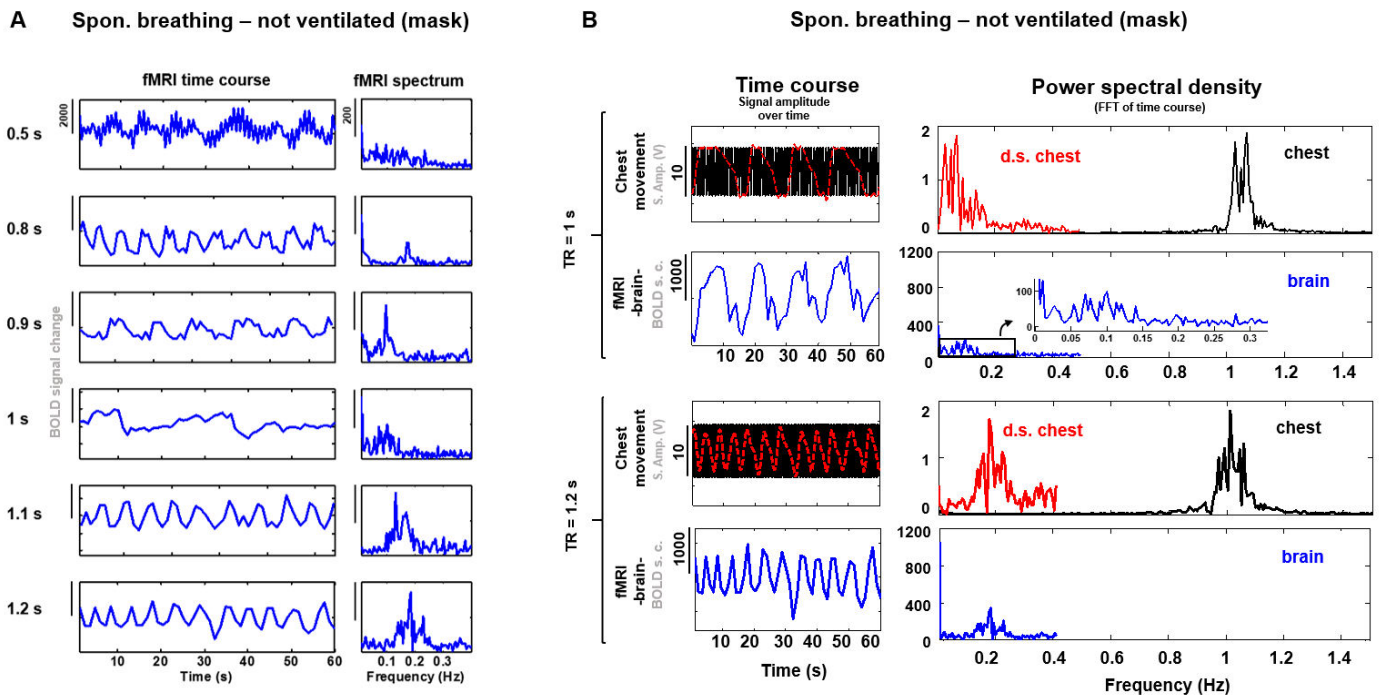
(**A**) The graphs show 1 minute of fMRI time course in a spontaneously breathing non-ventilated animal acquired at 6 different TRs and the corresponding PSDs. (**B**) Two examples showing the chest movement and fMRI signal in time and frequency domain, in an animal breathing through a mask, acquired at TR = 1 s (top graphs) and TR = 1.2 s (bottom graphs). Note how, at 1 s TR, the aliased signal appears within the 0.01 to 0.1 Hz frequency range.

Supplementary Figure 6. **Variability of the resting state network identified from non-paralyzed vs. paralyzed animals.**
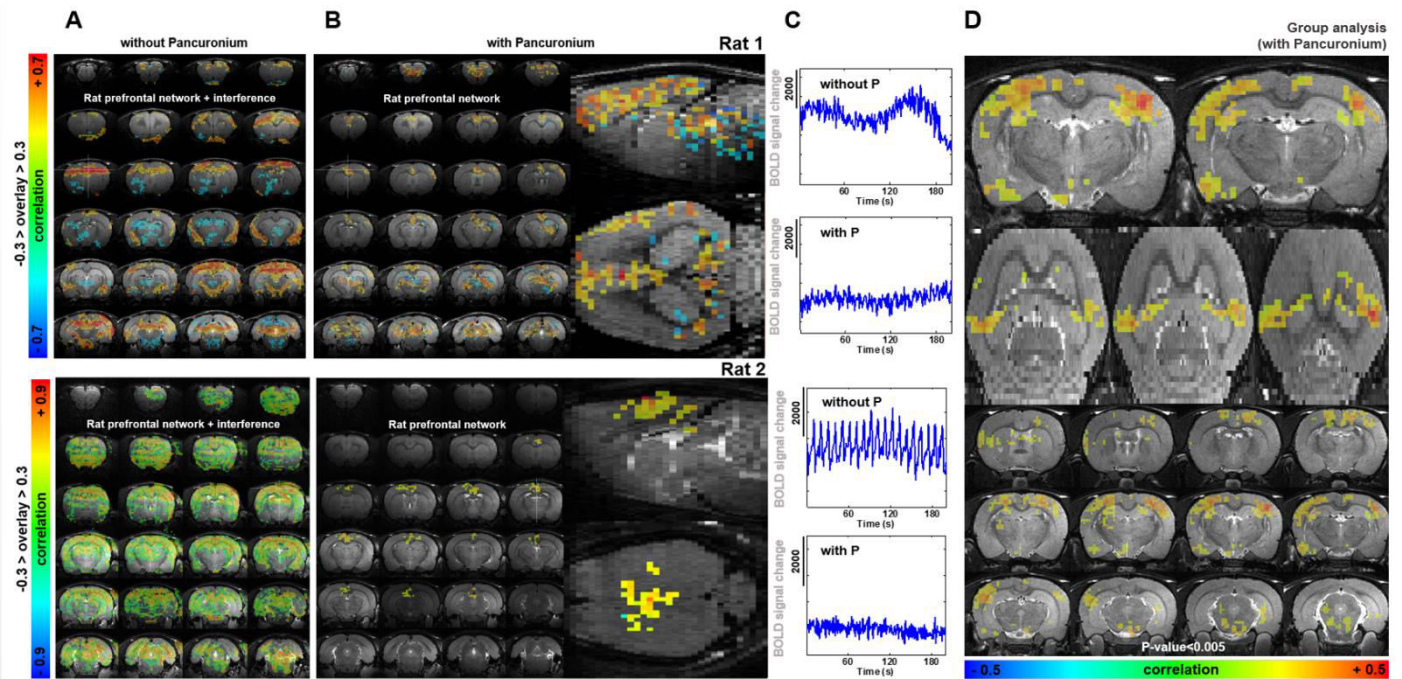
(**A**) Seed-correlation maps acquired from two spontaneously breathing animals ventilated at 60 bpm (TR in Rat 1 = 1 s, and TR in Rat 2 = 1.1 s). (**B**) Seed-correlation map in the same animals after infusion of the muscle relaxant Pancuronium. The cingulate cortex and other prefrontal areas can be clearly identified in the paralyzed animals (**B**) but are overshadowed in spontaneously breathing rats (**A**). (**C**) The graphs show a representative fMRI time course from each rat and condition in A and B. P: Pancuronium. (**D**) Averaged seed-based correlation map from 11 trials in 4 different animals anesthetized with 1.5-2% isoflurane and paralyzed with Pancuronium. Colored voxels exhibit a statistically significant correlation, with p-value < 0.005 in a 1 sample t-test. Note the clear identification of cortico-cortical connectivity bilaterally.

Supplementary Figure 7. **Aliased ventilation in multi-slice (2D) EPI.**
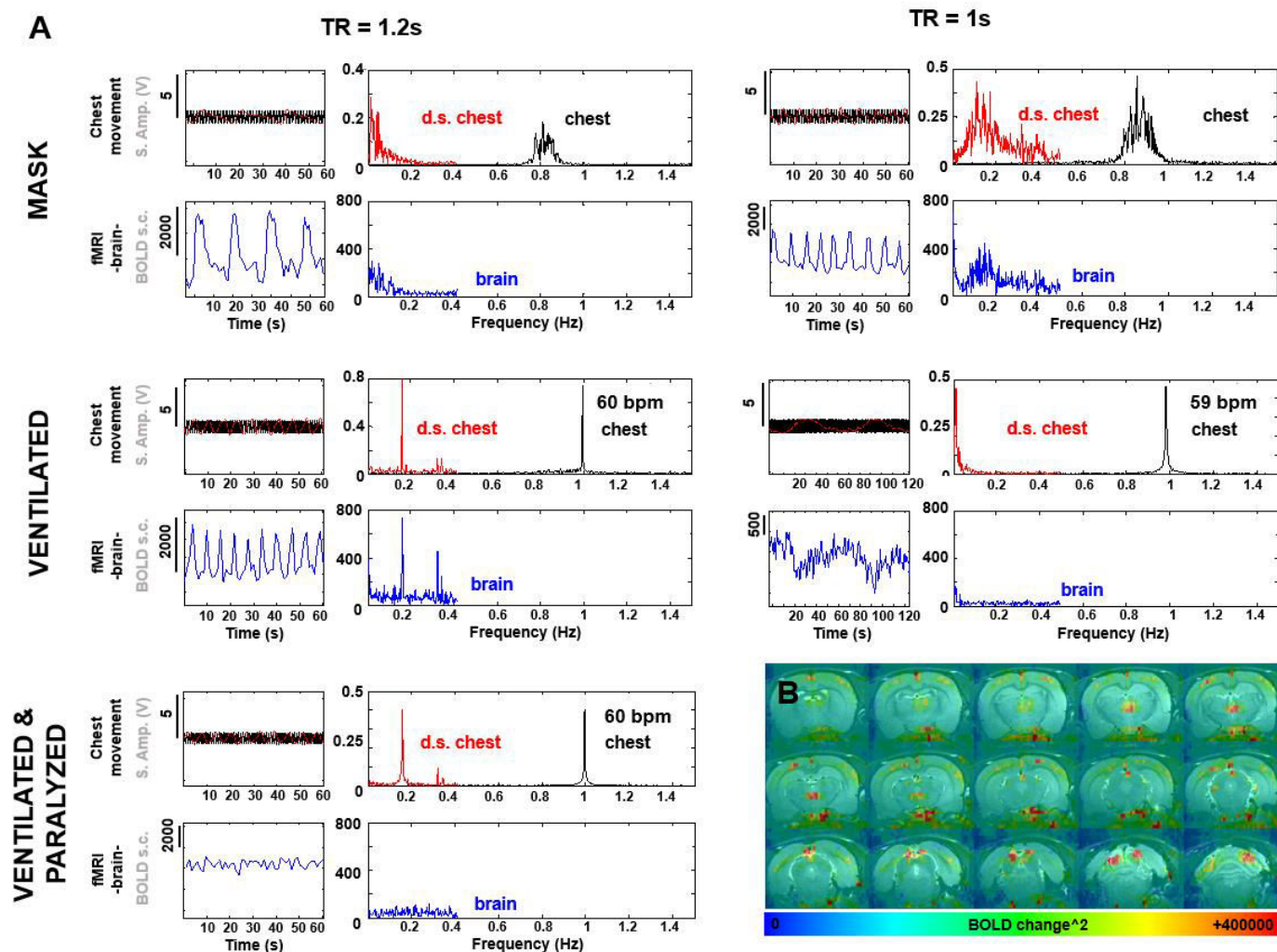
(**A**) The graphs show the time course and PSD of the respiratory chest motion and of the fMRI signal acquired at 2 different TRs in 3 different conditions: animal not ventilated, animal ventilated not paralyzed, and animal ventilated and paralyzed. d.s.: down-sampled to 1/TR. (**B**) The map shows the power distribution of the aliased signal in the ventilated non-paralyzed animal (average of 8 scans from one representative animal). Note the similarity of the aliasing effect between this figure and Fig. 2 (3D EPI), but also the difference in the power maps (the effect is less prominent in 2D EPI).

MRI-guided robotic arm drives optogenetic fMRI with concurrent Ca^{2+} recording

Yi Chen[1,2], Patricia Pais-Roldan[1,2], Xuming Chen[1,3], Michael H. Frosz [4] & Xin Yu [1,5]

Optical fiber-mediated optogenetic activation and neuronal Ca^{2+} recording in combination with fMRI provide a multi-modal fMRI platform. Here, we developed an MRI-guided robotic arm (MgRA) as a flexible positioning system with high precision to real-time assist optical fiber brain intervention for multi-modal animal fMRI. Besides the ex vivo precision evaluation, we present the highly reliable brain activity patterns in the projected basal forebrain regions upon MgRA-driven optogenetic stimulation in the lateral hypothalamus. Also, we show the step-wise optical fiber targeting thalamic nuclei and map the region-specific functional connectivity with whole-brain fMRI accompanied by simultaneous calcium recordings to specify its circuit-specificity. The MgRA also guides the real-time microinjection to specific deep brain nuclei, which is demonstrated by an Mn-enhanced MRI method. The MgRA represents a clear advantage over the standard stereotaxic-based fiber implantation and opens a broad avenue to investigate the circuit-specific functional brain mapping with the multi-modal fMRI platform.

[1] Research Group of Translational Neuroimaging and Neural Control, High-Field Magnetic Resonance, Max Planck Institute for Biological Cybernetics, 72076 Tuebingen, Germany. [2] Graduate Training Centre of Neuroscience, University of Tuebingen, 72076 Tuebingen, Germany. [3] Department of Neurology, Renmin Hospital of Wuhan University, Wuhan University, 430060 Wuhan, China. [4] Max Planck Institute for the Science of Light, 91058 Erlangen, Germany. [5] Athinoula A. Martinos Center for Biomedical Imaging, Massachusetts General Hospital and Harvard Medical School, Charlestown, MA 02129, USA. Correspondence and requests for materials should be addressed to X.Y. (email: xin.yu@tuebingen.mpg.de)

A multi-modal brain mapping platform for animals has been established by merging the fiber optic-mediated optogenetic activation and neuronal Ca^{2+} recording with functional magnetic resonance imaging (fMRI)[1–5]. Given its non-magnetic properties, the optical fiber can be used in combination with fMRI brain mapping without electromagnetic interference with the radio frequency (RF) transmission and magnetic gradient switching of the MR scanner[2,3,6,7]. The increased cellular specificity of genetic labeling reassures the advantageous usage of optical fiber recording/imaging to track neural spiking activity in the deep brain regions[8–13]. However, one emerged challenge is how to precisely target specific functional nuclei in the animal brain[8,14]. The procedure of fiber optic implantation in rodent studies has been commonly performed with conventional stereotaxic devices[2,3,7–11,14,15], but the success rate to precisely target the deep brain nuclei remains low, especially for the functional nuclei that cover only a few hundred microns space in the animal brain, e.g., the central thalamic nulcei[8]. A solution to precisely target the genetically labeled neuronal tracts or subdivisions of functional nuclei could significantly improve the reproducibility of basic scientific discoveries. Here, we report an MRI-guided robotic arm (MgRA) positioning device to maneuver the real-time fiber optic implantation into the animal brain inside a high-field MR scanner (14.1 T), intended for parallel optogenetics and/or calcium imaging and fMRI studies.

The genetic expression of channelrhodopsins (ChR2) has been extensively applied to target-specific cell types in the deep brain nuclei, such as the dopaminergic neurons in the midbrain[9], the orexin in the lateral hypothalamus (LH)[16,17] or noradrenergic neurons in the locus coeruleus[18]. The cell-type specific genetic labeling ensures the optogenetic activation on neuronal ensembles of interest assuming that the optical fiber is precisely located at the functional nuclei. However, the stereotaxic device-driven fiber optic implantation scheme shows little flexibility after the fiber tips are fixed in the brain for either fMRI mapping, electrophysiological recordings, or behavioral studies[8,19]. The precise coordinates of a certain functional brain nucleus can vary between different animals, and incorrect positioning may result in largely altered functional activation and behavioral outcomes. This systematic error, which is intrinsic to the blind optical fiber placement, can potentially conceal important discoveries and lead to inappropriate conclusions in causality analysis. Using MgRA assisted fiber-optic insertion in combination with real-time fMRI, we can provide a step-wise optogenetic activation scheme to allow multi-site targeting through a fiber insertion trajectory during the fMRI study. This strategy can not only improve the precision, but also provide a thorough view to examine the subtle differences in the whole brain activation patterns when targeting the sub-regions of the functional nuclei of interest.

Numerous efforts have been made to develop robotic positioning systems inside the MRI scanner for translational application from animals to the clinical practice, e.g., deep brain stimulation or brain tumor ablation[20–26]. In contrast to the growing access to robotic manipulation strategies inside large-bore MRI scanners (e.g., 1.5 or 3 T human scanner), there are only a handful of works that have implemented remote controlling systems inside high field MRI scanners with smaller bore (>7 T, <12 cm gradient bore size), which have been applied to adjust sample orientation within the B_0 field[27] or to tune RF coil arrays[28]. To the best of our knowledge, there is currently no MRI-compatible robotic control system to assist fiber optic insertion in small bore high field MRI scanners (>9.4 T) for optogenetic fMRI studies. Hence, as a proof-of-concept, we developed an MgRA to provide a flexible positioning system inside a 14.1 T MRI scanner which assists fiber optical brain intervention in animals. Besides an ex vivo precision evaluation, we present a series of in vivo studies showing the whole brain activity patterns upon optogenetic stimulation of MgRA-targeted nuclei in the LH or thalamus in a step-wise manner and with simultaneous fiber-optic calcium recordings to specify the region-specific optogenetic activation patterns. In addition, the MgRA system can be applied for region-specific deep brain microinjection. Here, we demonstrate a series of high precision brain interventional applications in the context of multi-modal neuroimaging using the MgRA system.

Results

Mechanical design of the MgRA with ex vivo operation. A stepper motor-driven MgRA was designed for real-time control of the insertion of an optical fiber into animal brains inside a 14.1
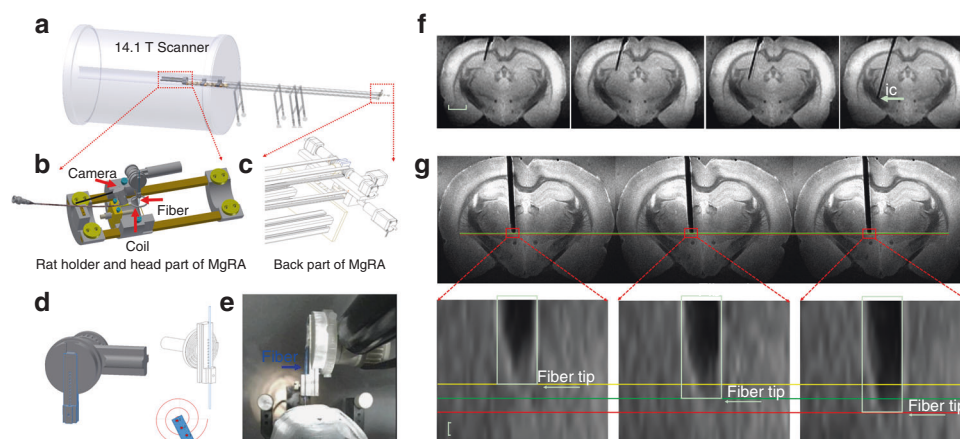
Fig. 1 3D view of the MgRA and its application in ex vivo studies. **a** Overview of the MgRA inside the 14.1 T MR scanner. **b** Schematic of the customized animal holder and head part of the MgRA. Both MR compatible camera and surface transceiver coil are included for monitoring the fiber optic insertion inside the MR scanner. **c** Stepper motors implemented at the back part of the MgRA to control up to four degrees-of-freedom movement. The long arm reaching 4.7 m away from the magnetic center point excludes the influence by the ultra-high magnetic field. **d** Schematic drawing of the Archimedean spiral design to transmit the dorsal–ventral movement. **e** Snapshot of the mechanically controlled fiber optic movement videotaped by the built-in camera. **f** Time-lapsed images showing the optical fiber targeting the hippocampus, thalamus, and internal capsule along the insertion trajectory. Scale bar, 2 mm. **g** Three continuous MRI anatomical images with step distance 50 μm (the MRI in-plane resolution is 50×50 μm^2, thus it can be seen that the distance moved in each step is approximately 50 μm). Scale bar, 50 μm

T scanner (Fig. 1a, 3D schematic view in Supplementary Movie 1, Supplementary Fig. 1). The MgRA contains two key parts: the front part (head of the MgRA) includes the driving pieces and a customized rat holder (Fig. 1b), and the back part accommodates the stepper motors to fulfill the optical fiber movement with multi-degree of freedom (Fig. 1c). The coupling of the actuator (back part) to the matching toothed pulley in the head was achieved by a synchronous belt drive (Fig. 1c) in a form-fit manner, without slippage and run at constant speed. Insertion of the optical fiber in the dorsal-ventral direction into the rat brain is executed using an Archimedean spiral mechanism to achieve high precision and accuracy (Fig. 1d). With a built-in MRI compatible camera, the insertion of the optical fiber could be monitored outside of the scanner to verify the effectiveness, safety, and feasibility of the MgRA (Fig. 1e and Supplementary Movie 2), simultaneously tracked with anatomical MRI. The assembly of all components provides the MgRA unique features in a portable frame that can be easily located inside the MRI room substituting the conventional subject table. A more detailed description of MgRA can be found in Methods and Supplementary Figs. 11–13.

The MgRA was first evaluated in perfused brains embedded in agarose (Fig. 1f), in order to simulate the procedure of intracerebral fiber insertion in the living animal. The optical fiber was first inserted into the agarose-embedded brain preparation in a 100 μm step-wise manner, and real-time MRI images were acquired to monitor the movement trajectory and to identify the location of the fiber tip (Supplementary Movie 3). Precision of the MgRA was determined as the smallest step in the dorsal–ventral direction that could be maneuvered based on the remote stepper motor controlling. Figure 1g shows the step-wise movement of the fiber inside the rat brain at 50 μm per step with high-resolution MRI time-lapsed 2D images (Supplementary Movie 4). It is worth noting that fiber insertion trajectories can be optimized with special angles to target specific deep brain nuclei or fiber bundles while avoiding disturbance of neural circuits, projection pathways of interest or certain brain vessels. For instance, an angled fiber optic insertion can be implemented to target the internal capsule to preserve the ascending pathway of the thalamocortical circuits (Fig. 1f and Supplementary Fig. 2). In summary, MgRA-based fiber optic insertion in the ex vivo brain verifies its functionality and demonstrates the stability in terms of remote motor control.

In vivo MgRA-driven fiber insertion with optogenetic fMRI. MgRA allows the insertion of optical fibers in vivo inside the 14 T MRI scanner, which induces great advantages for optogenetic fMRI studies[3,29,30]. To locate the fiber tip prior to intracerebral insertion inside the MRI scanner, two procedures were followed. First, we implemented two MRI-compatible cameras to visually locate the fiber tip, as well as the craniotomy on the animal skull (Fig. 2a and Supplementary Movie 5). Second, a prior application of a manganese-treated agarose gel was applied over the skull and the sequential lowering of the fiber was monitored with real-time anatomical MRI to locate the fiber tip as well as the craniotomy hole on the skull to guide the fiber targeting inside the brain (Supplementary Fig. 3). A more detailed description can be found in Methods, Supplementary Fig. 3. Figure 2b shows snapshots of the fiber tip outside the brain during the MgRA-driven fiber insertion. Figure 2c demonstrates an example of the in vivo fiber targeting of subcortical thalamic regions. Also noteworthy is the bleeding-induced T2-weighted signal drop when the fiber was inserted through the lateral ventricle (Fig. 2c). When a fiber tip first reaches a ventricle, its pushing force causes deformation of the surrounding ependyma, which can induce minor bleeding from the choroid plexus. This observation should raise a note of caution to target deep brain regions. The damage could be reduced by decreasing the insertion speed, which can be accomplished at approximately 20 μm/s with the MgRA (Supplementary Movie 5 and Supplementary Fig. 4).

Fiber optic insertions with customized angles can also be applied with MgRA for the in vivo animal fMRI environment. Figure 2d shows the step-wise fiber tip targeting to the hippocampus and ventral posteromedial nucleus (VPM) of the thalamus by inserting the optical fiber with a 40° angle from the midline. Figure 2e demonstrates the whole brain BOLD fMRI map upon optogenetic activation of either the hippocampus or the VPM, based on the MgRA-driven step-wise fiber tip localization. Thus, the implementation of MgRA in standard opto-fMRI workflows provides flexibility to guide an optical fiber along a certain insertion trajectory, allowing to target different nuclei in a single fMRI experiment, and hence, to study whole brain responses upon deliberate region-specific stimulation.

Whole brain fMRI with LH optogenetic activation. The MgRA can be used to target the deep brain nuclei with much higher precision for fiber optic-mediated optogenetic activation than the conventional stereotaxic-based fiber implantation on bench. For example, the LH is a heterogeneous nucleus with highly varied cell types across a few millimeter space in the ventral brain[31]. The MgRA-driven fiber optic positioning provides a reliable and precise targeting scheme for the LH optogenetic activation during fMRI. Figure 3a shows ChR2 expression with the AAV viral vector AVV9.CaMKII.ChR2.eYFP into the LH and the fiber optic trace to target the LH in the histological slice, as well as the MR image showing how the fiber tip coincides with the traced site of viral injection. The whole brain activation pattern upon the LH optogenetic activation is presented in Fig. 3b, showing the blood oxygen level dependent (BOLD) signal along the ascending projection to the basal forebrain from the LH. Figure 3c shows the temporal evolution of the optogenetically evoked BOLD signals in both LH and its projected basal forebrain regions with the mean time courses acquired at different stimulation durations. Figure 3d shows the mean BOLD signal time courses from both nuclei with varied optical light pulse frequencies and pulse widths (whole brain functional patterns at varied pulse width are shown in Supplementary Fig. 5). The BOLD amplitude dependency on the light pulse parameters provides strong evidence for reliable detection of the functional projections from the LH with optogenetic fMRI. It is also noteworthy that MgRA-driven fiber optic implantation ensures highly comparable activation patterns in the LH across different animals (results from 5 individual rats, Fig. 3b), as well as the activation of areas in the basal forebrain including the lateral preoptic area (LPO), medial preoptic area (MPA), and the strial part of the preoptic area (StA) (the co-registered brain atlas to the individual rat functional map, Fig. 3b). Additionally, the evoked calcium and BOLD signals in the barrel cortex (BC) were observed in these animals upon somatosensory whisker stimulation (Supplementary Fig. 6), which indicates a stable physiological state of the animal and therefore validates the biological data acquired from these experiments. These results indicate that MgRA provides high targeting accuracy and effectiveness to target deep brain circuits and produce optogenetically-driven brain activation in a highly reliable manner.

Step-wise optogenetically driven fMRI and calcium recording. The flexibility and high precision of MgRA-driven fiber optic targeting was further verified in a series of experiments that combined optogenetic activation with concurrent fMRI and calcium fiber optic recording (Fig. 4a). This multi-modal fMRI
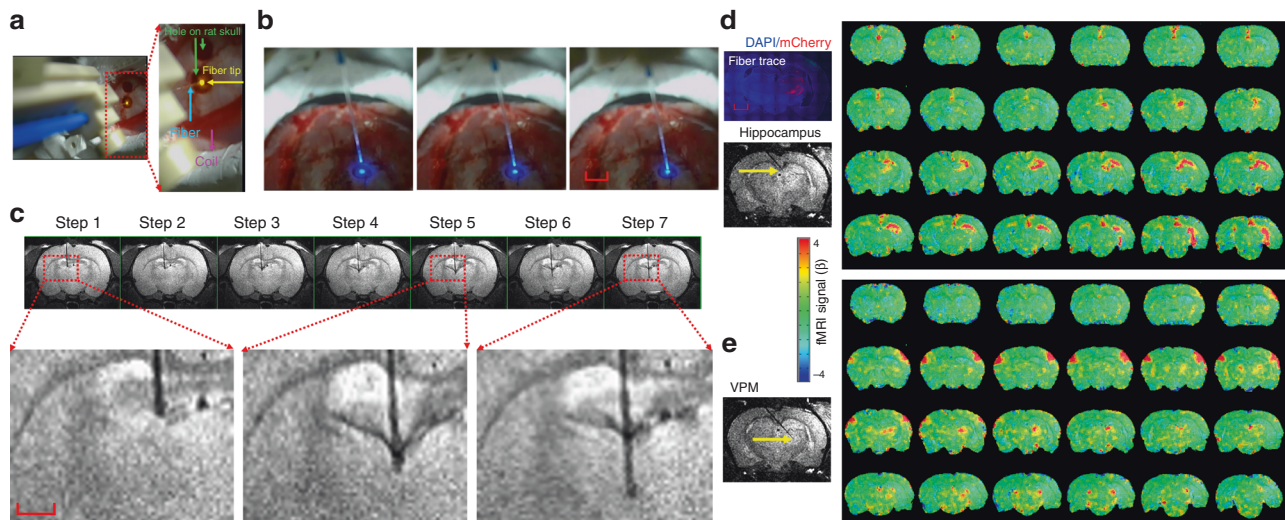
Fig. 2 Evaluation of MgRA for in vivo studies and brain-wide opto-fMRI patterns in multiple targets. **a** Snapshot of the optical fiber (tip with 589 nm wavelength laser light, yellow arrow) positioned above the burr hole (green arrow) on the skull of an anesthetized rat with the driving piece of the head part. **b** Camera-based fiber optic movement for three steps outside the rat brain. The fiber tip delivers blue laser light (473 nm wavelength). The bright ring-structure above the rat skull is the RF surface coil. Scale bar, 2 mm. **c** Potential collateral damage from the choroid plexus when the fiber was lowered to pass through the lateral ventricles, shown as a dark signal below the hippocampus. The step size was 300 μm. Scale bar, 1 mm. **d** Left, histological image demonstrates ChR2-mCherry expression in most of the thalamus and part of hippocampus. Red, ChR2-mCherry; blue, 4′,6-Diamidino-2-phenylindole (DAPI). Right, the fiber tip targets the hippocampal area and the BOLD fMRI map shows the activated area primarily located in the ipsilateral hippocampal structure. Scale bar, 2 mm. **e** The fiber tip targets the ventral postero-medial (VPM) thalamus and map of BOLD activity was detected in bilateral vibrissal S1 cortex in response to blue light stimulation. (For both (**d**) and (**e**), 3D whole brain EPI: 400 μm isotropic resolution, 1.5 s repetition time; stimulation block design: 8 s on 37 s off; laser pulse: 10 ms, 5 Hz, 3.7 mW/200 μm core diameter of fiber tip)

scheme with MgRA enables real-time feedback at the level of the whole brain (via fMRI) and specifically from the fiber tip (via optical fiber) regarding the activation of the projection structures upon region-specific stimulation. Here, calcium imaging was acquired from the neurons in the BC that received afferents from the subcortical thalamic region by using the calcium reporter GCaMP6[4,5,12]; optogenetic stimulation was performed on the VPM thalamic nuclei, after expression of the light-sensitive protein ChR2 (Fig. 4b–d)[2,3,32]. The recording fiber was directly implanted to record the GCaMP6f-mediated calcium signal in the BC, while the optogenetic activation fiber was controlled by the MgRA inside the scanner with real-time anatomical and functional MRI to track the insertion trajectory. The MgRA guided the fiber tip to deliver the optogenetic activation at multiple sites along the insertion trajectory (Fig. 4e and Supplementary Movie 6). Evoked calcium and BOLD signals from the somato-sensory cortex ipsilateral to the targeted thalamic nucleus increased in a stepwise manner as the optical fiber was moved closer to the VPM region, while, after the fiber bypassed the VPM region, BOLD and calcium signal decreased accordingly (Fig. 4f–i). There was a slightly different stepwise fMRI response from the contralateral somatosensory cortex as well (Fig. 4h, i), which has been previously reported with electrical stimulation[33,34]. To further demonstrate the reliability of MgRA, five power levels of light pulses were used to trigger increased BOLD and simultaneous calcium signals (Supplementary Fig. 7). Moreover, by altering the frequency of the light from 0.5 to 5 Hz, we could observe a fully recovered evoked calcium baseline signal at 0.5 Hz and elevated calcium signals from 1 to 3 Hz, while at 5 Hz, the overall plateau amplitude was not further increased (Supplementary Fig. 8). The BOLD signal increased with higher frequency, but not at 5 Hz, which was consistent with the calcium signal dynamics (Supplementary Fig. 8). Results from two additional rats with different or similar insertion trajectories

confirmed the reliability of the stepwise optogenetic activated fMRI and calcium signals acquired using the MgRA (Supplementary Figs. 9 and 10). These experiments further demonstrate the unique capability of the MgRA to specifically target sub-cortical nuclei, which, combined with cortical recordings in the projection area, allow unequivocal stimulation of the target sites.

MgRA-driven Mn-injection into CL and LH. The MgRA can also be used to guide the real-time microinjection with high precision inside the MRI scanner. MnCl$_2$ solution was used as the MR contrast agent and a modified MPRAGE sequence[35] (Mdeft, ~4 min) was implemented to detect the manganese-enhanced T1-weighted MRI signal[15,36–38]. As shown in Fig. 5a, a hollow core optical fiber[39–41] was used to target the central lateral thalamic nucleus (CL) and Mn solution was delivered in two consecutive steps. The initial stop was introduced to target the corpus callosum with a small dosage of Mn delivery (Fig. 5b), illustrating the real-time guided injection to target the callosal fibers with a few hundred micron thickness. When the fiber tip as located at the CL (position was verified with a T2-weighted MR image (RARE) overlapped with the brain atlas), Mn solution was injected for three times to show dose-dependent signal changes in the T1-weighted Mdeft images acquired before and after Mn injection (Fig. 5b). This result demonstrates the real-time injection capabilities of the MgRA.

Besides the multiple stops along the single trail of injection trajectory, the MgRA can be used to drive multi-trial microinjection, e.g., to the lateral hypothalamic nucleus from the same rat, inside the MRI scanner. As shown in Fig. 5c, the fiber tip was guided to target the LH. The Mdeft images were acquired before and after the injection (3 times, Fig. 5d, e), showing clear effective Mn delivery to the LH. In addition, we continuously acquired the Mdeft images within the first ~1 h following the injection, showing highly robust and confined Mn-enhanced signal of the
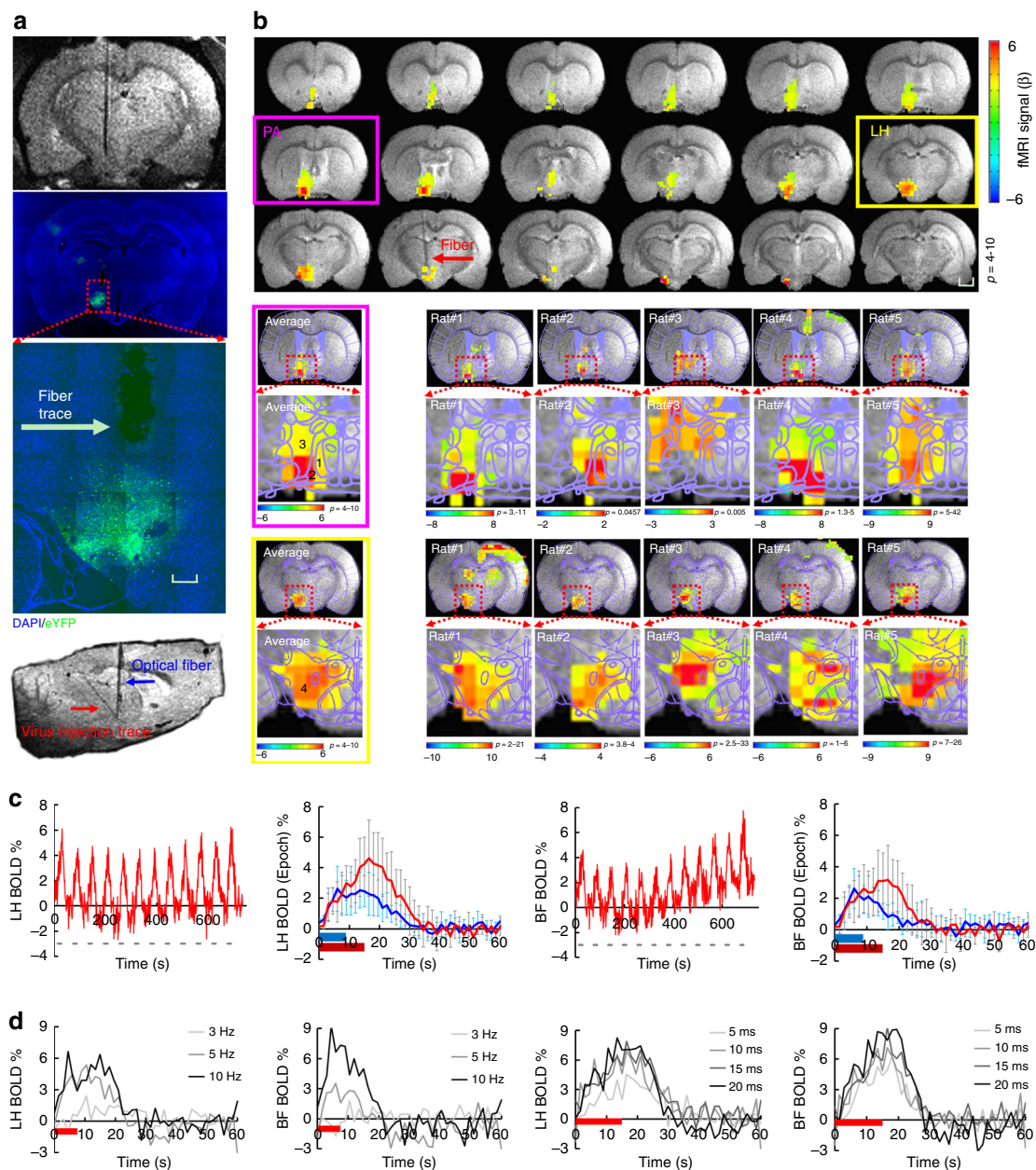
Fig. 3 MgRA-driven fiber optic targeting of the lateral hypothalamic nuclei with optogenetic fMRI. **a** Top: representative RARE anatomical image used to clarify the optical fiber location driven by MgRA for optical stimulation in LH. Middle: representative wide-field fluorescence image illustrating robust ChR2-eYFP expression focused on LH. Fiber optic insertion trace marked with white arrow. Scale bar, 200 μm. Bottom: sagittal RARE anatomical image showing the fiber optic trace (blue arrow) and virus injection trace (red arrow). **b** Top: average fMRI map of brain-wide activity during optogenetic stimulation of LH neurons at 5 Hz, 20 ms pulse width, 15 s duration. Middle: averaged evoked BOLD map (left) and the same map from 5 individual rats (right) zoomed in on the basal forebrain (BF) showing activation of the lateral preoptic nucleus (LPO) and medial preoptic area (MPA), overlaid with the brain atlas. Bottom: average evoked BOLD map (left) and 5 individual rats (right) in lateral hypothalamic region, overlaid with the brain atlas. GLM-based t-statistics in AFNI is used. Scale bar, 2 mm. **c** Average time courses of significantly modulated voxels showing fMRI signal changes within the ipsilateral LH and BF (n = 5 animals) upon optogenetic stimulation of block design: 15 s on/45 s off, 12 epoch, 20 ms light pulse, 5 Hz, 18.9 mW. The individual hemodynamic response shows the average BOLD signal upon different stimulation durations (8 s in blue, 15 s in red). Error bars represent mean ± SD across 5 animals. **d** Average stimulation duration-locked time evolution for both LH and BF depicting the frequency-dependent hemodynamic responses at 3, 5, and 10 Hz with 8 s stimulus duration, as well as pulse-width-dependent hemodynamic responses at 5, 10, 15, and 20 ms with 15 s stimulus duration, from one representative rat

targeted regions with limited diffusion (Fig. 5f and Supplementary Movie 7). The MgRA-driven microinjection was reproduced in multiple animals, suggesting a highly robust performance of the MgRA to target deep brain nuclei for injection purposes, as quantified in Fig. 5g. The high spatial specificity of MgRA-driven

microinjection can be used to improve the tract-tracing studies with MEMRI[15,36–38], as well as to optimize the real-time in vivo neuromodulation or molecular MRI by direct intracranial injection of drugs[42–44] and MRI contrast sensors for neuro-transmitters[45–49].
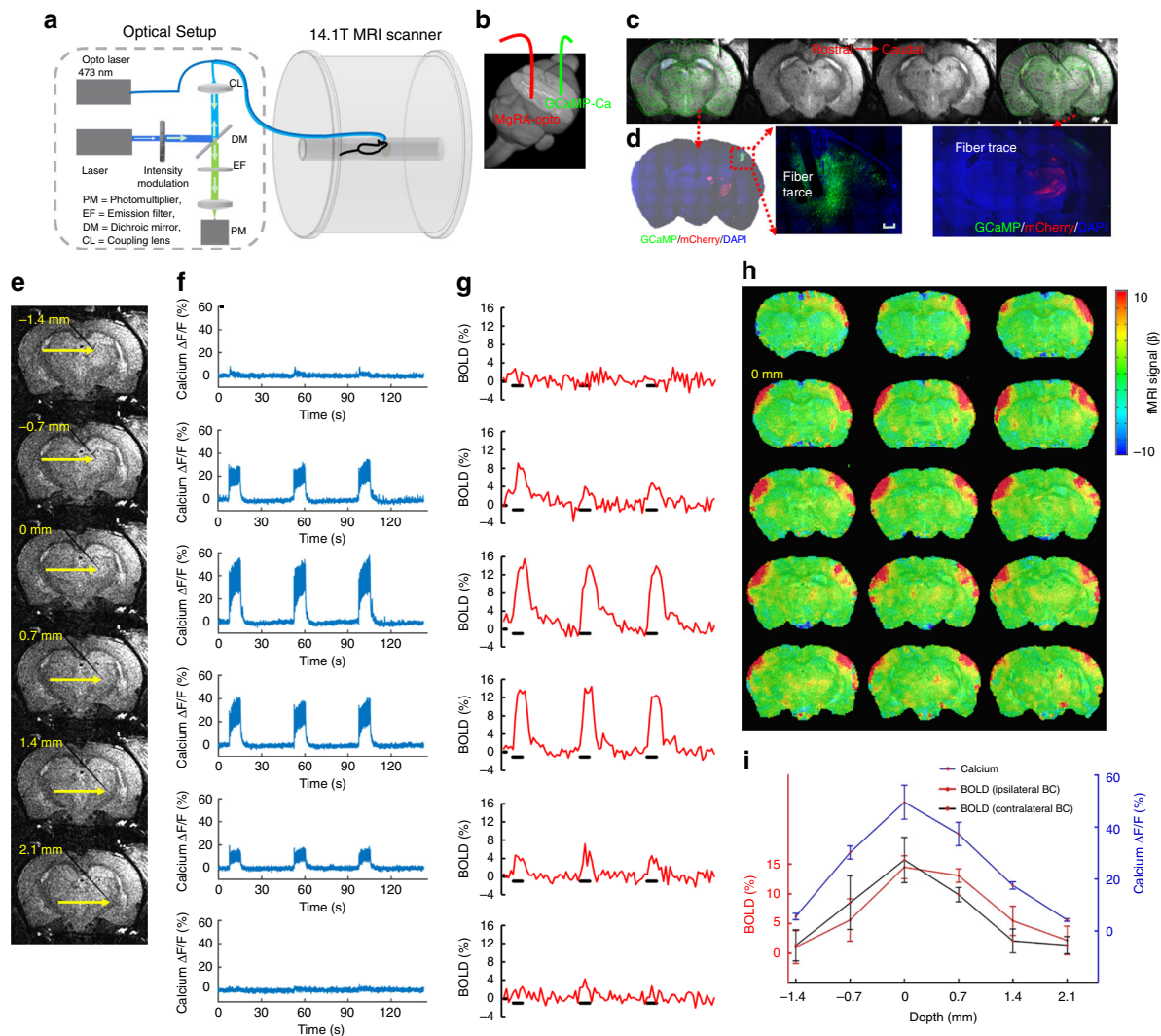
Fig. 4 MgRA-driven stepwise optogenetic activation of the thalamic nuclei with simultaneous fMRI and neuronal Ca^{2+} recordings. **a** Schematic drawing of the experimental setup to conduct optogenetic fMRI with simultaneous fiber optic calcium recording. The optical setup was placed outside the 14.1 T scanner. Opto Laser: laser for optogenetics. **b** Schematic of the fiber optic insertion inside the rat brain (3D view) with MgRA-controlled optical fiber for optogenetic activation (red) and a second optical fiber for calcium recording (green) in the barrel cortex. **c** The anatomical MRI images confirm the location of the recording fiber and the stimulation fiber targeting the VPM thalamic region. The brain atlas is superimposed on the anatomical image (green). **d** The immunostaining images show the ChR2 expression in the thalamic region (ChR2-mCherry marked in red), as well as the GCaMP6f expression (green) in the vibrissal S1 cortical neurons (BC) with the fiber trace. Scale bar, 200 μm. **e** Anatomical RARE MR images illustrate the fiber tip location at 6 steps, at a step-size of 700 μm. **f** Percentage changes of the evoked calcium signal for 3 epochs upon light stimulation (3 Hz, 10 ms pulse width, 3.7 mW laser power, 8 s on 37 s off block design). **g** Simultaneous BOLD signals for 3 epochs within the ipsilateral somatosensory cortex (see (h)). **h** Evoked BOLD fMRI map when the fiber tip was positioned at 0 mm along the insertion trajectory (zero considered as the position that leads to the peak fMRI and calcium signals). **i** Average amplitudes of the ipsilateral evoked calcium and BOLD signals of both hemispheres as a function of the fiber tip locations. Error bars represent mean ± SD

Discussion

This work presents an MRI compatible robotic arm as the navigation technique for accurate placement of optical fibers in multimodal fMRI studies in animals using ultra high-field MRI (14.1 T scanner). The MgRA was first developed and improved with a series of phantom tests and was posteriorly evaluated in vivo for deep brain optical fiber placement. MgRA-driven optogenetic activation at subcortical nuclei, e.g., LH and VPM, in a stepwise manner not only demonstrates the high precision of MgRA to target subcortical brain nuclei as deep as 8–9 mm from the skull surface, but also increases the reproducibility of the region-specific optogenetic activation for the whole-brain fMRI mapping in combination with the concurrent fiber optic calcium recordings. Also noted is that the mobility range of the MgRA (10 mm

in the rostral–caudal and medial–lateral directions) is sufficient to reach any brain structure in small animals for optogenetic fMRI and intracellular calcium recording. In addition, the MgRA was applied for real-time microinjection to specific deep brain nuclei, as demonstrated with an Mn-enhanced MRI method, demonstrating its microinjection capabilities for contrast agent or drug delivery with high precision inside the MRI scanner.

The main challenge when targeting deep brain structures is the potential error that appears between the actual and the calculated coordinates due to the variability in bregma location, skull thickness/angles, and potential shift of brain structures within the cranium after dura removal[50–52]. This potential error is particularly problematic when targeting some functional nuclei or neuronal fiber tracts of the rat brain that are less than 2–300 μm in
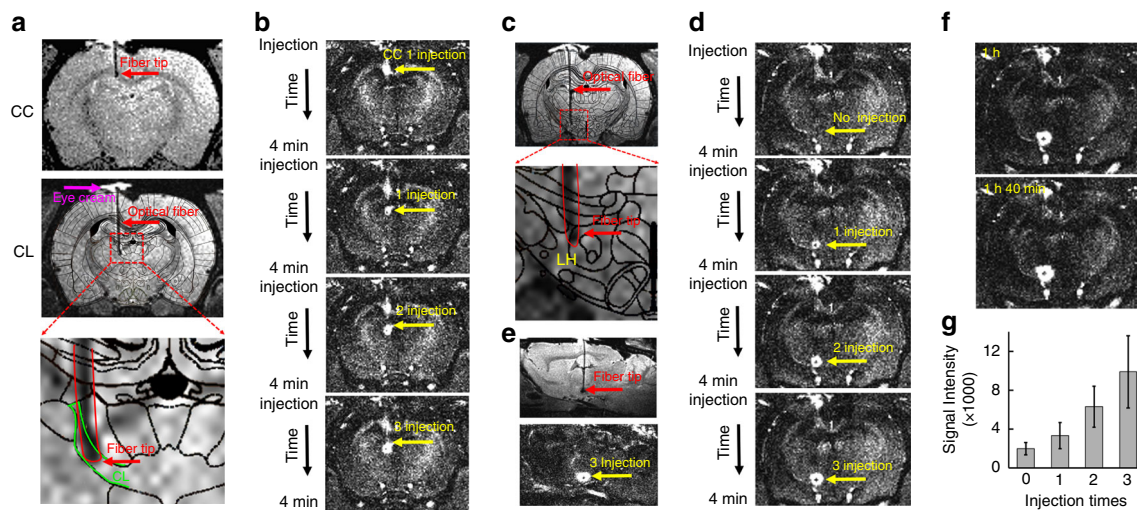
Fig. 5 MgRA-driven Mn-injection into CL and LH. **a** Top: the representative RARE anatomical image used to clarify the optical fiber location driven by MgRA for Mn injection in CC. Middle: the atlas overlapped RARE images to illustrate the fiber tip location at the CL. Eye cream is covering the craniotomy (magenta arrow). Bottom: enlarged image of fiber location. **b** T1-weighted MPRAGE image (Mdeft) showing enhanced signal from Mn injection site in the CC and CL with dose-dependency. **c** Top: the atlas overlapped RARE images to illustrate the fiber tip location at the LH, Bottom: enlarged image of fiber location. **d** T1-weighted MPRAGE image showing enhanced signal from Mn injection site in the LH with dose-dependency. **e** Sagittal view of RARE anatomical image and MPRAGE image after MnCl$_2$ solution injection. **f** T1-weighted MPRAGE image at 1 h and 1 h 40 min after the injection. **g** The analysis of MEMRI signal at no injection, 1 injection, 2 injection, and 3 injection times, as shown in (**b**, **d**) ($n = 5$ injection points from 3 animals). Error bars represent mean ± SD

one of their dimensions, such as the central thalamic nuclei or corpus callosal fibers[38,53]. This problem can produce high variability when we try to target the deeper brain nuclei, e.g., LH, since longer trajectories are subjected to larger errors[8,14]. In order to optimize the positioning of the optical fiber into precise coordinates of the rat brain, we propose to avoid the atlas-base blind implantation by using a real-time feedback strategy that allows visualization of the whole brain with MRI during fiber insertion. We designed an MRI-compatible robotic arm which allows lowering the optical fiber inside the rat brain with real-time MRI scanning. By combining MRI guidance with the precise control of four stereotactic parameters (radial angle, rostral–caudal, dorsal–ventral, medial–lateral), the MgRA can fine-tune the fiber positioning to conduct highly reproducible and stepwise optogenetic fMRI studies.

The number of applications for robotic arms in animal research is considerably increased as a result of their potential combination with MRI. Examples include an MR image-guided mini-DBS system for BOLD activation during subthalamic nucleus DBS in nonhuman primates in a 3 T scanner[26], an angle positioning system to increase the image signal intensity of fibrous microstructure in a 9.4 T 12 cm-bore scanner[27], an integrated system, driven by piezoelectric actuators, for auto-tuning of a multichannel transceiver array at 7 T[28] or MRI-compatible systems for focused ultrasound experiments in rodents in 3 T scanners[54,55]. Here, we developed a stepper motor-controlled compacted MgRA system in a 14.1 T horizontal MRI scanner with built-in MRI compatible cameras and RF surface coils to drive fiber optic insertion for optogenetic fMRI studies with concurrent intracellular calcium recordings. To our knowledge, this is the first time to combine the multi-modal fMRI neuroimaging platform with the MRI-guided robotic controlling system for in vivo rodent brain functional mapping.

There are two key advantages that need to be highlighted from the mechanical design of the MgRA system. In high-field MRI scanners, the open space inside the magnetic bore above the animal brain is usually less than 3–4 cm, which significantly limits the kinematic design options for mechanical movement. Also, the

ultra-high field (>11.7 T) also limits the commercially available motor supplies that avoid the electromagnetic interference with the MR scanning. We designed the MgRA head-probe based on an Archimedean spiral mechanism to achieve high precision and accuracy to maneuver the optical fiber insertion at less than 50 µm step-size along the dorsal–ventral axis (Fig. 1g, Supplementary Fig. 11, and Supplementary Movie 4). This head-probe is controlled by a synchronous belt drive, which can carry up to 4 degree-of-freedom movements inside the horizontal bore of the 14.1 T MRI scanner (Supplementary Fig. 12), and only occupies 1.5–2 cm space.

To deal with the MRI compatibility, in addition to hydraulic[56,57] or pneumatic[27,58–60] actuators, other types such as ultrasonic or piezoelectric motors, which have been the favorite so far due to their non-magnetic core, short response time and small size[61,62], could have been utilized. However, no commercially available piezo motors are available for the 14.1 T MRI scanner and it has been recently shown that piezo motors could induce geometric distortions in MR images even at a lower magnetic field strength[63,64]. Also, different MRI sequences could have effects on the behavior of ultrasonic motors[65]. To address the compatibility issue, remotely actuated MR-compatible manipulators were implemented using drive shafts, belts, chain drive, and linkages to transfer the motion to the distant actuated points[66–68]. We have applied the long robotic arm to allow us to apply the regular stepper motor to control the optical fiber insertion. As shown in the Supplementary Movies 2–5, the mechanical control of the optical fiber insertion remains highly precise and reliable in both ex vivo and in vivo tests. Our MgRA design not only provides a highly robust mechanical controlling system, but also solves the MRI compatibility issue with a reliable and economically affordable solution. We will further optimize our MgRA system by shortening the robotic arm and implementing the piezo motors with a safe distance to avoid electromagnetic interference.

Besides fulfilling the role of accurately placing the fiber tip at the desired coordinates, the MgRA provides a flexible platform (Fig. 1g) to identify, de novo, the ideal targets for deep brain

stimulation in pre-clinical studies. This could be easily investigated with the MgRA by moving the stimulating fiber and running opto-fMRI at different locations in one single study, particularly for "hypothesis-free" brain activity mapping studies. This application will be critical to optimize and specify the ideal subcortical targets aiming at controlling pathological tremor or searching for more reliable treatment for depression in animal models[69–71]. Importantly, certain effects inherent in the insertion of electrodes or optical fiber into the brain can be visualized and avoided using the MgRA strategy. One example is the case of the potential collateral damage to the choroid plexus (Fig. 2c) or other blood vessels, which could be well monitored by real-time imaging and avoided by changing the trajectory of the fiber. This is a particularly relevant feature of the MgRA, as it contributes to the maintenance of certain integrity of the surrounding tissue, which is beyond the capabilities of the standard implantation techniques with stereotactic devices and is crucial for potentially translational studies, as raised in a report showing MRI-guided cell transplantation into the brain[72].

Several limitations pertaining to the first version of the MgRA should be considered when interpreting the results of this study and for future optimization of the MgRA in high field MRI scanner for animal imaging. Firstly, the angle/direction of the optical fiber cannot be changed once that it has been placed inside the brain parenchyma, as this would lead to excessive tissue damage and/or bleeding. Instead, in case needed, the optical fiber should be withdrawn and reinserted; thus it is crucial to improve the algorithm to calculate the trajectory based on the location of the optical fiber tip in the agarose covering the craniotomy outside of the brain parenchyma. Secondly, it is noteworthy that, because of the long arm to keep the stepper motors work properly outside of the MRI scanner, the most precise movement occurs along the ventral–dorsal direction (Fig. 1g and Supplementary Movie 4). It will be an important step forward to implement the piezo motors with a safe distance to avoid electromagnetic interference, which would allow to dramatically shorten the robotic arm and, consequently, to optimize of the precision in all the axis. Thirdly, although we acquired the 3D anatomical images of the rat brain, the major registration procedure between atlas and MRI images is still based on a 2D registration algorithm, which is applied to control the fiber tip movement along the dorsal–ventral direction. In the future development, we will provide a real-time 3D registration system to take advantage of the full motor control movement capability of the MgRA system to achieve a fully automatic performance. Lastly, the precision measurement of the MgRA can be directly evaluated based on the real-time anatomical MRI images. However, the best resolution acquired so far in our MRI scanner is $50 \times 50\ \mu m$ in-plane. The MRI spatial resolution is much lower than the mechanistic movement precision provided by the MgRA system. For future piezo-based micron-resolution motor control system, the implementation of an optical encoder inside the ultra-high magnetic field will be needed for the close-loop feedback.

In summary, the real-time MRI-guidance in a robotic controlling system is verified and practiced for the optical fiber brain intervention in animals using the high field MRI scanner (>14 T). This MgRA positioning system serves as a key component for the future multi-modal fMRI platform merging concurrent fMRI with optogenetics, fiber optic-mediated optical imaging, micro-injection, and even electrophysiological recordings. The high flexibility and precision of MgRA to target the deep brain nuclei with neural circuit-specificity expands the brain functional mapping studies from the cellular levels, to the neural circuit levels, and eventually to the systems' levels in combination with behavioral tests in animals.

Methods

MgRA system. The MgRA was manufactured by the Fine Mechanical and Electrical Workshop in the Max Planck Institute for Biological Cybernetics, Tuebingen, Germany. This system consists of a positioning module, the head of the MgRA, and a custom-designed user interface. The positioning module (back part) accommodates the stepper motors (ST4118D1804-B, Nanotec, Germany) to fulfill the optical fiber movement with multi-degree of freedom, and the head of the MgRA (front part) includes the driving pieces, cameras, and a customized rat holder (Fig. 1b). The coupling of the actuators (back part) to the matching toothed pulley in the head was achieved by a synchronous belt (Optibelt OMEGA 3M, OPTI-BELT, Germany) drive in a form-fit manner. The driving pieces with Archimedean spiral mechanism were manufactured manually or with a 3D printer (Form 2, Formlabs, Germany). The detailed design and components are shown in Fig. 1a–c, Supplementary Figs. 11–13, with a table of all components and the European patent as the following link: https://patentscope.wipo.int/search/en/detail.jsf?docId=EP215319263&tab=PCTDESCRIPTION&maxRec=1000. The movements include three dimensions like conventional stereotactic devices, as well as pitch and yaw (manually). With MRI-compatible cameras (RS-OV7949-1818, Conrad Electronic, Germany), the user can watch the fiber insertion in real time, while the robot is executing a maneuver. If any movement needs to be modified, the user can start, stop, change, or resume the fiber movement at any time from the user-interface. Most of the other components are constructed from fully MRI-compatible materials like plastic, carbon fiber, and a minimal amount of non-ferrous metals like brass and anodized aluminum to avoid eddy currents and deterioration of magnetic field homogeneity. The MRI-compatible arm including the head part and aluminum holder were placed inside the MRI scanner room. Digital components including stepper motors (ST4118D1804-B, Nanotec, Germany), the motor controller (SMCI33-1, Nanotec, Germany) and motor power supply (NTS-24V-40A, Nanotec, Germany), were placed outside the scanner room (Supplementary Fig. 1).

Viral injection. The study was performed in accordance with the German Animal Welfare Act (TierSchG) and Animal Welfare Laboratory Animal Ordinance (TierSchVersV). This is in full compliance with the guidelines of the EU Directive on the protection of animals used for scientific purposes (2010/63/EU). The study was reviewed by the ethics commission (§15 TierSchG) and approved by the state authority (Regierungspräsidium, Tübingen, Baden-Württemberg, Germany). A total of 21 male Sprague–Dawley rats were used in this study.

Intracerebral viral injection was performed in 3–4-week-old male Sprague–Dawley to express the viral vectors containing the calcium-sensitive protein (GCaMP for calcium recording) or the light-sensitive protein channelrhodopsin-2 (ChR2 for optogenetics) in neurons. The construct AAV5.Syn.GCaMP6f.WPRE.SV40 (2.818e13 genome copies per milliliter) was used to express GCaMP in the BC and the constructs AAV9.CAG.hChR2(H134R)-mCherry.WPRE.SV40 (2.918e13 genome copies per milliliter) and AAV9.CaMKII.hChR2(E123A)-eYFP.WPRE.hGH (1.19e13 genome copies per milliliter) were used to express ChR2 in the thalamus and LH, respectively. Rats were anesthetized with 1.5–2% isoflurane via nose cone and placed on a stereotaxic frame, an incision was made on the scalp and the skull was exposed. Craniotomies were performed with a pneumatic drill so as to cause minimal damage to cortical tissue. For optogenetics, a volume of 0.6–1 μL was injected using a 10 μL syringe and 33-gauge needle. The injection rate was controlled by an infusion pump (Pump 11 Elite, Harvard Apparatus, USA). The stereotaxic coordinates of the injections were 2.5 mm posterior to Bregma, 5.0 mm lateral to the midline, 0.8–1.4 mm below the cortical surface to target the BC; 2.6–2.7 mm posterior to Bregma, 2.8 mm lateral to the midline, 5.5–6.0 mm below the cortical surface for the ventral posterior medial nucleus of thalamus (VPM); and 2.75–2.85 mm posterior to Bregma, 1.1 mm lateral to the midline, 7.5–7.9 mm below the cortical surface for LH. After injection, the needle was left in place for approximately 5 min before being slowly withdrawn. The craniotomies were sealed with the bone wax and the skin around the wound was sutured. Rats were subcutaneously injected with antibiotic and painkiller for 3 consecutive days to prevent bacterial infections and relieve postoperative pain.

Animal preparation for fMRI. Anesthesia was first induced in the animal with 5% isoflurane in chamber. The anesthetized rat was intubated using a tracheal tube and a mechanical ventilator (SAR-830, CWE, USA) was used to ventilate animals throughout the whole experiment. Femoral arterial and venous catheterization was performed with polyethylene tubing for blood sampling, drug administration, and constant blood pressure measurements. After the surgery, isoflurane was switched off and a bolus of the anesthetic alpha-chloralose (80 mg/kg) was infused intravenously. A mixture of Alpha-Chloralose (26.5 mg/kg/h) and pancuronium (2 mg/kg/h) was constantly infused to maintain the anesthesia/keep the animal anesthetized and reduce motion artifacts.

Fiber optic implantation and optogenetic stimulation. Before transferring the animal to the MRI scanner, 2 craniotomies were performed. Briefly, the animal was placed on a stereotaxic frame, the scalp was opened and two ~1.5 mm diameter burr holes were drilled on the skull. The dura was carefully removed and an optical fiber with 200 μm core diameter (FT200EMT, Thorlabs, Germany) was inserted

into the BC, at coordinates: 2.75–3.3 mm posterior to Bregma, 5.0 mm lateral to the midline, 1.2–1.4 mm below the cortical surface. An adhesive gel was used to secure the calcium recording fiber to the skull. The craniotomy for optogenetics (in VPM or LH) was covered by agarose gel for robotic arm-driven fiber insertion inside the MRI scanner. Toothpaste was applied within the ears to minimize MR susceptibility artifacts for the whole brain fMRI mapping. The eyes of the rats were covered to prevent stimulation of the visual system during the light-driven fMRI.

For optogenetic stimulation, square pulses of blue light (473 nm) were delivered using a laser (MBL-III, CNI, China) connected to the 200 µm core optical fiber (FT200EMT, Thorlabs, Germany) and controlled by Master 9 (Master-9, A.M.P.I., Israel). The light intensity was tested before each experiment, and was calibrated with a power meter (PM20A, Thorlabs, Germany) to emit 0.6–40 mW from the tip of the optical fiber for LH and thalamus. The power levels used for light-driven fMRI studies did not induce pseudo-BOLD signal due to heating effects, by testing in regions of interest both with and without ChR2 expression.

Immunohistochemistry. To verify the phenotype of the transfected cells, opsin localization, and optical fiber placement, perfused rat brains were fixed overnight in 4% paraformaldehyde and then equilibrated in 15 and 30% sucrose in 0.1 M PBS at 4 °C. 30 µm-thick coronal sections were cut on a cryotome (CM3050S, Leica, Germany). Free-floating sections were washed in PBS, mounted on microscope slides, and incubated with DAPI (VectaShield, Vector Laboratories, USA) for 30 min at room temperature. Wide-field fluorescent images were acquired using a microscope (Zeiss, Germany) for assessment of GCaMP expression in BC, ChR2 in LH and VPM. Digital images were minimally processed using ImageJ to enhance brightness and contrast for visualization purposes.

Optical setup. An OBIS laser was used as excitation light source (OBIS 488LS, Coherent, Germany) with a heat sink to enable laser operation throughout the entire specified temperature range from 10 to 40 °C. The light passed through a continuously variable neutral density filter (NDC-50C-2M-B, Thorlabs, Germany) and was reflected on a dichroic beam splitter (F48-487, AHF analysentechnik AG, Germany). The beam was collected into an AR coated achromatic lens (AC254-030-A, Thorlabs, Germany) fixed on a threaded flexure stage (HCS013, Thorlabs, Germany) mounted on an extension platform (AMA009/M, Thorlabs, Germany) of a fiber launch system (MAX350D/M, Thorlabs, Germany). The laser beam was injected into the fiber and propagated to the tip. The emitted fluorescence was collected through the fiber tip, propagated back and collimated by the achromatic lens, passed through the dichroic beam splitter and filtered by a band-pass filter (ET525/50M, Chroma, USA) and focused by an AR coated achromatic lens (AC254-030-A, Thorlabs, Germany). A silicon photomultiplier module (MiniSM 10035, SensL, Germany) was applied to detect the emitted fluorescence. The entire optical system was enclosed in a light isolator box. The photomultiplier output was amplified (gain = 100) by a voltage amplifier (DLPVA-100-BLN-S, Femto, Germany), digitized and detected by Biopac system (MP150 System, BIOPAC Systems, USA).

MRI image acquisition. All images were acquired with a 14.1 T/26 cm horizontal bore magnet interfaced to an Avance III console and equipped with a 12 cm gradient set capable of providing 100 G/cm over a time of 150 µs. A transceiver single-loop surface coil with an inner diameter of 22 mm was placed directly over the rat head to acquire anatomical and fMRI images. Magnetic field homogeneity was optimized first by global shimming for anatomical images and followed by FASTMAP shimming protocol for EPI sequence.

Anatomical images were acquired for approximate fiber location using 3D FLASH MRA sequence with the following parameters: repetition time, 20 ms; echo time, 2.82 ms; FOV: 2.28 cm × 2.28 cm × 2.28 cm, matrix = 114 × 114 × 114, spatial resolution = 0.2 mm × 0.2 mm × 0.2 mm. A high-resolution RARE sequence was used accurately identify the optical fiber in the coronal plane, with the following parameters: repetition time, 1200 ms; echo time, 7 ms; FOV: 1.92 cm × 1.68 cm, matrix = 128 × 112, resolution = 0.15 mm × 0.15 mm, slice thickness = 0.5 mm, RARE factor = 8, averages = 16.

Higher resolution (50 µm) RARE sequence, specifically for Fig. 1f, g, to accurately identify the optical fiber in the coronal plane, with the following parameters: repetition time, 1500 ms; echo time, 11.0428 ms; FOV: 1.92 cm × 1.56 cm, matrix = 384 × 312, resolution = 50 µm × 50 µm, slice thickness = 0.75 mm, RARE factor = 6, averages = 6.

For Mn injections and Mn tracing studies, rats received 150 nL of 5 mM MnCl$_2$ (MnCl$_2$, Sigma-Aldrich, Germany) solution for three times delivered by a hollow core photonic crystal fiber (diameter: ~240 µm)[39–41], manufactured by the Division of Photonic Crystal Fibre Science at Max-Planck Institute for the Science of Light, Erlangen, Germany. A magnetization prepared rapid gradient echo (MP-RAGE) sequence[35] was used. Eight coronal slices with FOV = 1.92 × 1.92 cm, matrix 128 × 128, thickness = 0.7 mm, (TR = 4000 ms, echo TR/TE = 15/1.7 ms, TI = 1000 ms, number of segments = 4, averages = 2), were used to cover the area of interest at 150 µm in-plane resolution with total imaging time 4 min 16 s. A same field of view T2-weighted RARE sequence was used with the following parameters: repetition time, 3000 ms; echo time, 8.3333 ms; FOV: 1.92 cm × 1.92 cm, matrix = 128 × 128,

resolution = 150 µm × 150 µm, slice thickness = 0.7 mm, RARE factor = 6, averages = 4.

Functional MRI acquisition. Adjustments to echo spacing and symmetry, and B$_0$ compensation were set up first. Functional images were acquired with a 3D gradient-echo EPI sequence with the following parameters: echo time 12.5 ms, repetition time 1.5 s, FOV 1.92 cm × 1.92 cm × 1.92 cm, 48 × 48 × 48 matrix size, spatial resolution = 0.4 mm × 0.4 mm × 0.4 mm. To reach steady state 10 dummy scans were used. For anatomical reference, the RARE sequence was applied to acquire 48 coronal slices with the same geometry of the fMRI images.

For fMRI studies, needle electrodes were placed on the forepaw or whisker pads of the rats, and electric pulses (333 µs duration at 1.5 mA repeated at 3 Hz for 4 s) were first used as stimulation to serve as positive control for the evoked BOLD signal. Once that reliable fMRI signals were observed in response to electrical stimulation, optical stimulation was performed. An optical fiber of 200 µm core diameter (FT200EMT, Thorlabs, Germany) was connected to a 473 nm laser source (MBL-III, CNI, China) using a built-in FC/PC coupler to deliver blue light pulses at 3-10 Hz, 5-20 ms pulse width with different durations. To reach steady state 10 dummy scans were used and followed by 10 pre-stimulation scans, 5 scans during stimulation, and 25 inter-stimulation scans for 10 epochs and 5 scans during stimulation and 35 inter-stimulation scans for 12 epochs for thalamus and LH, respectively. The stimulation control was established using the BIOPAC system (MP150 System, BIOPAC Systems, USA) and Master 9 (Master-9, A.M.P.I., Israel).

Data analysis. For evoked fMRI analysis, EPI images were first aligned to anatomical images acquired in the same orientation with the same geometry. The anatomical MRI images were registered to a template across animals, as well as EPI datasets. The baseline signal of EPI images was normalized to 100 for statistical analysis of the multiple runs of EPI time courses. The hemodynamic response function (HRF) used the block function of the linear program 3dDeconvolve in AFNI. BLOCK (L, 1) is a convolution of a square wave of duration L, makes a peak amplitude of block response = 1, with the $g(t) = t^4 e^{-t} / [4^4 e^{-4}]$ (peak value = 1). The HRF model is defined as follows:

$$\mathrm{HRF(t) = int(g(t - s), s = 0..min(t, L))}$$

In this case, each beta weight represents the peak height of the corresponding BLOCK curve for that class, i.e., the beta weight is the magnitude of the response to the entire stimulus block.

The fiber optical neuronal calcium signals were low-pass filtered at 100 Hz using zero-phase shift digital filtering. The relative percentage change of fluorescence ($\Delta F/F$) was defined as $(F - F_0)/F_0$, where F_0 is the baseline, that is to say, the average fluorescent signal in a 2 s pre-stimulation window. The amplitudes of the neuronal fluorescent signal in response to 4 s optogenetic stimulus (Fig. 4f) were calculated as the average of difference in $\Delta F/F$ in a time window 300 ms after stimulus. Error bars in Figs. 3c, 4i, 5g, and Supplementary Fig. 10f represent standard deviation.

Reporting summary. Further information on research design is available in the Nature Research Reporting Summary linked to this article.

Data availability
The raw data can be provided upon email request to the corresponding author. Excel files containing raw data and each quantitative plot included in the main figures can be found in the Source Data File. For the design of the robotic arm, detailed information can be directly downloaded through the official link of World Intellectual Property Organization (WIPO): https://patentscope.wipo.int/search/en/detail.jsf?docId=EP215319263&tab=NATIONALBIBLIO&maxRec=1000.

Code availability
The Analysis of Functional NeuroImages software (AFNI, NIH, USA) and Matlab (MATLAB, MathWorks, USA) were used to process the fMRI and simultaneously acquired calcium signals, respectively. The relevant source codes can be downloaded through https://afni.nimh.nih.gov/afni/. The related image processing codes can be provided upon direct email request to the corresponding author.

References
1. Yu, X.: When Photons Meet Protons: Optogenetics, Calcium Signal Detection, and fMRI in Small Animals. In: Small Animal Imaging: Basics and Practical Guide, pp. 773 – 791 (Eds Kiessling, F., Pichler, B.J. & Hauff, P.). (Springer, Cham, Switzerland 2017).

2. Lee, J. H. et al. Global and local fMRI signals driven by neurons defined optogenetically by type and wiring. *Nature* **465**, 788–792 (2010).
3. Yu, X. et al. Sensory and optogenetically driven single-vessel fMRI. *Nat. Methods* **13**, 337–340 (2016).
4. Wang, M., He, Y., Sejnowski, T. J. & Yu, X. Brain-state dependent astrocytic Ca(2+) signals are coupled to both positive and negative BOLD-fMRI signals. *Proc. Natl. Acad. Sci. USA* **115**, E1647–E1656 (2018).
5. He, Y. et al. Ultra-slow single-vessel BOLD and CBV-based fMRI spatiotemporal dynamics and their correlation with neuronal intracellular calcium signals. *Neuron* **97**, 925–939 (2018).
6. Logothetis, N. K., Pauls, J., Augath, M., Trinath, T. & Oeltermann, A. Neurophysiological investigation of the basis of the fMRI signal. *Nature* **412**, 150–157 (2001).
7. Schulz, K. et al. Simultaneous BOLD fMRI and fiber-optic calcium recording in rat neocortex. *Nat. Methods* **9**, 597–602 (2012).
8. Liu, J. et al. Frequency-selective control of cortical and subcortical networks by central thalamus. *eLife* **4**, e09215 (2015).
9. Ferenczi, E. A. et al. Prefrontal cortical regulation of brainwide circuit dynamics and reward-related behavior. *Science* **351**, aac9698 (2016).
10. Kim, C. K. et al. Simultaneous fast measurement of circuit dynamics at multiple sites across the mammalian brain. *Nat. Methods* **13**, 325–328 (2016).
11. Marshall, J. D. et al. Cell-type-specific optical recording of membrane voltage dynamics in freely moving mice. *Cell* **167**, 1650–1662 (2016).
12. Tian, L. et al. Imaging neural activity in worms, flies and mice with improved GCaMP calcium indicators. *Nat. Methods* **6**, 875–881 (2009).
13. Chen, T. W. et al. Ultrasensitive fluorescent proteins for imaging neuronal activity. *Nature* **499**, 295–300 (2013).
14. Resendez, S. L. et al. Visualization of cortical, subcortical and deep brain neural circuit dynamics during naturalistic mammalian behavior with head-mounted microscopes and chronically implanted lenses. *Nat. Protoc.* **11**, 566–597 (2016).
15. Yu, X., Qian, C., Chen, D. Y., Dodd, S. J. & Koretsky, A. P. Deciphering laminar-specific neural inputs with line-scanning fMRI. *Nat. Methods* **11**, 55–58 (2014).
16. Dergacheva, O., Yamanaka, A., Schwartz, A. R., Polotsky, V. Y. & Mendelowitz, D. Optogenetic identification of hypothalamic orexin neuron projections to paraventricular spinally projecting neurons. *Am. J. Physiol. Heart Circ. Physiol.* **312**, H808–H817 (2017).
17. Kosse, C., Schone, C., Bracey, E. & Burdakov, D. Orexin-driven GAD65 network of the lateral hypothalamus sets physical activity in mice. *Proc. Natl. Acad. Sci. USA* **114**, 4525–4530 (2017).
18. Carter, M. E. et al. Tuning arousal with optogenetic modulation of locus coeruleus neurons. *Nat. Neurosci.* **13**, 1526–1533 (2010).
19. Sparta, D. R. et al. Construction of implantable optical fibers for long-term optogenetic manipulation of neural circuits. *Nat. Protoc.* **7**, 12–23 (2011).
20. Li, G. et al. Robotic system for MRI-guided stereotactic neurosurgery. *IEEE Trans. Biomed. Eng.* **62**, 1077–1088 (2015).
21. MacDonell, J. et al. Robotic assisted MRI-guided interventional interstitial MR guided focused ultrasound ablation in a swine model. *Neurosurgery* **84**, 1138–1148 (2018).
22. MacDonell, J. et al. Magnetic resonance-guided interstitial high-intensity focused ultrasound for brain tumor ablation. *Neurosurg. Focus* **44**, E11 (2018).
23. Starr, P. A. et al. Subthalamic nucleus deep brain stimulator placement using high-field interventional magnetic resonance imaging and a skull-mounted aiming device: technique and application accuracy. *J. Neurosurg.* **112**, 479–490 (2010).
24. Stoianovici, D. et al. Multi-imager compatible, MR safe, remote center of motion needle-guide robot. *IEEE Trans. Biomed. Eng.* **65**, 165–177 (2018).
25. Gassert, R., Moser, R., Burdet, E. & Bleuler, H. MRI/fMRI-compatible robotic system with force feedback for interaction with human motion. *IEEE/ASME Trans. Mech.* **11**, 216–224 (2006).
26. Min, H. K. et al. Subthalamic nucleus deep brain stimulation induces motor network BOLD activation: use of a high precision MRI guided stereotactic system for nonhuman primates. *Brain Stimul.* **7**, 603–607 (2014).
27. Squires, A. et al. MAPS—a magic angle positioning system for enhanced imaging in high-field small-bore MRI. *J. Med. Robot. Res.* **1**, 1640004 (2016).
28. Keith, G. A. et al. Automated tuning of an eight-channel cardiac transceive array at 7 Tesla using piezoelectric actuators. *Magn. Reson. Med.* **73**, 2390–2397 (2015).
29. Ryali, S. et al. Combining optogenetic stimulation and fMRI to validate a multivariate dynamical systems model for estimating causal brain interactions. *NeuroImage* **132**, 398–405 (2016).
30. Lin, P., Fang, Z., Liu, J., Lee, J. H. Optogenetic Functional MRI. *J. Vis. Exp.* **110**, e53346, (2016). https://doi.org/10.3791/53346.
31. Bonnavion, P., Mickelsen, L. E., Fujita, A., de Lecea, L. & Jackson, A. C. Hubs and spokes of the lateral hypothalamus: cell types, circuits and behaviour. *J. Physiol.* **594**, 6443–6462 (2016).
32. Boyden, E. S., Zhang, F., Bamberg, E., Nagel, G. & Deisseroth, K. Millisecond-timescale, genetically targeted optical control of neural activity. *Nat. Neurosci.* **8**, 1263–1268 (2005).
33. Liu, J. V. et al. fMRI in the awake marmoset: somatosensory-evoked responses, functional connectivity, and comparison with propofol anesthesia. *NeuroImage* **78**, 186–195 (2013).
34. Yen, C. C., Papoti, D. & Silva, A. C. Investigating the spatiotemporal characteristics of the deoxyhemoglobin-related and deoxyhemoglobin-unrelated functional hemodynamic response across cortical layers in awake marmosets. *NeuroImage* **164**, 121–130 (2018).
35. Mugler, J. P. 3rd & Brookeman, J. R. Three-dimensional magnetization-prepared rapid gradient-echo imaging (3D MP RAGE). *Magn. Reson. Med.* **15**, 152–157 (2001).
36. Pautler, R. G., Silva, A. C. & Koretsky, A. P. In vivo neuronal tract tracing using manganese-enhanced magnetic resonance imaging. *Magn. Reson. Med.* **40**, 740–748 (1998).
37. Pautler, R. G. & Koretsky, A. P. Tracing odor-induced activation in the olfactory bulbs of mice using manganese-enhanced magnetic resonance imaging. *NeuroImage* **16**, 441–448 (2002).
38. Yu, X. et al. Thalamocortical inputs show post-critical-period plasticity. *Neuron* **74**, 731–742 (2012).
39. Cregan, R. F. et al. Single-mode photonic band gap guidance of light in air. *Science* **285**, 1537–1539 (1999).
40. Russell, P. Photonic crystal fibers. *Science* **299**, 358–362 (2003).
41. Knight, J. C., Birks, T. A., Russell, P. S. & Atkin, D. M. All-silica single-mode optical fiber with photonic crystal cladding. *Opt. Lett.* **21**, 1547–1549 (1996).
42. Turchi, J. et al. The basal forebrain regulates global resting-state fMRI fluctuations. *Neuron* **97**, 940–952 (2018).
43. Saleem, K. S. et al. Magnetic resonance imaging of neuronal connections in the macaque monkey. *Neuron* **34**, 685–700 (2002).
44. Schmid, M. C. et al. Blindsight depends on the lateral geniculate nucleus. *Nature* **466**, 373–377 (2010).
45. Okada, S. et al. Calcium-dependent molecular fMRI using a magnetic nanosensor. *Nat. Nanotechnol.* **13**, 473–477 (2018).
46. Ghosh, S., Harvey, P., Simon, J. C. & Jasanoff, A. Probing the brain with molecular fMRI. *Curr. Opin. Neurobiol.* **50**, 201–210 (2018).
47. Hai, A., Cai, L. X., Lee, T., Lelyveld, V. S. & Jasanoff, A. Molecular fMRI of serotonin transport. *Neuron* **92**, 754–765 (2016).
48. Lee, T., Cai, L. X., Lelyveld, V. S., Hai, A. & Jasanoff, A. Molecular-level functional magnetic resonance imaging of dopaminergic signaling. *Science* **344**, 533–535 (2014).
49. Barandov, A. et al. Sensing intracellular calcium ions using a manganese-based MRI contrast agent. *Nat. Commun.* **10**, 897 (2019).
50. Miyagi, Y., Shima, F. & Sasaki, T. Brain shift: an error factor during implantation of deep brain stimulation electrodes. *J. Neurosurg.* **107**, 989–997 (2007).
51. Kramer, D. R., Halpern, C. H., Danish, S. F., Jaggi, J. L. & Baltuch, G. H. The effect of intraventricular trajectory on brain shift in deep brain stimulation. *Stereotact. Funct. Neurosurg.* **90**, 20–24 (2012).
52. Pallavaram, S. et al. Effect of brain shift on the creation of functional atlases for deep brain stimulation surgery. *Int. J. Comput. Assist. Radiol. Surg.* **5**, 221–228 (2010).
53. Paxinos, G., Watson, C., Calabrese, E., Badea, A. & Johnson, G. A. *MRI/DTI Atlas of the Rat Brain* (Elsevier, Academic Press, London, San Diego, 2015).
54. Chopra, R., Curiel, L., Staruch, R., Morrison, L. & Hynynen, K. An MRI-compatible system for focused ultrasound experiments in small animal models. *Med. Phys.* **36**, 1867–1874 (2009).
55. Yiannakou, M., Menikou, G., Yiallouras, C., Ioannides, C. & Damianou, C. MRI guided focused ultrasound robotic system for animal experiments. *Int. J. Med. Robot.* **13**, e1804 (2017). https://doi.org/10.1002/rcs.1804
56. Kim, D., Kobayashi, E., Dohi, T. & Sakuma, I. A new, compact MR-compatible surgical manipulator for minimally invasive liver surgery. *Lect. Notes Comput. Sci.* **2488**, 99–106 (2002).
57. Moser, R. et al. An MR compatible robot technology. *IEEE International Conference on Robotics and Automation*, 670–675 (2003).
58. Chen, Y. et al. Robotic system for MRI-guided focal laser ablation in the prostate. *IEEE/ASME Trans. Mech.* **22**, 107–114 (2017).
59. Franco, E., Ristic, M., Rea, M. & Gedroyc, W. M. Robot-assistant for MRI-guided liver ablation: a pilot study. *Med. Phys.* **43**, 5347 (2016).
60. Yoon, H. et al. Metabolomics of breast cancer using high-resolution magic angle spinning magnetic resonance spectroscopy: correlations with 18F-FDG positron emission tomography-computed tomography, dynamic contrast-enhanced and diffusion-weighted imaging MRI. *PLoS One* **11**, e0159949 (2016).
61. Su, H. et al. Piezoelectrically actuated robotic system for MRI-guided prostate percutaneous therapy. *IEEE/ASME Trans. Mech.* **20**, 1920–1932 (2015).
62. Tsekos, N. V., Khanicheh, A., Christoforou, E. & Mavroidis, C. Magnetic resonance—compatible robotic and mechatronics systems for image-guided

interventions and rehabilitation: a review study. *Annu. Rev. Biomed. Eng.* **9**, 351–387 (2007).

63. Shokrollahi, P., Drake, J. M. & Goldenberg, A. A. Signal-to-noise ratio evaluation of magnetic resonance images in the presence of an ultrasonic motor. *Biomed. Eng. Online* **16**, 45 (2017).

64. Shokrollahi, P., Drake, J. M. & Goldenberg, A. A. Ultrasonic motor-induced geometric distortions in magnetic resonance images. *Med. Biol. Eng. Comput.* **56**, 61–70 (2018).

65. Shokrollahi, P., Drake, J. M. & Goldenberg, A. A. Comparing the effects of three MRI RF sequences on ultrasonic motors. *IFMBE Proc.* **51**, 846–849 (2015).

66. Chinzei, K., Hata, N., Jolesz, F. A. & Kikinis, R. MR compatible surgical assist robot: system integration and preliminary feasibility study. *Medical Image Computing and Computer-Assisted Intervention—MICCAI 2000*, 921–930 (2000).

67. Tajima, F. et al. A prototype master-slave system consisting of two MR-compatible manipulators with interchangeable surgical tools—part of a unified support system for diagnosis and treatment. *IEEE International Conference on Robotics and Automation Proceedings*, Vols. 1–5, 2505–2510 (2004).

68. Tsekos, N. V., Ozcan, A. & Christoforou, E. A prototype manipulator for magnetic resonance-guided interventions inside standard cylindrical magnetic resonance imaging scanners. *J. Biomech. Eng. Trans. ASME* **127**, 972–980 (2005).

69. Gradinaru, V., Mogri, M., Thompson, K. R., Henderson, J. M. & Deisseroth, K. Optical deconstruction of parkinsonian neural circuitry. *Science* **324**, 354–359 (2009).

70. Plaha, P., Khan, S. & Gill, S. S. Bilateral stimulation of the caudal zona incerta nucleus for tremor control. *J. Neurol. Neurosurg. Psychiatry* **79**, 504–513 (2008).

71. Ondo, W. G., Silay, Y., Almaguer, M. & Jankovic, J. Subthalamic deep brain stimulation in patients with a previous pallidotomy. *Mov. Disord.* **21**, 1252–1254 (2006).

72. Silvestrini, M. T. et al. Interventional magnetic resonance imaging-guided cell transplantation into the brain with radially branched deployment. *Mol. Ther.* **23**, 119–129 (2015).

Author contributions

X.Y. designed and supervised the research. Y.C., X.Y., P.P.-R., and X.C. performed animal experiments. Y.C., X.Y., and P.P.-R. acquired data. Y.C. analyzed data. X.C. and M.H.F. provided key technical support. X.Y. and Y.C. wrote the manuscript.

Additional information

Supplementary Information accompanies this paper at https://doi.org/10.1038/s41467-019-10450-3.

Competing interests: X.Y. and Y.C. are co-authors of a patent that describes the mechanical design of the MRI-guided robotic arm (EP3315064). The other authors declare no competing interests.

Reprints and permission information is available online at http://npg.nature.com/reprintsandpermissions/

Journal peer review information: *Nature Communications* thanks Cornelius Faber, Gregory Fischer, and other anonymous reviewer(s) for their contribution to the peer review of this work. Peer reviewer reports are available.

Publisher's note: Springer Nature remains neutral with regard to jurisdictional claims in published maps and institutional affiliations.

Supplementary Information

MRI-guided robotic arm drives optogenetic fMRI with concurrent Ca^{2+} recording

Chen et al.

Supplementary Table: 1
Supplementary Figures: 13
Supplementary Movies: 7

Corresponding author:
Dr. Xin Yu
Email: xin.yu@tuebingen.mpg.de
Address: Max-Planck-Ring 11, 72076, Tuebingen, Germany
Phone: +49 7071 601-740
Fax: +49 7071 601-701

Supplementary Table (1)

30

31

32 **Supplementary Table 1.** List of Components of MgRA

33

Name	Information
Archimedean spiral driving design	Custom-designed, MPI for BC Mechanic Workshop
Bearings for back/forward	JSM-2022-20, Igus, Germany
Bearings for left/right	BB-625-B180-10-GL, Igus, Germany
Belts	Optibelt OMEGA 3M, OPTIBELT, Germany
Camera	RS-OV7949-1818, Conrad Electronic, Germany
Carbon fiber tube (1)	7420182, R&G, Germany
Carbon fiber tube (2)	7420173, R&G, Germany
Charging condenser	Z-K4700/50, Nanotec, Germany
Cross table	Custom-designed, MPI for BC Mechanic Workshop
Encoder cable	ZK-NOE1-10-20000-S, Nanotec, Germany
Encoders	NOE2-05-B14, Nanotec, Germany
Gearbox	GPLE22-2S-12, Nanotec, Germany
Matching toothed pulley	Custom-designed, MPI for BC Mechanic Workshop
Motor controller	SMCI33-1, Nanotec, Germany
Platform for MgRA	Custom-designed, MPI for BC Mechanic Workshop
Power supply	NTS-24V-40A, Nanotec, Germany
Rat holder	Custom-designed, MPI for BC Mechanic Workshop
Robotic arm holder	Custom-designed, MPI for BC Mechanic Workshop
Stepper motor	ST4118D1804-B, Nanotec, Germany
USB cable for motor controller	ZK-USB, Nanotec, Germany
Cable lengthening	Custom-designed, MPI for BC Electronic Workshop
Other pieces of MgRA	Custom-designed, MPI for BC Mechanic Workshop

34

35

36

37 **Supplementary Figures (13)**
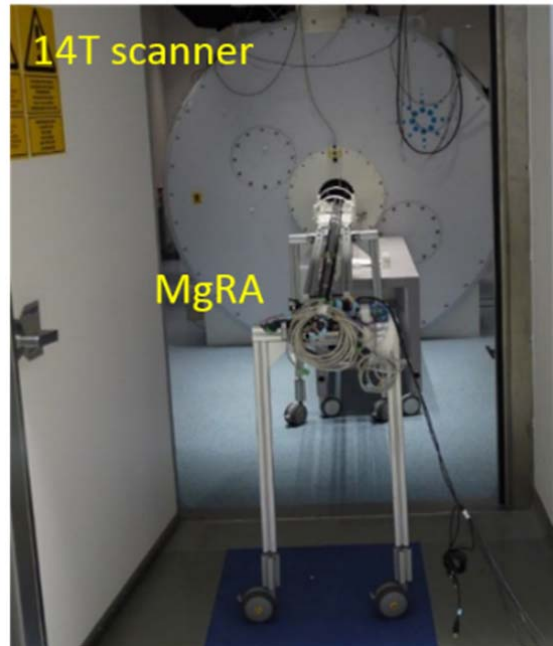
38

39 **Supplementary Figure 1.** MRI compatible MgRA mounted inside the 14T MRI scanner (picture taken from the control
40 room).

41
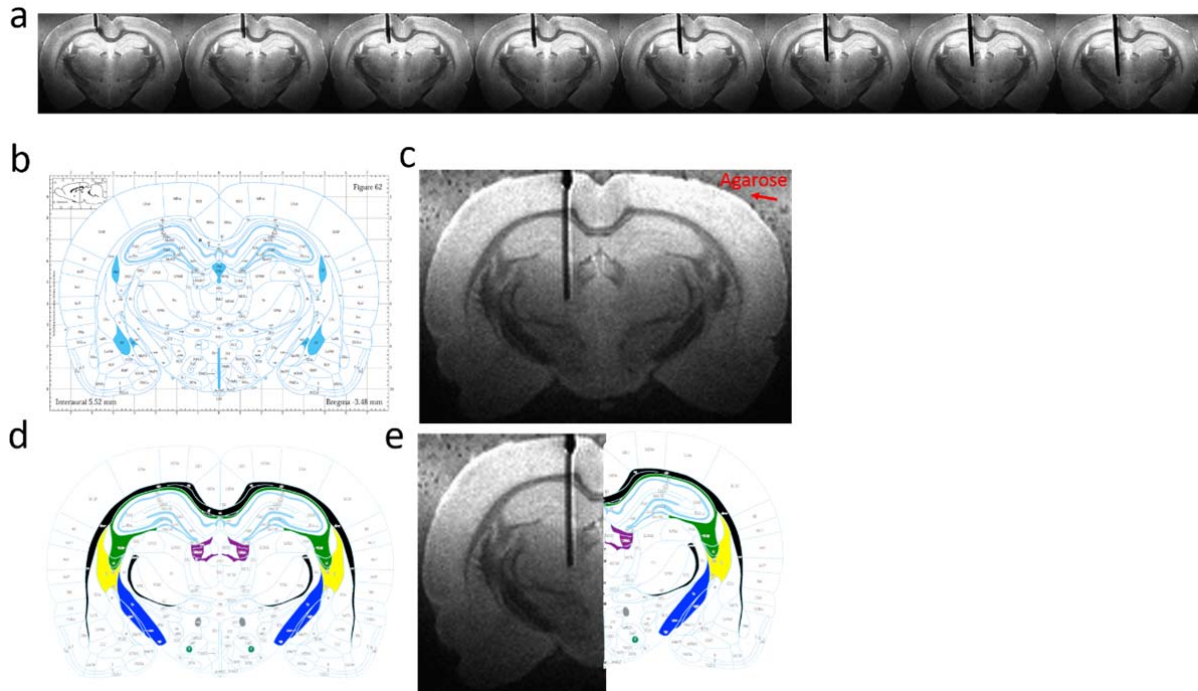
Supplementary Figure 2. Examples of optical fibers with different core diameters driven by MgRA for *in vitro* evaluation. **a** The T2-weighted MRI images show 8 different locations of the optical fiber (400 μm core diameter, black stripe) along the insertion trajectory in a perfused rat brain embedded in the soft agarose with manganese. **b** A coronal rat brain atlas diagram (reproduced from Paxinos and Watson, 2005). **c** Optical fiber (200 μm core diameter, black stripe) was inserted vertically into the perfused rat brain. **d** The same atlas diagram whose structures are selected to label and assigned a color code. **e** Anatomical image (left) is shown adjacent to the plate of atlas (right) after alignment. The Fiber was targeting the central thalamus.

52
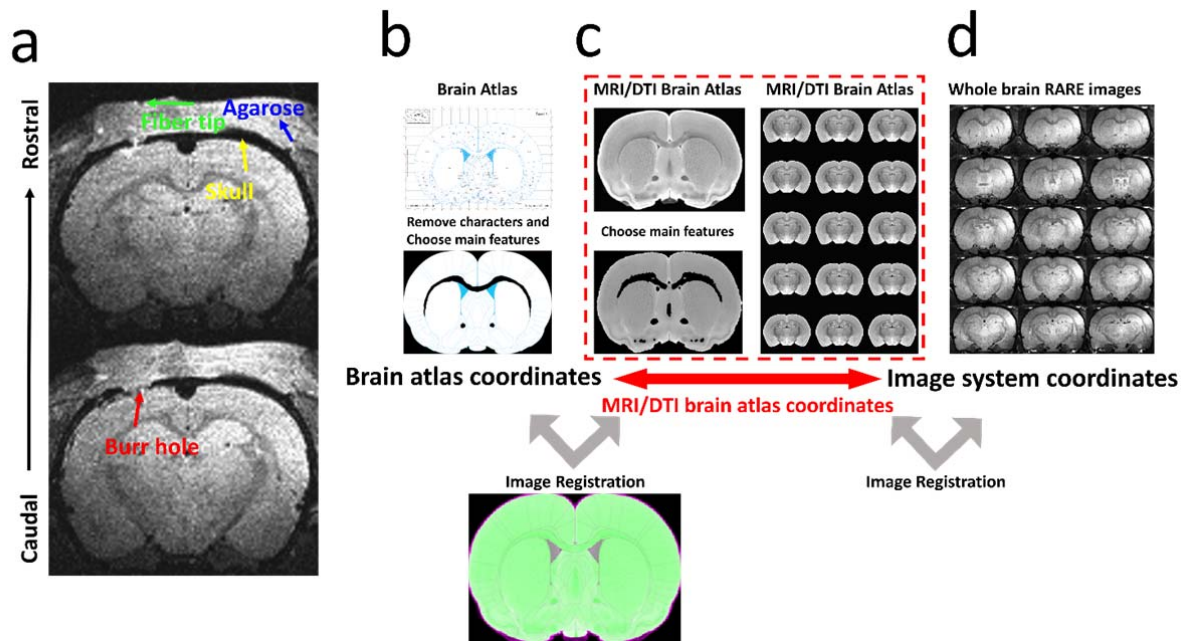
Supplementary Figure 3. MRI-based relocation outside of the rat brain and the registration of coordinates. **a** Agarose with manganese was applied to cover the skull (yellow arrow). By lowering the fiber into the agarose, we could calculate the distance between fiber tip (green arrow) and burr hole (red arrow) from the anatomical images. The burr hole is filled with agarose as well. **b** Brain atlas coordinates (Co1, Paxinos & Watson rat brain atlas, 6th edition). **c** MRI/DTI Atlas of the Rat Brain (Co2, George Paxinos, Charles Watson, Evan Calabrese, Alexandra Badea and G Johnson, 1st edition). **d** 3D anatomical images of an individual rat.

For coordinates registration, agarose has been previously applied above the burr hole of the skull and the fiber tip (previously positioned above the burr hole using the MgRA system under the guidance of the build-in camera inside the MR scanner) can be directly imaged to determine its coordinates in the MRI images (Supplementary Figure 3a). Then, an algorithm was designed to register a four coordinate system for the fiber tip position: Brain atlas coordinate (Co1, Paxinos & Watson rat brain atlas, 6th edition), MRI/DTI rat brain atlas (Co2, George Paxinos, Charles Watson, Evan Calabrese, Alexandra Badea and G Johnson, 1st edition), MRI coordinate (Co3) and robotic arm coordinate (Co4). In short, the Co1 is first transferred to the Co2 by the algorithm (Supplementary Figure 3b, c). By registering the 2D anatomical images of individual rat (Co3) to the MRI/DTI brain atlas (Co2), the transformation between the Co1 and Co3 is settled (Red arrow in Supplementary Figure 3c). Since the fiber tip position is directly detected in the MRI images above the craniotomy, the related coordinate offset from the fiber tip to the targeted function nuclei can be calculated based on the multiple transformation matrices.
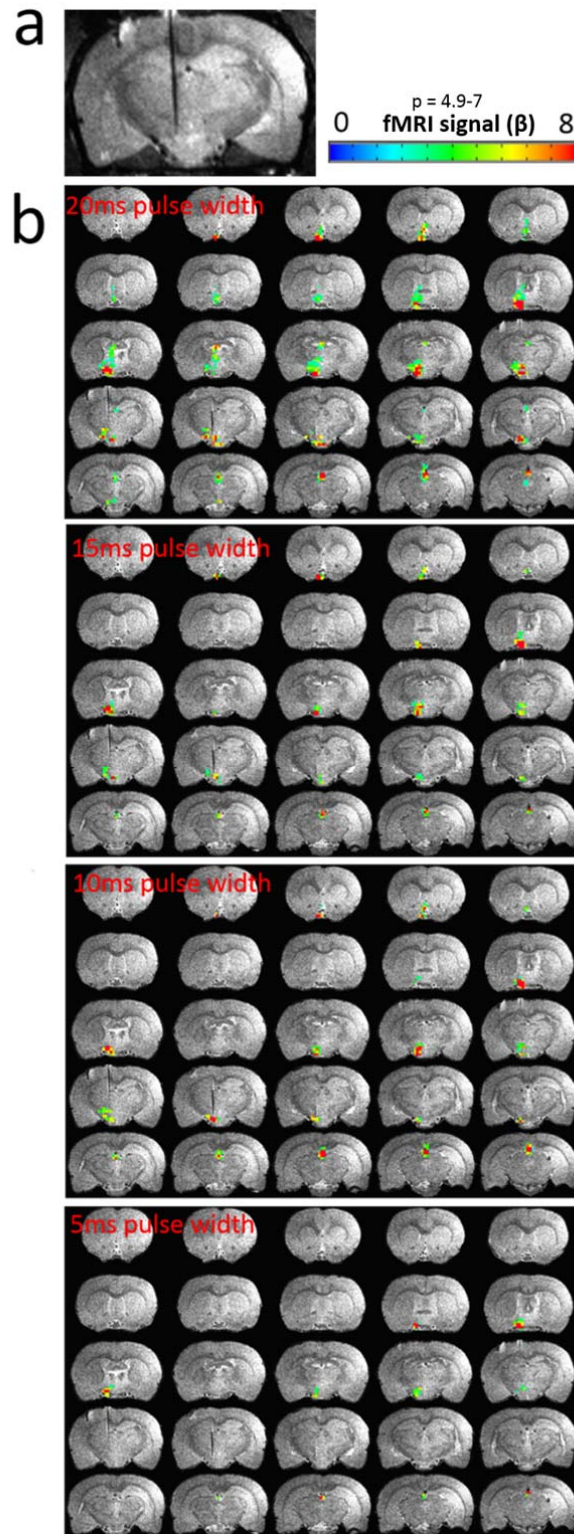
71
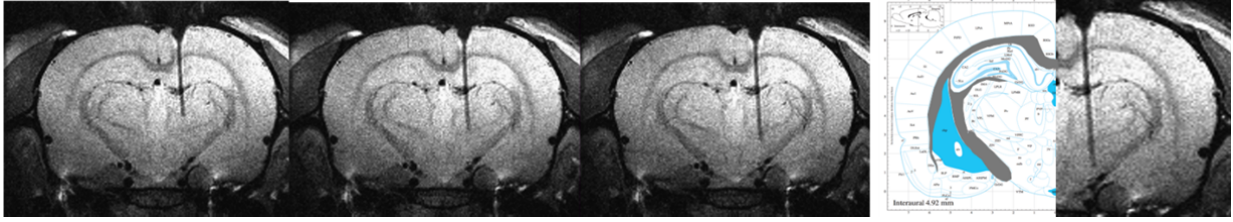
Supplementary Figure 4. The time-lapsed anatomical images to illustrate the optical fiber targeting the Lateral Hypothalamus for opto-fMRI studies.

74

Supplementary Figure 5. Whole brain activity maps in response to 15s LH optogenetic stimulation at different pulse widths. **a** Anatomical image showing the position of the optical fiber for delivering light. **b** BOLD activation maps of a representative animal exhibited a pulse width-dependent pattern in response to 20ms, 15ms, 10ms and 5ms pulse widths (5 Hz, laser power of 12.6 mW, 15 s on 45 s off, 12 epochs). GLM-based t-statistics in AFNI is used.

79
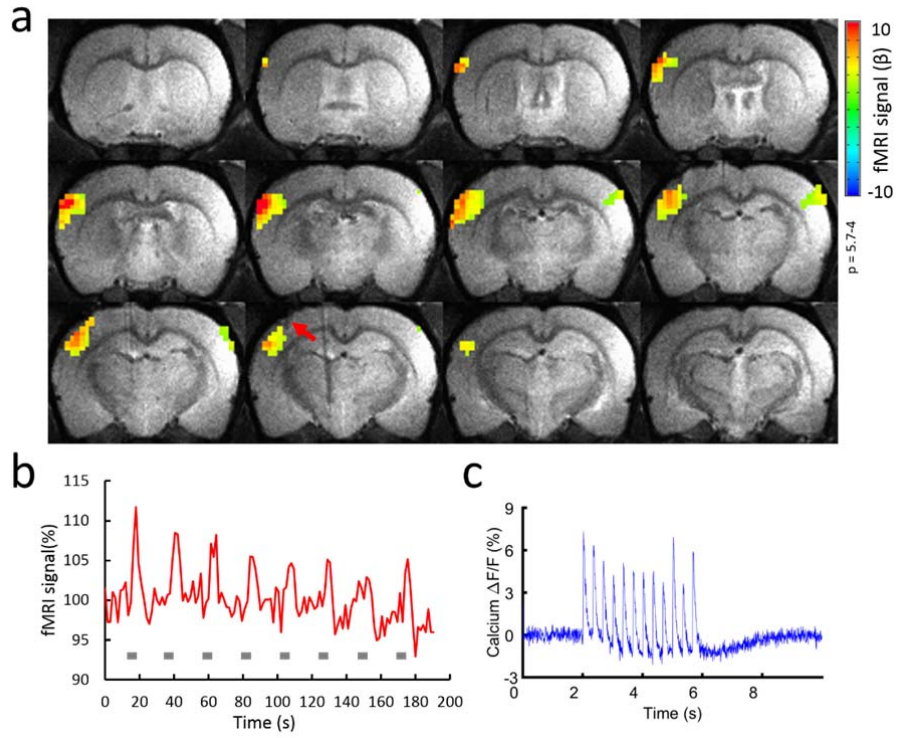
Supplementary Figure 6. Sensory-evoked neuronal Ca^{2+} recordings with simultaneous BOLD fMRI. **a** Representative color-coded BOLD-fMRI in response to a block design whisker-electrical stimulation. GLM-based t-statistics in AFNI is used. **b** The time course of evoked fMRI signal from BC-S1 ROI (see **a**) in the left hemisphere. **c** Average of simultaneously optical fiber (red arrow in **a**) recorded Ca^{2+} signals for one epoch (3 Hz, 4 s, 2 mA).
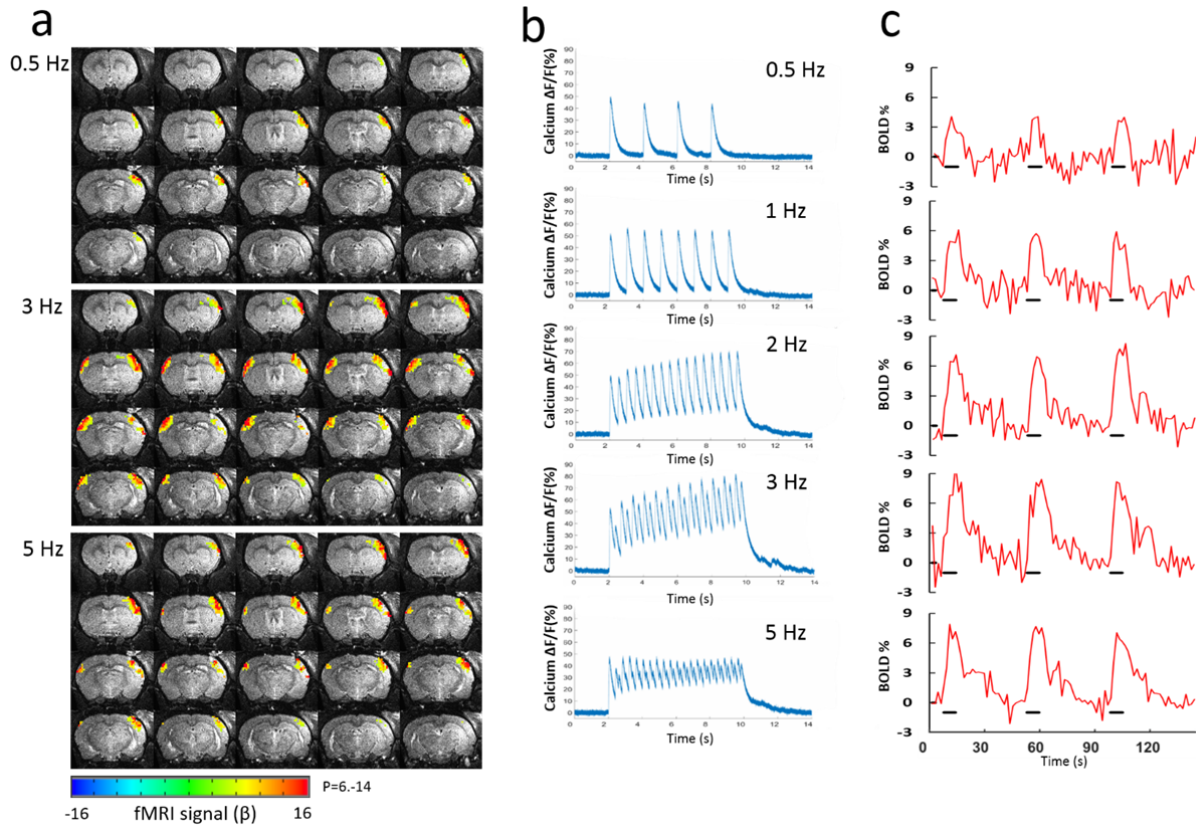
84
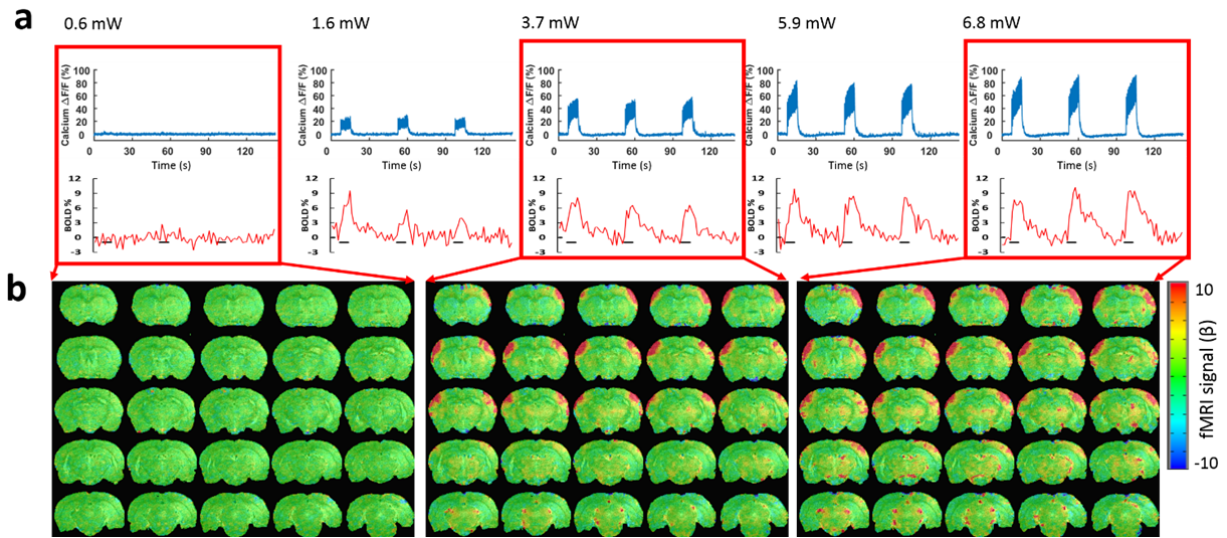
Supplementary Figure 7. Laser power dependent BOLD signals in S1 with simultaneous Ca^{2+} recordings (S1BF) upon light exposure in VPM. **a** Representative percentage changes of calcium signal (top) and BOLD responses (lower) for 3 epochs detected at 5 different laser powers. At 0.6 mW, hardly any fMRI and calcium signal was detected. BOLD and calcium signal increased proportionally with increased laser power. **b** Examples of whole brain activity maps at 0.6 mW, 3.7 mW and 6.8 mW.

Supplementary Figure 8. Frequency dependent BOLD signals in S1 with simultaneous Ca^{2+} recordings (S1BF) upon light exposure in the Thalamus. **a** Examples of BOLD maps in response to 0.5 Hz, 3 Hz, 5 Hz. The strongest response was induced by 3 Hz stimulation, instead of 5 Hz. GLM-based t-statistics in AFNI is used. **b** Averaged calcium signal percentage change in one epoch. Evoked calcium spikes with almost full recovery to the baseline in 2 s per spike at 0.5 Hz. From 1 Hz to 3 Hz, the calcium signal was elevated through the 8 s stimulation period, while at 5 Hz, some of the spikes per pulse were even missed and the overall plateau amplitude was not further increased. **c** BOLD signal for 3 epochs upon stimulation (black line) was increased according to the increased frequency, but not at 5 Hz, which is consistent with the calcium signal observation.

102
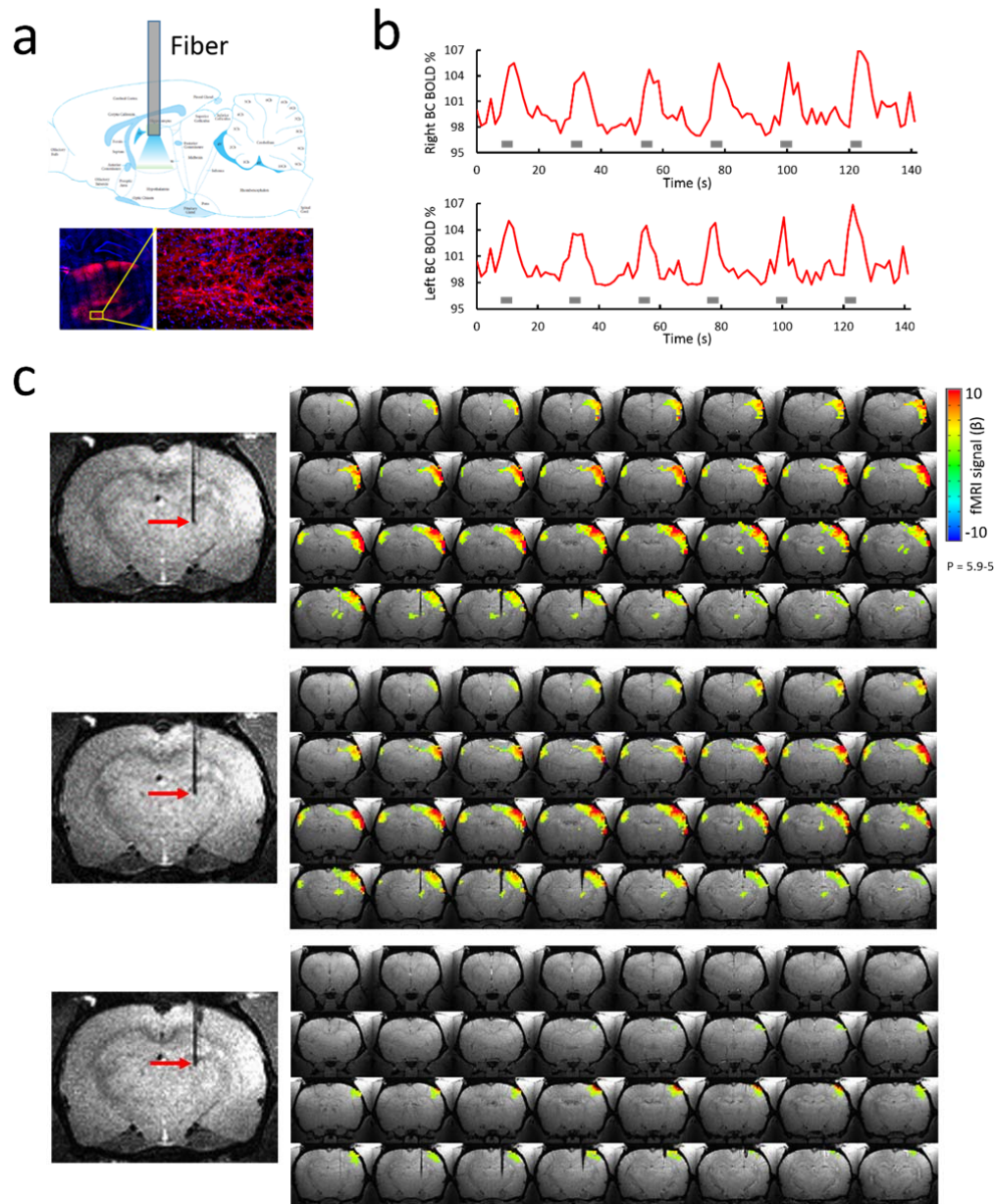
Supplementary Figure 9. Optogenetic excitation of thalamic cells drives local and Somatosensory cortical positive BOLD. **a** Top: Sketch showing the point of thalamic injection of AAV5.CAG.ChR2-mCherry and optical stimulation. Lower: histological image of ChR2-mCherry expression in the thalamus (left); higher magnification (right). Red, ChR2-mCherry; blue, 4′,6-Diamidin-2-phenylindol (DAPI). **b** Opto-fMRI haemodynamic response (averaged across activated voxels in Somatosensory cortical ROI, see **c**, whole brain top right) in both hemispheres during optical stimuli (5Hz, 4s on 18.5s off, 10 ms pulse width, laser power 5.5 mW). **c** BOLD activation at 3 different locations along the vertical insertion trajectory. GLM-based t-statistics in AFNI is used.

110

111
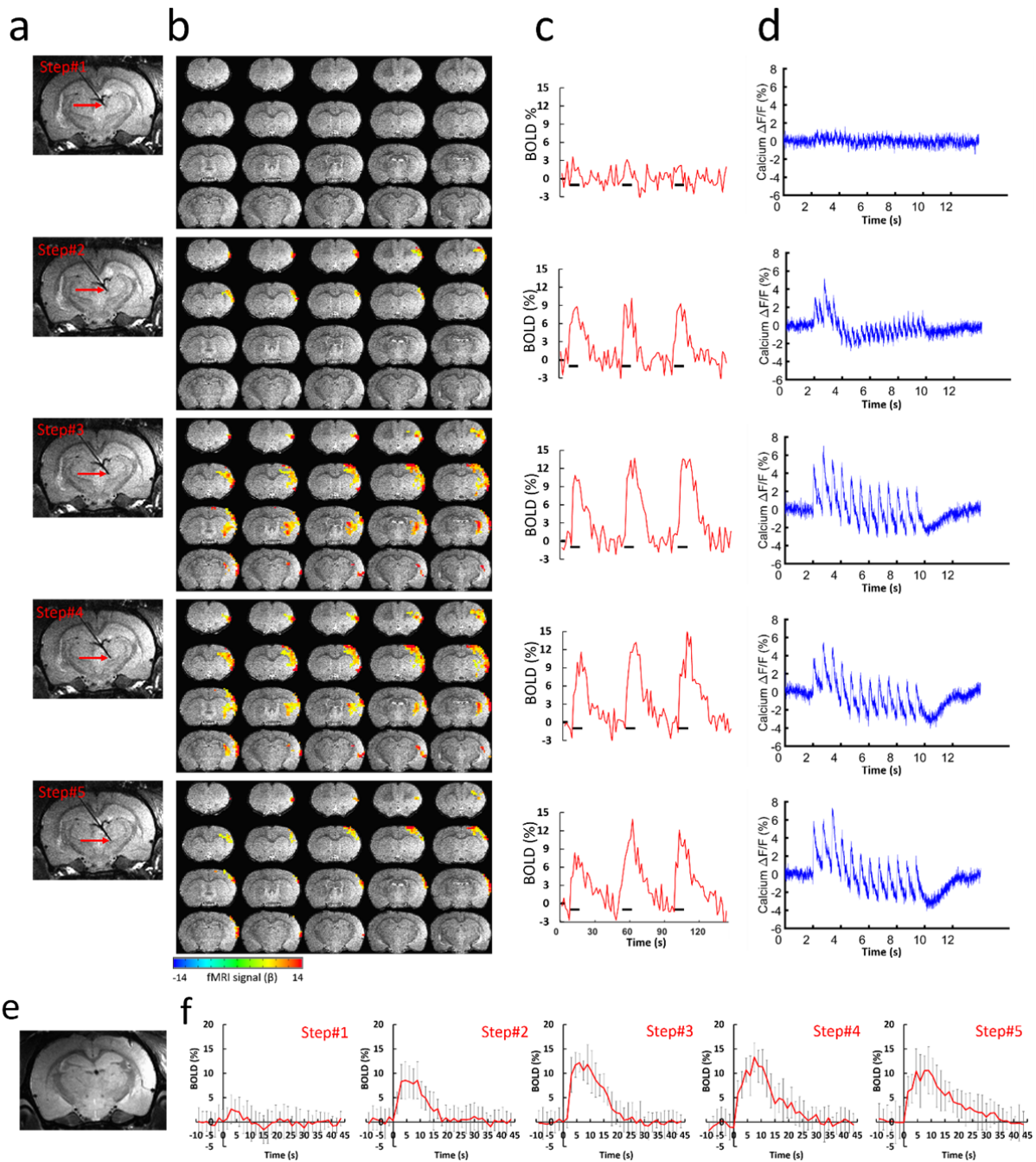
Supplementary Figure 10. Region-specific optogenetic activated neuronal Ca^{2+} recordings with simultaneous BOLD fMRI. **a** T2-weighted anatomical images illustrate five fiber locations. **b** Different BOLD fMRI in Somatosensory cortex evoked by optogenetic stimuli in different thalamic regions. **c** BOLD signals for 3 epochs (3 Hz, Laser power 4.2 mW, 8 s on 37 s off, 10 epochs) within ipsilateral Somatosensory cortex ROI (see b middle panel) corresponding to the different locations. **d** Simultaneously recorded evoked calcium signal through the 8 s stimulation period. **e** Anatomical RARE MR image illustrates the fiber tip location for calcium recording in Barrel cortex. **f** The average BOLD signals of ipsilateral hemisphere at different fiber tip locations. Error bars represent mean±SD.
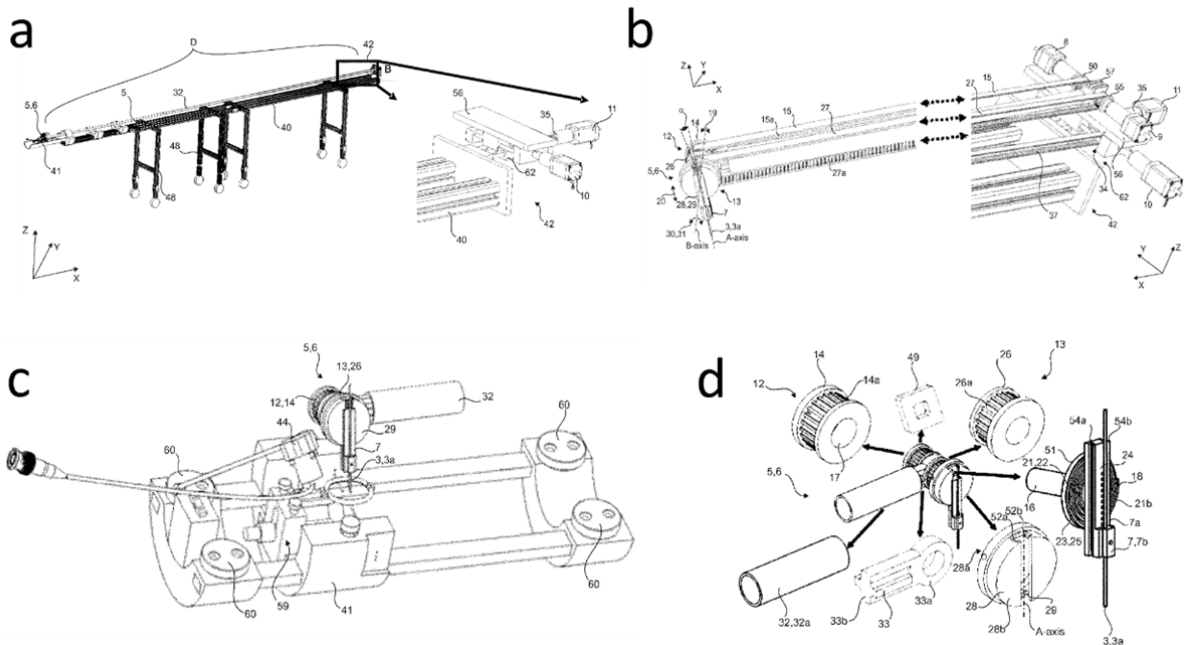
119
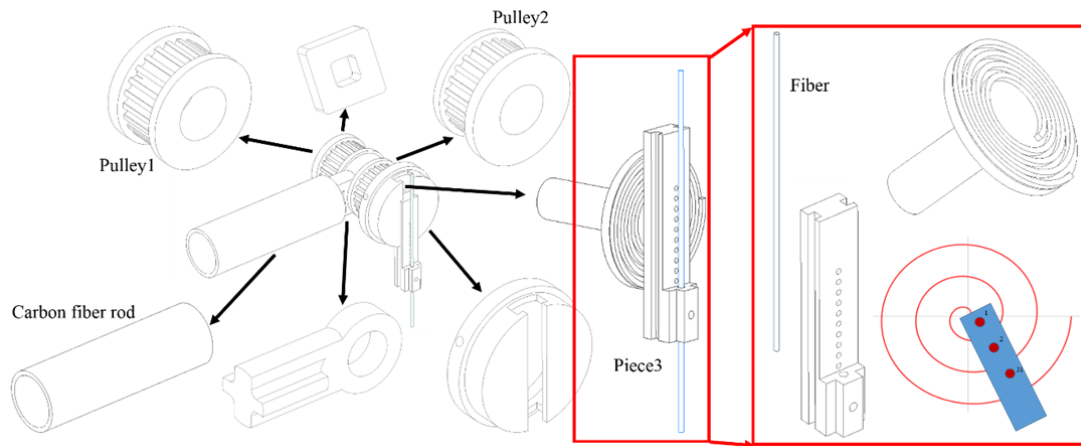
120

121   **Supplementary Figure 11**. Detailed design for head part of the MgRA.
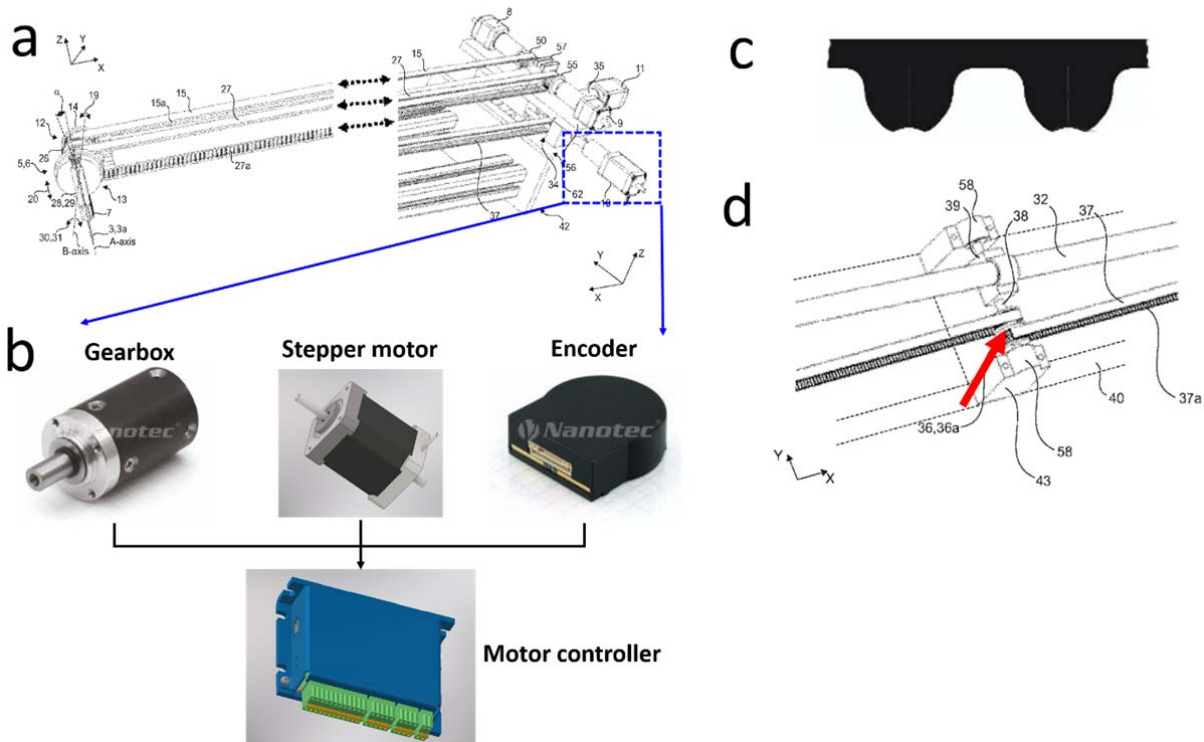
122

123

124

125 **Supplementary Figure 12**. Detailed design of the MgRA (figures from the approved European patent). **a** The schematic

126 view of the whole MgRA mechanical design including the cross table to mount the stepper motors. **b** The coupling of the

127 stepper motors (back part) to the matching toothed pulley in the head was achieved by a synchronous belt drive in a

128 form-fit manner. **c** Custom-designed rat holder with a built-in MRI compatible camera, surface coil and head part of the

129 MgRA. **d** The components of the head part of the MgRA. For more details see the approved European patent as

130 following   link:

131 (https://patentscope.wipo.int/search/en/detail.jsf?docId=EP215319263&tab=PCTDESCRIPTION&maxRec=1000).

132

133

134

Supplementary Figure 13. Detailed design of the back part of the MgRA. **a** The coupling of the stepper motors (back part) to the matching toothed pulley in the head was achieved by a synchronous belt drive in a form-fit manner. **b** The encoder (NOE2-05-B14, Nanotec, Germany) is used with motor controller (SMCI33-1, Nanotec, Germany) so that the stepper motor (ST4118D1804-B, Nanotec, Germany) can be run in a close-loop mode. All the images here are from Nanotec, Germany. **c** Multi-groove belt (optibelt OMEGA 3M, Optibelt, Germany) used to fit into a matching toothed pulley. The image of synchronous belt is from Optibelt, Germany. **d** Closed belts can be cascaded to transfer the motion (red arrow). All schematic figures shown here are from the approved MgRA European patent.

142

PART IV. CURRICULUM VITAE

Curriculum Vitae - Patricia Pais Roldán

EDUCATION

Max Planck Institute for Biological Cybernetics & Graduate Training Center of Neuroscience — Tübingen, Germany
PhD. Neuroscience — 2014-2019

Madrid Technical University — Madrid, Spain
MSc. Biomedical Engineering — 2013-2014

Alcalá University — Madrid, Spain
BSc. Medical Biology — 2009-2013

Gregorio Marañón — Madrid, Spain
High School in Science – graduated with honors

AWARDS

Nicolás Achucarro Best Scientific Poster Award — 2017
Spanish Society for Neuroscience (SENC) Meeting

Scientific Poster Presentation Award — 2015
European Society for Molecular Imaging (ESMI) Meeting

Trainee Stipend Award — 2015
International Society for Magnetic Resonance in Medicine (ISMRM)

RESEARCH EXPERIENCE

2019-present — **Forschungszentrum Jülich: Institute of Neuroscience and Medicine** (Prof. Dr. John Shah). Post-doc.

2014-2019 — **Max Planck Institute for Biological Cybernetics** (Dr. Xin Yu, Dr. med Brian Edlow & Prof. Dr. Klaus Scheffler). PhD-fellow.

2014-2015 — **Centre for Biomedical Technologies** (Prof. Dr. Ceferino Maestú & Dr. Irene Sendiña-Nadal). Graduate researcher.

2013-2013 — **Alcalá University** (Dr. Alberto Escarpa). Undergraduate researcher.

2012-2012 — **Alcalá University** (Dr. David Díaz Martín). Undergraduate researcher.

PEER-REVIEWED PUBLICATIONS

1. Pais-Roldan, P., Takahashi, K., Chen, Y., Jiang, Y., Zeng, H. and X. Yu (2019). "Indexing arousal with multi-modal fMRI merging pupillometry and optical fiber calcium recording." [In submission process]

2. Chen, Y., Pais-Roldan, P., Chen, X., Frosz, M. H. and X. Yu (2019). "MRI-guided Robotic Arm drives optogenetic fMRI with concurrent Ca2+ recording." Nat Commun **10**(1):2536.

3. Pais-Roldan, P., B. L. Edlow, Y. Jiang, J. Stelzer, M. Zou and X. Yu (2019). "Multimodal assessment of recovery from coma in a rat model of diffuse brainstem tegmentum injury." Neuroimage **189**: 615.

4. Pais-Roldan, P., B. Biswal, K. Scheffler and X. Yu (2018). "Identifying Respiration-Related Aliasing Artifacts in the Rodent Resting-State fMRI." Front Neurosci **12**: 788.

5. Pais-Roldan, P., A. P. Singh, H. Schulz and X. Yu (2016). "High magnetic field induced otolith fusion in the zebrafish larvae." Sci Rep **6**: 24151.

PRESENTATIONS AT SCIENTIFIC CONFERENCES

Poster presentations:

1. Pais Roldán P, Edlow B, Stelzer J, Jiang Y, Zou M and Yu X (June 2018): **Mapping the functional recovery of brainstem injury-induced comatose rats with eigenvector-centrality mapping and seed-based analysis of resting-state fMRI**. 26th Annual Meeting and Exhibition of the International Society for Magnetic Resonance in Medicine (ISMRM 2018), Paris, France.

2. Pais Roldán P, Edlow B, Stelzer J, Jiang Y and Yu X (June 2018): **Brain or cardiovascular oscillation: ultra-slow oscillations under 0.01 Hz detected by resting-state fMRI**. 26th Annual Meeting and Exhibition of the International Society for Magnetic Resonance in Medicine (ISMRM 2018), Paris, France.

3. Pais Roldán P, Edlow B, Jiang Y, Stelzer J, Zou M and Yu X (November 2017): **A rat model of coma pathogenesis and recovery**, 47th Annual Meeting of the Society for Neuroscience (SfN 2017), Washington, DC, USA.

4. Pais Roldán P, Edlow B, Jiang Y, Stelzer J, Zou M and Yu X (September 2017): **Experimental model for coma research**, 17th Annual Meeting of the Spanish Society for Neuroscience (SENC 2017), Alicante, Spain.

5. Chen Y, Pais Roldán P, Chen X and Yu X (April 2017): **Stepwise optogenetic activation of the rat thalamic nuclei with MRI-guided robotic arm (MgRA)**, 25th Annual Meeting and Exhibition of the International Society for Magnetic Resonance in Medicine (ISMRM 2017), Honolulu, HI, USA.

6. Pais Roldán P, Edlow B and Yu X (May 2016): **Developing a Rat Model of Brainstem Coma: Initial MRI and MRA Investigations of Basilar Artery Occlusion**, 24th Annual Meeting and Exhibition of the International Society for Magnetic Resonance in Medicine (ISMRM 2016), Singapore.

7. Pais Roldán P, Singh A, Merkle H, Schulz H and Yu X (March 2015): **Magnetic field-induced otolith fusion of the zebrafish larvae**, 10th Annual Meeting of the European Society for Molecular Imaging (EMIM 2015), Tübingen, Germany.

8. Pais Roldán P and Escarpa A (July 2013): **Portable microfluidic nanodevice for early diagnosis of Galactosemia**, VI Workshop on Analytical Nanoscience and Nanotechnology (VINyNA 2013), Madrid, Spain.

Oral Communications:

1. Pais Roldán P, Edlow B, Jiang Y, Stelzer J, Zou M and Yu X (March 2018): **Eigenvector centrality mapping and seed-based analysis of resting state fMRI during acute brainstem-coma recovery in the rat**, 13th European Molecular Imaging Meeting (EMIM 2018), San Sebastián, Spain.

2. Pais Roldán P, Jiang Y, Edlow B, Stelzer J, and Yu X (March 2018): **BOLD fluctuations under 0.01 Hz detected in resting-state functional MRI**, 13th European Molecular Imaging Meeting (EMIM 2018), San Sebastián, Spain.

3. Jiang Y, Chen X, Pais Roldán P and Yu X (November 2017): **Two channel fiber optic mediated glutamate and calcium recording with simultaneous fMRI**, 47th Annual Meeting of the Society for Neuroscience (SfN 2017), Washington, DC, USA.

4. Pais Roldán P, Singh A, Merkle H, Schulz H and Yu X (June 2015): **Sensing the high magnetic field: Fusion of otoliths in zebrafish larvae entails a hint**, 23rd Annual Meeting and Exhibition of the International Society for Magnetic Resonance in Medicine (ISMRM 2015), Toronto, Canada

PART V. ACKNOWLEDGEMENTS

I have to thank several people and non-human animals for their direct or indirect contribution to the development of this PhD Thesis.

Thanks, in the first place, to my PhD mentor, for believing in my potential when I first approached him. For giving me an honest feedback about the things that are good and the ones that are not, for sharing his feelings about the multiple faces of Science, for his motivational unexpected talks and for his will to help in anything that could improve my scientific career. For the wonderful people that I know thanks to him.

Thanks to all my colleagues, for the help, for the positive thinking, for the fun.

Thanks to Tina for explaining all I needed to know, for her patience, her warm treatment, and for my first bike in Germany.

Thanks to Hildegard for making all possible in the lab, and for feeling like family from the moment I arrived.

Thanks to Mihai, for finally always passing by and fixing every sudden problem on the PC.

Thanks to all the smart guys in the e- and m- workshops. Some projects would be just unimaginable without them.

Thanks to everyone who has given me a useful answer, a tip, or a smile when I was lost.

Special thanks to my family, for giving me always full support and reminding me that Science is not the most important thing of my life. To Inka, for waking me up every single morning and for always making me smile. To Isabel, for sharing her voice with me every single day.

Thanks to all the rats, always innocently kind to us before entering anesthesia, who have donated their brains to Science. Thanks to the vets and the animal caretakers, who put their efforts in making their life a little bit better day by day.